

**Developing a recombinant model of
the P2Y₁ and P2Y₁₁ receptor
interactions mediating relaxation in
gut smooth muscle**

Batoul Farran

A thesis submitted for the degree of Doctor
of Philosophy

September 2014

**Institute of Structural and Molecular Biology
University College London**

Declaration

The work presented in this thesis was undertaken at University College London. I, Batoul Farran, confirm that the work presented in this thesis is my own. Where information has been derived from other sources, I confirm that this has been indicated in the thesis.

Abstract

ATP and ADP mediate gut smooth muscle relaxation through two receptors, P2Y₁ and P2Y₁₁. This project aims to investigate the interaction between these two receptors by developing a recombinant model of the P2Y receptors expressed in gut smooth muscle cells (SMCs) by transfecting the human P2Y₁₁ receptor cDNA into CHO-K1 cells, which express an endogenous P2Y₁ receptor. Individual clonal cell lines expressing different densities of hP2Y₁₁ were isolated from this stably-transfected CHO-K1:P2Y₁₁ pool and characterized. A clone expressing a “high” density of hP2Y₁₁ (13) and a clone expressing a “low” density of hP2Y₁₁ (6) were selected for further study. Control 1321N1 cell lines expressing each receptor in isolation (1321N1-hP2Y₁ and 1321N1-hP2Y₁₁) were used for comparison purposes. The potency (EC₅₀) of eight different nucleotide agonists was determined in calcium assays in the co-expressing cell lines. ADP and 2meSATP responses were biphasic in clone 13 but monophasic in clone 6. To investigate the nature of the two sites of the biphasic curves in clone 13, the effect of MRS 2179, NF 340 and Reactive Red on agonist responses was determined. MRS 2179 antagonized the high affinity site of the biphasic ADP and 2meSATP responses in clone 13 without affecting the low affinity site. NF 340 had no effect on agonist responses in clone 13. Reactive Red antagonized both sites of the biphasic curves in clone 13. These data suggest that the high-affinity site of the biphasic ADP and

2meSAMP responses in clone 13 corresponds to P2Y₁. The low-affinity site of the 2meSAMP curve is most likely P2Y₁₁. The low-affinity site the ADP response displays both P2Y₁ and P2Y₁₁-like. The novel ADP site, therefore, is elicited by differences in the expression level of P2Y₁₁ and may correspond to a P2Y₁:hP2Y₁₁ receptor heteromer or a macromolecular complex containing both P2Y₁ and P2Y₁₁.

Acknowledgements

“And what, Socrates, is the food of the soul? Surely, I said, knowledge is the food of the soul.” Plato

Faced with the unfathomable vastness of the universe and animated by the desire to comprehend the mystery of existence and workings of the material world, the human species has engaged in an unrelenting quest of philosophical and scientific understanding. From Gilgamesh’s ancient journey in pursuit of wisdom and knowledge to the latest astronomical voyages into space, this millennial search has engendered the most exciting discoveries and an appreciation of the intricate, complex ways of Nature. Nature knows how to assemble, orchestrate interactions and disassemble structures in an organizational and communicational feat that research is only beginning to unmask. Growing up in a family that is passionate about intellectual endeavours, I was raised with a sense of curiosity and an interest for scientific enquiry since my early days. I dedicate this thesis to my parents, who have instilled me with a thirst for knowledge and a deep respect for every atom of the universe. I suppose the constant hammering about Plato and Einstein has led to something useful after all!! I also thank them for constantly encouraging me to transgress my own boundaries and explore novel avenues of life, in line with Gibran Khalil’s saying “Children are not your children. They are the sons and daughters of Life’s longing for itself.”

The completion of this thesis was only made possible by the assistance, guidance and unconditional help of my supervisor, Dr. Andrea Townsend-Nicholson. The philosopher Immanuel Kant states, “Science is organized knowledge”. This sentence perfectly depicts the progress of my doctoral research. I cannot thank Andrea enough for putting up with the sometimes chaotic nature of my thinking and for her persistent effort

to organise this untidiness. Her teaching and encouragement have taught me to think in a more logical fashion. For this, I am grateful to her for life, as she has moulded me into a better scientist.

In the course of my PhD I have had the chance to work with dedicated scientists, from whom I have learned a lot. I would like to thank Dr. Brian King and Dr. Saul Purton for their supervision and valuable suggestions on conducting my research. Your feedback has helped me expand and improve my scientific thinking and critical abilities. Thank you to Dr. Mina Edwards for her help with tissue culture facilities. Thank you to Dr. Peter Coveney for his guidance and advice. I would also like to thank the previous and current members of the Townsend-Nicholson lab, namely Qing Cai, Carmen Morcelle, Michael Baron and Nojood Al-Twajry, for their friendship, support and encouragement during the course of my PhD project. Thank you to Dr. Raquel Montenegro for her incessant support! Her unfailing encouragement and help have helped me navigate through the last months of my PhD.

Thank you to my enlarged family and friends for believing in me. Your kindness has inspired me to overcome my moments of doubt, regain faith in myself and march steadily towards my goal. I am grateful for your love. I would especially like to thank my younger sister, Sarah, for her comforting presence, her beautiful self and for challenging me to think differently, thus motivating me to become a better version of myself.

Batoul Farran

September 2014

Contents Page

Declaration.....	i
Abstract.....	i
Acknowledgements.....	iii
Table of Contents.....	v
List of Figures.....	ix
List of Tables.....	xiii
Abbreviations.....	xv
Chapter 1 – Introduction.....	01
1.1 G-protein coupled receptors.....	01
1.1.1 GPCR structure.....	01
1.1.2 GPCR activation.....	04
1.1.3 GPCR oligomerisation.....	05
1.1.4. The role of chaperones in GPCR oligomer formation.....	07
1.1.5 The dynamics of GPCR oligomerisation.....	10
1.1.6 Receptor mosaics.....	13
1.1.7 The physiological relevance of GPCR oligomerisation.....	15
1.1.8 Functional crosstalk.....	16
1.2 Purine receptors.....	17
1.2.1 Historical perspective on purine Discovery.....	17
1.2.2 Synthesis and breakdown of purines.....	18
1.2.3 Historical perspective on purine receptor Discovery.....	21
1.3 P2Y receptors.....	23
1.3.1 Pharmacology.....	23
1.3.2 Structure-function relationships of P2Y receptors.....	26
1.3.3 Pharmacology.....	26
1.4 The P2Y ₁ receptor.....	27
1.5 The P2Y ₁₁ receptor	29
1.6 Interaction between P2Y ₁ and P2Y ₁₁	32
1.7 Aims of the Project.....	33

Chapter 2 - Materials and Methods.....	35
2.1 Tissue culture techniques.....	35
2.1.1 Cell lines and cell culture conditions.....	35
2.1.2 Passaging, splitting and counting.....	35
2.1.3 Cellular density measurement.....	36
2.1.4 Transfection of cells with plasmid DNA.....	37
2.1.5 Generation of stable cell lines.....	38
2.1.6 Collection and freezing of stably transfected cell lines.....	38
2.1.7 Cloning by limiting dilution.....	38
2.2 The calcium mobilization assay.....	39
2.2.1 Cell plating.....	40
2.2.2 Dye loading.....	40
2.2.3 Creating ligand plates.....	41
2.2.4 Running the FLIPR assay.....	41
2.3 Data analysis.....	42
2.3.1 The Hill equation.....	44
2.4 A brief description of Prism equations and fits.....	46
2.4.1 Stimulation equations.....	46
2.4.2 Inhibition equations.....	48
2.5 Statistical Analysis using Prism®.....	50
2.6 Molecular Biology Techniques.....	51
2.6.1 RNA extraction from animal cells.....	51
2.6.2 Quantification of nucleic acids.....	52
2.6.3 DNase treatment of RNA.....	52
2.6.4 Single-stranded DNA synthesis.....	53
2.6.5 PCR primers design.....	54
2.6.6 Polymerase Chain Reaction (PCR).....	56
2.6.7 Gel electrophoresis.....	56
Chapter 3 - Creation and Characterization of Recombinant CHO-K1- hP2Y₁₁ Clones 6 and 13.....	57
3.1 Introduction.....	57
3.2 Selection of Clonal Cell Lines Expressing hP2Y ₁₁	58
3.2.1 Creation and characterization of stably transfected CHO-K1 cells expressing the human P2Y ₁₁ receptor.....	58
3.2.2 Identification of CHO-K1-hP2Y ₁₁ clonal cell lines expressing	

different densities of hP2Y ₁₁	62
3.3 Verification of hP2Y ₁₁ expression in clones 13 and 6 using RT-PCR.....	65
3.4 Calcium responses of clonal CHO-K1-hP2Y ₁₁ cell lines.....	67
3.4.1 Functional characterization of agonist responses in CHO-K1-hP2Y ₁₁ Clone 13, the ‘high’-expressing P2Y ₁₁ clone.....	67
3.4.2 Functional characterization of agonist responses in CHO-K1-hP2Y ₁₁ Clone 6, the ‘low’-expressing P2Y ₁₁ clone.....	73
3.5 hP2Y ₁₁ receptor density influences calcium responses elicited by nucleotides and nucleotide analogues.....	77
3.5.1 Comparison of time-dependent responses in CHO-K1-hP2Y ₁₁ clone 13 and CHO-K1-hP2Y ₁₁ clone 6.....	77
3.5.2 Comparison of agonist potencies in CHO-K1-hP2Y ₁₁ clone 13 and CHO-K1-hP2Y ₁₁ clone 6.....	79
3.6. Summary of the functional studies	84
3.7 Generation of co-immunoprecipitation and BiFC constructs.....	84
Chapter 4 - Pharmacological Characterization of Recombinant 1321N1- hP2Y₁ and 1321N1-hP2Y₁₁ Cell lines.....	88
4.1 Introduction.....	88
4.2 Pharmacological of characterization of a recombinant 1321N1-hP2Y ₁₁ cell line.....	89
4.2.1 Calcium response of 1321N1-hP2Y ₁₁ to carbachol.....	89
4.2.2 Functional investigation of the activity of nucleotide and nucleotide derivatives in 1321N1-hP2Y ₁₁	90
4.2.3 Antagonist studies in 1321N1-hP2Y ₁₁	96
4.3 Pharmacological characterization of a recombinant 1321N1-hP2Y ₁ cell line.	98
4.3.1 Calcium response of 1321N1-hP2Y ₁ to carbachol.....	99
4.3.2 Functional investigation of the activity of nucleotide and nucleotide derivatives in 1321N1-hP2Y ₁	100
4.3.3 Antagonist studies in 1321N1-hP2Y ₁	104
4.4 Conclusion.....	110
Chapter 5 - Antagonist Experiments in CHO-K1-hP2Y₁₁ Clone 13.....	116
5.1 Introduction.....	116
5.2 MRS 2179 Schild experiments in CHO-K1-hP2Y ₁₁ clone 13.....	116
5.2.1 Schild analysis of MRS 2179 activity at the ADP response.....	116
5.2.2 Schild analysis of MRS 2179 activity at the 2meSATP response....	120

5.3 NF 340 Schild analysis in CHO-K1-hP2Y ₁₁ clone 13.....	124
5.4 Reactive Red Schild against ADP in CHO-K1-hP2Y ₁₁ clone 13.....	126
5.5 MRS 2179 inhibition curves in CHO-K1-hP2Y ₁₁ clone 13.....	129
5.5.1 The calcium response to 100nM ADP in the presence of increasing concentrations of MRS 2179.....	129
5.5.2 The calcium response to 100µM ADP in the presence of increasing concentrations of MRS 2179.....	131
5.5.3 The calcium response to 100nM 2meSATP in the presence of increasing concentrations of MRS 2179.....	131
5.5.4 The calcium response to 100µM 2meSATP in the presence of increasing concentrations of MRS 2179.....	133
5.5.5 The calcium response to 10µM BzATP in the presence of increasing concentrations of MRS 2179.....	134
5.6 NF 340 Inhibition Curves in CHO-K1-hP2Y ₁₁ Clone 13.....	135
5.6.1 The calcium response to 100nM ADP in the presence of increasing concentrations of NF 340.....	135
5.6.2 The calcium response to 100µM ADP in the presence of increasing concentrations of NF 340.....	136
5.6.3 The calcium response to 100nM 2meSATP in the presence of increasing concentrations of NF 340.....	137
5.6.4 The calcium response to 100µM 2meSATP in the presence of increasing concentrations of NF 340.....	137
5.6.5 The calcium response to 10µM BzATP in the presence of increasing concentrations of NF 340.....	138
5.7 Reactive Red Inhibition Curves in CHO-K1-hP2Y ₁₁ Clone 13.....	139
5.7.1 The calcium response to 100nM ADP in the presence of increasing concentrations of Reactive Red.....	139
5.7.2 The calcium response to 100µM ADP in the presence of increasing concentrations of Reactive Red.....	142
5.7.3 The calcium response to 100nM 2meSATP in the presence of increasing concentrations of Reactive Red.....	144
5.7.4 The calcium response to 100µM 2meSATP in the presence of increasing concentrations of Reactive Red.....	147
5.8 Conclusion.....	149
Chapter 6 – Discussion.....	152

6.1 Introduction.....	152
6.2 The effect of co-expression on the BzATP response in CHO-K1-hP2Y ₁₁ clones 6 and 13.....	152
6.2.1 The density of hP2Y ₁₁ receptors affects the magnitude of the response to BzATP in clones 6 and 13.....	152
6.2.2 BzATP is more potent in CHO-K1-hP2Y ₁₁ clones 6 and 13 as compared to 1321N1-hP2Y ₁₁	153
6.3 The effect of co-expression on the calcium response to ATP, ATP γ S and UTP in clones 13 and 6.....	154
6.3.1 Co-expression does not alter the potency of ATP at hP2Y ₁₁ in clones 6 and 13.....	154
6.3.2 Co-expression does not alter the potency of ATP γ S at hP2Y ₁₁ in clones 6 and 13.....	155
6.3.3 The UTP response assumes a hP2Y ₂ -like character in clones 6 and 13.....	156
6.4 Co-expression reduces the affinity of hP2Y ₁₁ for $\alpha\beta$ meATP and $\beta\gamma$ meATP in clones 6 and 13.....	157
6.5 Co-expression modifies the rank order of agonist potency in clones 6 and 13.....	157
6.6 Co-expression alters the affinity of NF 340 to hP2Y ₁₁ in clones 6 and 13.....	159
6.7 The high-affinity site of the response to ADP in CHO-K1-hP2Y ₁₁ clone 13 is endogenous P2Y ₁	160
6.7.1 The high-affinity site of the biphasic response in clone 13 has reduced affinity for ADP.....	160
6.7.2 The high-affinity site of the ADP response is inhibited by MRS 2179.....	161
6.8 The high affinity site of the response to 2meSATP in CHO-K1-hP2Y ₁₁ clone 13 is endogenous P2Y ₁	163
6.8.1 The high-affinity site of biphasic 2meSATP curve in clone 13 has P2Y ₁ -like character.....	163
6.8.2 The high affinity site of the biphasic 2meSATP curve is inhibited by MRS 2179.....	164
6.9 Pharmacological evidence for P2Y ₁ and hP2Y ₁₁ interactions.....	164
6.9.1 The low-affinity site of the response to ADP and 2meSATP in clone 13 has P2Y ₁ and hP2Y ₁₁ -like characteristics.....	164

6.9.2 The low-affinity site of the response to ADP and 2meSATP results from the interaction between P2Y ₁ and hP2Y ₁₁ in clone 13.....	165
6.10 Predictive analysis of the binding pocket and conformational rearrangements involved in P2Y ₁ and hP2Y ₁₁ interaction.....	167
6.11 Conclusions.....	169
6.12 Future Work.....	172
Chapter 7 – References.....	179
Appendix 1.....	194

List of Figures

Figure 1.1 The G-protein coupled receptor unit.....	02
Figure 1.2 Ribbon drawing of Bovine Rhodopsin.....	03
Figure 1.3 Possible models of GPCR dimerization adapted from Gouldson et al. (81, 84, 86).....	12
Figure 1.4 Structure of adenosine diphosphate and adenosine triphosphate.....	21
Figure 2.1 Estimation of the increase in calcium fluorescence using a kinetic FLIPR trace.....	43
Figure 2.2 Examples of dose-response curve fits.....	48
Figure 2.3 Models of competitive antagonism.....	49
Figure 3.1 The hP2Y ₁₁ in pcDNA3 construct	59
Figure 3.2 Microscopic visualization of CHO-K1 and CHO-K1-hP2Y ₁₁ cells.	60
Figure 3.3 BzATP elicits a calcium response at 37°C in CHO-K1 cells stably expressing the human P2Y ₁₁ receptor.....	62
Figure 3.4 100µM BzATP elicits a calcium response in CHO-K1 clones expressing the human P2Y ₁₁ receptor.....	64
Figure 3.5 CHO-K1 clones expressing the human P2Y ₁₁ receptor give varying responses to 100µM BzATP.....	65
Figure 3.6 Agarose Gel Electrophoresis of PCR products in clones 6 and 13.....	66
Figure 3.7 Concentration-response curves of BzATP, ATP _γ S, ATP and αβmeATP on Ca ²⁺ mobilization in CHO-K1-hP2Y ₁₁ clone 13.....	69
Figure 3.8 Concentration-response curves of ADP, UTP, 2meSATP and βγmeATP on Ca ²⁺ mobilization in CHO-K1-hP2Y ₁₁ clone 13.....	70
Figure 3.9 Concentration-response curves of BzATP, ATP _γ S, ATP and αβmeATP on Ca ²⁺ mobilization in CHO-K1-hP2Y ₁₁ clone 6.....	73
Figure 3.10 Concentration-response curves of ADP, UTP, 2meSATP and βγmeATP on Ca ²⁺ mobilization in CHO-K1-hP2Y ₁₁ clone 6.....	75
Figure 3.11 The time dependence of the response to 100µM BzATP in CHO-K1-hP2Y ₁₁ clone 13 and CHO-K1-hP2Y ₁₁ clone 6.....	78
Figure 3.12 Visualization of differences in agonist responses in CHO-K1-hP2Y ₁₁ clone 13 and CHO-K1-hP2Y ₁₁ clone 6.....	80
Figure 3.13 Comparison of agonist responses in CHO-K1-hP2Y ₁₁ clone 13 and	

CHO-K1-hP2Y ₁₁ clone 6.....	81
Figure 3.14 Construct layout for P2Y ₁ and P2Y ₁₁	85
Figure 3.15 Map of EcoRV digestion.....	86
Figure 3.16 Agarose gel electrophoresis of EcoRI and EcoRV digests.....	87
Figure 4.1 Concentration-response curve elicited by carbachol in 1321N-hP2Y ₁₁	90
Figure 4.2 Concentration-response curves for BzATP, ATP γ S, ATP and $\alpha\beta$ meATP on Ca ²⁺ mobilization in 1321N1-hP2Y ₁₁	92
Figure 4.3 Representative concentration-response curves for BzATP, ATP γ S, ATP and $\alpha\beta$ meATP on Ca ²⁺ mobilization in 1321N1-hP2Y ₁₁	93
Figure 4.4 Comparison of the maximum responses of five tested agonists as a function of time in 1321N1-hP2Y ₁₁ cells.....	94
Figure 4.5 Representative concentration-response curves for ADP, UTP, 2meSATP and β meATP on Ca ²⁺ mobilization in 1321N1-hP2Y ₁₁	96
Figure 4.6 NF 340 inhibits the response to 10 μ M BzATP in a time-dependent fashion.....	97
Figure 4.7 NF 340 inhibits the response to 10 μ M BzATP in 1321N1-hP2Y ₁₁ cells.....	98
Figure 4.8 Concentration-response curve elicited by carbachol in 1321N-hP2Y ₁	99
Figure 4.9 Concentration-response curves for BzATP, UTP, $\alpha\beta$ meATP and β meATP in 1321N1-hP2Y ₁ cells.....	101
Figure 4.10 Comparison of the maximum responses of five tested agonists as a function of time in 1321N1-hP2Y ₁ cells.....	102
Figure 4.11 Concentration-response curves for ADP, 2meSATP, ATP and ATP γ S in 1321N1-hP2Y ₁ cells.....	103
Figure 4.12 Time dependence of the response to ADP in the presence of MRS 2179 in 1321N1-hP2Y ₁ cells.....	105
Figure 4.13 MRS 2179 inhibits the response to 1 μ M ADP in 1321N-hP2Y ₁	106
Figure 4.14 Time dependence of the response to ADP in the presence of Reactive Red in 1321N1-hP2Y ₁ cells.....	107
Figure 4.15 The calcium response to ADP in the presence of Reactive Red in 1321N1-P2Y ₁	108
Figure 4.16 Time dependence of the calcium response to ADP in the presence of NF 340 in 1321N1-hP2Y ₁ cells.....	109

Figure 4.17 NF 340 does not inhibit the response to 1 μ M ADP in 1321N1-P2Y ₁	110
Figure 4.18 Visualization of differences in agonist responses in 1321N1-hP2Y ₁₁ and 1321N1-hP2Y ₁	113
Figure 4.19 Comparison of agonist responses in 1321N1-hP2Y ₁ and 1321N1-hP2Y ₁₁	114
Figure 5.1 The effect of MRS 2179 on the calcium response to ADP in CHO-K1-hP2Y ₁₁ clone 13.....	117
Figure 5.2 EC ₅₀ Shift of the MRS 2179 and ADP Schild in CHO-K1-hP2Y ₁₁ clone 13.....	119
Figure 5.3 Schild plot for MRS 2179 against ADP in clone 13.....	120
Figure 5.4 The effect of MRS 2179 on the calcium response to 2meSATP in CHO-K1-hP2Y ₁₁ clone 13.....	121
Figure 5.5 EC ₅₀ Shift of the MRS 2179 and 2meSATP Schild in CHO-K1-hP2Y ₁₁ clone 13.....	123
Figure 5.6 Schild plot for MRS 2179 against 2meSATP in clone 13.....	124
Figure 5.7 The effect of NF 340 on the calcium response to ADP in CHO-K1-hP2Y ₁₁ clone 13.....	125
Figure 5.8 The effect of Reactive Red on the calcium response to ADP in CHO-K1-hP2Y ₁₁ clone 13.....	127
Figure 5.9 EC ₅₀ Shift of the Reactive Red and ADP Schild in CHO-K1-hP2Y ₁₁ clone 13.....	128
Figure 5.10 Schild plot for Reactive Red against ADP in clone 13.....	129
Figure 5.11 MRS 2179 inhibits the response to 100nM ADP in CHO-K1-hP2Y ₁₁ clone 13.....	130
Figure 5.12 MRS 2179 does not affect the response to 100 μ M ADP in CHO-K1-hP2Y ₁₁ clone 13.....	131
Figure 5.13 MRS 2179 inhibits the response to 100nM 2meSATP in CHO-K1-hP2Y ₁₁ clone 13.....	132
Figure 5.14 MRS 2179 does not affect the response to 100 μ M 2meSATP in CHO-K1-hP2Y ₁₁ clone 13.....	133
Figure 5.15 MRS 2179 does not affect the response to 10 μ M BzATP in CHO-K1-hP2Y ₁₁ clone 13.....	134
Figure 5.16 NF 340 does not affect the response to 100nM ADP in CHO-K1-hP2Y ₁₁ clone 13.....	135

Figure 5.17 NF 340 does not affect the response to 100 μ M ADP in CHO-K1-hP2Y ₁₁ clone 13.....	136
Figure 5.18 NF 340 does not affect the response to 100nM 2meSATP in CHO-K1-hP2Y ₁₁ clone 13.....	137
Figure 5.19 NF 340 does not affect the response to 100 μ M 2meSATP in CHO-K1-hP2Y ₁₁ clone 13.....	138
Figure 5.20 NF 340 does not affect the response to 10 μ M BzATP in CHO-K1-hP2Y ₁₁ clone 13.....	139
Figure 5.21 Time dependence of the response to 100nM ADP in the presence of increasing concentrations of Reactive Red in CHO-K1-hP2Y ₁₁ clone 13.....	141
Figure 5.22 Reactive Red inhibits the response to 100nM ADP in CHO-K1-hP2Y ₁₁ clone 13.....	142
Figure 5.23 Time dependence of the response to 100 μ M ADP in the presence of increasing concentrations of Reactive Red in CHO-K1-hP2Y ₁₁ clone 13.....	143
Figure 5.24 Reactive Red inhibits the response to 100 μ M ADP in CHO-K1-hP2Y ₁₁ clone 13.....	144
Figure 5.25 Time dependence of the response to 100nM 2meSATP in the presence of increasing concentrations of Reactive Red in CHO-K1-hP2Y ₁₁ clone 13.....	145
Figure 5.26 Reactive Red inhibits the response to 100nM 2meSATP in CHO-K1-hP2Y ₁₁ clone 13.....	146
Figure 5.27 Representative inhibition curve for Reactive Red versus 100nM 2meSATP in CHO-K1-hP2Y ₁₁ clone 13.....	147
Figure 5.28 Time dependence of the response to 100 μ M 2meSATP in the presence of increasing concentrations of Reactive Red in CHO-K1-hP2Y ₁₁ clone 13.....	148
Figure 5.29 Reactive Red inhibits the response to 100 μ M 2meSATP in CHO-K1-hP2Y ₁₁ clone 13.....	149

List of Tables

Table 1.1 GPCR heteromers.....	09
Table 1.2 The P2Y family of purinoceptors.....	25
Table 1.3 Percentage of identity (%) between the amino acid sequences of different P2Y ₁ species subtypes	29
Table 3.1 The calcium response to BzATP in pools 0.5 and 1.0 using F/F ₀ versus AUC analysis.....	61
Table 3.2 The calcium response elicited by BzATP in pools 0.5 and 1.0.....	62
Table 3.3 Steepness and maxima of the BzATP, ATP and ATP γ S curves in clone 13.....	68
Table 3.4 Steepness and maxima of the ADP, 2mesATP and UTP curves in clone 13.....	71
Table 3.5 The calcium response elicited by nucleotides and nucleotide analogues in CHO-K1-hP2Y ₁₁ clone 13.....	72
Table 3.6 Steepness and maxima of the BzATP, ATP and ATP γ S curves in clone 6.....	74
Table 3.7 Steepness and maxima of the ADP, 2meSATP and UTP curves in clone 6.....	76
Table 3.8 The calcium response elicited by nucleotides and nucleotide analogues in CHO-K1-hP2Y ₁₁ clone 6.....	76
Table 3.9 Maximum calcium response to 100 μ M BzATP in clones 13 versus 6.....	79
Table 3.10 Comparison of agonist potencies of the calcium response in CHO-K1-hP2Y ₁₁ clone 13 and CHO-K1-hP2Y ₁₁ clone 6.....	83
Table 4.1 The calcium response elicited by nucleotide analogues and carbachol in 1321N1-hP2Y ₁₁ and 1321N1-hP2Y ₁ cells.....	111
Table 4.2 Comparison of agonist potencies of the calcium response in 1321N1-hP2Y ₁ and 1321N1-hP2Y ₁₁	112
Table 4.3 The activity of antagonists in 1321N1-hP2Y ₁ versus 1321N1-hP2Y ₁₁ cells	115
Table 5.1 The EC ₅₀ shift of the calcium response to ADP in the presence of increasing concentrations of MRS 2179 in CHO-K1-hP2Y ₁₁ clone 13.....	118
Table 5.2 The EC ₅₀ shift of the calcium response to 2meSATP in the presence	

of increasing concentrations of MRS 2179 in CHO-K1-hP2Y ₁₁ clone 13.....	122
Table 5.3 The EC ₅₀ shift of the calcium response to ADP in the presence of increasing concentrations of NF 340 in CHO-K1-hP2Y ₁₁ clone 13.....	125
Table 5.4 The EC ₅₀ shift of the calcium response to ADP in the presence of increasing concentrations of Reactive Red in CHO-K1-hP2Y ₁₁ clone 13.....	127
Table 5.5 The K _B and IC ₅₀ values measured from Schild experiments in CHO-K1-hP2Y ₁₁ clone 13.....	150
Table 5.6 The IC ₅₀ values of MRS 2179, NF 340 and Reactive Red in CHO-K1-hP2Y ₁₁ clone 13.....	151

Abbreviations

1321N1	Human astrocytoma cell line
2MeSA TP	2-methylthio-adenosine-5'-triphosphate
7TM	Seven transmembrane receptor
ADP	Adenosine-5'-diphosphate
ATP	Adenosine-5'-triphosphate
ATP _γ S	Adenosine-5'-(3-thiotriphosphate)
AUC	Area under the curve
BzATP	2'-and 3'-O-(4-benzoyl-benzoyl)adenosine 5'- triphosphate
Ca ²⁺	Calcium
cAMP	Cyclic adenosine-3',5'-monophosphate
cDNA	Complementary DNA
CHO-K1	Chinese Hamster Ovary cells
C-terminus	Carboxyl terminus
DAG	Diacylglycerol
DPBS	Dulbecco's Phosphate Buffered Saline
EDTA	Ethylene-diamine-tetra-acetic acid
EL	Extracellular loop
ER	Endoplasmic reticulum
EtOH	Ethanol
FLIPR	Fluorescence Image Plate Reader
GPCR	G-protein couple receptor
GTP	Guanosine-5'-triphosphate
hP2Y1	human P2Y1
hP2Y2	human P2Y2

Chapter 1 Introduction

hP2Y11	human P2Y11
IL	Intracellular Loop
IP3	Inositol 1,4,5-trisphosphate
mRNA	messenger RNA
N-terminus	Amino-terminus
PBS	Phosphate Buffered Saline
UTP	Uridine-5'-triphosphate

Chapter 1

Introduction

1.1 G protein-coupled receptors

Membrane receptors constitute a major hub of information relay between the extracellular and intracellular milieus and are key players in cellular communication across the plasma membrane. The G protein-coupled receptor (GPCR) superfamily of seven transmembrane proteins represents the largest family of integral membrane receptors. Members of this superfamily are encoded by 4% of all genes and contribute to all known physiological processes in mammals (1-5). The GPCR family comprises around 800 human receptors (4), phylogenetically segregated into five main subfamilies, namely class A, class B, class C, frizzled and adhesion (2). Primary sequence analysis predicted a single receptor protein with seven transmembrane domains (see Figure 1-1). Given the remarkable diversity of their biological actions, GPCRs represent the most common target (up to 40%) of all known pharmaceutical drugs (6, 7).

1.1.1 GPCR structure

GPCRs are activated by a plethora of signals, including photons, ions, hormones, peptides, chemokines, nucleotides and other factors. Despite the diversity of ligands acting at GPCRs and of the signalling pathways they regulate, all GPCRs share a common core structure consisting of seven transmembrane spans. The first milestone in elucidating the structure of 7TM receptors was achieved in 2000, when bovine rhodopsin was crystallized from mixed micelles and the protein structure of this receptor was solved at 2.8Å (8) (see Figure 1-2). This study delineated a “structural template for other GPCRs”, consisting of a bundle of seven transmembrane α helices connected by six loops of different lengths. A second GPCR structure was obtained seven years later when Kobilka and his group resolved the crystal structural of the β_2 -adrenergic receptor in 2007 (9, 10). Other GPCR crystal structures published to date comprise the dopamine receptor D₃R (11), the muscarinic M₂R (12) and M₃R (13) receptors, CXCR₄ (14), μ opioid receptor (15), δ opioid receptor (16), κ opioid receptor (17), the nociceptin receptor (18), the adenosine A_{2A} receptor (19) and the histamine H₁ receptor (20).

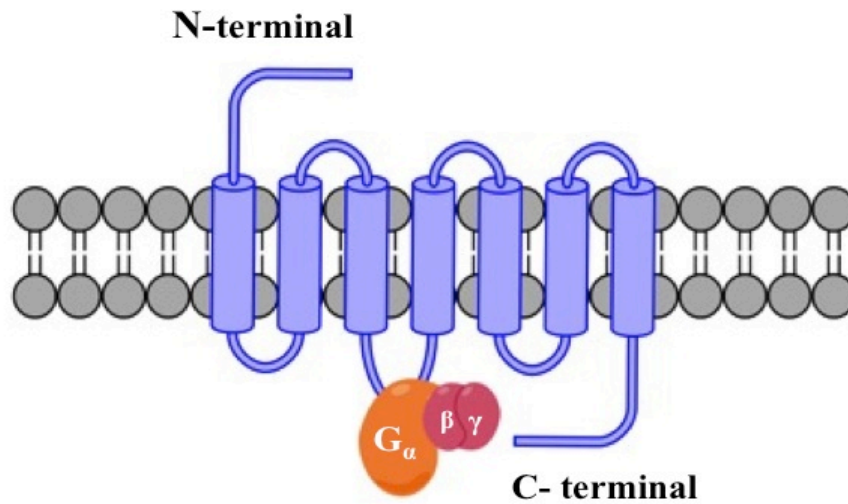


Figure 1.1 The G-protein coupled receptor unit

A G-protein coupled receptor consists of a single polypeptide chain composed of 7 transmembrane domains connected by 3 extracellular loops and 3 intracellular loops. It possesses an extracellular N-terminus, an intracellular C-terminus and binds to a heterotrimeric G protein (α, β, γ) at the plasma side of the membrane. The plasma membrane or lipid bilayer is shown in grey.

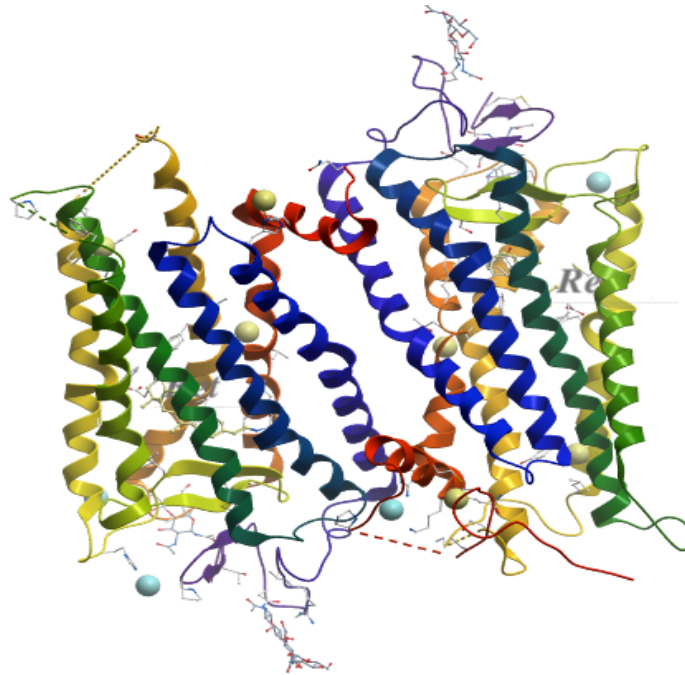


Figure 1.2 Ribbon drawing of Bovine Rhodopsin

The crystal structure of bovine rhodopsin, published by Palczewski et al. (8), was resolved using X-ray diffraction with a resolution of 2.8 Å. The structure was exported from the PDB entry 1F88 using Molsoft Browser Pro 4. This model contains several copies of the rhodopsin structure as well as heterogenic compounds such as ligands, co-factors, etc. The chains are coloured using a rainbow/spectral color gradient.

Analysis of these structures reveals that GPCRs display a rich complexity across receptor subtypes but exhibit a significant structural similarity (5, 7). The currently accepted model of GPCR structure postulates that these seven transmembrane α helices (7TMH) are connected by three extracellular loops (EL1-3) and three intracellular loops (IL1-3). The extracellular region comprises the N-terminus of the GPCR. Its organization is mediated by a disulphide bridge, conserved in most GPCRs, between extracellular loop II (EL2) and the extracellular end of helix III, ensuring the arrangement of the 7TM motif. The extracellular domain is characterized by a high structural diversity that allows GPCRs to recognise a wide repertoire of ligands of different shapes, sizes and electrostatic properties, with class C GPCR binding domains in the EC domain itself. Despite this structural diversity however, the binding pockets of GPCRs are rigid and undergo restricted conformational rearrangements during the activation process (5, 7). A number of interhelical bonds and hydrophobic interactions between highly conserved residues in GPCRs were found to impart the stability of the transmembrane region (8). In fact, the 7TM bundle comprises hydrophobic amino acid residues together with functionally important signature motifs including the D[E]RY motif in helix III, which is part of the ‘ionic lock’, the WXP motif in helix VI and the NPXXY motif in helix VII (7). It also harbours a number of kinks elicited by Pro residues, which segregate the receptor into ligand binding and receptor signalling “modules” (5). Crystallographic studies indicate that the overall structure of the 7TM fold is highly conserved in GPCRs but also delineate the diversity observed in the loop regions and the pitch and orientation of individual helices in the helical bundle.

1.1.2 GPCR activation

A central feature of GPCR signalling is that the ligand does not physically traverse the plasma membrane but conveys its signal to the cellular milieu through conformational changes in the receptor protein. Hence, the binding of a ligand to the receptor provokes a switch from its inactive to its active conformation, which opens up the helical bundle and exposes the binding site of the receptor for its cognate G-protein at the cytoplasmic side of the receptor (10, 21-23). As the Nobel press release presenting the 2012 Chemistry prize, awarded to Kobilka and Lefkowitz for their work on GPCRs, beautifully states: “If a ligand grips the bundle at one end, the bundle opens up like a bouquet of roses at the other end” (23). Structural studies of the β_2 adrenergic receptor have shown that this conformational change is mediated by the displacement of helix 6 and the subsequent opening of a hydrophobic cleft on the intracellular side of the receptor. Consequently, the

C-terminal helix of $G\alpha$ enters this cleft, inducing major structural changes in the G protein leading to its activation (21). The desensitization of the GPCR is initiated by its interaction with GRKs, or G protein-coupled receptor kinases, leading to its phosphorylation, usually at its carboxy-terminal end. This in turn elicits the binding of β -arrestins, which sterically hinder additional G protein coupling and ensure the termination of the agonist response (3).

G proteins are heterotrimeric entities composed of three subunits, namely $G\alpha$, $G\beta$ and $G\gamma$ expressed by 16, 5 and 12 genes in mammals, respectively. The $G\alpha$ subunit can be further divided into four sub-families consisting of $G\alpha_s$, $G\alpha_i$, $G\alpha_{q/11}$ and $G\alpha_{12/13}$ (22). The G-protein constitutes a molecular switch that cycles between a GDP-bound form in its inactive state versus a GTP-bound form in its active conformation. Upon ligand binding, the GPCR interacts with its associated G protein to catalyse the release of GDP from $G\alpha$ and the subsequent binding of GTP. This mechanism provokes a conformational modification that reduces the affinity of $G\alpha$ for $G\beta\gamma$, leading to the dissociation of the two subunits. The GTP-bound $G\alpha$ and the released $G\beta\gamma$ can now interact with effector proteins such as adenylyl cyclase and phospholipases to initiate numerous intracellular signalling cascades. The intrinsic GTP hydrolase activity of $G\alpha$, triggered by binding of RGS, or regulator of G protein signalling, reinstates the GDP-bound form of $G\alpha$ and restores its affinity for $G\beta\gamma$, thus reforming the inactive heteromeric unit (23).

1.1.3 GPCR oligomerization

“The eminent German thinker Arthur Schopenhauer wrote with philosophical clarity that all truth passes through three stages. First it is ridiculed. Second, it is violently opposed. Third, it is accepted as being self-evident. These observations aptly apply to GPCRs: an understanding of their oligomerisation has evoked much passion and continuing investigation” (24). The traditional positions on GPCR activity insisted that they signal as single monomeric units composed of identical subunits. The first notion of GPCR oligomerisation was advanced by Agnati and Fuxe, who envisaged a possible intramembrane neuropeptide and monoamine receptor-receptor interaction to explain the cross-talk between the two entities (25). The notion of GPCRs as monomeric signalling entities was further questioned by evidence from biochemical, physical and functional studies, pointing to a possible interaction between GPCRs (26). For instance, radio-ligand binding studies revealed the existence of interactions between neurokinin and 5-HT₁ receptors, neurotensin NTS₁ and dopamine D₂ receptors, as well neuropeptide Y (NPY)

and α_2 adrenergic receptors, to name a few (27). The first physical proof of dimerization, however, emerged from atomic-force microscopy analysis of the rhodopsin receptor, which was found to form paracrystalline arrays of dimers in mouse disc membranes (28).

The existence of dimers was further substantiated by the discovery that certain GPCRs, namely the members of the class C or metabotropic group of GPCRs, are obligate heteromers. In fact, the constitutive dimerization of these receptors is a prerequisite for the expression of a fully active and pharmacologically defined receptor at the plasma membrane (1, 14, 26). The γ -aminobutyric acid (GABA) receptor, composed of two subunits GbR₁ and GbR₂, constitutes an example of a mandatory heteromer. When expressed individually in heterologous systems, the GbR₁ subunit possesses a carboxy-terminal ER retention motif RXR(R) that retains the receptor in the endoplasmic reticulum (ER), while GbR₂ is expressed at the cell surface but is not able to activate downstream pathways on its own. This is explained by the fact that the GbR₁ subunit harbours the structural elements crucial for ligand binding but not for G-protein coupling, while the GbR₂ subunit mediates G-protein coupling but cannot bind ligands. The co-expression of the two subunits results in their dimerization, thus masking the ER retention motif and permitting the assembly of a functional signalling GABA_B receptor that is targeted to the cell surface (22, 29-32).

Research in both native and recombinant expression systems has identified other examples of GPCRs in which a single subunit is inactive in the absence of its dimeric partner (1, 33). For instance, the co-expression of taste receptors T1R₂/T1R₃, or T1R₁/T1R₃ is necessary to produce functional taste receptors that detect sweet and umami (34). Moreover, studies of the dopamine family of receptors have demonstrated that they dimerize with themselves and other receptors to yield 'multireceptor networks' with novel functional properties (35). In fact, ligand binding studies have confirmed the formation of D₂R oligomers, thought to be involved in the pathology of schizophrenia (36, 37). The D₂R receptor was also found to heterodimerize with the D₃R receptor, resulting in complexes with reduced agonist affinity and augmented coupling with adenylyl cyclase (35, 38). An additional example of dopamine receptor oligomerisation is D₁R/D₂R, which requires agonist binding to both receptor subunits for G protein activation and might contribute to dopamine-mediated synaptic plasticity in the brain. The selective activation of either receptor was found to provoke the co-internalization of these D₁R/D₂R heterodimers (39-42). Another oligomerisation partner of D₁R is the

dopamine D₃ receptor, resulting in a dimer that enhances the dopaminergic response in striatal neurons co-expressing both receptors (43, 44). Dopamine receptors have also been reported to oligomerize with other receptors, including the adenosine 2A receptor, the CB₁ cannabinoid receptor, the metabotropic glutamate type 5 receptor and the somatostatin-2 and -5 receptors (35, 45-50).

The formation of hetero-oligomers between P2 receptors, which are of particular interest to this study, has also been substantiated by numerous studies. For instance, the A₁ receptor was shown to engage in heteromeric assemblies with the P2Y₁ receptor in cotransfected HEK293T cells, generating A₁ receptors with P2Y-like agonist affinities (51). The existence of an A₁R/P2Y₁R dimer was further demonstrated *in vivo* using co-immunoprecipitation experiments and the oligomer was found to localize to rat cortex (52), hippocampus and cerebellum membranes (53). A proposed function for this A₁R/P2Y₁R dimer is the attenuation of neurotransmitter release from synaptic vesicles (53). Additional mentions of P2 hetero-dimerization encompass the interaction between A₁ and the dopamine D₁ receptor to form a functionally active complex thought to impinge on receptor trafficking and desensitization (54). A₁R can also heteromerize with the metabotropic glutamate type 1 α receptor, resulting in the modulation of glutamate excitotoxicity (27).

The A_{2A} receptor can dimerize with the metabotropic glutamate type 5 receptor and was found to engage in synergistic interactions at both the biochemical and behavioural levels. A study conducted by Ecke et al has also shown that the P2Y₁ and P2Y₁₁ receptors associate physically when co-expressed in HEK293T cells using co-immunoprecipitation, immunoprecipitation and FRET experiments (55). This hetero-oligomerisation alters the agonist profile of P2Y₁₁, allowing it to acquire novel functions when in tandem with P2Y₁. The study also revealed that oligomer formation induced the internalization of P2Y₁₁, a receptor that does not undergo endocytosis by itself. This finding suggests that the crosstalk between P2Y₁ and P2Y₁₁ receptors has a regulatory role and might be used by the cell to favour one GPCR signalling pathway over the other.

1.1.4 The role of chaperones in GPCR oligomer formation

The discovery that GPCRs are able to oligomerize has raised important questions. One such interrogation is where and how these complexes are formed and expressed at the cell surface. While heteromers can arise transiently in the plasma membrane,

accumulating evidence suggests that receptor dimerization and the assembly of GPCRs with their signalling complex may occur early during biogenesis, prior to trafficking to the plasma membrane (22, 56). Moreover, studies indicate that molecular chaperones may contribute to the proper folding of receptors as well as the assembly of signalling complexes, indicating that these complexes may be delivered to the plasma membrane as “complete signalling units” (22).

The oligomerisation literature suggests that receptor dimerization can occur in the endoplasmic reticulum (ER), where it might play a role in ER quality control and exit by masking the ER-retention motifs of some receptor sequences (1, 22, 57). One of the first evidences of constitutive dimerization during biogenesis emerged from mutagenesis of the β_2 -adrenergic receptor, targeting the putative dimerization interface. These studies showed that inhibiting β_2 AR dimerization caused its retention in the ER, thus supporting the hypothesis of receptor oligomerisation in this cellular compartment (57). Other examples of oligomerisation in the ER encompass the D₄ receptors (58), GABA_B receptors (29) and serotonin 5-HT_{2C} receptors (59). Studies have also proposed a possible involvement of molecular chaperones in the assembly of oligomeric complexes in the ER (60-62). An example of chaperone implication in receptor oligomerisation is RTP₄, reported to mediate the folding of the μ - δ opioid heteromer, thus masking the ER retention motif and permitting the export of the complex to the cell surface. Interestingly, RTP₄ is thought to stay bound to the μ - δ opioid heteromer at the plasma membrane and participate in the regulation of heteromer specific signalling (63). Another chaperone is calreticulin, which enhances the maturation and heterodimerization of the B₂ bradykinin receptor with the angiotensin II type 1 receptor (AT₁R) in heterologous and in vivo models (60, 61). These combined findings delineate a novel scenario of GPCR dimerization, in which receptor oligomers and GPCR signalling complexes composed of multiple interaction partners are gathered during biogenesis in the ER and delivered to the cellular membranes as pre-assembled functional units. This mechanism might contribute to the diversification and specificity of GPCR signalling complexes observed in mammalian cells.

Heteromer	Methods used to investigate receptor association	Crosstalk	Reference
GABA _{B1} :GABA _{B2}	TR-FRET-HTRF using Snaptag or antibodies	Increased agonist response of dimer versus two tetramer	(64)
H ₁ : α _{1B} AR	CoIP and TR-FRET	Cross-activation of G-proteins	(65)
D ₁ :D ₂	CoIP, confocal microscopy, BiFC	Novel pharmacological profile	(41, 66-68)
D ₁ :D ₃	FRET, confocal microscopy, BiFC	D ₃ stimulation enhances D ₁ agonist affinity	(43)
A _{2A} :D ₂	BiFC, FRET, CoIP, Immunofluorescence microscopy	A _{2A} decreases affinity of D ₂ for dopamine, Co-internalization and cross-desensitization	(45, 69)
D ₂ :CB ₁ :A _{2A}	BiFC, BRET, sequential BRET-FRET (SRET), confocal microscopy	Mediation of neuronal computation modulating striatal dopamine neurotransmission	(70-72)
A _{2A} :CB ₁	Colocalization, CoIP, BRET	CB ₁ signaling dependent on A _{2A} activation	(73)
mGlu ₅ :A _{2A} :D ₂	Colocalization, CoIP, BiFC, BRET and SRET,	Gs, Gi/o and Gq pathway regulation, and DARP-32, Erk and c-fos crossroads	(74)
mGlu _{2A} :5-HT _{2A}	BRET, CoIP, colocalization	mGlu ₂ regulates hallucinogen-induced coupling to G _{i/o} of 5-HT _{2A}	(75)
A ₁ :P2Y ₁	CoIP, confocal microscopy, BiFC	Generation of an adenosine receptor with P2Y-like agonist pharmacology, and inhibition of adenylyl cyclase activity via G _{i/o}	(51-53)

Table 1.1 GPCR heteromers

This table provides a list of heteromers that have been well described in the literature. The techniques employed to investigate receptor oligomerization and the functional crosstalk that arises from protomer interactions are detailed for each heteromer.

1.1.5 The dynamics of GPCR oligomerisation

Zoli et al. state that the term ‘heterodimerization’ was coined to delineate the ‘specific interaction’ between different types of G protein-coupled receptors (62, 76). Current research on GPCR dimers aims at investigating how they function by studying: 1) the agonists, partial agonists and antagonists of these dimers; 2) their binding site and optimal ligand occupancies; 3) the stoichiometry of the signalling complex; 4) the location of the dimerization interface and the identity of the interacting residues; and 5) the nature of the conformational change involved in this dimerization (77).

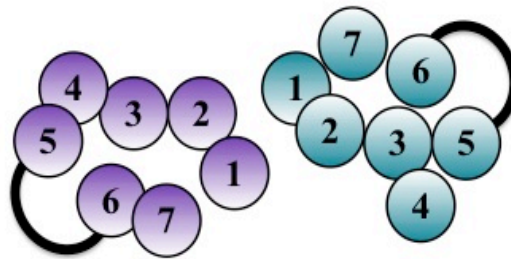
As the phenomenon of GPCR oligomerisation constitutes a relatively recent newcomer to the universe of GPCR research, it is not yet possible to seek complete and satisfying answers to these questions in the current literature. However, studies tackling heteromerisation dynamics suggest that ligand binding to one receptor protomer might provoke a conformational change in the neighbouring receptor within the oligomer unit, leading to an intricate signalling cascade (78). A possible insight into the spatial organization and binding interface of GPCR heteromers comes from imaging studies, which shed some light on the mechanisms of interaction between the monomeric subunits of oligomers. In 2003, Liang et al. published the first 3D molecular model of a GPCR oligomer, describing it as “the first semi-empirical model of a higher order structure of a GPCR in native membranes.” The model was resolved using atomic force microscopy (ATM) maps of rhodopsin in the native disk membrane and showed the arrangement of rhodopsin molecules in densely packed two-dimensional arrays of dimers (28, 79). According to this model, TM4, TM5 and the intracellular loop connecting TM3 and TM4 (IL2) of the rhodopsin dimers (shown in Figure 1-2) are implicated in the formation of rhodopsin dimers, or intra-dimeric interactions. These dimers then form rows through contacts between TM1, TM2 and the intracellular loop connecting TM5 and TM6 (IL3) (79). Further studies of the dopamine D₂ (D₂DR) homo-dimers corroborated the participation of TM4 and TM5 in dimer formation and indicated that TM4 also partakes in the conformational rearrangements corresponding to the agonist bound state of the dimer (80).

Data from computational studies and molecular simulations of dimerization on oligomeric proteins such as trimeric bacteriorhodopsin identified a number of dimerization interfaces with contacts between TM4-TM4, TM4-TM6 and TM5-TM6. Molecular predictions also ascertained that a protomer undergoes a conformational

change in the presence of its partner even when all the protomers are in the inactive state. Given that GPCRs have been found to interact through multiple interfaces, leading to spatial rearrangements of the protomeric subunits, they can form a panoply of oligomeric complexes with diverse pharmacological profiles, distinct from the signalling imprints of the individual protomeric receptors. This diversity makes it difficult to dress an inventory of all the biologically important interactions resulting in dimerization and of their biological functions (77).

The exact nature of the GPCR dimerization interface has not yet been fully unravelled. However, the literature describes two models of dimerization for transmembrane proteins. In the first model, two monomers touch each other, leading to the formation of a contact dimer. In the second model, the hinge loop of the dimer opens, causing the domains to exchange and produce a domain-swapped dimer (81) (shown in Figure 1.3). The concept of 3D domain swapping is well reviewed and accepted as a mechanism of oligomeric protein formation from monomeric constituents. According to this model, one entire domain from the monomeric subunit of a dimer is exchanged for another domain from the partner subunit, resulting in an “intertwined” dimer or higher oligomer (82, 83). Domain swapping has not been widely invoked in the context of GPCR oligomerisation. However, a number of computational and simulation studies have mentioned a possible role for the swapping of domains 5 and 6 in the formation of GPCR dimers (81, 84-86).

A.



B.

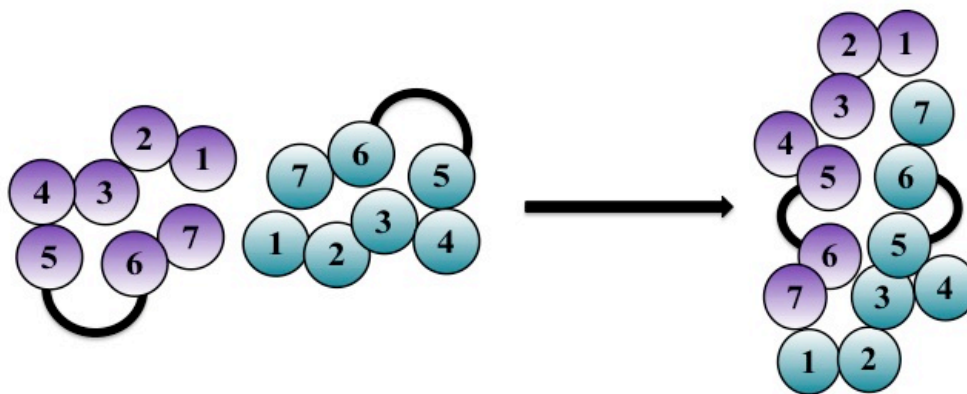


Figure 1.3 Possible models of GPCR dimerization adapted from Gouldson et al. (81, 84, 86)

A. 1,2-contact dimer. In contact dimers, receptor monomers are in direct contact through exterior residues. **B.** 5,6-domain swapped dimer. Domain swapping requires the exchange of transmembrane domain between the monomeric units of the dimers at the same sites involved in monomer formation. The shown dimer results from domain swapping at the 5-6 interface.

1.1.6 Receptor mosaics

The discovery that seven transmembrane receptors interact to form oligomeric assemblies with novel structural and functional features has generated a novel paradigm in GPCR signalling. This shift in understanding has in turn engendered specific terminologies that articulate the difference between the various forms in which GPCRs exist and signal. In a review published in 2010, Agnati et al. advanced a number of definitions used “in the study of protein networks at the plasma membrane level, and hence, also of the receptor function and the assembly of GPCRs into an integrative centre” (87).

The basic unit of GPCR signalling is the ‘microprocessor’. This term was first proposed by Kenakin to indicate that seven transmembrane receptors are not simply “on-off” switches. Rather they are sophisticated machines capable of elaborating information by adopting various structural conformations. In fact, GPCRs represent clusters of “interchanging conformations” known as ensembles. Ligand binding provokes modifications in these ensembles by favouring certain conformations compared to others, thus triggering the switch from inactive to active receptor states. The expanding GPCR literature suggests that conformational changes in different regions of the microprocessor may account for its ability to interact with different downstream effectors (87).

The next level of GPCR organisation is the receptor homodimer or heterodimer. This term refers to the coupling of receptors in the cellular membrane to produce a functional centre with novel structural and functional characteristics. Each receptor in the dimer is termed a ‘protomer’. Homodimers are pairs of the same protomer, while heterodimers are formed from distinct receptors. An oligomer is a multimeric protein formed from a small number of subunits in a state of reversible association with each other (87). The interaction between these two receptors, or receptor-receptor interactions (RRIs), is defined as the binding of a ligand to the orthosteric or allosteric sites of one receptor, causing a modification in the ligand recognition, decoding and trafficking processes of another receptor via allosteric interactions (88).

Recently, increasing evidence from coimmunoprecipitation (CoIP), bioluminescence resonance energy transfer (BRET), fluorescence resonance energy transfer (FRET) and bimolecular fluorescence complementation (BiFC) studies has pointed to the possible existence of a higher level of GPCR organisation. In fact, it

appears that GPCRs can form higher-order receptor oligomers composed of more than two protomers, in addition to classical homo- and hetero-dimers (22, 87-89). For instance, studies using combined bioluminescence/fluorescence energy transfer and complementation techniques revealed that four D₂ receptors or more associate to form higher order networks at physiological expression levels (90). Furthermore, higher-order oligomeric assemblages composed of at least three A_{2A} receptors were detected using combined BRET-BiFC (91). Coimmunoprecipitation studies using three different epitope tags have also shown the existence of aggregates consisting of trimeric M2 muscarinic cholinergic receptor associations in Sf9 cells (92).

Moreover, investigators have utilized novel techniques, combining Protein fragment complementation approaches (PCA), BiFC and sequential BRET/FRET (SRET) to identify the existence of higher order assemblies of A_{2A} homo- and heterodimers with CB₁ cannabinoid/D₂ dopamine receptors (22, 71, 88, 91, 93). This compilation of findings has supported the hypothesis that GPCRs can form high-order oligomers, or “islands of clusters” described as receptor mosaics (94). The notion of receptor mosaics was discussed by Agnati et al. in a number of papers (94-97), and postulates “that one can produce markedly different molecular aggregates of receptors by putting together the same building blocks to construct functionally different assemblies” (97).

According to Agnati, receptor mosaics are defined as macromolecular assemblies of more than two receptors that physically interact to form various spatial arrangements or topologies (87, 98). Moreover, receptor mosaics participate in both horizontal membrane networks (HMN) and vertical membrane networks (VMN). HMNs consist of proteins integrated into the membrane and grouped in specific topologies to form functional signalling-processing modules. VMNs, on the other hand, are molecular networks that extend to the cytoplasm and nucleus (87). Receptor mosaics can signal to both VMNs and HMNs, thus diversifying the elaboration of information, and they possess several mechanistic characteristics. First, a RM is functional only when one receptor regulates the biochemical and functional features of at least one other receptor of the assembly via allosteric RRIs (87). Second, the conformational re-distributions and ligand binding of each protomer is governed by the conformations and allosteric interactions with the other members of the cluster (87). Finally, the spatial arrangements and “allosteric” pathways interconnecting the RM members forge the RRIs that occur between the protomers (87, 99-101). On another note, the RM possesses “emergent properties” endowed with

recognition and decoding mechanisms distinctive from those of the protomers, a phenomenon described as “phenotype-plastic receptors” (87, 102).

In summary, recent research has debunked the traditional perception of GPCR receptors as monomeric units, revealing the inherent complexity of seven transmembrane signalling. The proposed nomenclature postulates the following hierarchical organization. The basic level consists of the “first-order microprocessor” which induces an intracellular cascade of the first order. If this unit interacts with another membrane protein, it gives rise to a first order HMN. The second level is formed from the “second-order microprocessor” or dimer, which evokes an intracellular signalling cascade of the second order. It can also produce a second-order HMN if it interacts with other membrane proteins. The third organizational level consists of higher-order microprocessors or RMs, which produce signalling cascades of the higher order. They result in higher-order HMNs when they interact with some membrane protein (87).

1.1.7 The physiological relevance of GPCR oligomerisation

As the literature reveals, the cellular membrane houses “hubs” of information transmission and processing in the form of monomers, homo- and heteromers and receptor mosaics. Oligomerisation is envisioned to fulfil an important physiological role by orchestrating a network of novel and diverse functions. First, heterodimerization could alter the agonist affinities of individual receptors, thus generating entities with novel agonist and antagonist pharmacologies. The A₁R-P2Y₁ complex offers an example of such signalling diversification through oligomerisation, whereby the association engendered an A₁R with P2Y₁R-like agonist patterns (51). Furthermore, the β-AR and AT₁R dimer provides an example of cross-inhibition, whereby the blockade of one protomer results in the uncoupling and inhibition of its interacting partner (103, 104).

Second, oligomer formation could modify the selectivity of GPCRs for distinct G-protein subsets, thus polarizing the hetero-oligomer towards different downstream signalling cascades upon agonist activation. For example, the D₁-D₂ heterodimer couples to G_{q/11}, leading to PLC-mediated intracellular calcium increase, a pathway that is not observed for the G_{s/olf}-linked D₁R or the G_i-linked D₂R (41, 66). In another instance, the 5-HT_{2A}-mGluR2 heteromer, a target of hallucinogenic drugs, was found to undergo conformational changes that allow 5HT_{2A}Rs to couple to G_{i/o} in addition to G_{q/11} upon ligand binding (75, 105). Moreover, the μ- and δ-opioid dimers were reported to be

insensitive to pertussis toxin (PTX), as opposed to the individual component receptors (42).

Third, oligomerisation might regulate desensitization and trafficking mechanisms by potentiating the internalization of receptors that cannot internalize on their own. For instance, the dimerization of the μ - and δ -opioid receptors provokes the cross-internalization of the μ -opioid upon activation of δ -opioid, thus reducing μ -opioid receptor-induced analgesia (22). Furthermore, the oligomerisation of the α_1A and α_1B -adrenergic receptor subtypes induced the co-internalization of the two protomers following agonist activation (106). This phenomenon was similarly observed for P2Y₁ and P2Y₁₁. In fact, oligomerisation of these two receptors induced the co-internalization of P2Y₁₁, which does not undergo endocytosis by itself (55). These integrated regulatory effects could help maintain the population of GPCRs in the cell under tight control while augmenting the diversity of GPCR signalling.

1.1.8 Functional crosstalk

The extensive GPCR research conducted in the past two decades has substantiated the existence and functional relevance of GPCR heteromers and higher-order complexes. Thus, receptor oligomerisation is now believed to constitute a major tool of communication and crosstalk between seven transmembrane receptors, allowing the diversification and fine-tuning of GPCR signalling. However, oligomerisation or physical crosstalk is not the only mechanism of receptor communication. In fact, 7TM interactions can arise from colocalized receptors partaking in signalling pathways, or from the synergistic regulation of signalling at crossroads, namely at the plasma membrane, the cytoplasm or nucleus, a phenomenon termed functional crosstalk (34). The mGlu_{1a} and GABA_B receptors illustrate this trend. For instance, the coactivation of both receptors augmented mGlu_{1a}-evoked calcium signalling (107, 108). Although oligomerisation was thought to occur, coimmunoprecipitation, BRET and Homogenous Time Resolved Fluorescence (HTRF) coupled to Snaptag labelling showed no evidence of physical contact between the two receptors (64, 109). Instead, the crosstalk was found to arise from signalling crossroads, whereby GABA_B receptors activated the $\beta\gamma$ subunits of G_{i/o}, which in turn enhanced the calcium response of the mGlu_{1a}-activated G_q (108, 109).

In summary, the interaction between heteromeric/oligomeric GPCRs is underpinned by three mechanisms (34):

- 1- Two receptors undergo functional crosstalk at the signalling level, without direct physical contact
- 2- Two receptors form a dimer. However, the crosstalk is not elicited by direct physical interaction but by functional crosstalk at the signalling level
- 3- Two receptors form a dimer, resulting in functional and physical crosstalk. This major means of receptor communication has been thoroughly described in this chapter

1.2 Purinergic receptors

1.2.1 Historical perspective on purine and pyrimidine discovery

Purine receptors are a subfamily of GPCRs activated by purine nucleotides and nucleosides such as adenosine and ADP. The first report of extracellular signalling by purines was published in 1929 by Drury and Szent-Györgyi (110), and described the effect of simple extracts from heart muscle, brain, kidney and spleen on the mammalian heart. Upon isolation and testing of the extract, the analysed substance was found to be similar or closely related to adenylic acid (adenosine monophosphate, AMP). When administered by intravenous injection in the guinea pig, it resulted in a block of the atrioventricular junctional tissue, thus impairing the conduction of cardiac impulses from the atria to the ventricles and inducing high-grade heart block. This strong action was not detected in the cat, rabbit and dog where adenylic acid only triggered a reduction of the heart rate (transient sinus bradycardia). Other observed effects of adenylic acid included vasodilation in the coronary arteries and peripheral vessels, provoking a decrease in blood pressure. Adenosine, obtained from yeast nucleic acid, produced an action identical to adenylic acid.

Another important hint of the role of purines as extracellular messengers was the discovery that dorsal root ganglia neurones of the rabbit ear release a vasodilator substance, which is neither acetylcholine nor histamine. Furthermore, denervation was found to increase the sensitivity of the rabbit's ear to this transmitter (111, 112). The response evoked by the substance had a latency period of about 10 sec. and was not abolished by atropine. Subsequent research revealed that the chemical transmitter responsible for antidromic vasodilation was ATP (113). In 1970, Burnstock et al. proposed that the autonomic nervous system harbours a component, distinct from the

adrenergic and cholinergic nerves, which releases ATP as a neurotransmitter (114). This third component was later termed “purinergic” and is highly expressed in the gastrointestinal tract (115, 116). Further identification and investigation of the extracellular actions of adenylyl purines confirmed the existence of “purinergic” receptors (117). Based on the analysis of the pharmacological profiles of the various adenylyl purines, Burnstock suggested that the receptors for the nucleotides ATP and ADP, whose structures are shown in Figure 1-6, were likely to be different from the receptors for nucleosides, leading to the subsequent division of purine receptors into P1 (adenosine) and P2 (ATP and ADP) receptors. P2 receptors were further subdivided into two different subtypes, P2X and P2Y, based on different response profiles to ATP analogues and selective antagonism (118). Additional evidence supported the existence of P2Y receptors that respond to pyrimidines as well as purines (119). The cloning of P2 receptors confirmed and extended the discrimination between P2 receptors to molecular structure, transduction mechanisms and effector systems (120). Seven subtypes of P2X and eight subtypes of P2Y have been identified to date (121-123).

1.2.2 Synthesis and breakdown of purines

Purines constitute a family of heterocyclic aromatic compounds composed of a five-membered nitrogen containing ring, or pyrimidine, fused to a six-membered nitrogen containing ring, or imidazole. They occur in high concentrations in living organisms. For instance, two of the four bases of nucleic acids are purines, namely adenosine and guanine. Other purines include xanthine, caffeine and uric acid. Purines are components of an important array of biologically significant molecules, such as ATP, cAMP, NADH and Coenzyme A, and as such partake in a number of vital metabolic cycles. One such cycle is that of adenylyl purine biosynthesis, which is initiated with a purine base such as adenine. The subsequent addition of a 5-carbon sugar or ribose to the nitrogen base of the purine results in the formation of a nucleoside. The addition of a phosphate group to the sugar portion of this nucleoside generates a nucleotide, also known as adenylic acid or adenosine 5'-monophosphate (AMP). When a second phosphate is added to AMP, a nucleoside diphosphate, or adenosine 5'-diphosphate (ADP) is produced. The addition of a third phosphate to ADP engenders a nucleoside triphosphate, known as adenosine 5'-triphosphate (ATP). Adenylyl purines can be salvaged through the breakdown of ATP into adenosine and adenine. These are then absorbed into red blood cells, which cannot synthesize ATP *de novo*, to permit nucleotide synthesis (124, 125). However, if the recycled adenosine and adenine remain unsalvaged, they are

catabolised. Purine catabolism occurs by deamination of adenosine to form inosine by adenosine deaminase, which is then cleaved to generate hypoxanthine and further oxidized to xanthine. The end product of purine degradation in man is uric acid.

Of the above-mentioned adenylyl purines, ATP constitutes the major energy “currency” of mammalian cells and is, subsequently, the most widely studied adenylyl purine. The breakdown of ATP into di- and mono-phosphates liberates energy that is employed by the cell to power a panoply of biological functions, including synthesis of biomolecules, signal transduction, active transport across the cell membrane, maintenance of resting membrane potential, neurotransmission and neuromodulation.

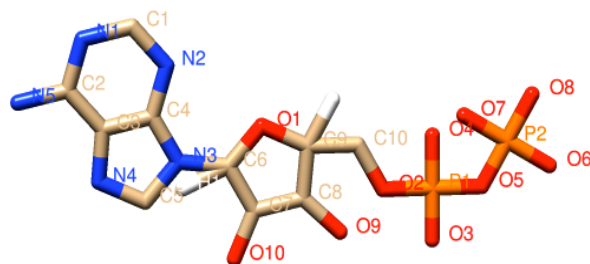
ATP is synthesized, stored into vesicles and released as a paracrine/autocrine molecule in the peripheral and central nervous systems (123, 126, 127). It functions as a fast excitatory neurotransmitter in the sympathetic, parasympathetic and enteric systems (128, 129). The concentration of nucleotides packaged into vesicles has been estimated to be 1000mM (127), whereas that of nucleotides secreted into the extracellular space ranges from 0.1 to 10 μ M (123). An extensive body of literature has demonstrated that ATP is released as a co-transmitter in conjunction with a number of other transmitters in the peripheral and central nervous systems (129). The first evidence of sympathetic co-transmission was reported by Westfall et al. who discovered that ATP and norepinephrine function as co-transmitters in the vas deferens of the guinea pig (130, 131). Later research revealed that ATP is released as a co-transmitter with noradrenaline in sympathetic nerves (132, 133), with acetylcholine in a number of tissues (134), as well as with 5-hydroxytryptamine, glutamate, dopamine and γ -aminobutyric acid (GABA) in the central nervous system (127).

Neuronal cells are not the only source of ATP, as it is also secreted from non-neuronal cells, such as astrocytes (135), glial cells (136) and pancreatic β cells (137), in response to a vast array of stimuli, including hypoxia, mechanical stress, agonists, acidosis, receptor stimulation, inflammation and osmotic shock (123, 126, 138). The concentration of ATP in the extracellular space is tightly regulated through an intricate balance between its release, catabolism and inter-conversion. Consequently, several enzymatic families are thus implicated in the breakdown of ATP released from neuronal and non-neuronal cells, including ecto-nucleotidase triphosphate diphosphoryl hydrolases

Chapter 1 Introduction

(E-NTPDases) and ectonucleotide pyrophosphatase kinases (E-NDPK) (139). The structures of ADP and ATP are shown in Figure 1.4.

A.



B.

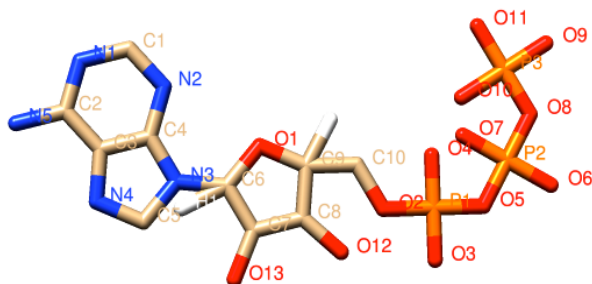


Figure 1.4 Structure of adenosine diphosphate and adenosine triphosphate

A. Pseudo 3D view of the molecular structure of ADP visualized using UCSF Chimera. Adenosine diphosphate, known as ADP, is a nucleoside diphosphate composed of three components, an adenine base (beige and blue), a ribose sugar at the centre (beige and red) and a negatively charged diphosphate chain (red and orange). The chemical formula of ADP is $C_{10}H_{15}N_5O_{10}P_2$. B. Pseudo 3D view of the molecular structure of ATP visualized using UCSF Chimera. Adenosine triphosphate, known as ATP, is a nucleoside triphosphate composed of three components, an adenine base (beige and blue), a ribose sugar at the centre (beige and red) and a negatively charged triphosphate chain (red and orange). The chemical formula of ATP is $C_{10}H_{16}N_5O_{13}P_3$.

1.2.3 Historical perspective on purine receptor discovery

In a seminal review published for the NC-IUPHAR Committee, Kenakin et al. proposed that “a completely” defined receptor would possess a unique pharmacological profile based on agonist and antagonist data, a known endogenous ligand, and a distinct amino acid sequence” (140). Due to the paucity of selective purinoceptor antagonists and their stability/insolubility (141, 142), the first proposed nomenclatures of purinoceptors were mainly delineated based on relative agonist potencies. This enterprise was further confounded by the fact that multiple purine receptor types can coexist on a single cell. The advent of recombinant DNA technology helped refine purinoceptor classification in light of molecular and structural findings coupled to pharmacological profiles.

The first evidence of the existence of adenosine receptors was advanced by Sattin and Rall in a key paper published in 1970 (143). In this work, the investigators monitored the content of cyclic AMP in guinea pig cerebral cortex slices and reported that it

increases 20-30 folds five minutes after exposure to 0.05 mM adenosine. They also noted that methylxanthines (0.5 mM) blocked the effect of adenosine, a blockade that was reversed by elevating adenosine concentration. Van Calcar et al. later showed that adenosine exerts a dual action in glial-like cells, leading to the increase and inhibition of cAMP concentration, respectively. This pointed to the existence of two different types of adenosine receptors, named A₁ and A₂ (144).

Burnstock proposed a “basis for distinguishing two types of purinoceptors” (118), according to four criteria: a) the selective action of antagonists, namely methylxanthines, which competitively inhibit adenosine but not ATP; b) the relative potencies of the multiple adenylyl purines at the different purine receptors; c) the activation of adenylate cyclase by adenosine, but not ATP; and d) the stimulation of prostaglandin synthesis by ATP, but not by adenosine. The two subtypes were termed P1 and P2, activated by adenosine and ATP respectively.

Later, Burnstock and Kennedy postulated that P2 receptors could be further subdivided into two distinct subgroups, called P2X and P2Y, respectively, in light of differing response profiles to various ATP analogues. The P2X subtype, for instance, exhibited the following agonist profile: $\alpha\beta\text{meATP} > \beta\gamma\text{meATP} > \text{ATP} \approx 2\text{meSATP} \approx \text{ADP}$, whereas P2Y receptors were preferentially activated by $2\text{meSATP} > \text{ATP} \geq \alpha\beta\text{meATP} \approx \beta\gamma\text{meATP}$ (118).

1.3 P2Y receptors

1.3.1 Nomenclature

P2Y receptors are metabotropic purine and pyrimidine nucleotide receptors that belong to the superfamily of rhodopsin-like G protein-coupled receptors. Eight mammalian P2Y receptors are currently recognized: P2Y_{1,2,4,6,11,12,13,14} (123). Pharmacologically, these receptors can be divided into 4 general groups: 1) adenine-nucleotide-preferring receptors activated by ADP and ATP, namely human and rodent P2Y₁₋₁₂₋₁₃ and human P2Y₁₁; 2) uracil nucleotide-preferring receptors which respond to either UDP or UTP, i.e. P2Y₄ and P2Y₆; 3) receptors of mixed selectivity, P2Y₂ and P2Y₄; and 4) receptors that respond to sugar nucleotides UDP-glucose and UDP-galactose only, mainly P2Y₁₄ (123, 145). The missing numbers constitute nonmammalian orthologues or receptors that possess sequence homology to P2Y receptors but do not respond to nucleotides (123). For instance, p2y3 may be a chicken orthologue of P2Y₆, while p2y8 and tp2y may be *Xenopus* and turkey orthologues of P2Y₄. P2y7 might be a leukotriene B4 receptor, while p2y5 and p2y10 are orphan receptors (123).

Furthermore, phylogenetic studies examining the evolutionary relationships between the members of the P2Y family have distinguished between two distinct subgroups of P2Y receptors (146). The first subgroup consists of the P2Y_{1,2,4,6,11} receptors which share 29 to 46% sequence homology, whereas the second subgroup comprises the P2Y_{12,13,14} receptors characterised by 21 to 48% homology (123). Alignment of the amino acid sequences of all members of the P2Y family reveals 21-57% identity between the various receptors (145). This phylogenetic partitioning can further be duplicated at the level of signal transduction mechanisms, as the two P2Y subgroups also diverge in their selectivity to G-proteins. In fact, the receptors of the first subgroup, i.e. P2Y_{1,2,4,6,11}, couple preferentially to G_{q/11} leading to the activation of the PLC_β/IP₃ pathway and mobilization of intracellular calcium. Conversely, the members of the second subgroup, i.e. P2Y_{12,13,14}, principally mediate their functional effects through coupling to members of the G_{i/o} family of G proteins (123).

An additional level of complexity transpires when amino acid structure is taken into account. P2Y receptors are G-protein coupled receptors consisting of a seven transmembrane motif. Particular amino acid motifs in TM6 and TM7 are thought to be crucial for the binding to GPCRs of extracellular nucleotides (147, 148). Evidence suggests that all human P2Y receptors possess the TM6 H-X-X-R/K motif required for

agonist activity (147, 149). However, the two subgroups differ in a defining motif situated on TM7 and implicated in ligand binding. For instance, the P2Y_{1,2,4,6,11} subclass possesses a Q/K-X-X-R motif in TM7, which is substituted by a K-E-X-X-L motif in the P2Y_{12,13,14} subclass, a disparity that might affect ligand binding affinities in these receptors (123).

In summary, the literature suggests that P2Y receptors can be segregated into two distinct subclasses based on a tripartite model encompassing 1) phylogenetic or sequence differences; 2) structural dissimilarities, notably the presence of differing motifs thought to be involved in ligand binding; and 3) differential coupling to G proteins (123). The tissue distribution, G protein coupling and pharmacology of P2Y receptors are summarized in table 1.2

Receptor Subtype (Accession Number)	Chromosome Location	Tissue Distribution	G-protein	Agonists (pEC ₅₀)	Antagonists (pIC ₅₀)
hP2Y₁ U42029, U42030, S81950	3q25.2	Wide, including platelets, heart, skeletal muscle, neuronal tissues, digestive tract	G _{q/11}	2-MeSADP (8.7-7.9), 2MeSATP (8.5-6.9), ADP (8.0-6.6), ATP (6.5-5.0), ATP _γ S (6.4), ADPβS (6.1-6.0)	MRS 2279 (7.3), MRS 2179 (6.5), PPADS (5.4), Suramin (5.8), BZATP (pKi, 5.4), 2MeSATP (pKi, 5.3), ATP (pKi, 5.2)
hP2Y₂ NM_002564	11q13.5	Wide including lung, heart, skeletal muscle, spleen, kidney	G _{q/11}	UTP (7.7-6.2), UTP _γ S (6.6), ATP (7.1-6.6), ATP _γ S (6.2-5.8), GTP (4.9) AP ₄ A (6.6-6.1)	Suramin (4.9-4.3), Reactive Blue
hP2Y₄ U40223, X91852, X96597	Xq13	Placenta, lung, Vascular smooth muscle, brain, liver	G _{q/11}	UTP (7.6-5.6) UTP _γ S (5.8) ATP (5.2-5.0) GTP (5.2)	PPADS (4.8), ATP (pk _b , 6.1), Reactive Blue 2 (4.7)
hP2Y₆ U52464, AF007891	11q13.5	Wide including lung, heart, aorta, spleen, placenta, thymus, intestine, brain	G _{q/11}	UDPβS (7.6) UDP (7.0-6.5) UTP (5.2- 5.0) ADP (4.5-4.2)	Reactive Blue 2 (4.5), MRS2567, PPADS
hP2Y₁₁ NM_002566	19p13.2	spleen, intestine, immune system, brain, pituitary	G _{q/11} and G _s	ATP _γ S (5.5-4.6), dATP (5.1-5.0), BzATP (5.1-4.2), ATP (4.9-4.2), 2-MeSATP (4.6-4.3), αβ-meATP (4.1-3.9), βγ-meATP (3.7)	Suramin (4.8), AMPS (3.5-2.5), NF157
hP2Y₁₂ AF313449, AF321815, AB052684	3q25.1	platelets, neural tissue	G _{i/o}	2-MeSATP (10-8.5), 2-MeSADP (10-7.9), ADP (7.4-6.5), ADPβS (7.0-6.4), ATP (6.2-5.9)	AR-C69931 (7.6), C-1330-7 (7.4), Reactive Blue-2 (5.9), 2-MeSAMP (5.9-5.3), Suramin (5.4)
hP2Y₁₃ NM_023914, NM_176894	3q24	spleen, leucocytes, bone marrow, liver, brain	G _{i/o}	ADP (8.0), 2-MeSADP (7.9), 2-MeSATP (7.1), ADPβS (7.4), ATP (6.6)	ARC69931M X, Reactive Blue 2, Suramin, PPADS
hP2Y₁₄ NM_014879	3q21-25	placenta, adipose tissue, spleen, intestine, brain	G _{i/o}	UDP-glucose (7.1), UDP-galactose (6.4) UDP-N-acetylglucosamine (6.1)	

Table 1.2 The P2Y family of purinoceptors

This table offers a description of chromosome location, cellular distribution, G-protein coupling and agonist potency of the various members of the P2Y family of purine receptors.

1.3.2 Structure-function relationships of P2Y receptors

P2Y receptors belong to the family of class A G protein-coupled receptors and as such exhibit the seven transmembrane domain tertiary structure characteristic of GPCRs. They consist of 308 to 377 amino acids, have a mass of 41 to 53 kDa after glycosylation (121) and share 17 to 61% identity (150). In depth understanding of the structural mechanisms that underlie agonist binding and conformational modifications in P2Y receptors, and GPCRs in general, has been hindered by the lack of high-resolution structural models of GPCRs due to their refractoriness to crystallization. In view of such obstacles, the main resources researchers have utilized to analyze the structure-activity relationships of P2Y receptors are structural homology to rhodopsin and P2Y receptor models employed for sequence analysis, site-directed mutagenesis and homology modelling studies.

One of the first studies to provide insights onto the molecular underpinnings of ATP binding to P2Y receptors utilized P2Y₂ receptors (147). Neutralization of three positively charged amino acid residues in TM6 and TM7 (His²⁶², Arg²⁶⁵, Arg²⁹²) of the receptors by substitution with uncharged leucine resulted in a 100-850 fold decrease in the potency of ATP and UTP without affecting their efficacy. This suggested that the modified residues interacted with the phosphate residues of ATP rather than the purine or pyrimidine groups of the nucleotides (147). Subsequent studies employing P2Y₁ receptor models further highlighted the critical involvement of positively charged lysine and arginine residues situated on the exofacial side of TMs 3, 6 and 7 in docking of the α -phosphate moieties of ATP (148, 151). The two disulfide bridges present in P2Y₁ were also found to contribute to the structural stability of the receptor, possibly by stretching the second extracellular loop (ECL2) over the opening of the TM cleft in order to position amino acids within the binding pocket (152).

1.3.3 Pharmacology

A broad range of naturally occurring nucleoside di- and triphosphates serve as agonists at P2Y receptors, each of which can be stimulated by several compounds. ADP serves as a full agonist at P2Y₁, the dog orthologue of P2Y₁₁, and P2Y₁₂₋₁₃, but is a partial agonist at P2Y₆ isoforms (150). ATP fully activates P2Y₂, some orthologues of P2Y₄ and P2Y₁₁ (150). The pyrimidine UTP acts as a full agonist at all orthologues of P2Y₂ and P2Y₄ and has also been found to elicit a response at P2Y₁₁ (153), while UDP is active at

all orthologues of P2Y₆ and P2Y₁₃. The P2Y₁₄ receptor exhibits a unique agonist profile as its preferred agonist is UDP-glucose (150).

Phosphate modifications of P2Y receptor agonists usually augment their stability toward breakdown by ecto-nucleotidases. The phosphorothioate ADPβS, for instance, is a potent agonist at P2Y₁, P2Y₁₂ (146) and P2Y₁₃ (154), while UDPβS is active at P2Y₆ and UTPγS at P2Y₂ and P2Y₄. The 2-thioalkyl derivatives (2-MeSADP and 2-MeSATP) function as non-selective agonists at P2Y₁, P2Y₁₁, P2Y₁₂ and P2Y₁₃. The ribose-modified derivative BzATP stimulates P2Y₂ and P2Y₁₁.

Structural analogues of adenosine bis-phosphates, such as MRS2179 and MRS2279, constitute potent antagonists of P2Y₁ receptors (155). In contrast, no potent and selective antagonists of pyrimidine-activated P2Y receptors have been developed to date. However, suramin has been reported to antagonise P2Y₂ and P2Y₁₁, Reactive blue 2 blocks P2Y₄ and P2Y₆ and PPADS inactivates P2Y₄, P2Y₆ and P2Y₁₁ (150).

1.4 The P2Y₁ receptor

The P2Y₁ receptor was first cloned from the chick brain and exhibited an agonist potency order of 2me-SATP ≥ ATP ≥ ADP (156). P2Y₁ was later cloned and characterized in human, rat, mouse, cow, turkey, guinea pig and *Xenopus* (123). In most species, ADP is more potent than ATP which functions as a partial agonist at P2Y₁R and constitutes an antagonist at low levels of receptor reserve (157). The first selective antagonists used against the P2Y₁ receptor were A3P5P and A3P5PS (158), later replaced by the more potent MRS2179 and MRS2279 (159), which exhibit high selectivity to P2Y₁ as compared to other P2Y and P2X receptors (159, 160) and whose potency can be significantly increased by the modification of the 2-position of the adenine moiety (161, 162) and

Site-directed mutagenesis studies helped elucidate some of the key residues implicated in ligand binding. According to the proposed model, Arginine 128 situated on TM3 and lysine 280 located on TM6 are thought to interact with the α and β phosphates of ATP, while arginine 310 (TM7) further contributes to the docking of the β phosphate and threonine 222 (TM5) to that of the γ phosphate (123). Glutamine 307 and serine 314 at TM7 are thought to assure the docking of the adenine ring. Comparison of the human, mouse, rat and hamster amino acid sequences of P2Y₁ revealed 97.3% and 96.8% similarity between these species (shown in Table 1-2). Amino acid segments

corresponding to the transmembrane domains of human P2Y₁ and residues crucial for ligand binding to this subtype were highly conserved across species. Moreover, the motifs GXXXN (TM1), LXXXD (TM2), DRY replaced by HRY (TM3) in P2Y₁, NPXXY substituted by DPXXY (TM7) in several P2YRs, RRS/QSKSE, thought to participate in interactions with a voltage-gated ion channel known as T_{in}, and DTSL, a canonical class I PDZ domain that binds the scaffold NHERF-2 were retained in the different species (163, 164). These findings reveal that the structure of P2Y₁ is highly conserved across various species.

The study of P2Y₁ mRNA expression patterns using quantitative reverse transcription-PCR techniques made it possible to delineate a map of P2Y₁ receptor distribution. hP2Y₁ was found to be widely distributed throughout the human body, with high expression levels detected in the brain, prostate gland and placenta (165). It is also expressed in the pituitary gland, lymphocytes, spleen, heart, lung, liver, kidney, stomach, intestine, skeletal muscle, adipose tissue and pancreas at varying levels (166).

P2Y₁ receptors are mainly coupled to the G_{q/11} pathway, which is insensitive to pertussis and cholera toxin. This pathway stimulates the formation of IP₃ and DAG and the mobilization of intracellular calcium, resulting in the modulation of various signalling pathways, namely PKC, PLA₂, Ca²⁺-dependent K⁺ channels, NOS and endothelium-derived relaxing factor (EDRF) formation, and the synthesis of endothelium-derived hyperpolarizing factor (EDHF). The formed DAG stimulates PKC, which may in turn activate PLC, PLD, the MAPK pathway and voltage Ca²⁺ channels.

%	P2Y ₁ Hamster	P2Y ₁ Rat	P2Y ₁ Mouse	P2Y ₁ Human
P2Y ₁ Hamster	100	48.5	47.7	48.3
P2Y ₁ Rat	49.3	100	97.1	95.2
P2Y ₁ Mouse	48.8	98.4	100	94.9
P2Y ₁ Human	49.3	97.3	96.8	100

Table 1.3 Percentage of identity (%) between the amino acid sequences of different P2Y₁ species subtypes

The sequences of human (GenBank: AAB47091.1), mouse (NCBI: NP_001268945.1), rat and hamster (GenBank: AAL09156.1) P2Y₁ were aligned using MacVector 13.0.4 by ClustaIW. Identity scores revealed 97.3% and 96.8% similarity between human, rat and mouse P2Y₁, respectively, revealing that the P2Y₁ amino acid sequence is highly conserved across various species.

One of the main functions attributed to hP2Y₁ is its participation in platelet physiology in tandem with hP2Y₁₂ (167). P2Y₁ deficient mice, for instance, suffer from impaired platelet aggregation, increased bleeding time and resistance to collagen, adrenaline or ADP induced thromboembolism (168, 169). P2Y₁ brings about platelet shape change through a rise in intracellular Ca²⁺ mediated by G_{αq11}-induced PLC stimulation (170), and its involvement in thrombin-dependent tissue factor induced thromboembolism renders it a potential target for antithrombotic drugs. Other reported functions of P2Y₁ include the formation and maintenance of postsynaptic specializations in neuromuscular junctions (171), the regulation of vascular tone in the placenta (172), modulation of bone formation and resorption (173), the parasympathetic inhibition of colonic smooth muscle (174) and possibly the inhibition of long-term depression in the prefrontal cortex (175).

1.5 The P2Y₁₁ receptor

P2Y₁₁ was first cloned from human placenta cells (176) and showed the following order of potency for agonist activity: AR-C67085MX ≥ ATPγS ≈ BzATP > dATP > ATP > 2meSATP >>> ADP (176-178), suggesting that it is the only P2Y receptor selective for ATP. UTP was also reported to induce Ca²⁺ mobilization at the P2Y₁₁ receptor (153). This receptor is competitively antagonized by suramin, AMPS and NF157 (150). The closest homolog of P2Y₁₁ is the P2Y₁ receptor, with which it shares 33% amino acid identity, followed by the P2Y₂ receptor (28%) (121).

The human P2Y₁₁ receptor possesses a unique profile among other P2Y receptors. In fact, it strongly couples to the dual activation of G_{q11} and G_s and as such is the only

P2Y receptor linked to the stimulation of adenylyl cyclase (149, 177, 179, 180). Experimental strategies including PLC inhibition, prostaglandin synthesis, chelation of intracellular calcium and down-regulation of PLC were employed to ascertain that the P2Y₁₁-mediated increase in cAMP is indeed a function of G_s and not a by-product of IP₃ and PKC activity (178, 181).

The gene for the P2Y₁₁ receptor maps to chromosome 19p31 (182). It possesses a unique feature, namely the presence of a 1.9-kb intron sequence that interrupts its open reading frame and separates the first exon of the gene from its second exon (183). Furthermore, the hP2Y₁₁ gene is contiguous to the gene encoding the human orthologue of SSF1 with which it was found to ubiquitously undergo intergenic splicing in human organs (183). The fusion protein produced from the chimeric transcripts, however, was only detected following recombinant overexpression.

The hP2Y₁₁ receptor is widely distributed throughout the human body. Northern blotting has detected significant levels of P2Y₁₁ mRNA in the human spleen, intestine and liver (176, 183). Quantitative RT-PCR analysis has further revealed that hP2Y₁₁ mRNA is relatively highly expressed in all tissues compared to other P2Y genes (166). hP2Y₁₁ is most abundant in the brain, pituitary, spleen and lymphocytes, localizes moderately to most other tissues, and is least present in liver, cartilage and bone (166).

The expression profile of hP2Y₁₁ and its differential coupling to two distinct signalling pathways points to its critical contribution to a palette of physiological responses. hP2Y₁₁ is involved in the modulation of the immune response by activation of human dendritic cells (DCs) (184). For instance, exposure to low levels of ATP triggers a graded action on maturing DCs. This up-regulates the expression of stimulatory molecules on one hand, but suppresses the production of cytokines such as TNF- α and IL-12, on the other, resulting in an altered chemokine-receptor profile (185). Low concentrations of ATP have also been found to potentiate the migration of Monocyte-derived DCs (MoDCs) into sites of inflammation. Upon arrival to the epicentre of inflammation, however, the accumulation of ATP inhibits cell movement, an effect that might prolong exposure to maturation inducing factors and aid in antigen internalization (186).

A number of studies also suggest a role for hP2Y₁₁ in the differentiation of cells of the early human myeloid lineage. In fact, hP2Y₁₁ has been reported to contribute to the ATP-induced differentiation of HL-60 promyelocytic leukemia cells through the activation of protein kinase A (187, 188). RT-PCR and northern blot analysis similarly spotted the expression of hP2Y₁₁ in NB4 promyelocytic leukemia cells, where it is envisioned to mediate the ATP-induced granulocytic commitment of the cells (189). The absence of hP2Y₁₁ expression in neutrophils, which constitute terminally differentiated myeloid cells, implies a preferential action in the early stages of maturation.

Another interesting patho-physiological role of hP2Y₁₁ is the induction of secretion in pancreatic duct epithelial cells (PDEC) through the activation of cystic fibrosis transmembrane conductance regulator (CFTR), a cAMP-activated Cl⁻ channel (190). Feng et al. also hinted to a possible implication of hP2Y₁₁ in mast cell physiology, whereby the receptor could attenuate cytokine production to help combat inflammation (191). The involvement of P2Y₁₁ in inflammation further extends to the field of cardiovascular disease, as the P2Y₁₁ polymorphism Ala-87-Thr is associated with both increased C-reactive protein and heightened risk of myocardial infarction, thus constituting a potential target for novel drug development (192).

Other effects attributed to hP2Y₁₁ embrace cell cycle arrest and sensitization to death in endothelial cells (193), abrogation of apoptosis in neutrophils (194), and the parasympathetic inhibition of colonic smooth muscle (174).

1.6 Interaction between P2Y₁ and P2Y₁₁

One of the most striking characteristics exhibited by the human stomach is its capacity for accommodative relaxation, i.e. its ability to expand from around 75mL to 2L upon food ingestion, a capacity mediated by hP2Y₁₁ in response to parasympathetic inhibition. Parasympathetic inhibition is provoked by the rapid hyperpolarization of SMCs following the activation of calcium-activated potassium channels (SK_{Ca} and BK_{Ca}). This phenomenon is mediated by several autonomic neurotransmitters, including extracellular ATP. Upon activation by ATP, P2Y receptors evoke a rapid rise in intracellular Ca²⁺ leading to the opening of SK_{Ca} and BK_{Ca} channels and to the subsequent hyperpolarization of the cell (174, 195). King and Townsend-Nicholson have provided evidence for the involvement of P2Y₁ and P2Y₁₁ receptors in the fast and slow relaxation of gut SMCs (174), proposing that P2Y₁₁-mediated purinergic inhibition may only be fully active when the cells are constantly excited and depolarized. cAMP, which acts as a molecular switch for the α subunit of BK_{Ca}, enhances the probability of the channel's open state via subunit phosphorylation (196). The coupling of cAMP production to the mobilization of intracellular Ca²⁺ thus seems to fine-tune the duration and amplitude of smooth muscle relaxations and the G_s-mediated P2Y₁₁ activity provides a mechanism for modulating this relaxation. For such a delicate balance to be maintained, intricate cross-talk between P2Y₁ and P2Y₁₁ may be required and could involve direct contact through oligomerisation. Additionally, P2Y₁₁ activation might also be implicated in the inhibition of insulin-mediated leptin production and stimulation of lipolysis. These interesting findings highlight the role of hP2Y₁₁ in obesity and reveal its importance as a potential pharmaceutical target (197).

The work undertaken for this doctoral project investigates the possible interactions between P2Y₁ and P2Y₁₁, thought to occur in the taenia coli of the guinea pig, by creating a recombinant model co-expressing both receptors. P2Y₁₁, which induces the slow relaxation of SMCs, is of particular interest as it has been reported to crosstalk with other receptor subtypes, including P2Y₁ and M₃-muscarinic receptors (55, 198). M₃ receptors mediate the excitation of SMCs upon activation by acetylcholine. Their excitatory action is suppressed by the non-selective antagonist atropine and can also be inhibited by extracellular ATP in a PLC-dependent fashion through the activation of P2YRs. Interestingly, the addition of forskolin to SMCs was found to result in an ambiguous effect on excitatory and inhibitory responses (198). For instance, the forskolin-mediated activation of adenylyl cyclase was found to cause a hyperpolarization of the cell. In

atropine-treated cells, inhibitory junction potentials (IJPs) were not affected by forskolin. However, in cells untreated with atropine, forskolin was reported to suppress IJPs and to induce excitatory junction potentials EJPs (198). This complex response was not influenced by a rise in intracellular cAMP concentration. A possible explanation of this observation is that cAMP increase activates protein kinase G, which in turn induces the opening of calcium-dependant potassium channels (174). However, this ambiguity could also point to possible interactions between M₃ receptors and P2Y receptors, especially P2Y₁₁, which couples to G_s.

The other proposed partner of P2Y₁₁ is the P2Y₁ receptor, which is thought to mediate the fast relaxations of smooth muscle cells. In a paper summarizing her doctoral work, Ecke reported that P2Y₁ and P2Y₁₁ are able to oligomerize, thus enabling the desensitization of P2Y₁₁. In fact, when expressed alone, the P2Y₁₁ receptor does not internalize. In the presence of its interacting partner, however, P2Y₁₁R was found to undergo endocytosis and this oligomerisation-induced internalization was reduced by the knock-down of P2Y₁ (55), suggesting that oligomerisation could regulate the expression levels of P2Y₁₁ at the plasma membrane.

1.7 Aims of the project

Building on this foundation, the project undertaken for this thesis sheds light on the pharmacology and interaction of two components of the tripartite (hP2Y₁- hP2Y₁₁-M₃) model involved in controlling gut smooth muscle function, namely P2Y₁ and P2Y₁₁. The driving motive behind this study is that a better understanding of the signalling profiles of co-expressing receptors, which often differ from those of individual receptor subtypes, offers novel avenues for the development of therapeutic targets. This is especially true if the co-expressing receptors participate in the formation of a functional heterodimer as it would enable structural information to be used to inform drug design. In particular, studying the interaction between P2Y₁ and P2Y₁₁ could permit the discovery of a drug that targets the relaxation of stomach SMCs in obese patients. Obesity constitutes a major eating disorder of our time and the most employed anti-obesity therapy is currently bariatric surgery, an invasive medical procedure associated with serious health hazards such as morbidity and mortality. Pharmacologically, three anti-obesity drugs, namely rimonabant, sibutramine and orlistat, were previously available in the market, two of which were recently withdrawn due to adverse health effects. For instance, the cannabinoid-1 receptor antagonist rimonabant, withdrawn in 2008, engendered a feeling

of satiety but provoked undesirable psychiatric symptoms such as anxiety and depression. Sibutramine, withdrawn in 2010, caused blood vessel constriction and hypertension. The third drug, orlistat, is still available although it leads to faecal incontinence, produces minor weight loss and is only used as a temporary support for dietary regimes (199). These failings underpin the lack of safe and effective anti-obesity medicaments, thus highlighting the pressing need for further pharmacological research in this field. Given the huge potential of GPCRs as drug targets, the study of P2Y₁ and P2Y₁₁, which are directly involved in stomach relaxation, falls into the effort to palliate this shortage of treatment options. The driving ambition behind this research is to devise a chemical gastric band that could replace aggressive bariatric procedures.

The aim of this thesis was thus to commence work in this area by investigating the pharmacology and ligand selectivity of P2Y₁ and P2Y₁₁ in a co-expressing system with the following three aims:

Aim 1: To study the effect of co-expression on the signalling profile of P2Y₁ and P2Y₁₁, by characterizing the nucleotide-mediated calcium responses of a recombinant system co-expressing both receptors.

Aim 2: To distinguish between P2Y₁ and P2Y₁₁ signalling properties and identify ligand responses specific to the co-expressing system by characterizing the pharmacological properties of the individual signalling profile of each receptor expressed in isolation.

Aim 3: To use antagonists to characterize novel pharmacological sties identified by aims 1 and 2.

Chapter 2

Materials and Methods

2.1 Tissue culture techniques

The following sections depict the basic cell culture splitting and passaging techniques employed in this project, as well as the protocols used to generate the stably transfected CHO-K1-hP2Y₁₁ clones 6 and 13 and the 1321N1-hP2Y₁ cell line.

2.1.1 Cell lines and cell culture conditions

Adherent CHO-K1 (Chines Hamster Ovary) cells were acquired from the European Collection for Cell Cultures (ECACC). The cells were grown in either a T₇₅ or T₁₅₀ tissue culture flask using a 50:50 Dulbecco's Modified Eagle's Medium (DMEM/Sigma)/Ham's Nutrient Mixture F-12 (Sigma) supplemented with 50mL of 10% Fetal Bovine Serum (FBS/Sigma) and 5mL of 10% L-Glutamine (Sigma). Adherent 1321N1 human astrocytoma cells (ECACC) were cultured in Dulbecco's Modified Eagle's Medium supplemented with 50mL of FBS and 5mL of 10% L-Glutamine. The used media were stored in a 4°C fridge for a maximum length of six weeks before replenishing the L-Glutamine. Cells were grown at 5% CO₂ in a 37°C humidified tissue culture incubator (Heraeus) and were passaged, transfected and manipulated in a class II Laminar flow safety cabinet (Heraeus).

2.1.2 Passaging, splitting and counting

The cells were split and passaged when they reached 100% confluence, forming a monolayer that occupied the entire surface area of the flask. The manipulated cells were first washed with 10mL of Dulbecco's Phosphate-Buffered Saline (DPBS/Sigma) following aspiration of the existing cellular medium. The cells were then incubated in 10mL of DPBS-EDTA buffer, containing 0.5mM EDTA, to detach them from the growth surface. The DPBS-EDTA buffer was left for three minutes at room temperature before the cells were lifted. The cells were then typically split and passaged at 1:5, 1:10 or 1:20 with respect to the surface area of the flask depending on the speed of their growth cycle. The resuspended cells were then used to 1) reseed the flask or other flasks, 2) create freezer ampules for storage of cell lines or 3) prepare 96 well plates used for high-throughput assays.

2.1.3 Cellular density measurement

To determine the volume of cell suspension needed to achieve the desired split, the density of resuspended cells was measured using the CASY® Cell Counter and Analyser System Model TT (INNOVATIS), a technology that performs “standardized cell counting methods, viability checks, aggregation correction, volumetric measurement with high measuring range dynamics.” A tailored setup, specifying the selected measuring parameters (used capillary, X axis or range of size distribution, sample volume and number of cycles), the evaluation parameters (dilution factor, Y axis, evaluation cursor, normalization cursor, % calculation, debris, aggregation correction, and mean volume) and output parameters (interface, page feed, print mode and graphic) was created and used throughout the project for all cell count measurements. After the cells were detached from the flask, approximately 1mL of the suspension was transferred into a clean 1.5mL Eppendorf test tube.

In order to perform the cell count, a CASY®-cup was first filled with 10mL of CASY®ton buffer (Roche). 100µL of the aliquoted cell suspension was then added to the buffer, following which the lid of the cup was secured and the cup was tilted a few times to mix the sample. The vial of diluted sample was placed on the platform below the measuring capillary, allowing an external electrode to be inserted into the sample. The START button was pressed to initiate the measurement, which calculates the number of cells present in a given sample based on the resistance measurement of pulse area analysis. During the measurement, 400µL of the sample was aspirated by a precision measuring capillary and slowly passed in a measuring pore, through which a low voltage was pulsed. The cells exhibited a size or dimension-dependent resistance to the voltage, whereby an isolated intact cell generated a higher resistance than a dead lysed cell. The resistance resulted from the nucleus membrane rather than the cell surface membrane, thus allowing the discrimination between living and dead cells. The density measurement was performed in triplicate. CASY® automatically operates the necessary steps, taking into account the dilution factor. A size distribution of the sample thus appears in the display, together with a complete numerical evaluation of the measurement data, specifying the number of viable cells in the measured sample in cells/mL and the percentage viability of the cells in the sample.

The density of resuspended cells was measured for each 1) cell passage and 2) FLIPR cell plate set-up in order to ensure that the same density of cells was plated across experiments for consistency and reproducibility purposes.

2.1.4 Transfection of cells with plasmid DNA

Generation of the stable CHO-K1 cell line expressing human P2Y₁₁ was undertaken using the calcium phosphate-DNA precipitate formed in BES method, a high efficiency technique suitable for the stable transformation of cells with circular plasmid DNA. Two different pools of CHO-K1-hP2Y₁₁ were generated by transfecting two independent aliquots of cells, each plated at the same density, with different amounts of hP2Y₁₁ cDNA.

The exponentially growing untransfected CHO-K1 cells were grown in the tissue culture flask until they reached 100% confluence. The cells were then split and transferred into a clean 50mL Falcon tube. The densities were then counted and cell suspensions of 20,000 to 25,000 cells/cm² were each plated in two 10cm petri dishes. The cells were incubated overnight in 10mL of DMEM/ Ham's F12 mixture until they achieved 100% confluence and were ready for transfection. For this purpose, two different mixtures of calcium phosphate-DNA, containing different amounts of hP2Y₁₁ in pcDNA3 plasmid DNA, were prepared in order to establish two different pools of CHO-K1-hP2Y₁₁, pools 0.5 and 1.0. In a 15mL Falcon tube, 15μL of caesium-purified hP2Y₁₁ in pcDNA3 plasmid DNA (15μg) was mixed with 50μL of 2.5M CaCl₂ and 435μL of ddH₂O. The mixture was gently vortexed with the cap off, while 500μL of 2xBBS was added dropwise to the mixture, following which it was incubated for 20 minutes at room temperature. The entire mixture (1mL) was added dropwise to the untransfected CHO-K1 cells and the mixture was gently swirled to allow even distribution of the DNA mix in the medium. The transfected CHO-K1 plate was then placed in a capsule filled with 3% CO₂, sealed and incubated inside the 37°C incubator for 24 hours. After removal from the 3% CO₂ chamber, the transfected CHO-K1-hP2Y₁₁ pools 0.5 and 1.0 were passaged using 2.5mL PBS-EDTA, transferred to a T₇₅ flask each, and then placed in the 5% CO₂ incubator for an additional 24 hours before the selection for stable transformants was initiated using a protocol modified from Chen and Okayama (200).

2.1.5 Generation of stable cell lines

After transfection of the CHO-K1 cells with hP2Y₁₁ cDNA, the newly produced CHO-K1-hP2Y₁₁ pools 0.5 and 1.0 were subjected to selection for three weeks in growth medium containing Geneticin (G418). The cell lines were washed using DPBS, replenished with fresh DMEM/ Ham's F12 mixture following which the antibiotic Geneticin was introduced at a final concentration of 400µg/µL to the T₇₅ flasks containing pools 0.5 and 1.0, respectively. The selected cell lines were kept in the 37°C incubator, washed with DPBS and replenished with fresh medium containing the antibiotic once every 5 days for approximately 3 weeks. During the selection process, mass death of untransfected cells, coupled to the expansion of cellular colonies bearing successfully transfected cells resistant to Geneticin, were observed. When cell death had finally ceased, and the successfully transfected cells had grown to 100% confluence, the established CHO-K1-hP2Y₁₁ pools were aliquoted for freezing purposes, and cloned to generate CHO-K1-hP2Y₁₁ clones of varying hP2Y₁₁ receptor density.

2.1.6 Collection and freezing of stably transfected cell lines

Freezer cryotubes were created and labeled for the long-term storage of the newly created cell lines. The monolayer of cells in the T₇₅ flask was first washed with DPBS then detached using 15mL DPBS-EDTA buffer at room temperature for two minutes. The cell suspension was transferred to a clean 50mL Falcon tube, centrifuged for 5min at 1000rcf, following which the tube was removed from the centrifuge and the supernatant was aspirated. A 10% DMSO-FBS mixture was prepared by adding 9mL of thawed FBS to 1mL of DMSO. The cell pellet was resuspended in the DMSO-FBS mixture, and the obtained preparation was distributed into cryotubes (1mL/tube). The ampoules were stored in a -80°C freezer.

The steps described in the previous section were also employed for the creation of a stably transfected CHO-K1-hP2Y₁₁ clones 6 and 13 as well as a 1321N1-hP2Y₁ cell line, which was generated using hP2Y₁ in pcDNA3 plasmid DNA provided by Dr. Andrea Townsend-Nicholson.

2.1.7 Cloning by limiting dilution

Limited dilution cloning was used in order to isolate single clones derived from a stably transfected pool. This was achieved by creating a series of increasing dilutions of

the parent cell cultures, seeding aliquots of the obtained suspensions in the wells of 96 well plates, then screening the plates for wells containing monoclonal cell colonies.

The confluent cells were detached from a flask, transferred to a clean 50mL Falcon tube and counted to determine the volume of cell suspension required to generate a 5×10^4 cells/mL dilution. The appropriate volume of cells was transferred to a sterile 1.5mL Eppendorf tube and culture medium was loaded to achieve the final volume. Sequentially, 1mL of the obtained 5×10^4 dilution was dispensed into another tube and loaded with cell medium to generate a dilution of 5×10^3 cells/mL. 1mL of this dilution was then added to another tube following which culture medium was loaded to produce a 5×10^2 cells/mL dilution. Five additional serial dilutions were performed using this final dilution (5×10^2 cells/mL). In fact, for each pool respectively, 5.6mL of the 5×10^2 cells/mL dilution were added to 44,4mL medium to generate a dilution of 10 cells/well. Then, 25mL of this dilution were added to 25mL of medium to produce a dilution of 5 cells/well and this sequential dilution was repeated (2.5 cells/well and 1.25 cells/well) until a final dilution of 0.625 cells/well was obtained. Of these different dilutions, only the 1.25 cells/well and 0.625 cells/well dilutions were retained for both pools. The 1.25 and 0.624 dilutions were loaded onto a separate 96 well plate each at a concentration of $180 \mu\text{L}/\text{well}$ for each pool respectively. The resulting plates were incubated in the 5% CO_2 incubator at 37°C for approximately 3 weeks. Each plate was regularly screened using a light microscope and the wells containing a single colony were marked and regularly checked. Of the various wells containing single clonal lines, 30 clones (wells) were randomly selected and allowed to grow to confluence. The 24 most confluent wells were passaged and transferred into a T_{75} flask each for further experimentation. They were also aliquoted into cryotubes for storage at -80°C .

2.2 The calcium mobilization assay

The Fluorometric Imaging Plate Reader (FLIPR) is a technology employed for intracellular calcium mobilisation assays. The basic premise behind these assays is that studied cells are loaded with a calcium-sensitive dye that emits fluorescent signals upon the binding of calcium mobilized from intracellular stores in response to activation of $G_{\alpha q}$ coupled GPCRs. This technique constitutes a standard approach for the pharmacological characterization and determination of relative potencies of ligands at receptors, thus allowing a quantification of agonist effects. The used dye is commercially available and supplied in an assay kit containing the relevant reagents and buffers. All the experiments

conducted in this project utilized the Fluo-4 NW Calcium Assay Kit (Starter Pack with Buffer, Invitrogen™/ Molecular Probes®, F36206). The Fluo-4 dye is supplied with pre-treatment of the acetoxymethyl esters, which provide high permeability through the cell membrane. Moreover, the dye absorbs strongly at a wavelength of 488nm upon excitation by an LED laser. Because of this strong absorption, Fluo-4 exhibits high fluorescence emission, and is able to detect calcium concentration at a K_d of 345nM. In the FLIPR assay, the Fluo-4 dyes were loaded, per the manufacturer's instructions, in an assay buffer containing 1) HEPES to maintain an optimal pH level of 7.3 and 2) probenecid to avoid anion exchange protein extrusion of the dyes.

2.2.1 Cell Plating

Cells were grown in a T₇₅ flask until they became 100% confluent, washed in DPBS and lifted in 10mL DPBS-EDTA as previously described. The cells were counted in order to measure the volume of suspension required for a 2×10^6 cells/mL dilution. The appropriate volume of cells was then added to the medium for a final volume of 15mL, and 100 μ L of the mixture was seeded onto each well of a 96 well poly-D-Lysine black plastic plate with clear bottom (final concentration approximately 10,000 cells per well). The plate was then incubated for 48 hours at 37°C in the cell-culture incubator, or until a confluent monolayer of cells was observed in each well.

2.2.2 Dye loading

77mg of probenecid powder were resuspended in 1050 μ L of assay buffer and the mixture was vortexed until a homogeneous solution was obtained. The dye vial was heated for 15 min in a 37°C incubator. After removal from the incubator, 10.5mL of assay buffer and 105 μ L of probenecid were dispensed into the dye vial, following which the lid was secured and the vial was tilted a few times to ensure the even mixing of the components. The content of the vial was then poured into a plastic reservoir. Meanwhile, the 96-well FLIPR cell plate was taken out of the incubator, and the medium was flicked off into the sink. Using an eight-channel pipette, 100 μ L of dye mixture was loaded into each well of the 96 wells of the plate. The plate was then wrapped in aluminum foil to protect the dye from the light and incubated in the 37°C incubator for 30 minutes, then for an additional 30 minutes at room temperature to allow the dye to load.

2.2.3 Creating ligand plates

In order to investigate the functional response of the assayed cells to agonists and antagonists of interest, serial dilutions were created for each drug. The concentrations were calculated in $-\log$ units and the correct volumes needed for the dilutions were determined. The serial dilutions were prepared as 10x concentrated stocks in DPBS. The agonist dilutions were loaded separately into clear V-bottom 96 well plates (Greiner Bio-one). Seeing as each well of the drug plate contains about 15-30 μ L of 'dead space' where the aspiration of the liquid becomes difficult, a sufficient volume of ligands (15-30 μ L) was thus added to each well of the drug plate to ensure proper removal of the agonist during the assay. Antagonist dilutions, on the other hand, were added, when required, to the incubating cells at a volume of 10 μ L within the first five minutes of the one hour incubation in order to allow a minimum of 25 minutes for the antagonist-receptor binding equilibrium to occur.

2.2.4 Running the FLIPR assay

The calcium measurement assays were conducted using the FLIPR® (Fluorometric Imaging Plate Reader) Tetra High Throughput Cellular Screening System (Molecular Devices). This technology comprises an integrated 96-, 384-, or 1536- well pipettor and can accommodate multiple reagent reservoirs. The FLIPR machine captures an image of each well of the plate simultaneously using a cooled charge-coupled device (CCD) at the speed of an image per second, a feature that is fundamental to the measurement of the rapid calcium response initiated by GPCRs. Hence, the FLIPR machine emits a beam at 488nm as mentioned above, and records the change in fluorescence signal emitted by the dye loaded onto the cells over a given time course, thus drawing a calcium profile of the studied agonists.

After an hour of incubation at 37°C, the lid of the cell and agonist plates were removed. The plates were placed in their respective reading positions in the FLIPR machine previously set at 37°C, and the tips were loaded. Before agonist addition into the cell plate, a test signal reading in arbitrary fluorescence units (RFU) was conducted in order to evaluate the dye-loading efficiency and variability across the cell plate. Furthermore, the CCD camera has a specific saturation level above which the camera cannot resolve changes in fluorescence. The maximum saturation of the CCD in the FLIPR Tetra reportedly occurs at 9000RFU, and the standard deviation error should be less than 10%, ideally. Hence, at the beginning of the assay, the camera exposure length

was lowered from 0.4 to 0.1. The shutter speed and the laser power were also adjusted based on the initial fluorescence levels prior to agonist activation to ensure optimal signal detections. Once the signal test was performed, and the camera gain and excitation intensity parameters were fixed, the reading run was initiated.

The internal robotic system of the FLIPR® Tetra machine was programmed to aspirate 21µL agonist/antagonist from the drug plate, to dispense 11µL of the aspirated volume into each well of the cell plate. The agonists were aspirated from each well at the same time, and simultaneously dispensed into the corresponding wells on the cell plate. The fluidics of FLIPR® Tetra do not employ the gas pressure system and the pipette tips were thus immersed into the medium during dispensing. Moreover, the machine utilizes an LED excitation system whereby fluorescent signals are emitted from the dye following excitation and passed through an emission filter (515-575nm for FLIPR® Tetra). These emission filters connect to the CCD camera located underneath the cell plate, allowing fluorescent signals to be collected every second.

Following initiation of the run, the agonists were added to the cell plate at t=10 seconds, allowing a visualization of the baseline fluorescence existing in the studied wells prior to agonist addition (t=0 to 9 seconds). Upon agonist introduction into the cell plate, the change in calcium fluorescence due to the mobilization of calcium from intracellular stores was recorded over 180 seconds by the CCD camera and the output was sent to a PC coupled to the FLIPR device. The recorded data saved and exported onto the Excel software for statistical analysis. They were then subjected to further analysis using GraphPad Prism.

2.3 Data analysis

The statistical and quantitative analysis of data was conducted using Microsoft Excel and GraphPad Prism®. Excel was used for primary calculations based on raw data from FLIPR Tetra® to generate a $\Delta F/F_0$ value for each well in the analysed plate. Figure 2.1 shows a time course trace obtained from the well of a FLIPR plate as visualised in an Excel sheet. F_0 constitutes the average baseline calcium fluorescence measured between $t = 0$ to $t = 9$ seconds prior to agonist addition and is expressed in relative fluorescence units (RFU). ΔF represents the average calcium fluorescence in relative fluorescence units (RFU) due to agonist addition to the well and is calculated using the following equation: $\Delta F = F_{\max} - F_{\min}$. F_{\min} is the minimum calcium fluorescence value detected

following agonist addition and usually occurs between $t = 10$ to $t = 13$ seconds. This decrease is thought to result from the mechanical action of the tip dispensing the agonist. F_{\max} represents the maximum calcium response to the agonist and usually occurs between $t = 20$ to $t = 30$ seconds. The F_{\max} and F_{\min} values were calculated using the appropriate Excel formulas within constrained intervals to ensure that the calculated F_{\min} strictly corresponds to the calcium decrease caused by agonist addition. The obtained ΔF value was divided by the average baseline fluorescence of the well, or F_0 , to generate an absolute unitless value of the increase in calcium fluorescence produced by the agonist:

$$F = (F_{\max} - F_{\min}) / F_0 = \Delta F / F_0.$$

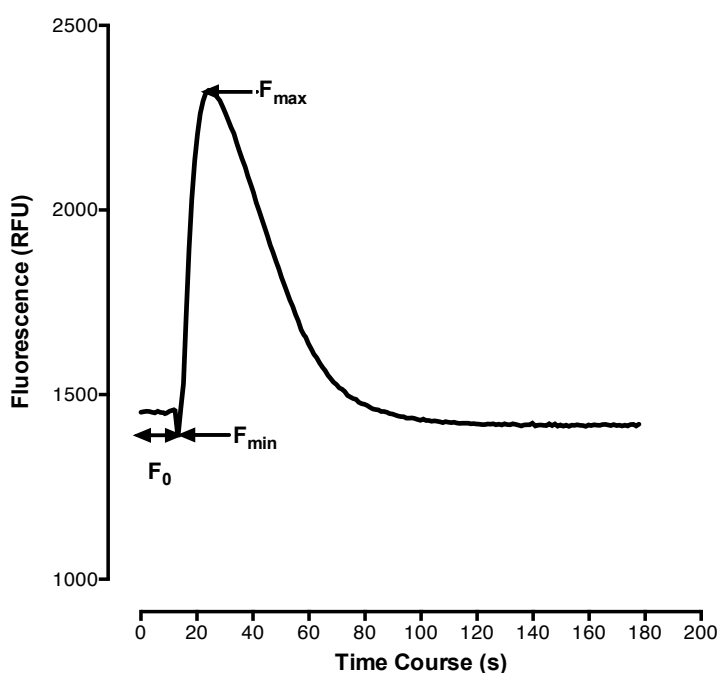


Figure 2.1 Estimation of the increase in calcium fluorescence using a kinetic FLIPR trace

The graph shows a kinetic signal trace for a given well of a FLIPR plate as displayed in an Excel sheet. The x-axis corresponds to the time course of the calcium response to a given agonist in seconds while the y-axis shows the change in fluorescence over time in relative fluorescence units (RFU). F_0 represents the baseline fluorescence detected prior to agonist addition from $t = 0$ to 9 seconds. F_{\min} is the minimum calcium fluorescence measured following agonist addition while F_{\max} is the peak calcium fluorescence elicited by the agonist. The increase in calcium fluorescence for a given well is calculated by normalizing ΔF against F_0 using the following formula: $(F_{\max} - F_{\min}) / F_0 = \Delta F / F_0$.

The Prism® software was employed for the analysis of data processed using Excel, including curve fitting through non-linear regression and statistical comparison of

calculated parameters using unpaired t-tests and one-way analysis of variance (ANOVA). Each represented data set consisted of three or more replicates ($n=3$) for each concentration level. The following section presents an in-depth analysis and comparison of the mathematical fits utilized to analyze the performed dose-response experiments.

The activity of purinoceptors in the studied cell lines (CHO-K1-hP2Y₁₁ clone 6 and 13, 1321N1-hP2Y₁ and 1321N1-hP2Y₁₁) was examined through FLIPR using 8 agonists that will be described in detail in the Results chapters. The obtained results were thoroughly analysed according to several mathematical fits. The aim of this comparison was to detect the mathematical fit that best describes the dynamics of a receptor's response to a drug and to pinpoint a rigorous strategy of computing the representative EC₅₀ values. The necessity of conducting this evaluation was dictated by the fact that the studied CHO-K1-hP2Y₁₁ system comprises several expressed receptors, each of which can be activated on its own or in combination with other receptors upon stimulation by agonists like ATP. This co-expression results in an altered pharmacological profile, whereby the response of a given receptor protomer to agonists can be significantly shifted to the left or the right in the presence of its interacting partner(s) as opposed to the receptor when expressed on its own in a null system. Not only is the response shifted to the left or right, but some curves do not achieve a clear maximum, making it difficult to interpolate an EC₅₀ in the absence of a known maximum. These observed tendencies prompted the search for 1) a method to determine the complexity of a response from looking at a curve and 2) tools to distinguish between the different components of the response. The evaluated methods were 1) the Hill plot method, 2) Prism three-parameter equation, 3) Prism four-parameter equation, 4) Prism five-parameter (asymmetric) equation, 5) Prism biphasic equation, and 6) Gaddum/Schild EC₅₀ shift.

2.3.1. The Hill equation

Two methods were employed to determine the EC₅₀ value of an agonist response. Historically, and prior to the development of the computational power required for non-linear regression analyses, EC₅₀ values were obtained from graphical plots. The first attempts to quantify agonist concentration and receptor response relationships emerged from the study of haemoglobin binding and cooperativity, which provided the first insights into receptor behaviour. In 1910, Archibald Vivian Hill, then Scholar of Trinity College, Cambridge, proposed a number of equations in an effort to describe the relationship between oxygen tension and the percent saturation of haemoglobin (Hb) with

oxygen (201, 202). His aim was to introduce a general mathematical formula capable of accounting for the differential measurements of Hb saturation by oxygen in solutions of various salts, as recorded by Joseph Barcroft. Hill hypothesized that the presence of different aggregates of Hb in solution could translate into the co-existence of various possible equilibrium states between oxygen and Hb, resulting in various oxygen-Hb dissociation curves. He concluded that his equation (III), now known as the Hill equation, is the best suited for predicting the dynamics of the studied system, since “the oxygen dissociation curves of haemoglobin under various conditions all obey the following equation:

$$y = Kx^n / (1 + Kx^n) \text{ (III)}$$

where y is the percentage of haemoglobin saturation with oxygen, and x the partial pressure of O_2 . K and n , which are two constants, constitute the parameters of this equation (201, 202).

Hill, however, was perfectly aware that his equation lacked a tangible physical basis: “My object was rather to see whether an equation of this type can satisfy all the observations, than to base any direct physical meaning on n and K ” (202, 203). Hill’s observation pinpoints the major shortcoming of the Hill method, i.e. that it postulates a typical behavior of the system independent of the actual parameters/context of the interaction. Despite this caveat, the Hill equation was adopted and extended to all major fields of bioscientific enquiry due to its inherent ‘curve-fitting descriptive’ powers. For instance, the discipline of pharmacokinetic-pharmacodynamic modelling, aimed at elucidating the relationship between drug dose and drug effect, is centered on a derivation of the original Hill equation:

$$E = E_{\max} C^x / EC_{50}^x + C^x$$

where E is the predicted effect of the drug, E_{\max} the maximum effect, C the drug concentration at time t and EC_{50} is the drug concentration for which half of the maximum effect is obtained. α is the Hill coefficient of sigmoidicity (204).

In a critical review of the Hill equation and its various implications, Goutelle et al. indicate that this “aspect of the Hill equation is descriptive, pseudo-deterministic.

However, the use of the Hill equation in this way is restricted to its mathematical properties” (205). Despite its failings, the Hill equation/model remains unavoidable as all currently employed curve fitting equations/models constitute derivations of this original equation. In a discussion I had with him about the Hill equation, Professor David Colquhoun concluded: “The Hill equation plots a curve through point predictions. If we look at it empirically, the Hill equation gives a reasonable fit. Thus, you have no option but to stick by it.”

2.4 A brief description of Prism equations and fits

2.4.1 Stimulation equations

With this background in mind, the different mathematical options and in-built parameter options that Prism offers were explored. The Prism software fits curves according to a certain set of mathematical assumptions, which for the most constitute derivations or modifications of the original Hill equation. However, its flexibility lies in that it is able to compare between different fits in order to determine the fit that best describes a given dose-response curve. Several curve fitting models are available, including the three-parameter dose-response model, the four-parameter (variable slope) model, the 5 parameter or asymmetric model, which can be utilized to quantify what Prism qualifies as ‘asymmetric’, or complex curves as well as the biphasic curve, which accounts for responses with two distinct phases.

The three parameter dose-response model is most suited for fits that do not involve many data points (Figure 2.1). It generates dose-response curves that possess a standard slope, equivalent to a Hill slope of 1.0. The four-parameter dose-response curve, on the other hand, is intended for larger data sets. It does not presuppose a Hill slope of 1.0 but rather interpolates the slope from the data, hence its appellation (variable). This “logistic equation” generates a curve by fitting the top and bottom plateaus, the EC_{50} and the Hill slope factor, thus yielding a curve that is ‘symmetrical’ around its midpoint. This equation, however, fails to account for curves that are not symmetrical, a shortcoming that was overcome by adding a fifth parameter, S or unitless symmetry parameter, to create a five-parameter logistic equation. An asymmetric curve is generated when S is distinct from 1.0. In contrast to the straight-forwardness of software computation which

calculates the Hill slope and EC₅₀ of a given agonist response, the Hill plot method involves a two-step operation, consisting of transformation followed by linear regression.

Software equation: $Y = \text{Bottom} + (\text{Top} - \text{Bottom}) / (1 + 10^{-(\text{LogEC}_{50} - X)})$

where top and bottom correspond to the plateaus in the units of the Y axis.

Given that the four-parameter or variable slope equation was the preferred fit for most of the analysed data sets, this equation was adopted as the most suitable model for curve fitting and calculation of EC₅₀ values of obtained experimental results. In the case of data that could not be fit using non-linear regression analysis, connecting lines were drawn across the data points and the EC₅₀ values were generated using the Hill equation. These various mathematical approaches are valid for the analysis of single-site concentration response curves.

To perform the Hill transformation of monophasic curves, the Y_{max} value or highest agonist concentration, which yields the greatest calcium response, is entered for software calculations. If the highest concentration of ligand tested does not produce the maximum response, a value from a lower concentration corresponding to the greatest response is input instead. A linear regression line is plotted through the data points and the resulting intercept with the X-axis constitutes the logEC₅₀ of the ligand. However, in cases where the data progressed from its minimum to its maximum over four log units of agonist concentration and the above-mentioned equations failed to fit a curve through the analysed data-points, the data were fit using the biphasic curve (Figure 2.2). The biphasic-response curve consists of two single monophasic curves, each of which has its own Y_{max} value. The software calculates the LogEC₅₀ value of both the high- and low-affinity sites, as well as the fraction or proportion of the maximum response due to the more potent phase. The nH₁ and nH₂ values, or Hillslopes of the two portions of the response were restricted to 1 for agonist stimulation responses as recommended by the Prism[®] software help.

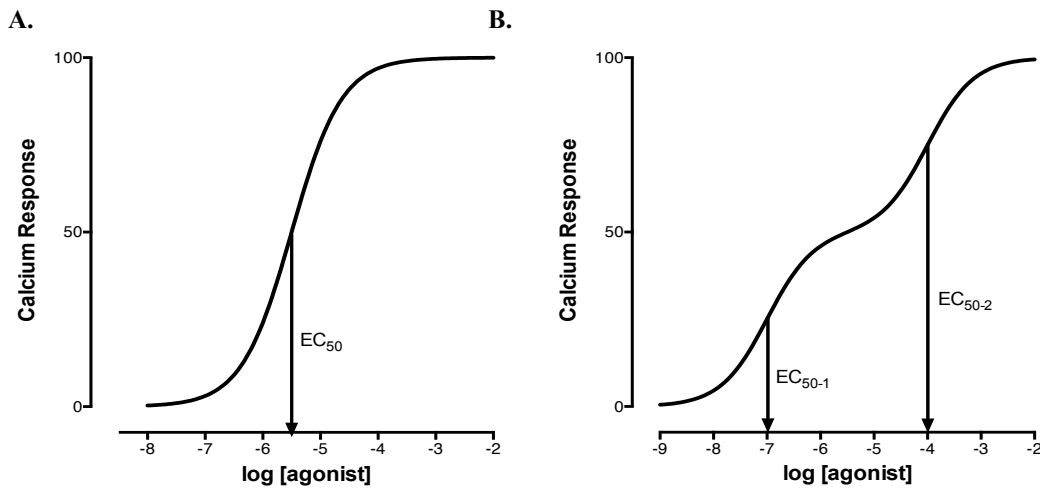


Figure 2.2 Examples of dose-response curve fits

A. Sigmoidal curve. A sigmoidal monophasic response is symmetrical and is normalized to run between 0% and 100%. It has a single EC₅₀ value, which denotes the concentration of agonist that yields a response halfway between the bottom and the top. The Prism software estimates the Hill slope or steepness of the curve. B. Biphasic curve. The biphasic curve is a derivation of the monophasic curve and consists of two distinct phases or components of the response, a high-affinity site and a low-affinity site. Each phase has its own EC₅₀ value, shown on the graph as EC₅₀₋₁ and EC₅₀₋₂.

2.4.2 Inhibition equations

In 1947, Heinz Schild, from the Pharmacology Department of University College London proposed a method for determining the affinity of an antagonist for its receptor. As David Colquhoun points out, the greatest achievement of Schild was to show that a physical constant such as the equilibrium constant for binding of an antagonist to a receptor could be determined even when agonist action is unknown (206). According to the Schild equation,

$$r = 1 + c_B$$

where r is the dose ratio and c_B is the concentration of the antagonist B, which constitutes a multiple of its equilibrium constant for binding to its site (206). c_B is thus defined as:

$$c_B = [B]/K_B$$

The advantage of this equation is that it relies solely on antagonist concentration, signifying that the concentration, affinity or efficacy of the agonist as well as the relationship between agonist occupancy and response are irrelevant to these calculations. Thus, the dose ratio, or extent of the rightward shift of the agonist dose-response curve due to the antagonist, is independent of the nature and magnitude of the agonist response (206) (Figure 2.3).

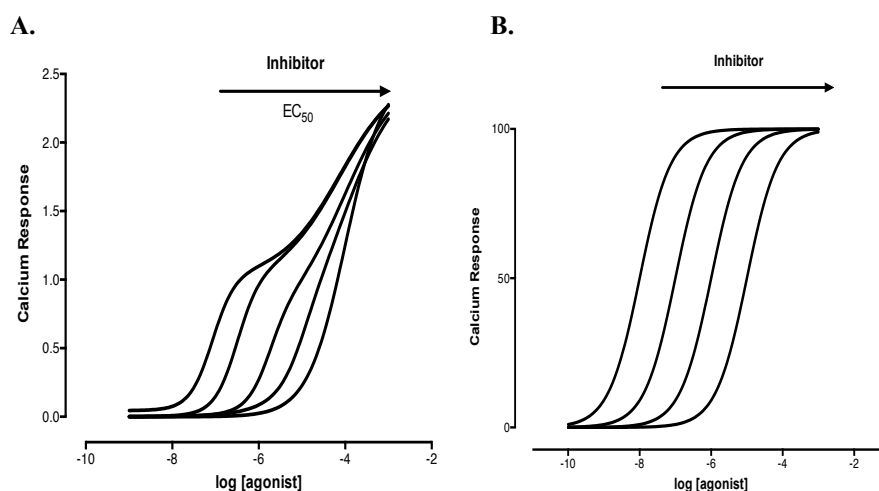


Figure 2.3 Models of competitive antagonism

A. Schild experiment. A Schild experiment consists in adding different concentrations of antagonist to increasing concentrations of agonist. In the theoretical example shown above, the inhibitor is competitive. It provokes a rightward shift of the agonist response and a reduction in agonist potency, thus converting the biphasic agonist response to a monophasic response with a significantly lower EC₅₀ value. B. Gaddum/EC₅₀ shift. The curves from **A.** were fit using the Gaddum/EC₅₀ shift equation, which provides a measure of the antagonist action exerted by the inhibitor. The antagonist caused a parallel rightward shift of the agonist response, indicating that the inhibitor is competitive.

The Schild experiments conducted in the CHO-K1-hP2Y₁₁ clones were analysed using the Prism[®] software in two steps. First, the various dose-response curves, corresponding to agonist response in the presence of different concentrations of a given antagonist, were analysed to draw the Schild graph. Using global non-linear regression, which can define a family of curves as opposed to a single curve, each of the calcium curves was fit individually using a comparison of two equations, namely the four-parameters equation versus the biphasic equation, to ensure that the best fit was achieved. Next, the data were analysed using the Gaddum/EC₅₀ shift equation to determine the K_B and pA₂ values of the tested antagonist. The equation generates a number of values

shared by the various dose-response curves of the Schild experiment, including 1) the EC_{50} and $\log EC_{50}$ value of the agonist response in the absence of inhibitor, 2) the pA_2 value which corresponds to the negative logarithm of the antagonist concentration needed to shift the dose-response curve by a factor of 2, 3) the K_B value or the equilibrium dissociation constant (Molar) of the inhibitor binding to the receptor, 4) the Hill slope or steepness of the family of studied curves, and 5) the Schild slope which measures how well the observed rightward shift agrees with the prediction of competitive antagonism. In fact, if the inhibitor is competitive, the Schild slope should equal 1.0. To further confirm the prediction of competitive antagonism generated by the Gaddum equation, a Schild plot was also drawn for each Schild experiment. To obtain the concentration ratio values, the data was fit using the sigmoidal-dose response curve (variable slope) and the log of the dose ratios or $\log(DR-1)$ appeared in the summary table attached to the main table of results. Unfortunately, in some instances the software failed to calculate the dose ratios for all the antagonist concentrations used. This prompted me to calculate the $\log(DR-1)$ values manually, using the equation $DR = 1 + c_B = 1 + ([B]/K_b)$. The $\log(DR-1)$ values were then plotted in a separate data file and fit using linear regression analysis. If the antagonist is competitive, the slope of the obtained line should be 1.0. The Schild plot results obtained from both software and manual calculations were closely compared to ensure that the results were compatible and accurate.

Finally, the inhibition curves gathered from inhibition experiments in 1321N1-hP2Y₁, 1321N1-hP2Y₁₁ and the CHO-K1-hP2Y₁₁ clones were analysed using a comparison of two equations, the $\log(\text{inhibitor})$ versus normalized response- variable slope (three parameters) versus the $\log(\text{inhibitor})$ versus normalized response- variable slope (four parameters), to determine the best fit for the curves. The used equations calculate the IC_{50} value of the studied antagonist, corresponding to the concentration of inhibitor required to reduce agonist response half way between the top and bottom plateaus of the curve.

2.5 Statistical Analysis using Prism®

The results described in this thesis were obtained from a minimum of three trials or repeats ($n \geq 3$) each performed in triplicate or quadruplicate for a given experiment. The biological repeats (n) were performed using the same cell line, plated at a similar concentration of detached cells and grown to a comparable confluence level for all repeats to minimise variations across plates. The same agonist and antagonist dilutions

were performed for all trials, following which the plates were incubated with the Fluo-4 dye and run using an identical FLIPR protocol. The obtained results were expressed as the mean \pm s.e.m of all performed repeats for a given experiment. Analyses of statistical significance were performed using GraphPad Prism®. The two-tailed t-test (95% confidence interval), which conducts a comparison between two unmatched groups, and one-way ANOVA analysis, which performs a comparison between three or more unmatched groups, were chosen to assess the difference in mean values.

2.6 Molecular Biology Techniques

2.6.1 RNA extraction from animal cells

CHO-K1-hP2Y₁₁ clones 6 and 13 cells were grown in a T₁₇₅ flask until they reached a 100% confluence following which they were washed in DPBS and detached using DPBS-EDTA. The cell suspension was transferred to a clean 50mL Falcon tube and centrifuged for 5 minutes at 1000 rpm. The supernatant was discarded and the harvested cell pellet was frozen in the -20°C freezer. For RNA extraction purposes, the cell pellet was thawed on ice, resuspended in 7.5 mL of denaturation solution and left on ice for 15 min. The cell suspension was sheared using a 19-21G syringe needle until the pellet was dissolved. It was loaded onto a 2.5 mL caesium chloride cushion (5.7M Caesium chloride (Sigma), 0.1 M EDTA (Gibco) pH 7.5, Sodium Acetate pH 5.5) in Polyallomer Quick-Seal™ Centrifuge tubes (Beckman). The ultracentrifugation tubes containing the different cell suspensions were precisely balanced against each other, with mineral oil where necessary, to exclude air bubbles from the tubes, after which they were heat-sealed using the Beckman tube-sealer (Beckman, Palo Alto, California). The tubes were centrifuged overnight for more than 14 hours at 31.000 rpm in a SW41 rotor at 20°C in a Beckman Coulter OPTIMA L-100 XP centrifuge. Upon completion of the run, the tubes were removed from the ultra centrifuge. To extract the RNA, the supernatant including the DNA band was collected using a syringe to about 1 cm of the bottom of each tube. The remaining liquid was decanted and the tubes were inverted to drain. The bottom 1 cm of the tubes was cut and 20µL of 100% ethanol was added to the RNA cell pellet to permit its visualization. The bottom of the tubes was then inverted to drain, after which the content of the tubes was washed using 150µL TES buffer (10 mM Tris-Cl (Sigma) pH 7.4, 5 mM EDTA, 1% SDS made from 10% SDS (Gibco)) then transferred to clean Eppendorf tubes. Two additional washes with 150µL TES buffer were performed and the

consecutively obtained volumes were transferred to the same Eppendorf tube. 450µL of chloroform: isoamyl alcohol mixture solution (24:1, Sigma) was added to the Eppendorf tubes containing the washed RNA, mixed and centrifuge for 5 min at 13.5 rpm in a mini-centrifuge (Eppendorf). The upper aqueous phase containing the extracted RNA was removed and transferred to a new Eppendorf tube. 350µL of the Tris-EDTA-SDS buffer was then added to the remaining phase and the content of the tube was mixed and centrifuged for 5 minutes at 13.5 rpm. The upper phase was aspirated and added to the product yielded by the first extraction. The final volume of 800µL was subsequently divided into two, whereby 400µL of solution were added to a 1.5 mL Eppendorf tube each. To precipitate the RNA, 40µL of sodium acetate (3M) and 1mL of ethanol were added to the tubes. The obtained volume was mixed and left at 20°C overnight to allow the RNA to precipitate. The RNA was then recovered by centrifugation for an hour at 12,000rpm and 4°C. The obtained supernatant was decanted and the RNA pellet was washed using 500µL of 70% ethanol. Each tube was centrifuged for five minutes at 13,000rpm for 5 minutes, following which the liquid was aspirated. A second wash was performed using 500µL of 100% ethanol followed by centrifugation at 13,000rpm for 2 minutes. The liquid was then decanted and the tube was covered with a tissue paper and kept open for 30 min to dry. The RNA was resuspended in 100µL of RNase free distilled water.

2.6.2 Quantification of nucleic acids

The extracted RNA was quantified using Nanodrop measurements, which can determine the absorbance of a given sample at different wavelengths. The RNA concentration was measured in ng/µL and the OD_{260/280} ratio of the analysed sample was determined. This ratio indicates the purity of RNA, whereby a ratio of approximately 2 is accepted as pure for RNA. .

2.6.3 DNase treatment of RNA

The extracted RNA was treated using RQ1 RNase-free DNase, a DNase I (endonuclease) which degrades both double and single-stranded DNA endonucleotidically, producing 3'-OH oligonucleotides. It was used to make sure that any contaminating DNA was removed from the RNA sample prior to RT-PCR, thus warranting the integrity of the RNA. The DNase digestion reaction was set up as follows:

x μ L of RNA (10-20 μ g)

1 μ L of RQ1 RNase-Free DNase 10X Reaction Buffer

or 1 μ L of 5 x transcription buffer from the Superscript III enzyme (Invitrogen™)

RQ1 RNase-Free DNase (1u/ μ g RNA)

Nuclease-free water to a final volume of 10 μ L

The mixture was incubated at 37°C for 30 minutes. It was then loaded with sterile distilled water up to a final volume of 200 μ L and extracted using phenol: chloroform. For this purpose, 400 μ l of Phenol-chloroform:isoamyl alcohol mixture (25: 24: 1, Sigma) was added to the mixture and the tube(s) was centrifuged for 5 minutes at maximum speed. The upper aqueous phase was removed and transferred to a new 1.5 ml Eppendorf tube and the previous step was repeated a second time. To precipitate the RNA, 0.1V of 3M sodium acetate (NaOAc) and 2.5V of 100% ethanol were added to the decanted phase and the tube was placed at -20°C overnight. It was then centrifuged at maximum speed for 30 minutes. The supernatant was decanted and 1 ml of 100% Ethanol was added to the pellet, and the tube(s) was left at room temperature for 2 minutes. The tube(s) was then centrifuged for 15 minutes at maximum speed following which the supernatant was discarded. The pellet was additionally washed with 1ml of 70% Ethanol and the tube(s) was spun in the centrifuge for 5 minutes at maximum speed. The ethanol containing the supernatant was discarded and the pellet(s) was dried at room temperature for 5 minutes.

2.6.4 Single-stranded cDNA synthesis

The purified RNA was converted to single-strand cDNA using SuperScript® II Reverse Transcriptase (Invitrogen™), a DNA polymerase that synthesises a complementary DNA strand from single stranded RNA, DNA or RNA: DNA hybrid. The enzyme is genetically engineered through point mutations in its RNase H active centre to reduce RNase activity, thus eliminating RNA degradation during single-strand cDNA synthesis, and increase thermal stability. The kit contains 1) SuperScript® II RT, 2) 5X First-Strand Buffer (250 mM Tris-HCl, pH 8.3 at room temperature; 375 mM KCl; 15 mM MgCl₂), and 3) 0.1 M DTT. Each of the reagents employed for the synthesis reaction was mixed and centrifuged before use.

For a single-strand cDNA synthesis reaction, a 20 μ L reaction volume was used for 500ng of RNA. The following components were added to a nucleus-free microcentrifuge tube:

1 μ L of Oligo(dT)12-18 (500 μ g/ mL)
x μ L of RNA (500ng)
1 μ L of dNTP Mix (10mM)
sterile distilled water to a final volume of 12 μ L

The mixture was heated to 65°C for 5 minutes and quickly chilled on ice. The contents of the tube were collected by brief centrifugation then the following reagents were added to the tube:

4 μ L of 5X First-Strand Buffer
2 μ L of 0.1 M DTT
1 μ L of RNaseOUT™ (40 units/ μ L)

The contents of the tube were gently mixed then incubated at 42°C for 2 minutes. 1 μ L of SuperScript® II RT (200 units) was added to the tube and mixed by pipetting gently up and down. The mixture was incubated at 42°C for 50 minutes following which the reaction was inactivated by heating at 70°C for 15 minutes.

2.6.5 PCR primers design

Forward and reverse primer sequences were designed for 1) hamster P2Y₁, 2) hamster P2Y₂, 3) human P2Y₁₁, 4) the housekeeping hamster GAPDH and β -actin using MacVector 12.7.4. The primers were generated according to three constrained parameters, including size: 20-25 nucleotides, melting temperature or T_m (°C): 60-75 and percentage G+C content: 45-65. The final primers were selected from a list of primers and are described below. Oligonucleotides were synthesized by Eurofins MWG Operon.

1- Human P2Y₁₁ cds AF030335:

[F3] 53-74 5'- ACAAACTCAGTGGGTTCCAGGG -3'

22 nt forward primer

pct G+C: 54.5 T_m: 56.6

[B2] 361-339 5'- TGATGCAGGTGATGAAGATGACG -3'

23 nt backward primer

pct G+C: 47.8 T_m: 57.3

2- Hamster P2Y₁ cds AY049063:

[F1] 54-77 5'- TTCCATGTAAACCTCTATGGCAGC -3'

24 nt forward primer

pct G+C: 45.8 Tm: 56.3

[B2] 303-280 5'- AACTTCGTAGGTACTCATCGGTGG -3'

24 nt backward primer

pct G+C: 50.0 Tm: 55.4

3- Hamster P2Y₂ cds AF314034:

[F1] 114-137 5'- ACCTGTGCTCTACTTCGTCACCAC -3'

24 nt forward primer

[B2] 392-371 5'- AGGAAGCAGAGGGTAAAAACGG -3'

22 nt backward primer

pct G+C: 50.0 Tm: 55.6

4- Hamster GAPDH NM-001244854:

[F3] 228-250 5'- CAAGTTCAAAGGCACAGTCAAGG -3'

23 nt forward primer

pct G+C: 47.8 Tm: 55.5

[B2] 537-516 5'- TAAGCAGTTGGTGGTGCAGGAC -3'

22 nt backward primer

pct G+C: 54.5 Tm: 56.5

5- Hamster β ACT NM-001244575:

[F1] 172-195 5'- GCCCAGAGCAAGAGAGGTATTCTG -3'

24 nt forward primer

pct G+C: 54.2 Tm: 57.4

[B1] 421-400 5'- ACAGCACAGCCTGAATGGCTAC -3'

22 nt backward primer

pct G+C: 54.5 Tm: 55.8

2.6.6 Polymerase Chain Reaction (PCR)

PCR reactions were carried out to amplify the above-mentioned genes in order to verify whether they are expressed in CHO-K1-hP2Y₁₁ clones 13 and 6. 25µL reactions were prepared in flat cap PCR tubes and contained:

- 12.5µL 2xACCUZYME™ Mix or 2xBioMix™ or 2xBioMixRed™ (Bioline)
- 1.5µL forward primers
- 1.5µL reverse primers
- 2µL cDNA
- 7.5µL distilled water

The PCR reactions were conducted in the PCR Express Thermal Cycler (Thermo Hybaid) and performed in three stages. The first stage consisted of a 5 minutes denaturation at 95°C for a single cycle. This was followed by a second stage comprising 1) 30 seconds of denaturation at 95°C for 30 cycles, 2) 30 seconds of primer annealing at the annealing temperature corresponding to each gene for 30 cycles and 3) 1 minute of extension at 72°C for a single cycle. The final stage consisted of a 5 minutes extension at 72°C for one cycle. The finished reaction was held at 4°C. In order to check the presence of the amplified PCR products, agarose gel electrophoresis was performed.

2.6.7 Gel electrophoresis

To view the PCR products, a 2% agarose gel in 1x TAE buffer was prepared and the gel was pre-stained with ethidium bromide (10 mg/ml). cDNA samples were prepared by adding 0.5µL of 5x Loading Buffer (Bioline) to 2.5µL of PCR reaction. The gel was run in 1x TAE buffer for 30 minutes at 100V. The Invitrogen 1 Kb Plus DNA ladder was used as standard marker. DNA bands were visualized under a UV- Transilluminator (Syngene).

Chapter 3

Creation and Characterization of Recombinant CHO-K1-hP2Y₁₁ Clones 6 and 13

3.1 Introduction

P2Y₁ and P2Y₁₁ receptors contribute to the relaxation of gut smooth muscle and a study of their interaction would shed light on the mechanisms of this relaxation. Characterization of the coordinated signalling of two independent P2Y receptors would be more readily done in a cell line rather than in a complex tissue, using the detection tools applicable to GPCRs. As previously explained, GPCRs transmit their signals through the activation of a number of G protein targets, which in turn lead to the mobilization, or production, of secondary intracellular messengers, such as calcium and cAMP, respectively.

A number of different functional assays for GPCRs have been developed in order to permit the screening of GPCR agonist and antagonist activity, thus aiding in the identification of candidate drugs for this group of pharmacologically relevant proteins. These screens include assays of fluorescence and/or chemiluminescence detection, which measure calcium, cAMP or IP accumulation. Of these various tools, only calcium assays constitute a High-Throughput Screening (HTS) technique. The Fluorometric Imaging Plate Reader (FLIPR), an HTS calcium device, is available at UCL and will thus be selected as a suitable platform for the characterization of both P2Y₁ and P2Y₁₁ activity within recombinant cell lines. In order to distinguish between the activity of each of these two receptors, a selective agonist will be selected for each receptor subtype depending on its particular pharmacological profile when activated by a series of nucleotide analogues. BzATP will be used to characterize P2Y₁₁ while the nucleotide ADP will be employed for P2Y₁.

This chapter will describe the establishment of a co-expression model of P2Y₁ and P2Y₁₁ using CHO-K1, which expresses P2Y₁ endogenously, as the parental cell line into which hP2Y₁₁ will be transfected. This chapter will also describe the use of BzATP to correlate functional responses with P2Y₁₁ receptor expression levels in individual P2Y₁₁-expressing CHO-K1 clones. The relative expression levels of P2Y₁ and P2Y₁₁ in gut

smooth muscle are, at present, unknown. Following an initial estimation of recombinant P2Y₁₁ receptor densities, a further characterization of the clones expressing the highest and the lowest level of hP2Y₁₁ receptor protein, respectively, will be performed in order to establish pharmacological profiles that can be used to select the recombinant model that most closely fits the *ex vivo* model of the guinea pig taenia coli.

Previous research has identified the formation of a P2Y₁:P2Y₁₁ heteromer (55), providing an opportunity to examine the pharmacological properties of P2Y₁ in the presence of two different densities of hP2Y₁₁. Since the oligomerisation of GPCRs may alter the pharmacological profile of the individual receptor components, resulting in a novel entity with modified agonist and antagonist affinities, the work undertaken in this chapter will investigate the calcium responses in the high expressing versus low expressing CHO-K1-hP2Y₁₁ clones using a set of 8 purinergic agonists. The resulting data will be compared using appropriate statistical tools to evaluate calcium responses. Differences in the agonist profiles of P2Y₁ and hP2Y₁₁ between the clones could reflect the creation of novel sites of agonist activity or oligomerisation of the two purinoceptors that could be attributed to the difference in hP2Y₁₁ receptor density.

3.2 Selection of Clonal Cell Lines Expressing hP2Y₁₁

3.2.1 Creation and characterization of stably transfected CHO-K1 cells expressing the human P2Y₁₁ receptor

A recombinant CHO-K1 cell line expressing the human P2Y₁₁ receptor was created using an hP2Y₁₁ construct comprising the cDNA sequence of the receptor (GenBank accession number AF030335), cloned between the HindIII and XbaI sites of the pcDNA3 vector (shown in Figure 3.1). This construct was employed to stably transfect CHO-K1 cells (shown in Figure 3.2). The CHO-K1 cell line expresses endogenous P2Y₁ (207), P2Y₂ (208) and P2X₇ (209). Two different pools of CHO-K1-hP2Y₁₁ were created by transfecting two distinct aliquots of cells, each plated at the same density, with different amounts of hP2Y₁₁ cDNA. The stably transfected pools expressing hP2Y₁₁ were subsequently selected using the antibiotic Geneticin.

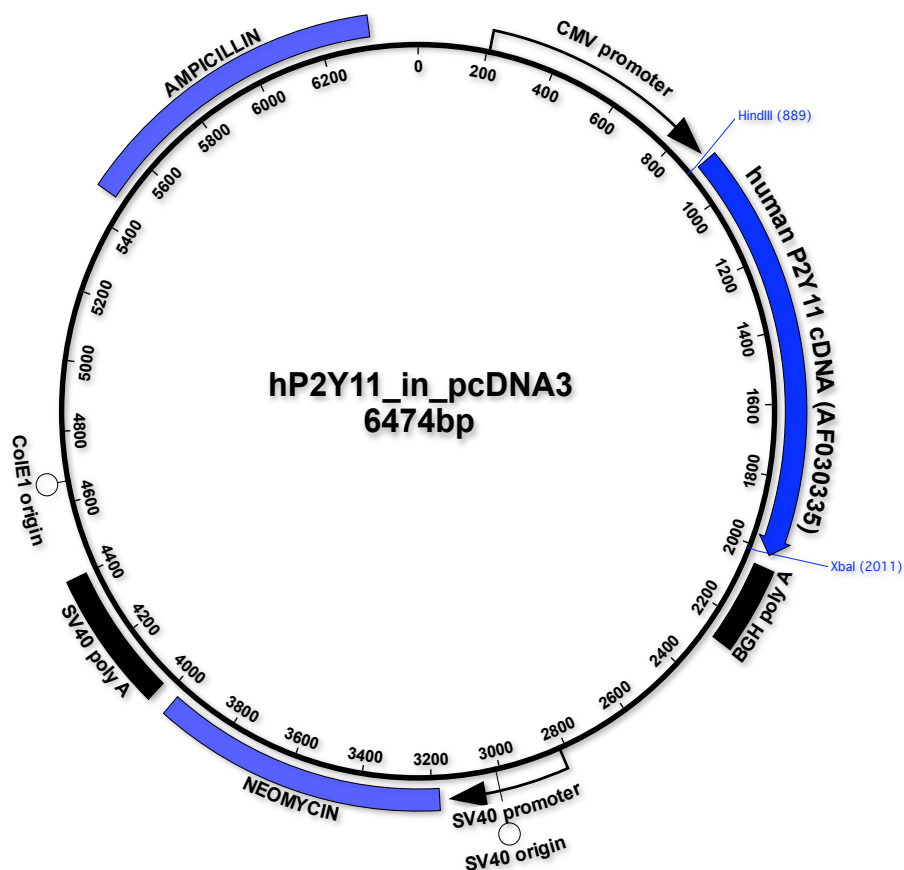


Figure 3.1 The hP2Y₁₁ in pcDNA3 construct

The cDNA sequence (GenBank accession number AF030335) of the human hP2Y₁₁ receptor, which is 1113 bp long, was cloned between the HindIII and XbaI sites of the human expression vector, pcDNA3 (6474bp), which ensures high-expression stable transfection in mammalian cells. This vector possesses a CMV promoter as well as ampicillin and neomycin-resistance markers. The formed construct was used to transfect CHO-K1 cells in order to create a CHO-K1 cell line stably expressing the human P2Y₁₁ receptor.

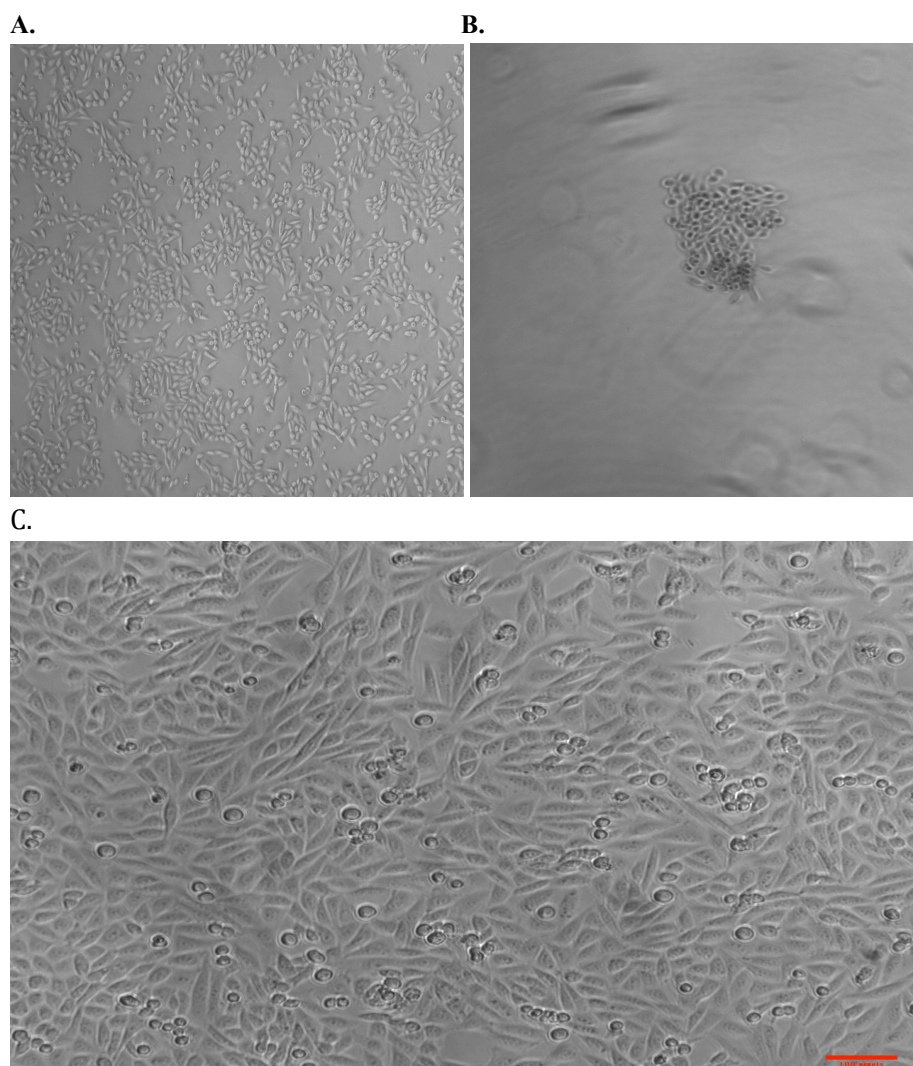


Figure 3.2 Microscopic visualization of CHO-K1 and CHO-K1-hP2Y₁₁ cells

A. CHO-K1 cells pre-transfection. 5x magnification of CHO-K1 cells prior to their transfection with the human P2Y₁₁ receptor cDNA. *B. CHO-K1-hP2Y₁₁ colony.* 5x magnification of a colony of CHO-K1 cells after their transfection with human P2Y₁₁ cDNA. The formed CHO-K1-hP2Y₁₁ colonies were screened using 100 μ M BzATP to determine different levels of hP2Y₁₁ coupling. *C. CHO-K1-hP2Y₁₁ clone 13.* 10x magnification of CHO-K1-hP2Y₁₁ clone 13, which was identified as the clone expressing the highest coupling of hP2Y₁₁.

A Ca²⁺ signalling assay using FLIPR was employed in order to determine whether the transfected hP2Y₁₁ receptor protein was expressed in each of the two pools: pool 1.0 and pool 0.5. Figure 3.3 shows the functional responses of pools 0.5 and 1.0 to 100 μ M UTP and increasing concentrations of BzATP at 37°C, the physiological temperature of mammalian cells. The curves shown in this figure represent the mean of four independent experiments, each performed in triplicate, and were fitted using non-linear regression with a comparison of two different equations (the three parameter versus the variable slope or four parameter equation) to determine the best fit for each curve. Graph A. displays the concentrations-response curves obtained following mathematical analysis of

the calcium response to each agonist concentration using the F/F₀ method, while graph B. presents the curves generated for peaks measured using area under the curve method (AUC). This double analysis was performed to determine whether the data integrated using these two methods would look similar. Table 3.1 lists the calcium response in F/F₀ versus AUC for each BzATP dose used.

As the figure shows, BzATP elicited a concentration-dependent response in pools 1.0 and 0.5 for both methods, signifying that the transfection was successful. The pools gave sigmoidal dose-response curves that achieved their maximum over two log units of agonist concentration, ranging from 10nM to 1 μ M BzATP (log value: -6 to -8). The EC₅₀ and pEC₅₀ values for pools 0.5 and 1.0 using the F/F₀ versus AUC method are shown in Table 3.2. Using unpaired t-tests, there was no statistically significant difference between the EC₅₀ values calculated from the F/F₀ versus AUC measurement for pool 0.5 (p value = 0.9455) and pool 1.0 (p value = 0.6605). Furthermore, BzATP displayed the same potency in pool 0.5 versus 1.0 using both measurements (p value = 0.4224 and 0.4863, respectively). Moreover, ANOVA analysis revealed no statistically significant difference between the pEC₅₀ values of pools 1.0 and 0.5 using the F/F₀ versus AUC measurement (p value = 0.6581). These statistical tests imply that the BzATP response in the pools is consistent across the two peak analysis methods and both can be safely utilized to fit the calcium data. For the purposes of this project, the F/F₀ method was adopted for peak analysis of all the presented data.

Agonist Concentration	Calcium Response			
	Pool 0.5 F/F ₀	Pool 0.5 AUC	Pool 1.0 F/F ₀	Pool 1.0 AUC
-4	1.83	3413	1.96	4021
-4.5	1.76	3332	1.98	3955
-5	1.73	3225	1.92	3826
-5.5	1.44	2971	1.52	3331
-6	1.02	2131	0.75	2261
-7	0.12	1302	0.08	1355
-8	0.08	1315	0.07	1293

Table 3.1 The calcium response to BzATP in pools 0.5 and 1.0 using F/F₀ versus AUC analysis

The calcium peaks elicited by increasing concentrations of BzATP, ranging from -8 to -4, in pools 0.5 and 1.0 were measured using the F/F₀ versus area under the curve (AUC) methods. The values represent the mean of four different experiments, each performed in triplicate.

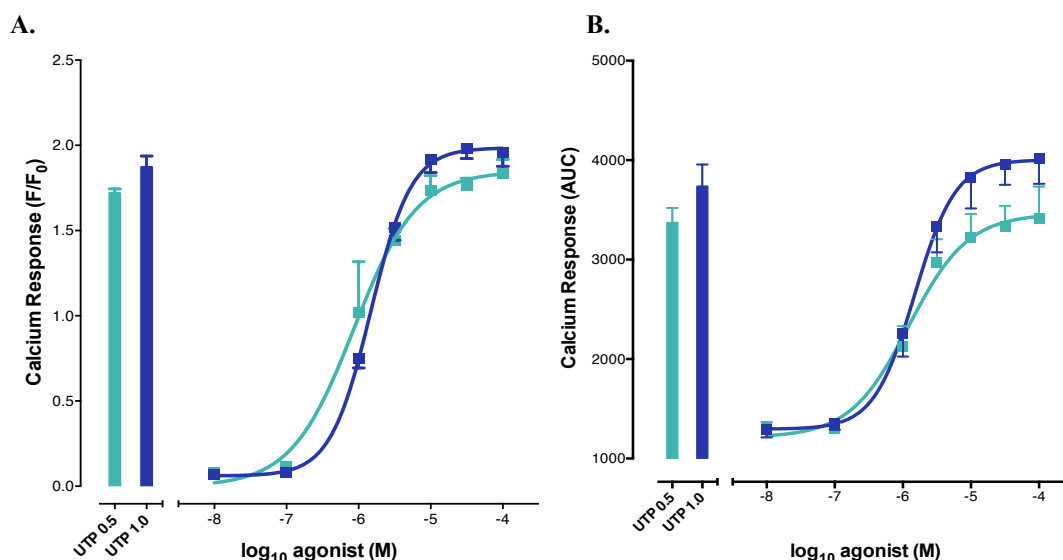


Figure 3.3 BzATP elicits a calcium response at 37°C in CHO-K1 cells stably expressing the human P2Y₁₁ receptor

The calcium response to increasing concentrations of BzATP was determined at 37°C for two stably transfected pools of CHO-K1 expressing the human P2Y₁₁ receptor. The results are expressed as the average \pm s.e.m of four independent experiments, each performed in triplicate. The response to 100 μ M UTP is shown for pool 0.5 (■) and pool 1.0 (■). *A.* The calcium peaks were calculated using the F/F₀ method. *B.* The calcium peaks were calculated using area under the curve (AUC) analysis.

	EC ₅₀ (μ M)		pEC ₅₀	
	F/F ₀	AUC	F/F ₀	AUC
Pool 0.5	1.29 \pm 0.17	1.27 \pm 0.20	5.90 \pm 0.06	5.92 \pm 0.07
Pool 1.0	1.42 \pm 0.05	1.52 \pm 0.22	5.85 \pm 0.01	5.83 \pm 0.06

Table 3.2 The calcium response elicited by BzATP in pools 0.5 and 1.0

The EC₅₀ and pEC₅₀ values of BzATP were determined in pools 0.5 and 1.0 for the F/F₀ and AUC data. The results are expressed as the mean EC₅₀ and the mean pEC₅₀ of four independent experiments, each performed in triplicate.

3.2.2 Identification of CHO-K1-hP2Y₁₁ clonal cell lines expressing different densities of hP2Y₁₁

CHO-K1-hP2Y₁₁ clones of differing receptor densities were generated through dilution sub-cloning of pools 0.5 and 1.0. The 24 most rapidly growing clones were then selected and screened using 100 μ M BzATP at 37°C. Figure 3.4 shows the average calcium response obtained for each of the 24 clones. As the figure shows, the tested CHO-K1-hP2Y₁₁ clones yielded varying calcium responses upon application of a fixed concentration of BzATP. One-way ANOVA analysis was performed to evaluate the

statistical significance of the observed differences in response. The p values obtained from this analysis made it possible to distribute the 24 screened clones into 5 groups with a single level of calcium response each (shown in Figure 3.5).

As the figure shows, CHO-K1-hP2Y₁₁ clone 13 gave the highest calcium response to 100μM BzATP and was therefore picked as the clone of reference to which the calcium responses of the remaining clones were compared. The responses of clones 7 through 12 showed no statistically significant difference to clone 13 and thus formed a group of clones with a comparable calcium response profile. Clones 2 and 19, clones 1 and 24, and clones 6, 17 and 18 were statistically significantly different to clone 13 ($p < 0.05$; $p < 0.01$ and $p < 0.001$, respectively). Due to the lack of quantitative techniques allowing the precise determination of receptor density in cellular membranes, and for the purposes of this work, the level of calcium response of the screened clones to 100μM BzATP was considered as an indicator of receptor density, whereby a high level of calcium response would correlate with a high density of receptor expression, and a low level of response with a low density of receptors in the cellular membrane. Accordingly, clone 13 was identified as the highest expressing clone, or the clone expressing the highest density of the hP2Y₁₁ receptor protein, while clone 6 was identified as the lowest expressing clone or the clone expressing the lowest density of the hP2Y₁₁ receptor protein. These two clones were selected for further study in order to establish the specific pharmacological profile of P2Y₁₁ when co-expressed with P2Y₁ in the recombinant CHO-K1-hP2Y₁₁ cell line.

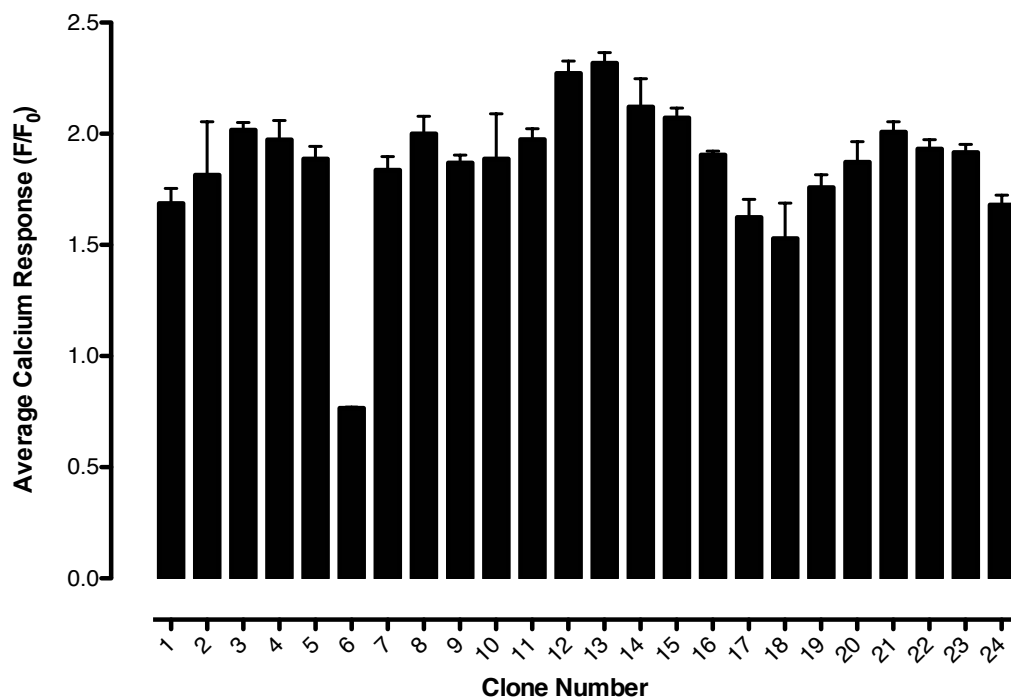


Figure 3.4 100 μ M BzATP elicits a calcium response in CHO-K1 clones expressing the human P2Y₁₁ receptor

The calcium response to 100 μ M BzATP was determined at 37°C for 24 CHO-K1 clones expressing the human P2Y₁₁ receptor. The results are expressed as the average \pm s.e.m. of three independent experiments, each performed in triplicate.

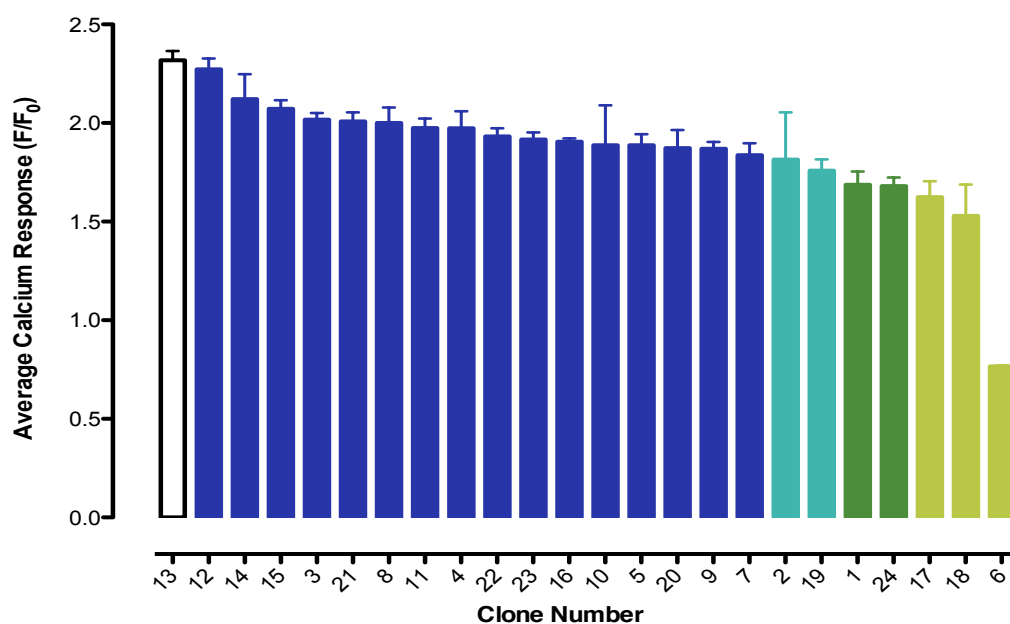


Figure 3.5 CHO-K1 clones expressing the human P2Y₁₁ receptor give varying responses to 100 μ M BzATP

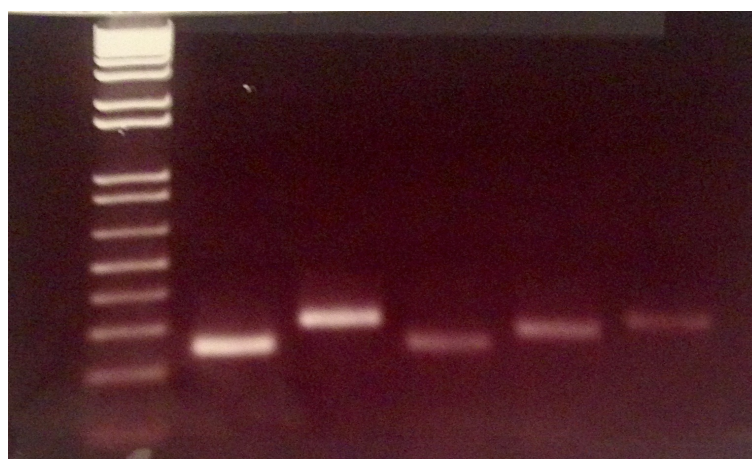
The 24 CHO-K1-hP2Y₁₁ clones shown in Figure 3-5 have been ordered from left to right from largest response to smallest. One-way ANOVA was used to determine the statistical significance of differences in response. Clone 13 was identified as giving the greatest calcium response to 100 μ M BzATP. Clones 12-7 showed no statistically significant difference to clone 13. Clones 2,19 gave significantly lower responses to clone 13 ($P < 0.05$). Clones 1,24 gave significantly lower responses to clone 13 ($p < 0.01$). Clones 17,18, 6 gave significantly lower responses to clone 13 ($p < 0.001$). Clones 13 and 6 were identified as the highest and lowest responding clones, respectively, of the 24 clones screened and were selected for further study.

3.3 Verification of hP2Y₁₁ expression in clones 13 and 6 using RT-PCR

To confirm that the hP2Y₁₁ receptor was successfully transfected into the recombinant CHO-K1-hP2Y₁₁ clones 6 and 13 and provide an estimate of the levels of receptor expression in these cell lines, mRNA was extracted from both clones and reverse transcribed into cDNA. PCR reactions were performed using forward and reverse primers for P2Y₁, P2Y₂, P2Y₁₁ and the control housekeeping genes β -actin and GAPDH (Glyceraldehyde-3-phosphate dehydrogenase). For both clones 6 and 13, each PCR reaction generated a product that matches the calculated length for the corresponding amplified gene, and the distances are shown in Figure 3.6. These results confirm the success of the transfection, demonstrating that P2Y₁, P2Y₂ and hP2Y₁₁ are all co-expressed in clones 6 and 13. The PCR reactions for both clones were then run on a single agarose gel to compare the band sizes corresponding to P2Y₁, P2Y₂ and hP2Y₁₁

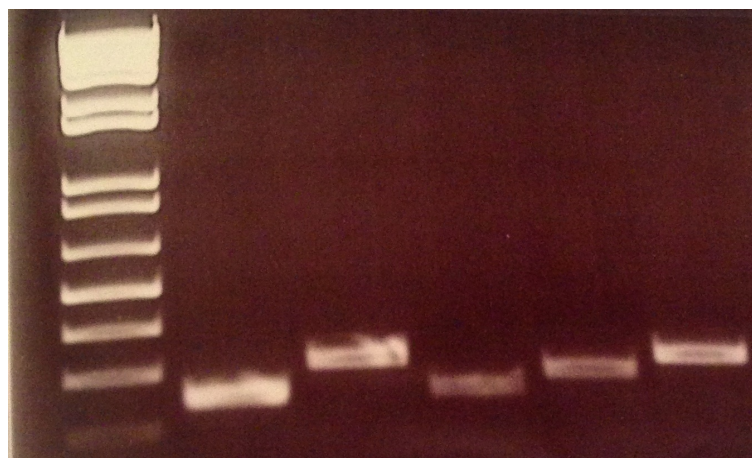
and quantify the relative levels of hP2Y₁₁ expression in clone 6 versus 13. However, the bands were very faint and the quality of the gels poor. Attempts to improve the quality of the obtained bands were unsuccessful and the experiments were not carried forward.

A.



Lane 1 Lane 2 Lane 3 Lane 4 Lane 5 Lane 6

B.



Lane 1 Lane 2 Lane 3 Lane 4 Lane 5 Lane 6

Figure 3.6 Agarose Gel Electrophoresis of PCR products in clones 6 and 13

A. Amplification products for clone 6. Lane 1 shows the 1 control KB plus DNA ladder. The band in lane 2 corresponds to β -actin and migrated to 250bp, which matches the expected size of the fragment (250 nucleotides). The band in lane 3 is GAPDH, which migrated to approximately 300 bp and matches the expected length of this fragment (310 nucleotides). The bands in lanes 3,4 and 5 are P2Y₁, P2Y₂ and hP2Y₁₁ respectively and migrated to 250, 270 and 300 bp, respectively, matching the expected lengths of the corresponding genes (250, 279 and 309 nucleotides, respectively). B. Amplification products for clone 13. Same as clone 6

3.4 Calcium responses of clonal CHO-K1-hP2Y₁₁ cell lines

This section describes the characterization of clones 13 and 6 using a set of eight carefully chosen agonists targeting the three P2Y receptors expressed in CHO-K1-hP2Y₁₁ cells: P2Y₁, P2Y₂, and hP2Y₁₁. The agonists were selected according to their potency at activating their target receptors (210). For instance, hP2Y₁₁ was characterized using three agonists of different potencies, BzATP, $\alpha\beta$ meATP and $\beta\gamma$ meATP (BzATP > $\alpha\beta$ meATP > $\beta\gamma$ meATP). The activity of P2Y₁ was studied using ADP, which has been reported to potently activate this receptor (157), while that of P2Y₂ was tested using UTP. Three other purinergic agonists, namely ATP, 2meSATP and ATP γ S, which can activate more than one receptor, were used to examine the combined activity of the purinoceptors. ATP acts at P2Y₁, P2Y₂ and P2Y₁₁ (157, 174, 208, 211) although it is most potent at P2Y₂ and P2Y₁ than P2Y₁₁. 2meSATP activates both P2Y₁ and P2Y₁₁ but exhibits a higher affinity for P2Y₁ as opposed to P2Y₁₁ (157, 208). ATP γ S is an agonist of P2Y₁, P2Y₂ and P2Y₁₁, respectively (157, 174, 208, 211).

The calcium response to each of the tested agonists was measured in three separate experiments performed in triplicate and the obtained data were analysed to calculate a mean EC₅₀ for each ligand. The EC₅₀ values of clones 13 and 6 were then compared using unpaired t-test analysis to determine differences in agonist profiles between the clones.

3.4.1 Functional characterization of agonist responses in CHO-K1-hP2Y₁₁ Clone 13, the ‘high’-expressing P2Y₁₁ clone

Following the identification of CHO-K1-hP2Y₁₁ clone 13 as the clone expressing the highest density of hP2Y₁₁ receptor, the potency of a set of 4 ligands (BzATP, ATP γ S, ATP and $\alpha\beta$ meATP) was tested using FLIPR at 37°C. Figure 3.7 shows the mean calcium response of clone 13 cells following the addition of the agonists at increasing concentrations, ranging from 1nM to 100 μ M (log values: -9 to -4). The tested agonists successfully induced calcium mobilization in a concentration-dependent manner, whereby increasing agonist concentrations resulted in the release of increasing amounts of intracellular calcium from intracellular stores, as reflected by the increase in fluorescence detected by the FLIPR Tetra.

The concentration-response curves of the four studied ligands were analysed using non-linear regression with a comparison of two different equations (variable slope, or four parameter, equation versus asymmetric, or five parameter, equation) to determine the best fit for each dataset. The calcium response to ATP, ATP γ S and BzATP is sigmoidal monophasic and occurs over two log units of agonist concentration, namely 10nM to 1 μ M (log value: -8 to -6) for ATP and ATP γ S and 100nM to 10 μ M (log value: -7 to -5) for BzATP. Non-linear regression analysis reveals that the preferred fit for these ligands is the variable slope, or four parameter, equation. The maximum calcium response to BzATP and ATP γ S occurs at 100 μ M, while ATP achieved its maximum response at 10 μ M. Using one-way ANOVA analysis, there is no statistically significant difference between the maxima for BzATP, ATP γ S, ATP and 100 μ M UTP control in clone 13 (p value= 0.97). The maximum responses and the Hill slope of the concentration-response curves are listed in Table 3.3.

Agonist	Hill Slope	Maximum Response (F/F ₀)	Maximum Response (% of 100 μ M UTP)
ATP	1.10 \pm 0.3	1.99 \pm 0.15	101 \pm 5%
ATP γ S	1.29 \pm 0.1	1.91 \pm 0.15	97 \pm 4%
BzATP	1.50 \pm 0.2	1.99 \pm 0.1	101.5 \pm 1.7

Table 3.3 Steepness and maxima of the BzATP, ATP and ATP γ S curves in clone 13

The Hill slopes of the concentration-response curves for BzATP, ATP and ATP γ S in clone 13 were estimated using non-linear regression analysis. The maximum response to each agonist (F/F₀) was determined and expressed as a percentage of the maximum response to the 100 μ M UTP control. The values shown in this table constitute the average \pm s.e.m of three independent experiments, each performed in triplicate.

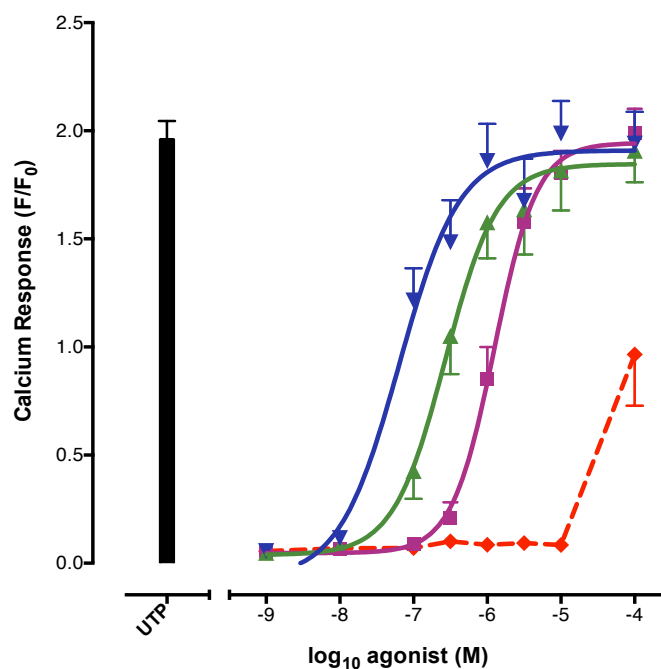


Figure 3.7 Concentration-response curves of BzATP, ATP γ S, ATP and $\alpha\beta$ meATP on Ca²⁺ mobilization in CHO-K1-hP2Y₁₁ clone 13

The calcium response to increasing concentrations of BzATP (■), ATP γ S (▲), ATP (▼) and $\alpha\beta$ meATP (◆) at 37°C in CHO-K1-hP2Y₁₁ clone 13, which expresses the highest density of the human P2Y₁₁ receptor of all clones characterised. The results are expressed as the average \pm s.e.m of three independent experiments, each performed in triplicate. The response of clone 13 to 100 μ M UTP is shown.

In contrast, non-linear regression failed to fit a curve to the $\alpha\beta$ meATP data and its EC₅₀ value could not be determined. In fact, the calcium response to this ligand began at 10 μ M and did not reach a clear asymptote by the highest concentration of agonist applied (100 μ M). The maximum $\alpha\beta$ meATP response is 0.97 ± 0.2 , constitutes $49 \pm 11\%$ of the 100 μ M UTP control and is statistically significantly different from both 100 μ M UTP and the maximal responses to BzATP, ATP γ S and ATP (**, p value= 0.003). The $\alpha\beta$ meATP curve is connected using a dotted line for visualization purposes.

Following this initial round of characterization, CHO-K1-hP2Y₁₁ clone 13 was subjected to a second round of investigation using a different set of four agonists (ADP, UTP, 2meSATP and $\beta\gamma$ meATP) at 37°C. Figure 3.8 shows the mean concentration response curves for these ligands, generated using non-linear regression analysis. The tested agonists were applied at increasing concentrations, ranging from 0.1nM to 100 μ M (log values: -10 to -4) and elicited calcium mobilization in a time-dependent fashion.

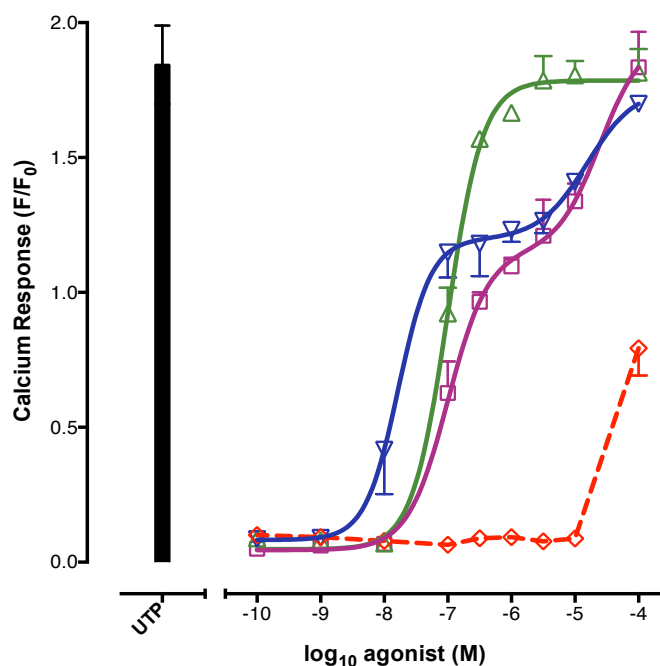


Figure 3.8 Concentration-response curves of ADP, UTP, 2meSATP and $\beta\gamma$ meATP on Ca^{2+} mobilization in CHO-K1-hP2Y₁₁ clone 13

The calcium response to increasing concentrations of ADP (\square), UTP (\triangle), 2meSATP (∇) and $\beta\gamma$ meATP (\diamond) at 37°C in CHO-K1-hP2Y₁₁ clone 13, which expresses the highest density of the human P2Y₁₁ receptor of all clones characterised. The results are expressed as the average \pm s.e.m of three independent experiments, each performed in triplicate. The response of clone 13 to 100 μM UTP is shown.

As the Figure shows, the calcium response potentiated by UTP is sigmoidal and achieves its maximal value over two log units of agonist concentration, ranging from 10nM to 1 μM (log value: -8 to -6). The preferred model for the UTP data is the variable slope (four parameter) equation, which fits a monophasic curve to the data. The calcium response to UTP reaches its maximum at a concentration of 100 μM . Using a one-way ANOVA test, there is no statistically significant difference between the maxima for ADP, UTP, 2meSATP and 100 μM UTP response in clone 13 (p value= 0.67).

The calcium responses produced by ADP and 2meSATP were different from those of the other six agonists tested. Although they were concentration-dependent, the responses progressed from their minimum to their maximum over four log units of agonist concentration. Non-linear regression analysis using a comparison of two equations (four parameter versus five parameter equation) was unable to fit a curve through these datasets, suggesting that they might be better fit with a biphasic as opposed

to a monophasic equation. In fact, all three individual ADP and 2meSATP trials resulted in a biphasic concentration-response curve with two distinct plateaus. The first phase of the ADP response ranges over two log units of agonist concentration, from 10nM to 1 μ M (log value: -8 to -6,) while the second phase spans over two log units, ranging from 1 μ M to 100 μ M (log value: -6 to -4). The maximum response is achieved at 100 μ M ADP. The fraction of the curve, or proportion of the maximal response due to the high-affinity site, is 0.6 ± 0.05 , indicating that this site accounts for approximately 60% of the calcium response to ADP. The maximum response (F/F_0) to ADP is 1.83 ± 0.13 , achieved at 100 μ M, and can be expressed as $101 \pm 5.4\%$ of the 100 μ M UTP response. In the case of 2meSATP, the high affinity site of the response ranges from 1nM to 100nM (log value: -9 to -7) whereas the low affinity site occurs between 100nM and 10 μ M (log value: -7 and -5). The fraction of the curve is 0.67 ± 0.04 , indicating that the higher affinity site comprises approximately 70% of the calcium response elicited by 2meSATP. The maximum response is achieved at 100 μ M 2meSATP. The maximum responses and Hill slopes of the concentration-response curves for ADP, 2meSATP and UTP are listed in Table 3.4.

Agonist	Hill Slope		Maximum Response (F/F_0)	Maximum Response (% of 100 μ M UTP)
	nH ₁	nH ₂		
ADP	1.4 ± 0.3	5 ± 2.5	1.83 ± 0.13	$101 \pm 5.4\%$
2meSATP	3.4 ± 1.6	1.4 ± 0.8	1.70 ± 0.021	$94 \pm 3.5\%$
UTP		1.2 ± 0.2	1.82 ± 0.09	100%

Table 3.4 Steepness and maxima of the ADP, 2mesATP and UTP curves in clone 13

The Hill slopes of the concentration-response curves for ADP, 2meSATP and UTP in clone 13 were estimated using non-linear regression analysis. nH₁ and nH₂ refer to the Hill slopes of the high and low affinity sites of the biphasic ADP and 2meSATP curves. The maximum response to each agonist (F/F_0) was determined and expressed as a percentage of the maximum response to the 100 μ M UTP control. The values shown in this table constitute the average \pm s.e.m of three independent experiments, each performed in triplicate.

As in the case of $\alpha\beta$ meATP, non-linear regression analysis failed to fit a curve to the $\beta\gamma$ meATP data, which was represented using a dotted connecting line. These data gave an ambiguous fit, failing to reach a maximum response within the concentration range of agonist tested, and it was not possible to determine an EC₅₀ value for this ligand. The maximum response to $\beta\gamma$ meATP is 0.8 ± 0.1 , obtained at a concentration of 100 μ M $\beta\gamma$ meATP, constitutes $43 \pm 3\%$ of 100 μ M control and is statistically significantly

different from both 100 μ M UTP and from the maximal responses of ADP, UTP and 2meSATP, as revealed by one way ANOVA analysis (***, p value= 0.0001).

The mean EC₅₀ and pEC₅₀ values of the tested agonists were calculated using non-linear analysis and are listed in Table 3.5. Although the data analysis was carried using log values, the EC₅₀ value was used as a measure of variation instead of the pEC₅₀ value in all the sections of this project. Four out of six agonists (BzATP, ATP, ATP γ S and UTP) gave a monophasic response with a single EC₅₀ value. ADP and 2meSATP gave biphasic responses with two distinct EC₅₀ values. $\alpha\beta$ meATP and $\beta\gamma$ meATP failed to produce a complete calcium response and are not shown in the table. The high affinity site of 2meSATP elicited the most potent calcium response in clone 13 while the low affinity sites of ADP and 2meSATP produced the least potent responses. The agonist potencies at these low affinity sites were not statistically significantly different, suggesting that ADP and 2meSATP might be activating the same unknown population of receptors detected at this site. In summary, the order of potency of the 8 agonists in clone 13 is:

**2meSATP (1) > ATP > UTP > ADP (1) > ATP γ S > BzATP > ADP (2) \approx 2meSATP (2)
> $\beta\gamma$ meATP \approx $\alpha\beta$ meATP**

Agonist	EC ₅₀ (nM \pm S.E.M.)	pEC ₅₀
2meSATP (EC₅₀₋₁)	21 \pm 10	7.76
ATP	47 \pm 20	7.41
UTP	89 \pm 22	7.08
ADP (EC₅₀₋₁)	110 \pm 6	6.98
ATP γ S	274 \pm 48	6.58
BzATP	1,270 \pm 150	5.90
ADP (EC₅₀₋₂)	12,700 \pm 1,770	4.91
2meSATP (EC₅₀₋₂)	13,430 \pm 674	4.87

Table 3.5 The calcium response elicited by nucleotides and nucleotide analogues in CHO-K1-hP2Y₁₁ clone 13

The EC₅₀ and pEC₅₀ values of a set of 8 agonists were determined in CHO-K1-hP2Y₁₁ clone 13. The results are expressed as the mean EC₅₀ and the mean pEC₅₀ of three independent experiments, each performed in triplicate. Agonists are ranked from highest to lowest potency. Two agonists, 2meSATP and ADP, gave a biphasic response with two distinct EC₅₀ values.

3.4.2 Functional characterization of agonist responses in CHO-K1-hP2Y₁₁ Clone 6, the 'low'-expressing P2Y₁₁ clone

Following characterization of the high expressing CHO-K1-hP2Y₁₁ clone 13, the calcium responses elicited by the eight previously described agonists were investigated in CHO-K1-hP2Y₁₁ clone 6, which expresses a low density of hP2Y₁₁. The characterization was carried out as previously, in two sets of four agonists using FLIPR. Figure 3.9 shows the mean calcium response of clone 6 upon the addition of BzATP, ATP γ S, ATP and $\alpha\beta$ meATP at 37°C. The agonists were applied at increasing concentrations, ranging from 10nM to 100 μ M (log values: -8 to -4) and produced calcium responses in a dose-dependent manner.

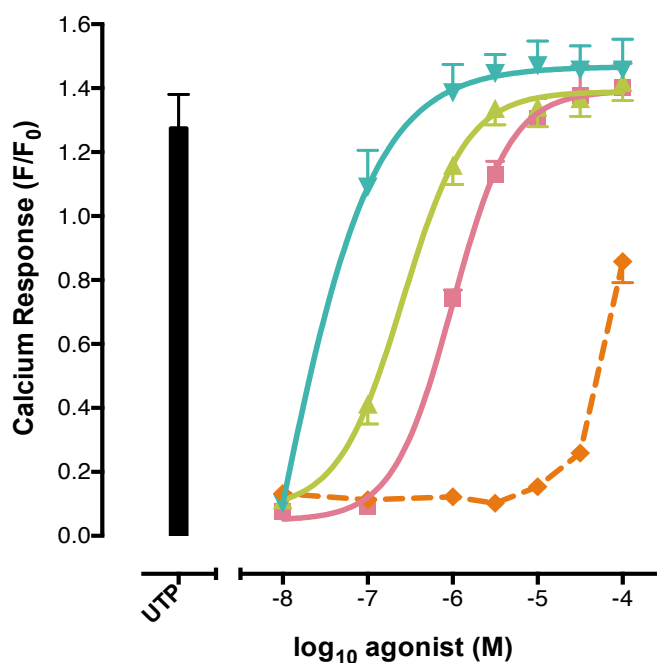


Figure 3.9 Concentration-response curves of BzATP, ATP γ S, ATP and $\alpha\beta$ meATP on Ca²⁺ mobilization in CHO-K1-hP2Y₁₁ clone 6

The calcium response to increasing concentrations of BzATP (■), ATP γ S (▲), ATP (▼) and $\alpha\beta$ meATP (◆) at 37°C in CHO-K1-hP2Y₁₁ clone 6, which expresses the lowest density of the human P2Y₁₁ receptor of all clones characterized. The results are expressed as the average \pm s.e.m of three independent experiments, each performed in triplicate. The response of clone 6 to 100 μ M UTP is shown.

The response curves of the four agonists were generated through non-linear regression analysis using a comparison of two fits (variable slope, or four parameter,

equation and asymmetric, or five parameter, equation) and represent the mean of three independent experiments performed in triplicate. The preferred fit for the BzATP, ATP γ S and ATP data in clone 6 is the variable slope, or four parameter, equation, resulting in sigmoidal monophasic curves. ATP γ S achieved its minimum to maximum response over two log units of agonist concentration ranging from 10nM to 1 μ M (log value: -9 to -7) agonist concentration, whereas ATP and BzATP reached their plateaus between 100nM and 10 μ M agonist (log value: -7 to -5). BzATP and ATP γ S reached their maximum calcium response at 100 μ M, while ATP achieved its maximum at 10 μ M. Using one-way ANOVA analysis, there is no statistically significant difference between the maxima for BzATP, ATP γ S, ATP and the 100 μ M UTP response in clone 6 (p value= 0.4). The maximum responses and Hill slopes of the concentration-response curves are listed in Table 3.6.

Agonist	Hill Slope	Maximum Response (F/F ₀)	Maximum Response (% of 100 μ M UTP)
ATP	0.75 \pm 0.13	1.5 \pm 0.08	117 \pm 5%
ATP γ S	1.16 \pm 0.13	1.4 \pm 0.06	112 \pm 5%
BzATP	1.28 \pm 0.07	1.4 \pm 0.08	111 \pm 3%

Table 3.6 Steepness and maxima of the BzATP, ATP and ATP γ S curves in clone 6

The Hill slopes of the concentration-response curves for BzATP, ATP and ATP γ S in clone 6 were estimated using non-linear regression analysis. The maximum response to each agonist (F/F₀) was determined and expressed as a percentage of the maximum response to the 100 μ M UTP control. The values shown in this table constitute the average \pm s.e.m of three independent experiments, each performed in triplicate.

As in clone 13, non-linear regression was unable to fit a curve to the $\alpha\beta$ meATP data and it was not possible to calculate an EC₅₀ value for this agonist. The calcium response started at 10nM (log value: -8) and failed to reach a plateau by 100 μ M (log value: -4), the highest concentration tested. The maximum calcium response (F/F₀) produced by $\alpha\beta$ meATP is 0.9 \pm 0.07, constitutes 67 \pm 3% of the 100 μ M UTP control, and is statistically significantly different from both 100 μ M UTP and the maximal responses of BzATP, ATP γ S and ATP (**, p value= 0.0015). A dotted connecting line was inserted across the data points for visualization purposes.

Following this initial characterization, the potencies of the second set of agonists (ADP, UTP, 2meSATP and $\beta\gamma$ meATP) were investigated. Figure 3.10 presents the mean

calcium responses following the addition of increasing agonist concentrations ranging from 1 nM to 100 μ M (log value: -9 to -4) at 37°C. The concentration-response curves for each agonist were plotted using non-linear regression analysis. No biphasic responses were detected for either ADP or 2meSATP in clone 6, as opposed to the biphasic behaviour observed for both agonists in clone 13. The preferred fit for the ADP, UTP, and 2meSATP data was the variable slope, or four parameter equation, resulting in a monophasic sigmoidal curve for all three agonists. The calcium response produced by ADP and 2meSATP was achieved over approximately two log units of agonist concentration, ranging from 1nM to 100nM (log value: -9 to -7, approximately). The calcium response generated by UTP, however, occurred over 1 log unit, spanning from 10 nM to 100 nM (log value: -8 to -7), resulting in a curve with a steep slope. ADP and 2meSATP elicited their maximum response at 100 μ M while UTP reached its maximum at 10 μ M. . Using a one-way ANOVA test, there is no statistically significant difference between the maxima for ADP, UTP and 2meSATP and 100 μ M UTP response in clone 6 (p value= 0.7). The maximum responses and Hill slopes of the concentration-response curves for these agonists are displayed in Table 3.7.

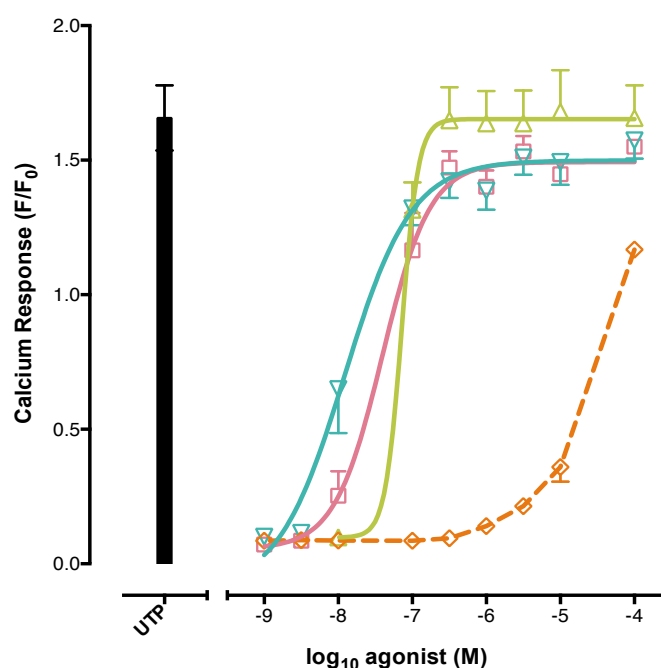


Figure 3.10 Concentration-response curves of ADP, UTP, 2meSATP and $\beta\gamma$ meATP on Ca^{2+} mobilization in CHO-K1-hP2Y₁₁ clone 6

The calcium response to increasing concentrations of ADP (\square), UTP (\triangle), 2meSATP (∇) and $\beta\gamma$ meATP (\diamond) at 37°C in CHO-K1-hP2Y₁₁ clone 6, which expresses the lowest density of the human P2Y₁₁ receptor of all clones characterised. The results are expressed as the average \pm s.e.m of three independent experiments, each performed in triplicate.

Agonist	Hill Slope	Maximum Response (F/F ₀)	Maximum Response (% of 100μM UTP)
ADP	1.4 ± 0.18	1.6 ± 0.01	95 ± 6.4%
2meSATP	1.04 ± 0.27	1.6 ± 0.07	96.3 ± 3%
UTP	2.0 ± 0.6	1.7 ± 0.15	100%

Table 3.7 Steepness and maxima of the ADP, 2meSATP and UTP curves in clone 6

The Hill slopes of the concentration-response curves for ADP, 2meSATP and UTP in clone 6 were estimated using non-linear regression analysis. The maximum response to each agonist (F/F₀) was determined and expressed as a percentage of the maximum response to the 100μM UTP control. The values shown in this table constitute the average ± s.e.m of three independent experiments, each performed in triplicate.

In contrast to the calcium responses generated by ADP, UTP and 2meSATP, βγmeATP, like αβmeATP, gave a response that started at 10nM (log value: -8) and was not able to reach a plateau by 100μM (log value: -4), the highest concentration tested. Non-linear regression analysis yielded an ambiguous fit to the data and it was not possible to determine an EC₅₀ value for this ligand. Unlike the other agonists tested, the maximum calcium response produced by βγmeATP is 1.2 ± 0.03 at a concentration of 100μM ligand, and is statistically significantly different from both 100μM UTP and from the maximal responses of BzATP, ATPγS and ATP, as revealed by one-way ANOVA analysis (*, p value= 0.0125). This response constitutes 71.2 ± 5.6% of the 100μM UTP response. The data were connected using a dotted line is shown for visualization purposes. The EC₅₀ and pEC₅₀ values of the tested agonists are shown in Table 3.8. The rank order of agonist potency for clone 6 is:

2meSATP > ATP > ADP > UTP > ATPγS > BzATP > βγmeATP > αβmeATP

Agonist	EC ₅₀ (nM ± S.E.M.)	pEC ₅₀
2meSATP	21 ± 6	7.70
ATP	33 ± 6	7.50
ADP	35 ± 19	7.67
UTP	67 ± 22	7.24
ATPγS	260 ± 39	6.59
BzATP	992 ± 100	6.00

Table 3.8 The calcium response elicited by nucleotides and nucleotide analogues in CHO-K1-hP2Y₁₁ clone 6.

The EC₅₀ and pEC₅₀ values of a set of 8 agonists were determined in CHO-K1-hP2Y₁₁ clone 6. The results are expressed as the mean EC₅₀ and the mean pEC₅₀ of three independent experiments, each performed in triplicate. No biphasic response was detected for either ADP or 2meSATP in clone 6.

3.5 hP2Y₁₁ receptor density influences calcium responses elicited by nucleotides and nucleotide analogues

3.5.1 Comparison of time-dependent responses in CHO-K1-hP2Y₁₁ clone 13 and CHO-K1-hP2Y₁₁ clone 6

To determine whether hP2Y₁₁ receptor density influences the calcium response to the potent P2Y₁₁ agonist BzATP in clones 13 versus 6, the changes in fluorescence elicited by 100µM BzATP (log value: -4) over a time course of 180 seconds were investigated using FLIPR. Figure 3.11 shows the time-dependent calcium response to 100µM BzATP in the clones. The curves represent the mean response obtained from three different experiments, each performed in triplicate, minus the baseline fluorescence measured prior to the addition of the ligand. The data points are shown using a connecting line only, as symbols and error bars have been excluded to facilitate the visualisation of the represented curves.

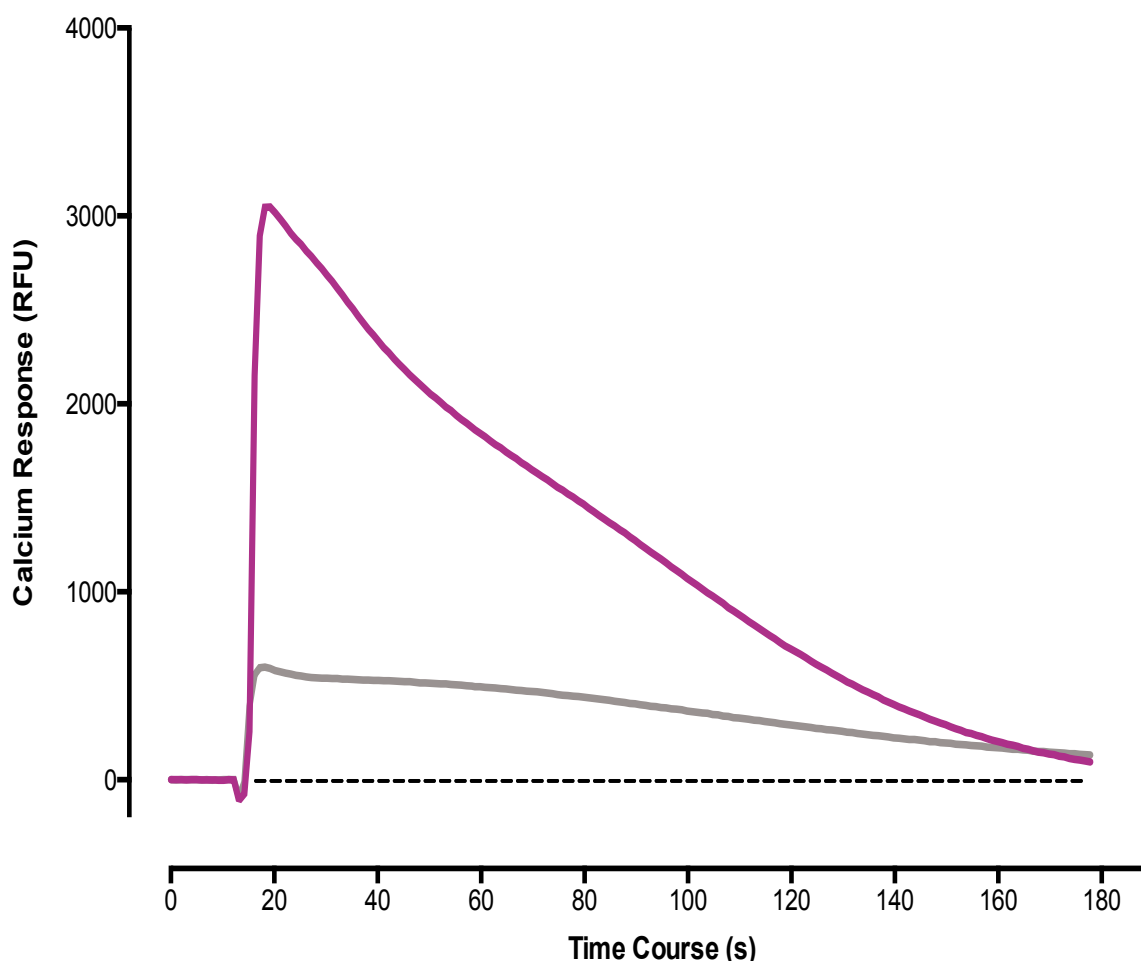


Figure 3.11 The time dependence of the response to 100 μ M BzATP in CHO-K1-hP2Y₁₁ clone 13 and CHO-K1-hP2Y₁₁ clone 6

The calcium response to 100 μ M BzATP was measured over time in CHO-K1-hP2Y₁₁ clone 13 (—), which expresses the highest density of the human P2Y₁₁ receptor, and CHO-K1-hP2Y₁₁ clone 6 (—), which expresses the lowest density of the human P2Y₁₁ receptor in all clones screened. The curves represent the mean calcium response obtained from three independent experiments, each performed in triplicate, minus the baseline fluorescence which was measured prior to the introduction of ligand at $t=10$ seconds. The results are expressed as relative fluorescence units. Error bars have been omitted to ensure a better visualisation of the curves.

The ligand was added at $t = 10$ seconds in the assay, allowing the device to measure the baseline calcium level that exists in the cells prior to stimulation with the ligand. The initial decrease in fluorescence detected at $t = 10$ seconds for both curves is typically observed following ligand addition. BzATP induces an increase in calcium fluorescence, corresponding to the release of calcium from intracellular stores in both clones 13 and 6. The agonist response proceeds from its minimum to its maximum and tails off within 180 seconds. A larger increase in fluorescence is observed for clone 13 as opposed to clone 6, although the peak response is achieved within the same time of agonist addition for both clones. The maximum calcium responses to BzATP for the

clones, calculated using column statistics and area under the curve analysis, are shown in Table 3.9. There was a statistically significant difference between clones 13 and 6 using both methods (***, p value= 0.0004; ***, p value = 0.0002, respectively). The area under the curve is $448,604 \pm 25,785$ for clone 13 and $221,732 \pm 8,250$ for clone 6 and these values are statistically significantly different (**, p value = 0.0011).

Clone	Maximum Response (RFU)	
	Column Statistics	AUC
13	3048 ± 220	4428 ± 220
6	599.1 ± 46	1503 ± 45.6

Table 3.9. Maximum calcium response to 100 μ M BzATP in clones 13 versus 6

The maximum response to a fixed concentration of BzATP was calculated for clones 13 and 6 using column statistics and area under the curve analysis. The values represent the average \pm s.e.m of three different experiments, each performed in triplicate, and are expressed in relative fluorescence units (RFU).

3.5.2 Comparison of agonist potencies in CHO-K1-hP2Y₁₁ clone 13 and CHO-K1-hP2Y₁₁ clone 6

As described in the introduction to this chapter, the aim of the functional characterization undertaken in clones 13 and 6 is to identify a recombinant co-expression model that reflects the co-expression of P2Y₁ and P2Y₁₁ in guinea pig taenia coli. As part of this, it was necessary to vary the expression level of hP2Y₁₁ as the relative levels of expression of P2Y₁ and P2Y₁₁ in the taenia coli are unknown. Consequently, a series of statistical analyses, comparing the efficacies and potencies of each of the agonists tested in clones 13 versus 6, was performed. The dose response curves of each of the ligands tested in the clones were plotted on a single graph to facilitate the comparison process, and are shown in Figures 3.12 and 3.13. The mean average responses of the clones to 100 μ M BzATP are employed as controls in each figure.

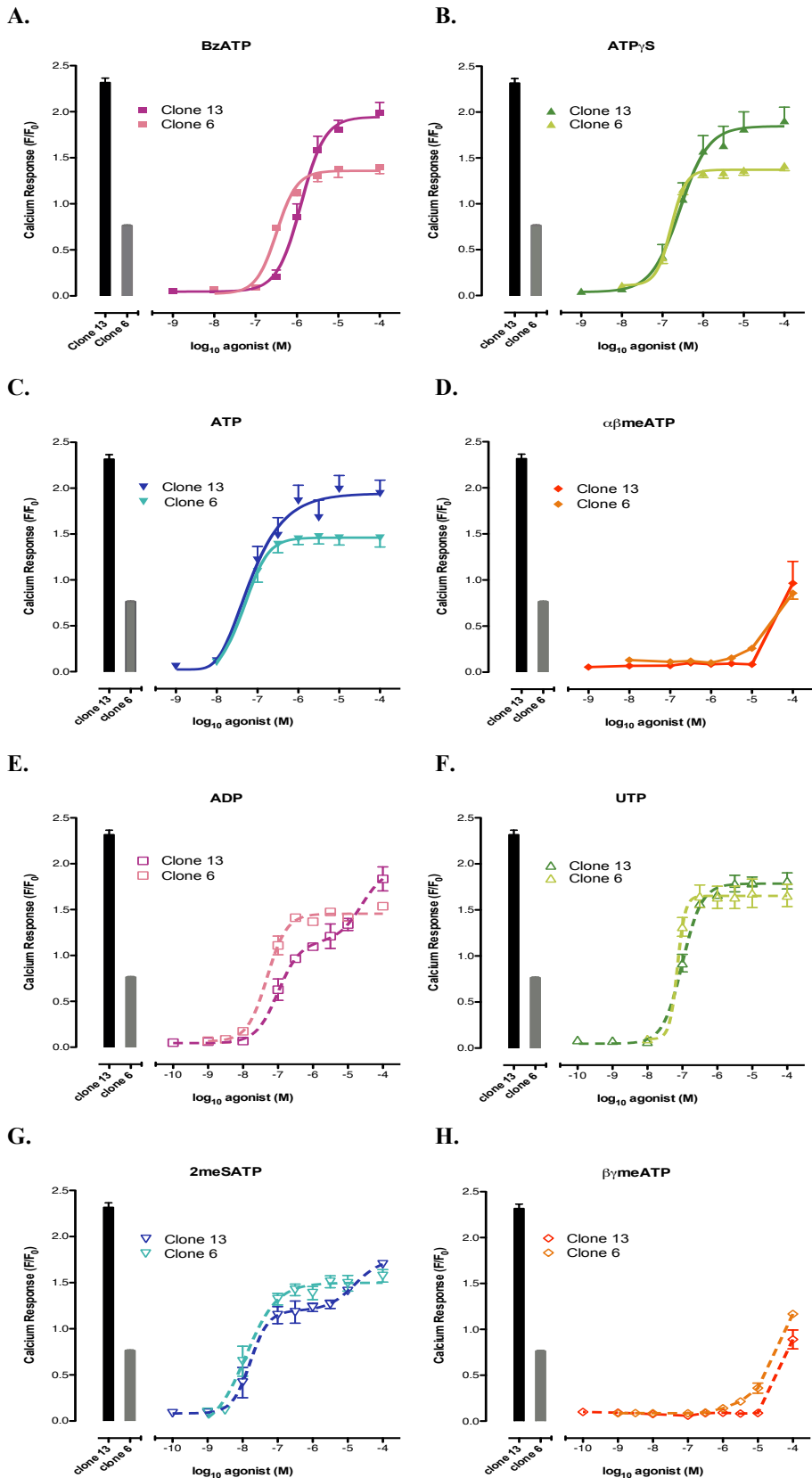
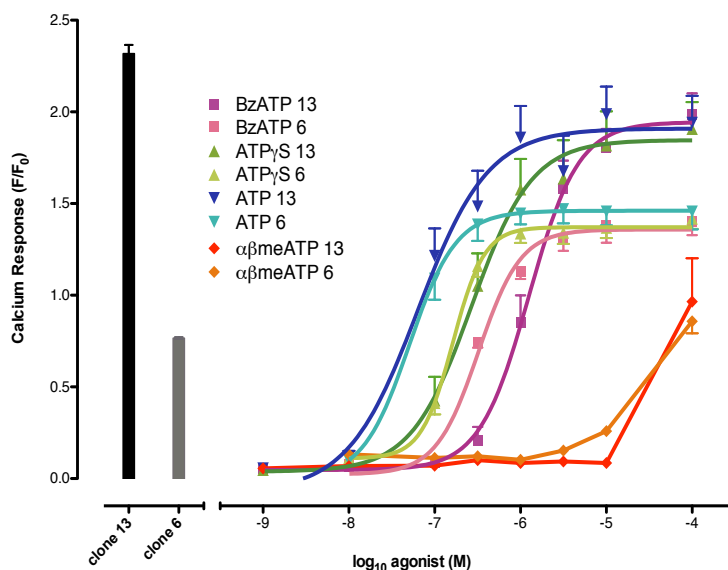


Figure 3.12 Visualization of differences in agonist responses in CHO-K1-hP2Y₁₁ clone 13 and CHO-K1-hP2Y₁₁ clone 6

The calcium responses of CHO-K1-hP2Y₁₁ clone 13 and CHO-K1-hP2Y₁₁ clone 6 to each agonist tested are shown on a single graph to aid comparison of the functional responses in each clone. A) BzATP; B) ATP_γS; C) ATP; D) αβmeATP; E) ADP; F) UTP; G) 2meSATP and H) βγmeATP. The control bars show the calcium response of clones 13 and 6 to 100μM BzATP.

A.



B.

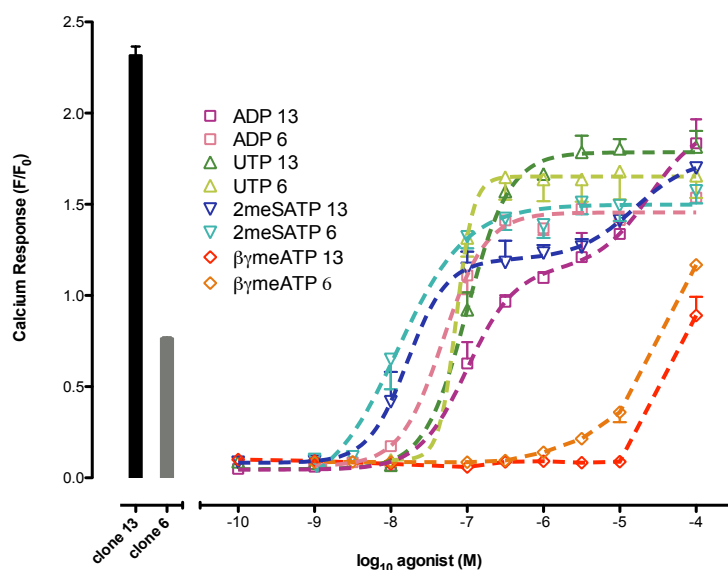


Figure 3.13 Comparison of agonist responses in CHO-K1-hP2Y₁₁ clone 13 and CHO-K1-hP2Y₁₁ clone 6

The calcium responses of CHO-K1-hP2Y₁₁ clone 13 and CHO-K1-hP2Y₁₁ clone 6 to two distinct sets of agonists are shown on two different graphs to aid in comparison of the functional responses in each clone. *A.* set 1: BzATP, ATP γ S, ATP and $\alpha\beta$ meATP; *B.* set 2: ADP, UTP, 2meSATP and $\beta\gamma$ meATP. The control bars show the calcium response of clones 13 and 6 to 100 μ M BzATP.

As the figures reveal, the calcium responses elicited by the first set of agonists (BzATP, ATP γ S, ATP) in clones 13 and 6, are all monophasic. Using an unpaired t-test, there is a statistically significant difference between the maximal response of BzATP with respect to 100 μ M UTP response in clone 13 versus clone 6 (*, p value= 0.0475), indicating that BzATP reaches a different maximum in these clones. Statistical analyses of the maximal responses of ATP γ S, ATP and $\alpha\beta$ meATP with respect to 100 μ M UTP in clones 13 and clone 6 reveals no statistically significant difference between the two clones, signifying that these agonists have similar maxima in both the high expressing and low expressing clones. In order to compare between the potencies of the calcium responses elicited by these agonists in the clones, the ratio of the mean EC₅₀ value in clone 13 was divided by the mean EC₅₀ in clone 6 for each of the agonists tested and unpaired t-tests were performed (shown in Table 3.10). The resulting ratio is 1.28 and there is no statistically significant difference between the EC₅₀ values calculated in both clones (p value= 0.19). The ratio of ATP γ S is 1.05 (p value= 0.98) while that of ATP is 1.42 (p value= 0.54). These analyses indicate that BzATP, ATP γ S and ATP have the same potency in each clone. In summary, statistical analyses show that ATP γ S and ATP have similar efficacies and potencies in clone 13 and clone 6, whereas BzATP has a higher efficacy but the same potency in the high expressing versus low expressing clone.

The second set of agonists tested (ADP, UTP, 2meSATP) was also subjected to the same series of numerical comparisons. Statistical analysis shows that there is no significant difference between the maximal responses of ADP, UTP and 2meSATP with respect to 100 μ M UTP response in clone 13 versus clone 6, indicating that these ligands have similar efficacies in both clones.

Agonist	Ratio (clone 13/ clone 6)	p value
BzATP	1.28	0.19
UTP	1.33	0.52
ATP	1.42	0.54
ATP γ S	1.05	0.84
2meSATP (EC ₅₀₋₁)	1.00	0.98
ADP (EC ₅₀₋₁)	3.14*	0.0246
ADP (EC ₅₀₋₂)	362**	0.0020
2meSATP (EC ₅₀₋₂)	639***	0.0001

Table 3.10 Comparison of agonist potencies of the calcium response in CHO-K1-hP2Y₁₁ clone 13 and CHO-K1-hP2Y₁₁ clone 6

The ratio of the mean EC₅₀ in CHO-K1-hP2Y₁₁ clone 13 divided by the mean EC₅₀ in CHO-K1-hP2Y₁₁ clone 6 is shown for each of the agonists tested. An unpaired t-test was used to compare the EC₅₀ values for each agonist in clone 13 versus clone 6. The p values for each comparison are shown. Each of the two EC₅₀ values obtained for both ADP and 2meSATP in clone #13 were compared with the single EC₅₀ value obtained for these agonists in clone #6 (* = p<0.05; ** = p<0.01; *** = p<0.001).

The mean EC₅₀ values of the agonists tested in clones 13 and 6 were also compared in order to evaluate the potencies of these ligands in the two clones. As Figures 3.13 and 3.14 show, both ADP and 2meSATP generated biphasic responses with two EC₅₀ values each in clone 13, as opposed to monophasic responses with a single EC₅₀ value in clone 6. The EC₅₀ values of these two agonists in clone 13 versus clone 6 were compared using unpaired t-tests. Statistical analysis shows that there is a statistically significant difference between the EC₅₀ values of both the high affinity and low affinity sites of ADP in clone 13 and the mean EC₅₀ of ADP in clone 6 (*, p value= 0.0246; **, p value= 0.002, respectively). The ratio of the EC₅₀ of the high affinity site of ADP (13) with respect to the EC₅₀ of this agonist in clone 6 is 3.14, while the ratio of the low affinity site is 362, signifying that ADP has different potencies in clone 13 as compared to clone 6. In contrast, the EC₅₀ value of the high affinity site of 2meSATP in clone 13 is not statistically significantly different from the EC₅₀ of this ligand in clone 6 (p value = 0.98; ratio =1.00), indicating that the same population of receptors might be involved in the response to this drug in the high affinity site of clone 13 and the single 2meSATP site in clone 6. However, the EC₅₀ of the low affinity site of 2meSATP (13) is statistically significantly different from the EC₅₀ of 2meSATP in clone 6 (***, p value= 0.0001; ratio= 639), signifying that 2meSATP has different potencies in the low affinity site of clones 13 versus 6.

Unlike ADP and 2meSATP, UTP generates a monophasic response in both clones. The ratio of the EC₅₀ of clone 13 with respect to clone 6 is 1.33 and there is no statistically significant difference between the EC₅₀ values calculated in both clones (p value= 0.52), indicating that this drug possesses a similar potency in clones 13 and 6.

3.6 Summary of the functional studies

Following the creation of two stable pools of CHO-K1 expressing hP2Y₁₁, twenty-four clones expressing different densities of hP2Y₁₁ were created and screened for their response to 100µM BzATP. Using one-way ANOVA analysis, clone 13 was identified as producing the greatest calcium response while clone 6 was identified as producing the lowest calcium response, and these two clones were retained for further investigation.

A set of eight agonists (BzATP, ATP_γS, ATP, αβmeATP, ADP, UTP, 2meSATP and βγmeATP) was chosen for the in-depth pharmacological characterization of clones 13 and 6. Analysis of the obtained agonist responses revealed that BzATP, ATP_γS, ATP and UTP exhibited similar potencies in clones 13 and 6 while αβmeATP and βγmeATP failed to produce a complete calcium response in both clones. In contrast, ADP and 2meSATP elicited a biphasic response in clone 13 versus a monophasic response in clone 6. This difference in behaviour may reflect the formation, at higher expression levels of hP2Y₁₁, of a P2Y₁: P2Y₁₁ heteromer with a novel calcium profile, thus accounting for the low affinity site of the biphasic ADP and 2meSATP responses in clone 13.

3.7 Generation of co-immunoprecipitation and BiFC constructs

The original experimental design of this project envisaged a functional as well as molecular approach to test the interaction between hP2Y₁ and hP2Y₁₁ receptors using co-immunoprecipitation and BiFC experiments in 1321N1 cells. Unfortunately, these experiments were not completed due to difficulties in finalizing the constructs. This section provides a brief description of the generation of co-immunoprecipitation constructs undertaken prior to abandoning this part of the project. Two co-immunoprecipitation constructs: 1) Myc-hP2Y₁ + stop and 2) HA-hP2Y₁₁ + stop were first designed using the construct layout shown in Figure 3.14. hP2Y₁ cDNA was then amplified using a set of forward and reverse primers. The resulting product bearing the 5' and 3' additions was 1180 bps long and was clearly visualized using agarose gel electrophoresis. This fragment was assembled through ligation into a pCR-Blunt II-TOPO vector, which possesses both kanamycin and zeocin resistance genes. The ligation

reaction product was transfected into Mach1T1^R phage-resistant chemically competent E.coli, following which the transformation was plated on kanamycin selective agar plates. A small-scale isolation of plasmid DNA (Miniprep) was performed and a Restriction Enzyme digestion was conducted to test for the successful insertion of Myc-hP2Y₁ into the Topo vector. The purified DNA was cut with NheI and EcoRV, yielding two fragments of the right size corresponding to the Topo vector (3519bps) and Myc-hP2Y₁ (1180bps) respectively.

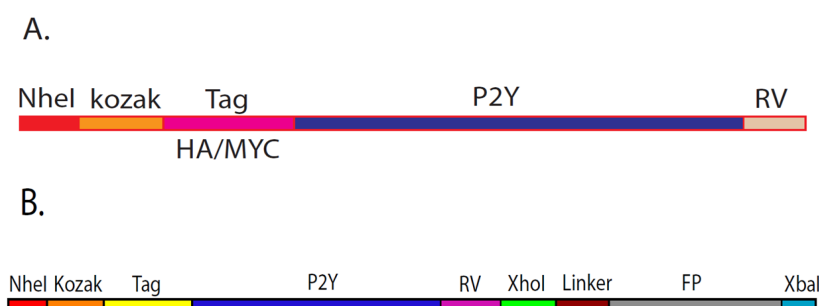


Figure 3.14 Construct layout for P2Y₁ and P2Y₁₁.

A. Construct design for co-immunoprecipitation. B. Construct design for BiFC.

Cesium-chloride gradient large-scale isolation of plasmid DNA was subsequently carried out to amplify Myc-hP2Y₁, following which the purified DNA was digested using EcoRI and EcoRV, respectively, to determine the orientation of Myc-hP2Y₁ insertion into the TOPO vector. Two insertion orientations are possible for Myc-hP2Y₁ due to its asymmetric 5' and 3' ends (NheI and EcoRV, respectively). Since the TOPO vector and construct both harbor an EcoRV recognition site, each orientation imparts a specific EcoRV digestion pattern, as described in Figure 3.15.

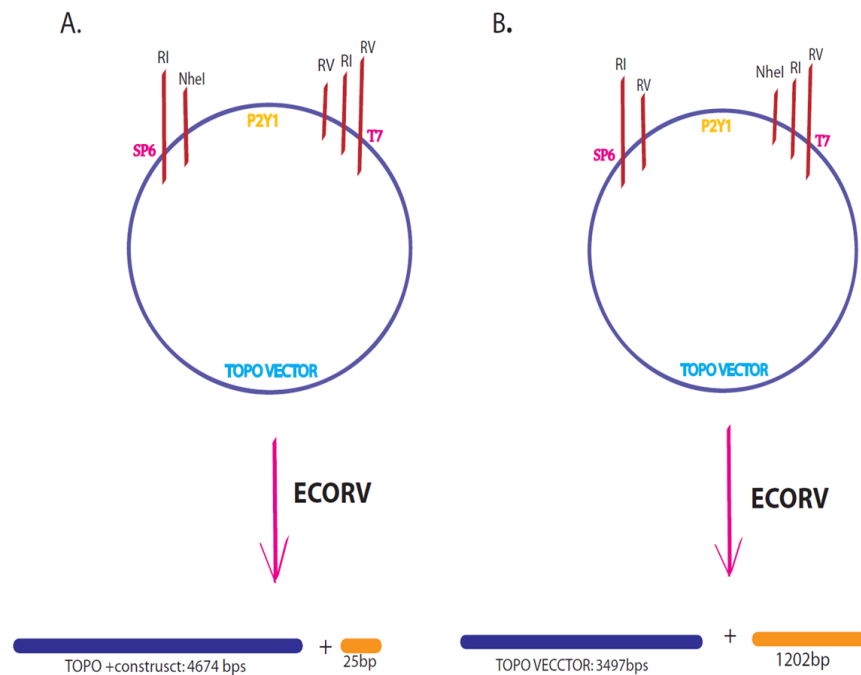
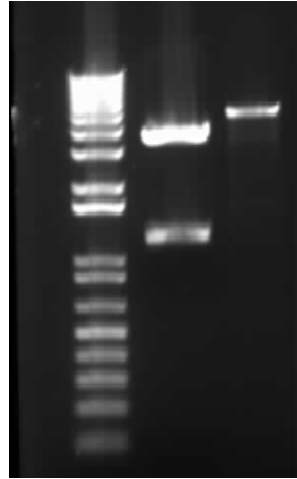


Figure 3.15 Map of EcoRV digestion

A, Clockwise proximal insertion. This orientation places the EcoRV recognition sites of TOPO and Myc-hP2Y₁ in close proximity. Digestion with EcoRV produces one large and one small fragment. The small fragment is 25 bps long and consists of RI-RV recognition sites. The larger fragment includes TOPO and Myc-hP2Y₁ minus the RV-RI-RV digest and is 4674 bps long. *B*. Anticlockwise distal insertion. In this orientation, the RV recognition sites of TOPO and Myc-hP2Y₁ are spaced out; two fragments closely corresponding to TOPO and Myc-hP2Y₁ are generated. The 1202 bps fragment consists of Myc-hP2Y₁ plus the TOPO RI-RV sites. The larger fragment corresponds to TOPO minus RI-RV and is 3497bps long.

Digestion of the purified DNA with EcoRI produced two fragments of expected lengths corresponding to the TOPO vector and Myc-hP2Y₁, respectively. However, digestion with EcoRV resulted in a single band that migrated to approximately 5000 bps. The same pattern was detected upon repetition of the digestion reaction. The digestion products are shown in Figure 3.16. It was concluded that the large band corresponded to the 4674bps TOPO fragment produced when the clockwise proximal Myc-hP2Y₁ insert is digested. To further ascertain that the sequence was ligated into the TOPO vector, the purified DNA product was sequenced. The results corroborated the previous observations and confirmed that Myc-hP2Y₁ insertion was clockwise. Furthermore, a HA-hP2Y₁₁ + stop construct was generated using the same techniques used for Myc-hP2Y₁ + stop. Additionally, two BiFC constructs were designed (Figure 3.14): 1) Myc-hP2Y₁ minus

stop codon conjugated to YFP 1-173 (Myc-hP2Y₁₁-YFP₁₋₁₇₃) and 2) HA-hP2Y₁₁ minus stop codon fused to YFP 156-239 (HA-hP2Y₁₁-YFP₁₅₆₋₂₃₉), but they were not completed.



Lane 1 Lane 2 Lane 3

Figure 3.16 Agarose gel electrophoresis of EcoRI and EcoRV digests

Lane 1 shows the 1KB plus DNA ladder (Invitrogen). Lane 2 shows the EcoRI digestion products. The large band has migrated to around 4000bps and corresponds to the TOPO segment (3495bps). The smaller band has migrated to around 1200bps and corresponds to Myc-hP2Y₁₁ (1204bps). Lane 3 shows the EcoRV digestion product. Only one band is detected. It has migrated to around 5000bps and corresponds to the 4674bps segment generated from digestion of proximal construct insertion.

Chapter 4

Pharmacological Characterization of Recombinant 1321N1-hP2Y₁ and 1321N1-hP2Y₁₁ Cell lines

4.1 Introduction

Chapter 3 described the creation of a recombinant system (CHO-K1-hP2Y₁₁) co-expressing the purine receptors P2Y₁ and P2Y₁₁. Two versions of this system, a clone expressing a high density of P2Y₁₁ (13) and a clone expressing a low density of the receptor (6), were generated and characterized using a set of eight nucleotides and nucleotide derivatives. The aim behind this experimental setup was to determine whether co-expression alters the signalling profiles of the individual receptor subtypes. Three interesting signalling features were observed: 1) both clones 13 and 6 respond to the P2Y₁₁ agonist BzATP; 2) the response to ADP, a P2Y₁ agonist, is biphasic in clone 13 as opposed to clone 6 where it is monophasic, suggesting that two distinct receptor populations might contribute to the response to ADP in clone 13; and, 3) the response to 2meSATP, a P2Y₁ and P2Y₁₁ agonist, is also biphasic in clone 13 but not in clone 6. The changes in the nature of the response to ADP and 2meSATP in the high versus low-expressing clone were detected in the context of an increase in the levels of expression of hP2Y₁₁.

To put the signalling alterations observed in the recombinant CHO-K1-hP2Y₁₁ clones 6 and 13 into perspective, the signalling properties of each of the two receptors co-expressed in CHO-K1-hP2Y₁₁ were studied individually through the creation of a P2Y₁-only cell line and a P2Y₁₁-only cell line, which were characterized using the same set of agonists described in chapter 3. The aim behind this endeavour was to generate a suitable platform for comparing the agonist profiles of the P2Y₁-only, P2Y₁₁-only and P2Y₁+P2Y₁₁ systems to disentangle the components of the biphasic responses detected in clone 13. This could possibly help to answer the question formulated in chapter 3: Does the co-expression of P2Y₁ and P2Y₁₁ result in the formation of novel sites of agonist activity through the formation of complexes containing both receptor subtypes, leading to differences in agonist responses?

4.2 Pharmacological characterization of a recombinant 1321N1-hP2Y₁₁ cell line

1321N1 astrocytoma cells have been shown to signal through cholinergic, muscarinic and P1 receptors but have not been found to express any P2 receptors (212), making them an appropriate null cell line in which to characterize the individual human P2Y₁ and P2Y₁₁ receptors. For the purpose of this study, a recombinant 1321N1 astrocytoma cell line, expressing the gene for the human P2Y₁₁ receptor (GenBank accession number AF030335), that had previously been studied in the laboratory, was provided by Dr. Andrea Townsend-Nicholson.

4.2.1 Calcium response of 1321N1-hP2Y₁₁ to carbachol

The calcium response of the 1321N1 cell line to carbachol, which is mediated by the endogenously expressed muscarinic M3 receptor, has been widely investigated and documented in the literature (213-220). In order to compare the activity of nucleotide agonists in the recombinant 1321N1-hP2Y₁₁ cell line, these cells were subjected to increasing concentrations of carbachol, ranging from 1mM to 100nM (log value: -3 to -7) at physiological temperature (37°C). Non-linear regression analysis using a comparison of two different equations (three-parameter equation versus variable slope, or four-parameter, equation) was performed to determine the most suitable fit for the obtained carbachol data. As Figure 4.1 shows, the response to carbachol was sigmoidal and evolved from its minimum to its maximum over three log units of agonist concentration, namely 360nM to 360μM (log value: -6.5 to -3.5). The preferred mathematical fit for this data is the three parameter equation, which generates a sigmoidal monophasic curve with a Hill slope of 1. The average maximal value elicited by the carbachol agonist is 0.81 ± 0.07 (F/F₀) at 360μM carbachol. The average EC₅₀ and pEC₅₀ values for the carbachol response in the studied 1321N1-hP2Y₁₁ cell line are $2.9 \pm 0.5\mu\text{M}$ and 5.54, respectively. Given the potency of the endogenous muscarinic response in 1321N1-hP2Y₁₁ cells, carbachol was employed as the control against which the calcium responses to the studied nucleotide and nucleotide derivatives in the 1321N1-hP2Y₁₁ cell line were normalized.

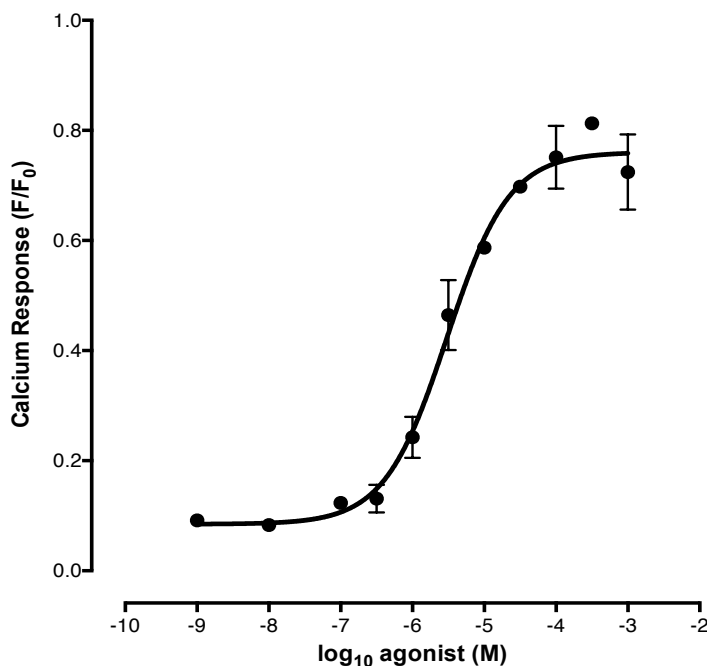


Figure 4.1 Concentration-response curve elicited by carbachol in 1321N-hP2Y₁₁

The calcium response to increasing concentrations of carbachol was determined at 37°C in 1321N1-hP2Y₁₁ cells. The results are expressed as the average \pm s.e.m of three independent experiments, each performed in triplicate. The calculated EC₅₀ value for carbachol in this cell line is $2.9 \pm 0.5 \mu\text{M}$ ($\text{pEC}_{50} = 5.55$).

4.2.2 Functional investigation of the activity of nucleotide and nucleotide derivatives in 13211N-hP2Y₁₁

As was mentioned in the chapter's introduction, the aim behind the pharmacological characterization of the 1321N1-hP2Y₁₁ cell line was to determine the signalling profile of hP2Y₁₁ receptor expressed in a background devoid of endogenous P2 responses, with the aim of comparing its measured calcium responses to the distinctive calcium profile observed in clone 13. Hence, 1321N1-hP2Y₁₁ was tested using the same set of eight nucleotides and nucleotide derivatives described in Chapter 3.

The first set of ligands tested consisted of four potent P2Y₁₁ agonists, namely BzATP, ATP γ S, ATP and $\alpha\beta\text{meATP}$. Figure 4.2 shows the mean calcium response of the 1321N1-hP2Y₁₁ cell line following the addition of BzATP, ATP γ S, ATP and $\alpha\beta\text{meATP}$ at 37°C. The larger errors observed at some concentrations (around 13% of the calcium response) are caused by the variability in the maxima of the responses obtained between independent experiments. Figure 4.3 shows the degree of error obtained from a

representative experiment. Agonists were applied at increasing concentrations ranging from 100nM to 1mM (log value: -7 to -3) or 10nM to 1mM (log value: -8 to -3) depending on the lowest concentration at which a calcium response was obtained. The response curves of the four agonists were generated through non-linear regression analysis using a comparison of two fits (three parameter versus variable slope, or four parameter, equation). As figures 4.2 and 4.3 reveal, all four tested agonists produced sigmoidal monophasic curves with a single EC₅₀ value.

The concentration-response curve of BzATP, which represents the average of four independent experiments, and that of ATP γ S, which represents the average of three independent experiments, follow a similar pattern of calcium fluorescence. Both curves progress from their minimum to maximum responses over three log units of agonist concentration, ranging from 100nM to 100 μ M agonist (log value: -7 to -4). On the other hand, the ATP curve is shifted to the right of the BzATP and ATP γ S curves and, unlike these two agonists, ATP achieves its minimum to maximum response over two log units of agonist concentration, i.e. 1 μ M to 100 μ M agonist (log value: -6 to -4). The concentration-response curve of $\alpha\beta$ meATP is shifted to the right of the three previously described curves (BzATP, ATP γ S and ATP). It is distinctive in that the minimum response begins at 3.16 μ M and reaches a maximum at 1mM (log value: -5.5 to -3) following a steep increase.

Nonlinear regression analysis shows that the preferred model with which to fit the BzATP, ATP γ S, ATP and $\alpha\beta$ meATP data in 1321N1-hP2Y₁₁ is the simpler model, or three parameter equation, which assumes a Hill slope of 1. The EC₅₀ values for these four agonists are $3.1 \pm 0.26\mu\text{M}$, $3.2 \pm 0.26\mu\text{M}$, $9 \pm 1.4\mu\text{M}$ and $71 \pm 11.5\mu\text{M}$, respectively. The maximum calcium response to BzATP, ATP γ S, ATP and $\alpha\beta$ meATP relative to the 1mM carbachol control is $101 \pm 16\%$, $92 \pm 13\%$, $87 \pm 14\%$ and $98.6 \pm 12\%$, respectively. One-way ANOVA analysis shows that although maxima vary between trials on different calcium assay plates, there is no statistically significant difference between the maxima of the tested agonists relative to the carbachol control ($p = 0.90$) within one experimental setup (same assay plate).

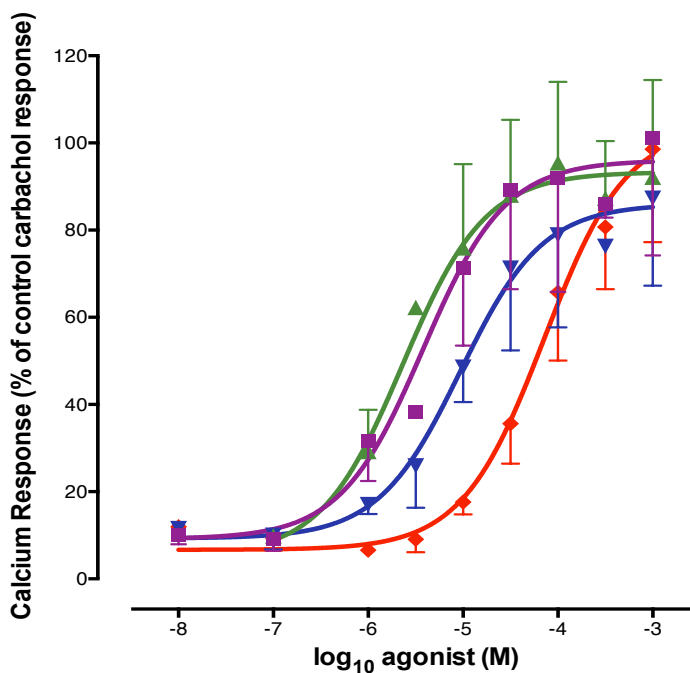


Figure 4.2 Concentration-response curves for BzATP, ATP γ S, ATP and $\alpha\beta$ meATP on Ca²⁺ mobilization in 1321N1-hP2Y₁₁

The calcium response elicited by increasing concentrations of BzATP (■), ATP γ S (▲), ATP (▼) and $\alpha\beta$ meATP (◆) was determined at 37°C in 1321N1-hP2Y₁₁ cells. The results represent the average \pm s.e.m of three independent experiments, each performed in triplicate, and are expressed as a percentage of the response of 1321N1-hP2Y₁₁ to 1mM carbachol.

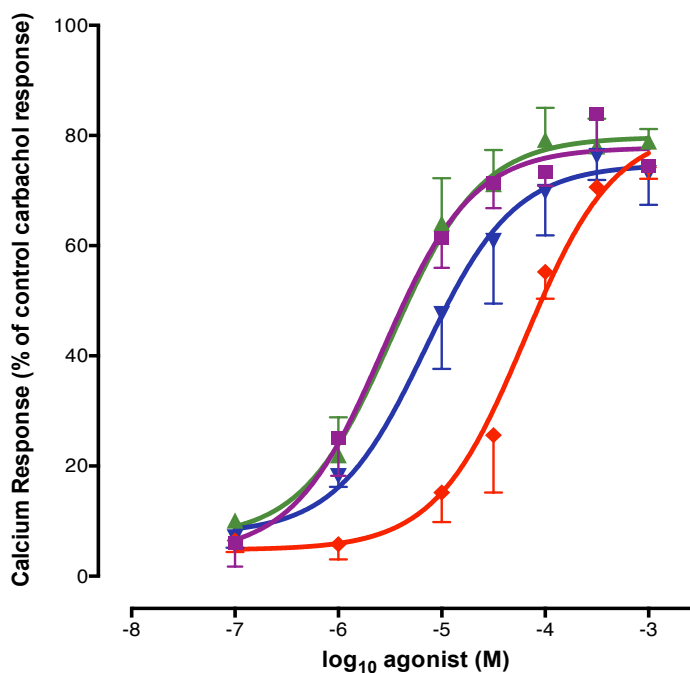


Figure 4.3 Representative concentration-response curves for BzATP, ATP γ S, ATP and $\alpha\beta$ meATP on Ca²⁺ mobilization in 1321N1-hP2Y₁₁

The calcium response elicited by increasing concentrations of BzATP (■), ATP γ S (▲), ATP (▼) and $\alpha\beta$ meATP (◆) was determined at 37°C in 1321N1-hP2Y₁₁ cells. The results represent the average \pm s.e.m of one independent experiment performed in triplicate, and are expressed as a percentage of the response of 1321N1-hP2Y₁₁ to 1mM carbachol.

To complete the pharmacological study of the hP2Y₁₁ receptor expressed in 1321N1 cells, the recombinant cell line was characterized using ADP, $\beta\gamma$ meATP, 2meSATP and UTP. Figure 4.4 presents a comparison of the maximum calcium responses evoked by the naturally occurring nucleotides ATP and ADP, the nucleotide derivatives BzATP and 2meSATP and the muscarinic control carbachol over a period of 180 seconds in the studied cell line. As the graph demonstrates, the potent P2Y₁₁ agonist BzATP produced the highest increase in calcium fluorescence in 1321N1-hP2Y₁₁ cells. The nucleotide ADP, on the other hand, failed to induce a significant increase in calcium fluorescence in P2Y₁₁-only cells as compared to the other illustrated agonists.

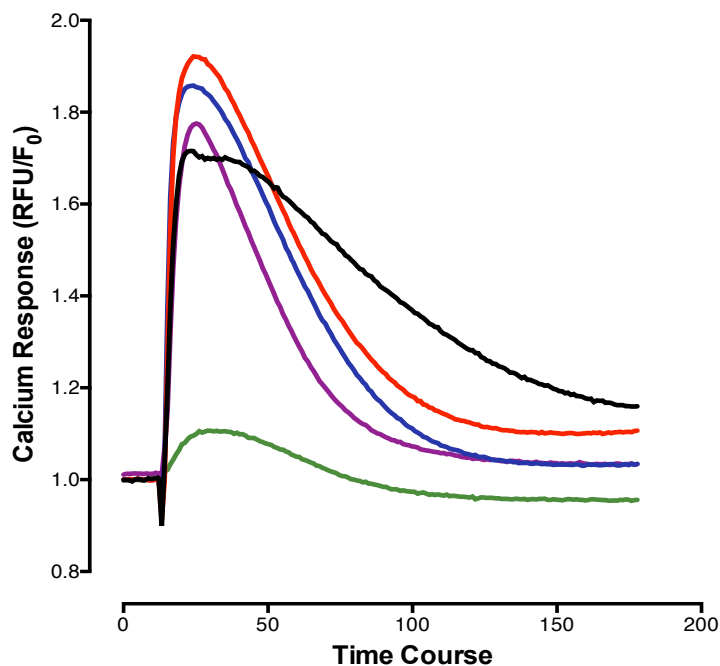


Figure 4.4 Comparison of the maximum responses of five tested agonists as a function of time in 1321N1-hP2Y₁₁ cells

The maximum responses of BzATP, ATP, 2meSATP, ADP and the muscarinic control carbachol over a time course of 180 seconds are shown. The maximum response to BzATP (red), ATP (navy) and ADP (green) was reached at 316 μ M (log value: -3.5) agonist whereas the maximum response to 2meSATP (purple) occurred at 100 μ M (log value: -4) agonist. The maximum response to the carbachol control was achieved at 100 μ M (log value: -4) agonist and is shown in black. The nucleotide derivative BzATP elicited the highest increase in calcium fluorescence in 1321N1-hP2Y₁₁ cells whereas the naturally occurring nucleotide ADP produced the smallest response.

Figure 4.5 shows representative calcium curves for ADP, UTP, 2meSATP and β ymeATP. In contrast to previous ligands, the average response curves for this particular set of agonists were not displayed because the errors on the 2meSATP and β ymeATP curves are substantial (up to 46%) due to variability in the detected maxima of the responses across experimental repeats.

ADP, UTP and 2meSATP were introduced at increasing concentrations ranging from 100nM to 1mM (log value: -7 to -3), while β ymeATP was added at concentrations ranging from 100nM to 316 μ M (log value: -7 to -3.5). Non-linear regression analysis using a comparison of two fits (three parameter versus variable slope, or four parameter, equation) was performed to determine the best mathematical fit for each of the studied ligands. As figure 4.5 shows, the calcium responses to the P2Y₁ and P2Y₁₁ agonist

2meSATP and the P2Y₁₁ agonist $\beta\gamma$ meATP were sigmoidal monophasic and were best fit using the simpler model, or three parameter equation. These curves achieved their plateaus over three log units of agonist concentration, ranging from 1 μ M to 316 μ M agonist (log value: -6 to -3.5). The calculated average (all trials included) EC₅₀ values for 2meSATP and $\beta\gamma$ meATP are 10.5 \pm 2.5 μ M and 64 \pm 19 μ M, respectively, and the average maximum calcium responses (all trials included) are expressed as 108 \pm 42% and 87 \pm 6% of the response to 1mM carbachol, respectively. Using unpaired t-test analysis, there was no statistically significant difference between the average maximal responses calculated for 2meSATP and $\beta\gamma$ meATP (p value=0.73). Furthermore, comprehensive one-way ANOVA analysis showed no statistically significant difference between the maxima of all six agonists (BzATP, ATP γ S, ATP, $\alpha\beta$ meATP, 2meSATP and $\beta\gamma$ meATP) relative to 1mM carbachol (p=0.985).

In contrast, non-linear regression was unable to fit a curve to the calcium data for ADP and UTP. In fact, UTP failed to increase calcium fluorescence in 1321N1-hP2Y₁₁, resulting in a response that did not depart from baseline calcium level. ADP, on the other hand, induced a concentration-dependent response but only at concentrations above 100 μ M with a maximum response at 316 μ M (log value: -3.5), the highest concentration tested. This maximum constituted 25 \pm 1.6% relative to 1mM carbachol. For visualization purposes, the concentration-curves of UTP and ADP were represented using a dotted connecting line.

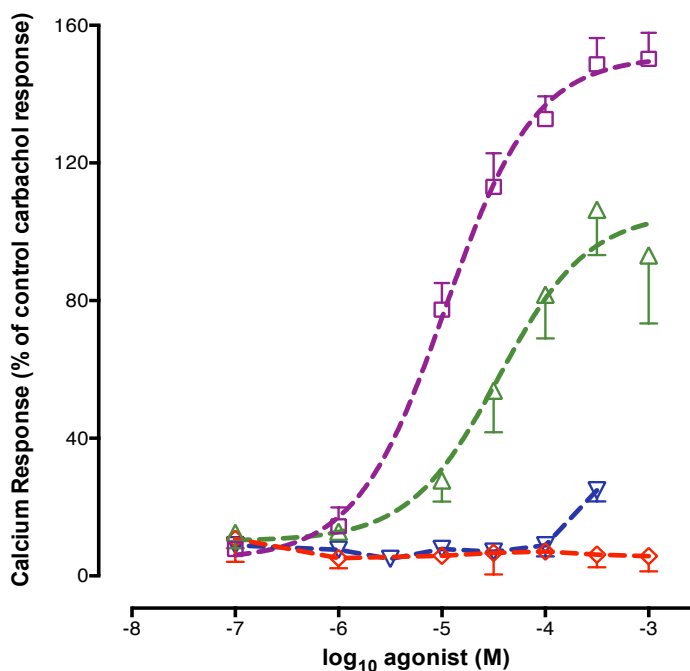


Figure 4.5 Representative concentration-response curves for ADP, UTP, 2meSATP and βγmeATP on Ca²⁺ mobilization in 1321N1-hP2Y₁₁

The calcium response to increasing concentrations of ADP (▽), UTP (◇), 2meSATP (□) and βγmeATP (△) was determined at 37°C in 1321N1-hP2Y₁₁ cells. The results represent the average ± s.e.m of a single representative experiment performed in quadruplicate and are expressed as a percentage of the response of 1321N1-hP2Y₁₁ cells to 1mM carbachol.

4.2.3 Antagonist studies in 1321N1-hP2Y₁₁

NF 340 is a highly selective P2Y₁₁ antagonist that has been reported to function as a competitive inhibitor of ATPγS (221). To investigate the inhibitory potency of this drug in 1321N1-hP2Y₁₁ cells, the response to a fixed concentration of BzATP, namely 10μM (log value: -5), was tested in the presence of increasing concentrations of NF 340, ranging from 1nM to 100μM (log value: -9 to -4), at 37°C. Figure 4.6 delineates the progress of the concentration-inhibition response exerted by NF 340 over a time course of 180 seconds. As the displayed traces show, high concentrations of the antagonist, i.e. 100μM and 10μM (log value: -4 and -5), suppress the response of hP2Y₁₁ to its agonist BzATP (10μM, log value: -5) as compared to the calcium response exhibited by the same concentration of agonist in the absence of NF 340 (control shown in black on the graph). The calcium response to 10μM BzATP is first recovered at 1μM NF 340 (log value: -6) and is fully restored at NF 340 concentrations between 10nM to 0.1nM (log value: -8 to -10).

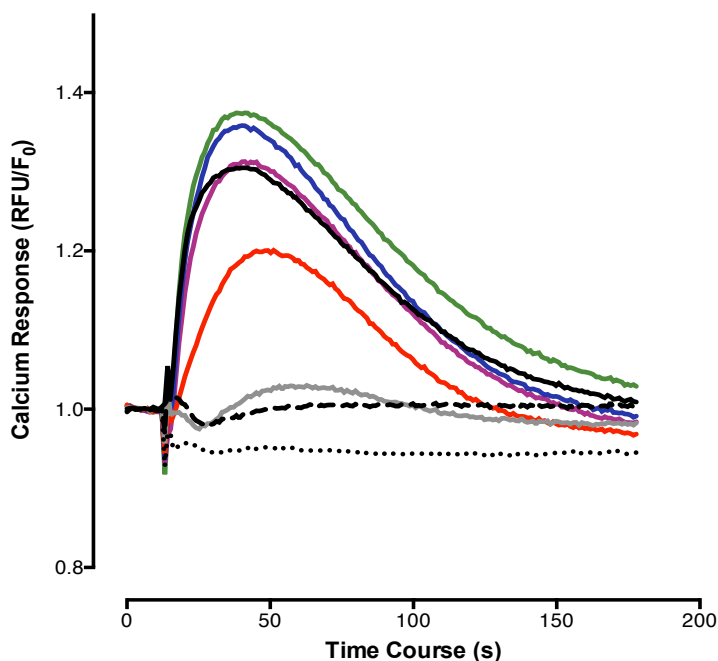


Figure 4.6 NF 340 inhibits the response to 10 μ M BzATP in a time-dependent fashion

The effect of increasing concentrations of NF 340, a P2Y₁₁ antagonist, on the response elicited by 10 μ M BzATP was assessed over time in 1321N1-hP2Y₁₁. The log₁₀ concentrations of NF 340 used were: -4 (····), -5 (---), -6 (grey), -7 (red), -8 (navy), -9 (purple) and -10 (green). The calcium fluorescence trace elicited by the 10 μ M BzATP control is shown (black). The traces represent the mean calcium response obtained from one independent experiment performed in quadruplicate, divided by the baseline fluorescence measured prior to the introduction of ligand at t=10 seconds. The results are expressed as RFU/F₀. Error bars have been omitted to permit a better visualization of the responses.

The NF 340 inhibition experiment was completed in nine different trials, each performed in quadruplicate. Figure 4.7 shows the mean inhibition response for NF 340 in 1321N1-hP2Y₁₁, obtained from six independent trials. The last three trials were omitted due to variability in the maxima of the calcium responses. The collected data were first analysed through non-linear regression analysis using a comparison of two equations (log (inhibition) three parameters versus log (inhibition) variable slope or four parameters) followed by Leff's null method, as refined by Lazareno and Birdsall (222, 223), to determine the K_B value. The resulting curve is monophasic sigmoidal and goes from its minimum to its maximum value over three log units of antagonist concentration, 10 μ M to 10nM (log value: -5 to -8). The maximum response constitutes 102 \pm 8% of the response to 1mM carbachol and is reached at 1nM NF 340 (log value: -9). One-way ANOVA analysis indicates that there is no statistically significant difference between the calcium response to the 10 μ M BzATP control and the responses to 10 μ M BzATP in the presence

of 10nM and 1nM NF 340 (log value: -8 and -9; p value= 0.95). The mean IC₅₀ value for NF 340 in 1321N1-hP2Y₁₁ cells is 261 ± 29.6 nM, the mean pIC₅₀ value is 6.6 ± 0.05 and the K_B is 156 ± 18 nM.

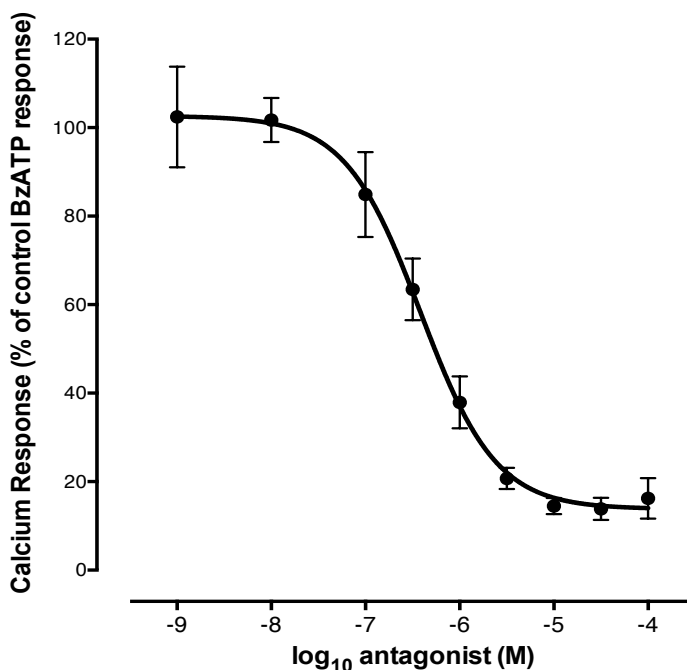


Figure 4.7 NF 340 inhibits the response to 10μM BzATP in 1321N1-hP2Y₁₁ cells

The effect of increasing concentrations of NF 340, a P2Y₁₁ antagonist, on the calcium response to 10μM BzATP at 37°C in 1321N-hP2Y₁₁ was tested. The curve represents the average ± s.e.m of six independent experiments, each performed in quadruplicate. The results are expressed as a percentage of the response to 10μM BzATP.

4.3 Pharmacological characterization of a recombinant 1321N1-hP2Y₁ cell line

In order to gain insights about the pharmacological signature of the P2Y₁ receptor when expressed individually, a recombinant 1321N1-P2Y₁ cell line was created and examined with the same set of agonists employed to study of 1321N-hP2Y₁₁. The construct used to generate the recombinant cell line was provided by Dr. Andrea Townsend-Nicholson and comprised the cDNA sequence of the human P2Y₁ receptor cloned between the HindIII and XbaI sites of the pcDNA3 vector. A batch of 1321N1 cells was stably transfected with the human P2Y₁ cDNA construct, following which the stably transfected cell line was selected using the antibiotic Geneticin.

4.3.1 Calcium response of 1321N1-hP2Y₁ to carbachol

The newly created cell line was first assayed using carbachol to verify the endogenous muscarinic response of 1321N1-hP2Y₁. Increasing concentrations of agonist ranging from 1mM to 1nM (log value: -3 to -9) were applied at physiological temperature (37°C). Non-linear regression analysis using a comparison of two different equations (three parameter equation versus variable slope, or four parameter, equation) was subsequently performed to determine the best model with which to fit the obtained carbachol data. Figure 4.8 shows the average calcium response curve of 1321N1-hP2Y₁ cells following carbachol addition. The data was best fit using the three parameter equation, resulting in a sigmoidal curve that progressed from its minimum to its maximum over three log units of agonist concentration, ranging from 100nM to 31.6μM (log value: -7 to -4.5). The average maximal response elicited by carbachol is 1.38 ± 0.07 (F/F₀), achieved at 360μM (log value: -3.5) carbachol. The average EC₅₀ value for carbachol in 1321N1-hP2Y₁ is 688 ± 120 nM and the average pEC₅₀ value is 6.17.

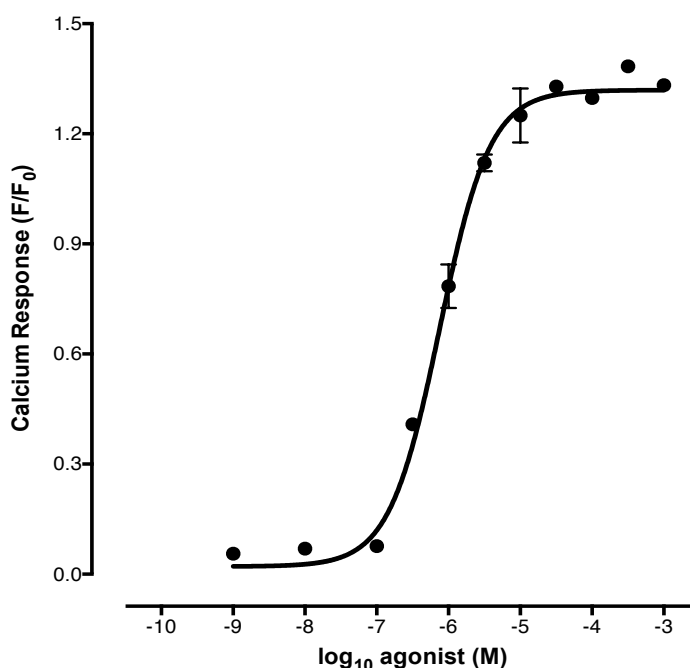


Figure 4.8 Concentration-response curve elicited by carbachol in 1321N-hP2Y₁

The calcium response to increasing concentrations of carbachol was determined at 37°C in 1321N1-hP2Y₁ cells. The results are expressed as the average \pm s.e.m of three independent experiments, each performed in quadruplicate.

4.3.2 Functional investigation of the activity of nucleotide and nucleotide derivatives in 13211N-hP2Y₁

A pharmacological characterization of the P2Y₁ receptor expressed in isolation in 1321N1 cells was performed using the 1321N1-hP2Y₁ cell line that was generated as described in section 4.2. The fluorescence data gathered for BzATP, UTP, $\alpha\beta$ meATP and $\beta\gamma$ meATP was mathematically analysed through non-linear regression using a comparison of two equations (three parameter equation versus variable slope, or four parameter, equation). Figure 4.9 shows the mean calcium response of the four agonists, obtained from one representative trial. No further experimental repeats were performed for these agonists as all ligands except UTP failed to produce a curve, indicating that these nucleotide derivatives are not active at the P2Y₁ receptor. Although the Prism software was able to fit a curve to the BzATP, $\alpha\beta$ meATP and $\beta\gamma$ meATP data according to the simple model, or three parameter equation, statistical analysis of these data revealed that this mathematical fit is ambiguous and not applicable. For instance, one-way ANOVA analysis of the calcium response (n=3) to BzATP shows that there is no statistically significant difference (p= 0.0745) between all seven concentrations of agonist tested (100 μ M to 10nM, log value: -4 to -8). Similarly, the calcium responses to the tested $\beta\gamma$ meATP concentrations were not statistically significantly different (p= 0.3867) using one-way ANOVA analysis.

Given the ambiguity of the BzATP, $\alpha\beta$ meATP and $\beta\gamma$ meATP data, it was not possible to calculate EC₅₀ and pEC₅₀ values for these agonists. In contrast, non-linear regression analysis of the UTP data resulted in a sigmoidal monophasic curve that was best fit using the three parameter equation. The resulting curve progressed from its minimum to its maximum over one log unit of agonist concentration, i.e. 100nM to 1 μ M (log value: -7 to -6) agonist. It achieved its maximum value, namely 32.6 \pm 0.5% relative to 1mM carbachol, at 100 μ M (-4) UTP and had an EC₅₀ of 382nM and a pEC₅₀ value of 6.41.

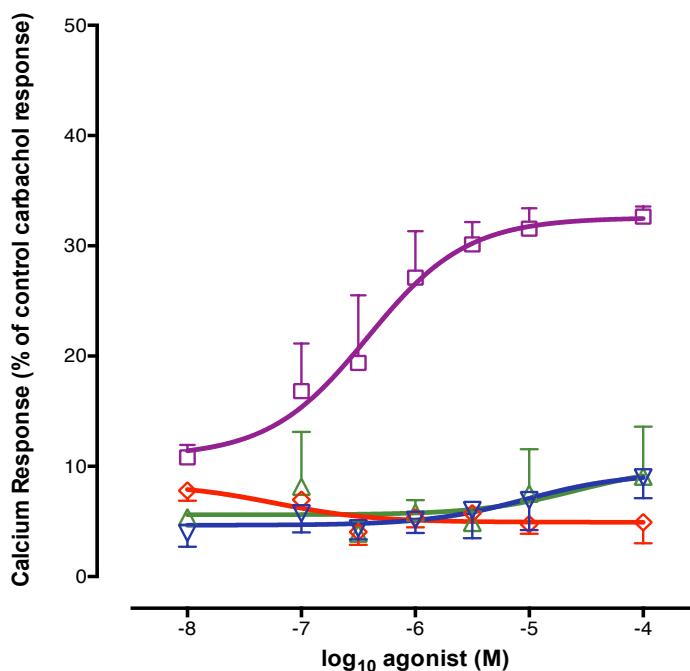


Figure 4.9 Concentration-response curves for BzATP, UTP, αβmeATP and βmeATP in 1321N1-hP2Y₁ cells

The calcium response to increasing concentrations of BzATP (▽), UTP (□), αβmeATP (◇) and βmeATP (△) was determined at 37°C in 1321N1-hP2Y₁ cells. The results represent the average ± s.e.m of one independent experiment performed in triplicate, and are expressed as a percentage of the response of 1321N1-hP2Y₁ cells to 1mM carbachol.

The second set of experiments studied the calcium responses to agonists with known activity at P2Y₁, namely ADP, 2meSATP, ATP and ATP_γS. Figure 4.10 displays a visual comparison between the maximum responses to ADP, ATP, 2meSATP, BzATP and the carbachol control over a time course of 180 seconds in 1321N1-hP2Y₁ cells. As the graph shows, the muscarinic carbachol control elicited the highest increase in calcium fluorescence in this cell line. Among the studied purinergic receptor agonists, the potent P2Y₁ agonist ADP evoked the highest peak in calcium fluorescence detected. The potent P2Y₁₁ agonist BzATP, on the other hand, failed to produce a significant rise in calcium levels relative to the measured baseline fluorescence.

The mean calcium response curves for ADP, 2meSATP, ATP and ATP_γS in the recombinant 1321N1-hP2Y₁ cell line are shown in Figure 4.11. The concentrations of ADP and 2meSATP used went from 10μM to 10pM (log value: -5 to -11). ATP was added at concentrations ranging from 100μM to 0.1nM (log value: -4 to -10) whereas ATP_γS concentrations ranged from 10μM to 0.1nM (log value: -5 to -9). The agonist data

was subjected to non-linear regression analysis using a comparison of two equations (three parameter versus four parameter, or variable slope, equation) to determine the best fit for each agonist. The calcium curves of all four ligands achieved their plateaus over three log units of agonist concentration, ranging from 0.1nM to 100nM (log value: -10 to -7) for ADP and 2meSATP, 10nM to 10 μ M (log value: -8 to -5) for ATP and to 100 μ M (log value: -9 to -6) for ATP γ S.

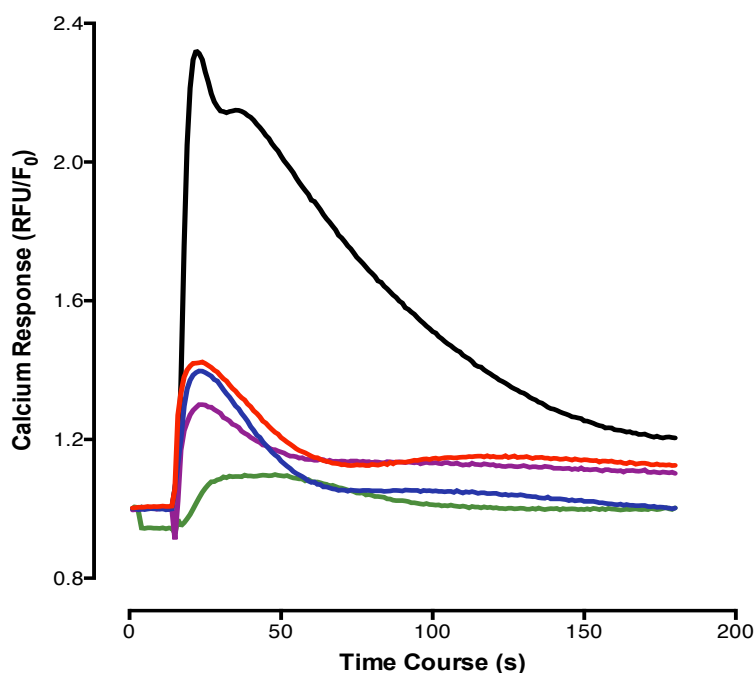


Figure 4.10 Comparison of the maximum responses of five tested agonists as a function of time in 1321N1-hP2Y₁ cells

The maximum responses of BzATP, ATP, 2meSATP, ADP and the muscarinic control carbachol over a period of 180 seconds are shown. The maximum calcium response occurred at 100 μ M (log value: -4) for ATP (purple) and BzATP (green), 10 μ M (log value: -5) for ADP (red) and 100nM (log value: -7) for 2meSATP (navy). The maximum response to the carbachol control was achieved at 100 μ M (log value: -4) agonist and is shown in black. The naturally occurring nucleotide ADP elicited the highest increase in calcium fluorescence in 1321N1-hP2Y₁ cells whereas the nucleotide derivative BzATP produced the smallest fluorescence trace.

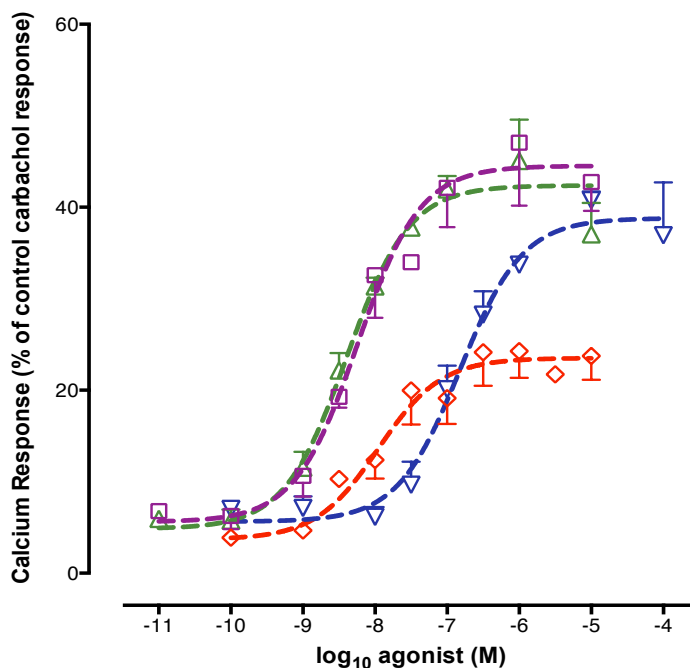


Figure 4.11 Concentration-response curves for ADP, 2meSATP, ATP and ATP γ S in 1321N1-hP2Y₁ cells

The calcium response to increasing concentrations of ADP (\square), 2meSATP (\triangle), ATP (∇) and ATP γ S (\diamond) was determined at 37°C in 1321N1-hP2Y₁ cells. The results represent the average \pm s.e.m of three independent experiments, each performed in triplicate, and are expressed as a percentage of the response of 1321N1-hP2Y₁ cells to 1mM carbachol.

The calcium responses to ADP, 2meSATP, ATP and ATP γ S were best fit using the simpler model, or three parameter equation, which resulted in monophasic sigmoidal curves for all four agonists. The maximum response to ADP occurred at 1 μ M (-6) agonist and constituted $47 \pm 4\%$ of the response to the 1mM carbachol control. The mean EC₅₀ value calculated for ADP is 5.8 ± 1 nM. The nucleotide derivative 2meSATP elicited its maximum response, i.e. $45 \pm 2.6\%$ relative to 1mM, at 1 μ M (-6) agonist and has a mean EC₅₀ value of 4.7 ± 1.3 nM. The maximum response to ATP is 40.8 ± 0.7 of the response to 1mM carbachol, reached at 10 μ M (-5) agonist and the mean EC₅₀ value for this nucleotide is 151 ± 40 nM. The agonist ATP γ S produced its maximum response, i.e. $24.3 \pm 1.7\%$ relative to 1mM carbachol, at 100 μ M (-4) agonist and has a mean EC₅₀ value of 15.6 ± 3.6 nM. Using one-way ANOVA analysis, there was no statistically significant difference between the mean maximum responses, relative to 1mM carbachol control, for the agonists ADP, 2meSATP and ATP ($p=0.1842$). However, ANOVA analysis revealed that there is a statistically significant difference between the maximum responses to these three ligands compared to the maximum response elicited by ATP γ S (**, $p=0.0015$).

4.3.3 Antagonist studies in 1321N1-hP2Y₁

Having determined the agonist profile of the receptor, an investigation of its antagonist profile was carried out. This was achieved using three antagonists: an established P2Y₁ antagonist, MRS 2179 (151), the P2Y-selective antagonist and ecto-nucleotidase inhibitor Reactive Red (224) and a P2Y₁₁ selective antagonist, NF 340 (221). The antagonist studies were conducted in the form of IC₅₀ inhibition curves where increasing concentrations of antagonist were added to a fixed concentration of agonist. ADP was selected as the agonist of choice for these experiments given its potency in activating P2Y₁ and the fact that it resulted in a biphasic response in the recombinant CHO-K1-hP2Y₁₁ clone 13.

The first ligand to be investigated was the P2Y₁ inhibitor, MRS 2179. The antagonist was added at increasing concentrations ranging from 1mM to 1nM (log value: -3 to -9) to a fixed concentration of agonist, 1μM ADP (log value: -6), which corresponds to the concentration at which the maximum response to ADP is observed, as described in section 4.3.2. MRS 2179 exerted a concentration-dependent inhibitory action against the ADP response in 1321N1-hP2Y₁. Figure 4.12 shows a representative time course of this inhibitory activity over a period of 180 seconds. As the traces reveal, higher concentrations of antagonist, namely 1mM and 316μM (log value: -3 and -3.5) completely block the response to ADP, suppressing it to baseline level. The effect of the antagonist on the ADP response subsides starting from 100μM MRS 2179 (-4) as the calcium fluorescence elicited by the agonist progressively increases. The ADP response is 93% of the control response to 1μM ADP (measured in the absence of antagonist) at the lowest concentration of antagonist tested, i.e. 100nM (log value: -7) MRS 2179.

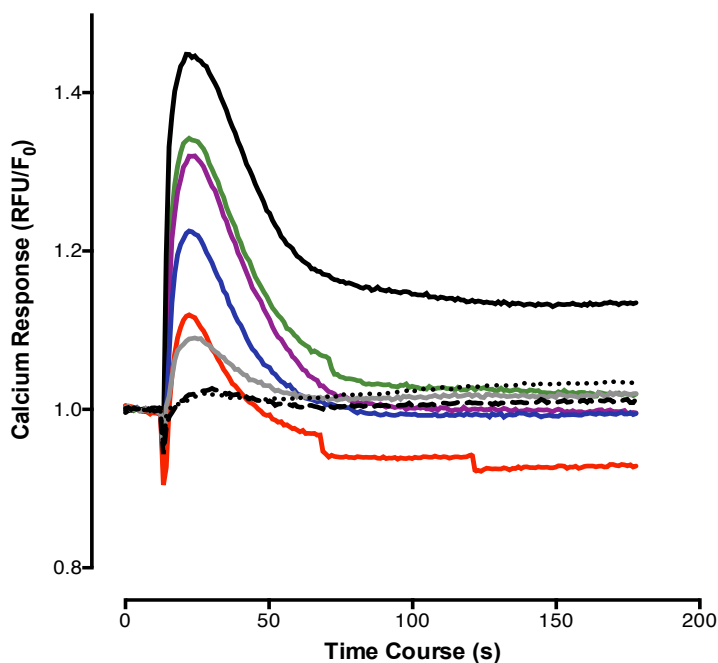


Figure 4.12 Time dependence of the response to ADP in the presence of MRS 2179 in 1321N1-hP2Y₁ cells

The effect of increasing concentrations of MRS 2179, a P2Y₁ antagonist, on the response elicited by 1 μM ADP was assessed over time in 1321N1-hP2Y₁ cells. The log₁₀ concentrations of MRS 2179 used were: -3 (···), -3.5 (---), -4 (grey), -4.5 (red), -5 (navy), -6 (purple) and -7 (green). The calcium fluorescence elicited by the 1 μM ADP control is shown (—). The traces represent the mean calcium response obtained from one independent experiment performed in triplicate, divided by the baseline fluorescence measured prior to the introduction of ligand at t=10 seconds. The results are expressed as RFU/F₀. Error bars have been omitted to permit a better visualization of the responses.

The MRS 2179 data, obtained from four independent trials, were normalized against the response to the 1 μM ADP (-6) control and analysed using non-linear regression and Leff's null method. A comparison of two inhibitory dose-response models, namely the log (inhibitor) three parameter equation versus the log (inhibitor) four parameter, or variable slope, equation was performed. The preferred model for all four trials was the simpler model, or three parameter equation. Figure 4.13 shows the mean IC₅₀ inhibition curve for MRS 2179 in 1321N1-hP2Y₁ cells. The depressive action exerted by the antagonist on the response to 1 μM ADP was concentration dependent and occurred over five log units of antagonist concentration, i.e. 1 mM to 10 nM (log value: -3 to -8) MRS 2179. The average maximum response to ADP in the presence of MRS 2179 was measured at 10 nM (-8) antagonist. The mean IC₅₀ value for MRS 2179 in 1321N1-hP2Y₁ cells is 22 ± 3 μM, the mean pIC₅₀ is 4.68 ± 0.07 and the K_B is 124 ± 17 nM.

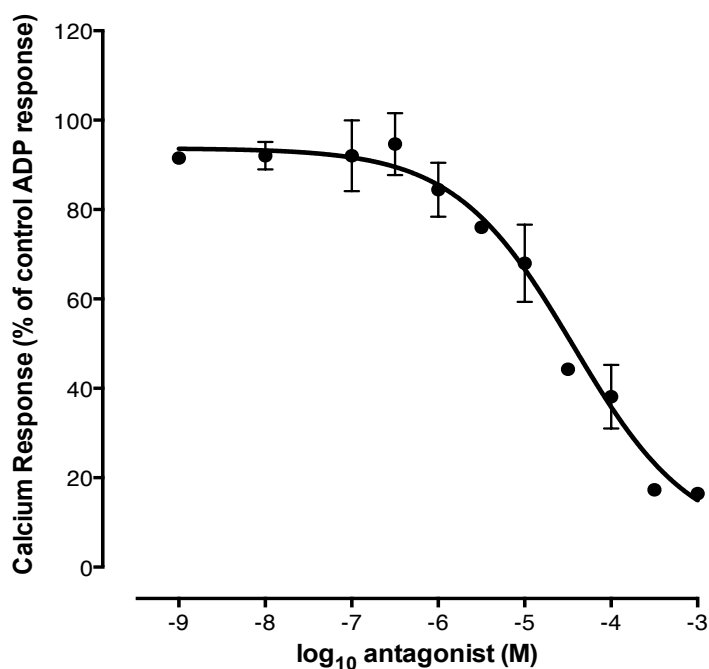


Figure 4.13 MRS 2179 inhibits the response to 1 μ M ADP in 1321N-hP2Y₁

The effect of increasing concentrations of MRS 2179, a P2Y₁ antagonist, on the calcium response to 1 μ M ADP was tested at 37°C in 1321N1-hP2Y₁. The curve represents the average \pm s.e.m of four independent experiments, performed in triplicate or quadruplicate. The results are expressed as a percentage of the response to the 1 μ M ADP control.

The next antagonist to be investigated was Reactive Red, which was added to 1 μ M ADP at increasing concentrations ranging from 100 μ M to 10nM (log value: -4 to -8). Figure 4.14 displays a time course of the response to 1 μ M ADP in the presence of Reactive Red. As the figure shows, Reactive Red failed to alter the response to ADP at concentrations between 10 μ M and 10nM (log value: -5 to -8) but provoked a decline in calcium fluorescence at the higher concentrations of Reactive Red tested, i.e 31.6 μ M and 100 μ M (log value: -4 and -4.5). The data was further evaluated using non-linear regression analysis through a comparison of two equations (log (inhibitor) three parameter equation versus log (inhibitor) four parameter, or variable slope, equation). Figure 4.15 shows the mean IC₅₀ inhibition curve for Reactive Red in 1321N1-hP2Y₁. Analysis revealed that both fits were ambiguous and it was not possible to calculate an IC₅₀ value for the Reactive Red data in 1321N1-hP2Y₁.

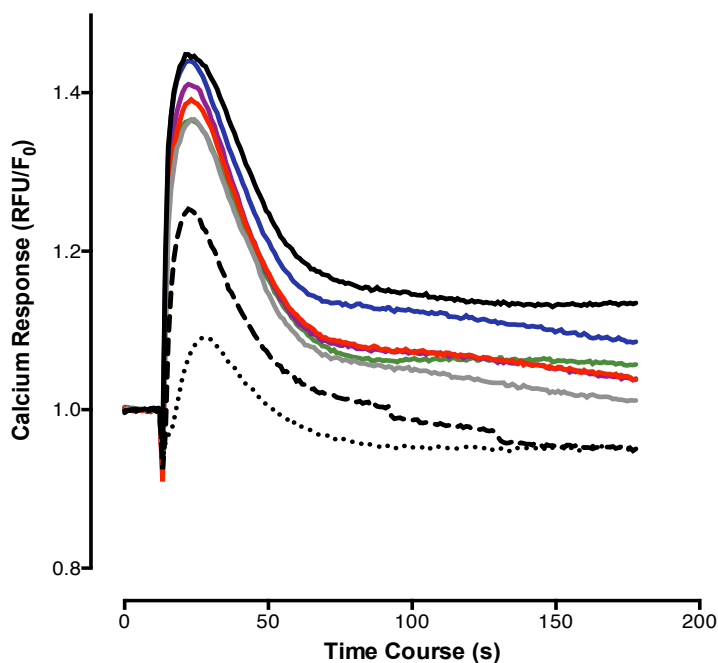


Figure 4.14 Time dependence of the response to ADP in the presence of Reactive Red in 1321N1-hP2Y₁ cells

The effect of increasing concentrations of Reactive Red, a P2Y selective inhibitor, on the calcium response to 1 μ M ADP was assessed over time in 1321N1-hP2Y₁ cells. The log₁₀ concentrations of Reactive Red used were: -4 (···), -4.5 (- -), -5 (grey), -5.5 (red), -6 (navy), -7 (purple) and -8 (green). The calcium fluorescence elicited by the 1 μ M ADP control is also shown (—). The traces represent the mean calcium response obtained from one independent experiment performed in triplicate, divided by the baseline fluorescence measured prior to the introduction of ligand at t=10 seconds. The results are expressed as RFU/F₀. Error bars have been omitted to permit a better visualization of the responses.

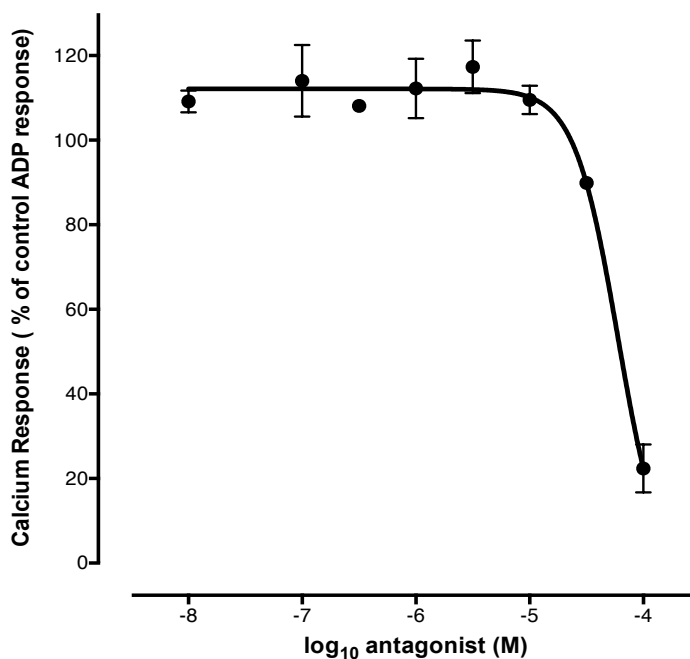


Figure 4.15 The calcium response to ADP in the presence of Reactive Red in 1321N1-P2Y₁

The effect of increasing concentrations of Reactive Red, a P2Y selective antagonist, on the calcium response to 1 μ M ADP was tested at 37°C in 1321N-hP2Y₁ cells. The curve represents the average \pm s.e.m of four independent experiments, each performed in triplicate. The results are expressed as a percentage of the response to 1 μ M ADP.

The last ligand to be tested was the P2Y₁₁ selective inhibitor NF 340, which was added to 1 μ M ADP at increasing concentrations ranging from 100 μ M to 0.1nM (log value: -4 to -10). Figure 4.16 shows a representative time course of the response to ADP in the presence of NF 340 in 1321N1-hP2Y₁ cells. As the graph reveals, none of the tested concentrations of antagonist were able to alter the level of calcium fluorescence elicited by 1 μ M ADP. Non-linear regression analysis using a comparison of the log (inhibitor) three parameter equation versus the log (inhibitor) four parameter, or variable slope, equation was also performed and the mean IC₅₀ inhibition curve is shown in Figure 4.17. Both models were ambiguous and failed to fit a curve to the measured data.

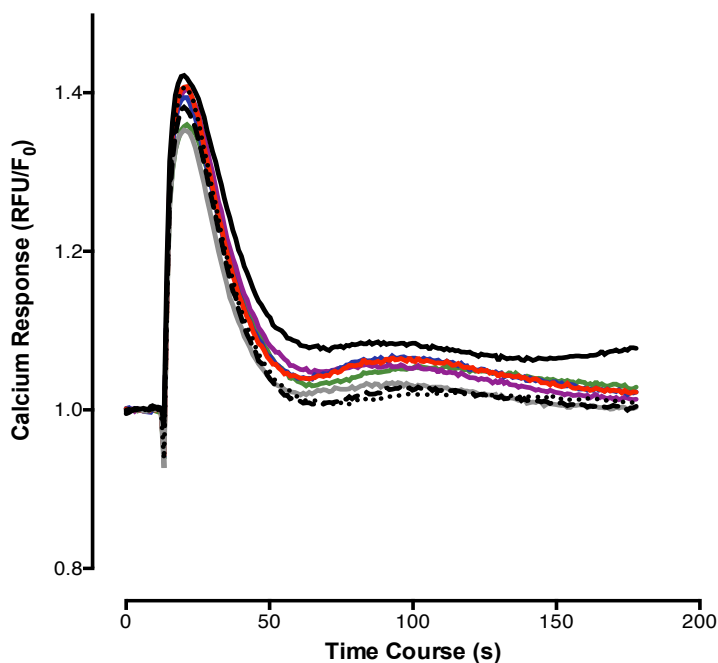


Figure 4.16 Time dependence of the calcium response to ADP in the presence of NF 340 in 1321N1-hP2Y₁ cells

The effect of increasing concentrations of NF 340, a P2Y₁₁ antagonist, on the response to 1 μ M ADP was investigated over time in 1321N1-hP2Y₁ cells. The log₁₀ concentrations of NF 340 used were: -4 (---), -4.5 (- -), -5 (grey), -5.5 (red), -6 (navy), -7 (purple) and -8 (green). The calcium fluorescence elicited by the 1 μ M ADP control is also shown (—). The traces represent the mean calcium response obtained from one independent experiment performed in triplicate, divided by the baseline fluorescence measured prior to the introduction of ligand at t=10 seconds. The results are expressed as RFU/F₀. Error bars have been omitted to permit a better visualization of the responses.

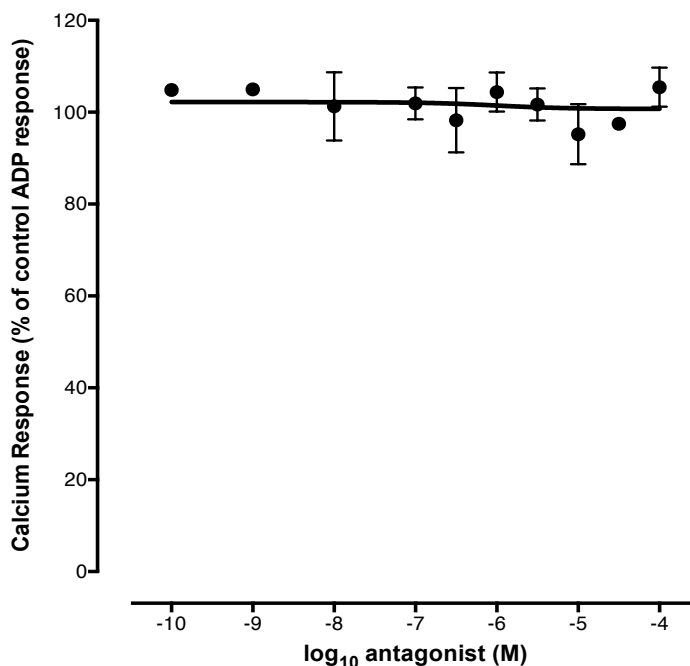


Figure 4.17 NF 340 does not inhibit the response to 1 μ M ADP in 1321N1-P2Y₁

The effect of increasing concentrations of NF 340, a P2Y₁₁ antagonist, on the calcium response to 1 μ M ADP was tested at 37°C in 1321N-hP2Y₁. The curve represents the average \pm s.e.m of four independent experiments, each performed in triplicate. The results are expressed as a percentage of the response to the 1 μ M ADP control. One-way ANOVA analysis shows that none of the increasing concentrations of NF 340 has an effect on the response to 1 μ M ADP.

4.4 Conclusion

In this chapter, two distinct systems, 1321N1-hP2Y₁ and 1321N1-hP2Y₁₁, were characterized. Table 4.1 shows the average EC₅₀ and pEC₅₀ values measured for eight different nucleotides and nucleotide derivatives and carbachol in both cell lines. 1321N1-hP2Y₁ cells were activated by five out of eight tested nucleotide analogues, namely ADP, 2meSATP, ATP γ S, ATP and UTP, but did not respond to the P2Y₁₁ agonists BzATP, $\alpha\beta$ meATP and $\beta\gamma$ meATP. The rank order of agonist potency in 1321N1-hP2Y₁ is:

2meSATP (8.33) \approx ADP (8.24) > ATP γ S (7.81) > ATP (6.82) > UTP (6.41) > carbachol (6.17).

1321N1-hP2Y₁₁ cells responded to six out of eight tested ligands, including BzATP, $\alpha\beta$ meATP, $\beta\gamma$ meATP, ATP, ATP γ S and 2meSATP. ADP and UTP, on the other hand, failed to elicit a response in these cells. The rank order of agonist potency in 1321N1-hP2Y₁₁ is:

Carbachol (5.54) \approx BzATP (5.51) \approx ATP γ S (5.50) > ATP (5.05) \approx 2mesATP (4.98) > $\beta\gamma$ meATP (4.19) \approx $\alpha\beta$ meATP (4.15)

To formulate a comparative rank order of agonist potencies in 1321N1-hP2Y₁ versus 1321N1-hP2Y₁₁, the mean EC₅₀ value of each agonist was divided by the mean EC₅₀ value for 2meSATP in each cell line (ratios shown in Table 4.2). 2meSATP was chosen as the control ligand against which agonist potencies were normalized because it activates both P2Y₁ and P2Y₁₁ receptors and was found to elicit a biphasic response in clone 13.

Agonist	EC ₅₀ (nM \pm s.e.m.)		pEC ₅₀	
	1321N1-P2Y ₁	1321N1-P2Y ₁₁	1321N1-P2Y ₁	1321N1-P2Y ₁₁
ADP	5.8 \pm 1.0	ND	8.24	ND
ATP	151 \pm 40	9000 \pm 1400	6.82	5.05
UTP	382	ND	6.41	ND
2meSATP	4.7 \pm 1.3	10500 \pm 2500	8.33	4.98
$\alpha\beta$ meATP	ND	70800 \pm 11500	ND	4.15
$\beta\gamma$ meATP	ND	64000 \pm 19000	ND	4.19
ATP γ S	15.6 \pm 3.6	3200 \pm 260	7.81	5.50
BzATP	ND	3100 \pm 260	ND	5.51
Carbachol	672 \pm 154	2900 \pm 500	6.17	5.54

Table 4.1 The calcium response elicited by nucleotide analogues and carbachol in 1321N1-hP2Y₁₁ and 1321N1-hP2Y₁ cells

The EC₅₀ and pEC₅₀ values of a set of seven nucleotide analogues and carbachol were determined in 1321N1-hP2Y₁ and 1321N1-hP2Y₁₁ cells. The results are expressed as the mean EC₅₀ and the mean pEC₅₀ of three independent experiments, each performed in triplicate. The ND sign (not determined) refers to agonists that failed to elicit a significant calcium response and for which it was not possible to determine an EC₅₀ or pEC₅₀ value.

The rank order of agonist potencies in 1321N1-hP2Y₁ cells using the mean EC₅₀ of 2meSATP as a reference is

2meSATP (1) > ADP (1.23) > ATP γ S (3.32) > ATP (32) > UTP (81) > carbachol (142)

where 2meSATP = 1.0, >1 = less potency and <1 = greater potency than the reference ligand. The rank order of agonist potencies in 1321N1-hP2Y₁₁ cells using 2meSATP as a reference is:

Carbachol (0.28) > BzATP (0.3) = ATP γ S (0.3) > ATP (0.86) > 2meSATP (1) > $\beta\gamma$ meATP (6.1) > $\alpha\beta$ meATP (6.74)

where 2meSATP = 1.0, >1 = less potency and <1 = greater potency than the reference ligand.

Agonists	Ratio	
	1321N1-P2Y ₁	1321N1- P2Y ₁₁
ADP	1.23	ND
ATP	32	0.86
UTP	81	ND
2meSATP	1	1
$\alpha\beta$ meATP	ND	6.74
$\beta\gamma$ meATP	ND	6.1
ATP γ S	3.32	0.3
BzATP	ND	0.3
carbachol	142	0.28

Table 4.2 Comparison of agonist potencies of the calcium response in 1321N1-hP2Y₁ and 1321N1-hP2Y₁₁

The ratio of the mean EC₅₀ of each of the tested agonists was divided by the mean EC₅₀ of 2meSATP in both 1321N1-hP2Y₁ and 1321N1-hP2Y₁₁. 2meSATP was chosen as the reference agonist because it acts on both P2Y₁ and P2Y₁₁ receptors thus allowing a comparison of potencies in the two cell lines. The ND sign (not determined) refers to agonists that failed to elicit a significant calcium response and for which it was not possible to determine a ratio.

Figures 4.18 and 4.19 offer a visual comparison between the calcium response curves for the eight nucleotides and nucleotide derivatives tested in 1321N1-hP2Y₁ versus 1321N1-hP2Y₁₁. As the graphs show, the calcium responses of the agonists achieved higher maxima relative to carbachol control in 1321N1-hP2Y₁₁ cells as opposed to 1321N1-hP2Y₁ cells and one-way ANOVA analysis confirms that they are statistically significant different (****; $p < 0.0001$). In contrast, calcium response curves in 1321N1-hP2Y₁ cells were shifted to the left as compared to 1321N1-hP2Y₁₁, signifying that the agonists were more potent in the Y₁-only as opposed to the Y₁₁-only cells.

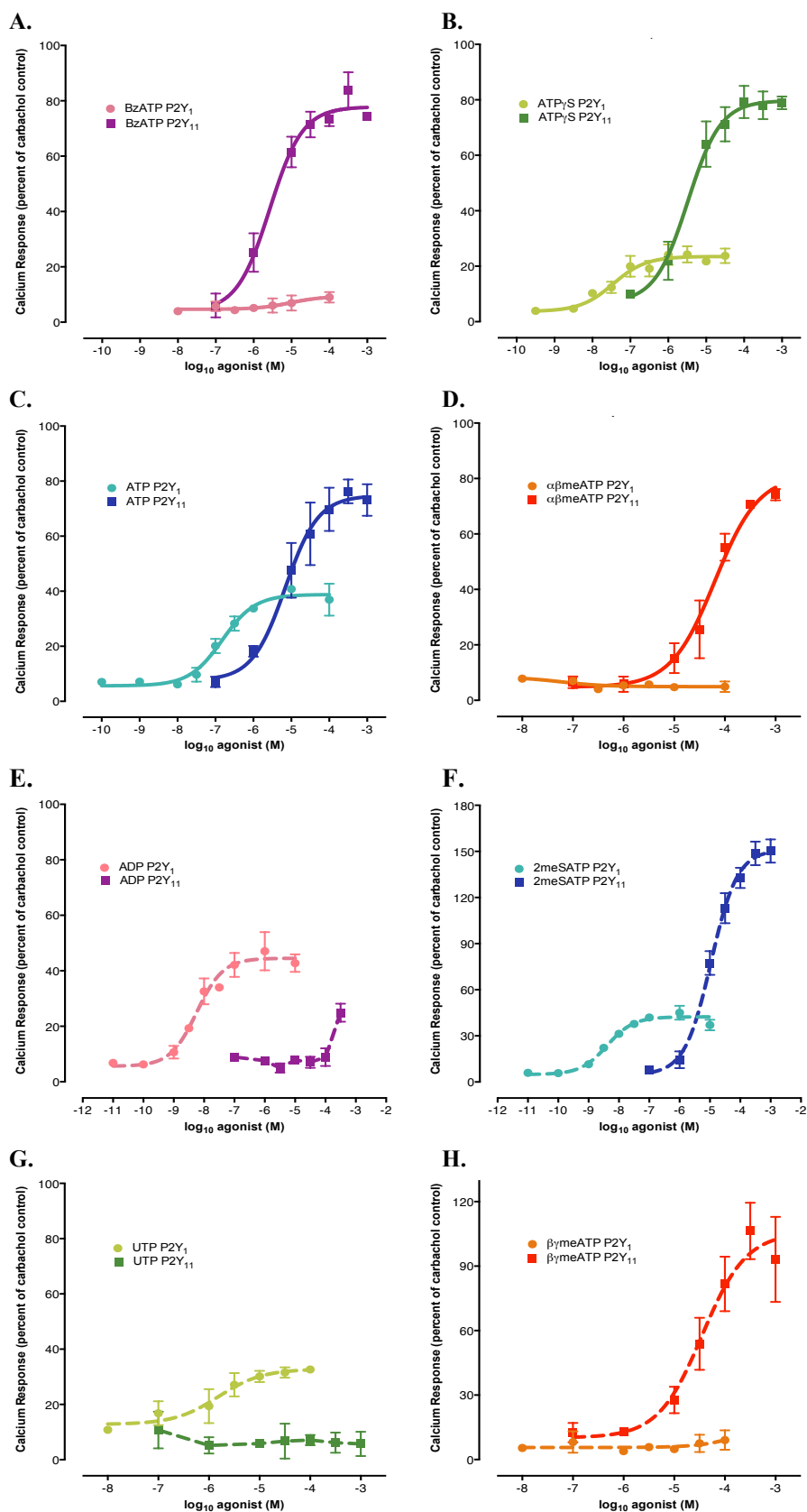


Figure 4.18 Visualization of differences in agonist responses in 1321N1-hP2Y₁₁ and 1321N1-hP2Y₁

The calcium responses of 1321N1-hP2Y₁ and 1321N1-hP2Y₁₁ to each of the eight tested agonists are shown on a single graph to allow comparison of the functional responses in each recombinant cell line. A) BzATP; B) ATP_γS; C) ATP; D) αβmeATP; E) ADP; F) UTP; G) 2meSATP and H) βγmeATP.

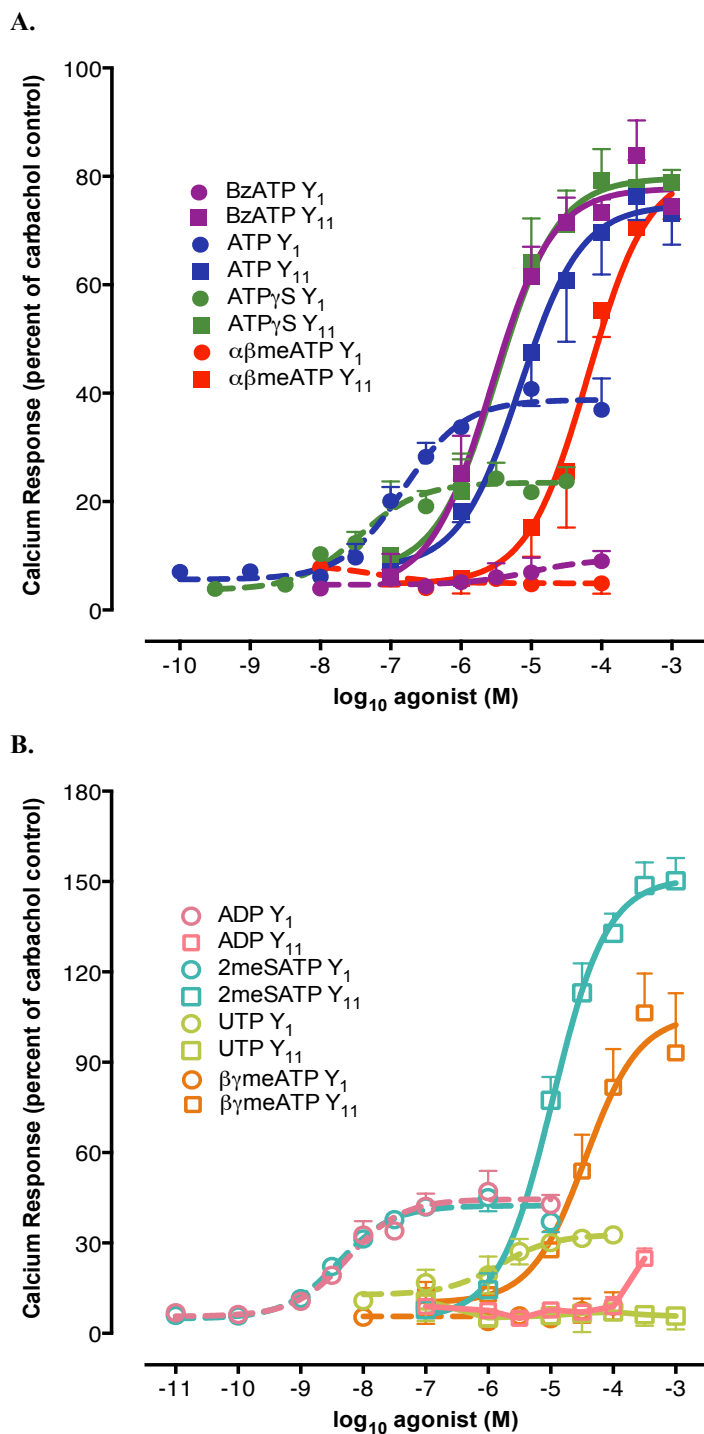


Figure 4.19 Comparison of agonist responses in 1321N1-hP2Y₁ and 1321N1-hP2Y₁₁

The calcium responses of 1321N1-hP2Y₁ and 1321N-hP2Y₁₁ to two distinct sets of agonists are shown on two different graphs to allow comparison of the functional responses in the Y₁-only cell line versus the Y₁₁-only cell line. **A.** BzATP, ATP_γS, ATP and αβmeATP; **B.** ADP, UTP, 2meSATP and βγmeATP.

In conclusion, the detailed pharmacological investigation of 1321N1-hP2Y₁ and 1321N1-hP2Y₁₁ reveals that ADP activates 1321N1-hP2Y₁ cells only while BzATP activates 1321N1-hP2Y₁₁ cells only when the receptor subtypes are expressed in a null system. In contrast, 2meSATP acts at both hP2Y₁ and hP2Y₁₁ but has greater potency at the hP2Y₁ receptor as compared to hP2Y₁₁. Finally, ATP and ATP γ S activate both receptors with a similar order of potency.

Inhibition studies were subsequently performed in both cell lines to identify antagonists for each receptor. For instance, the calcium response of 1321N1-hP2Y₁ cells to ADP was tested in the presence of three ligands, the P2Y₁ antagonist MRS 2179, the P2Y₁₁ antagonist NF 340 and Reactive Red. As was expected, MRS 2179 competitively inhibited the ADP response in these cells whereas NF 340 failed to antagonise it. Reactive Red reduced this response at concentrations above 10 μ M only. In 1321N1-hP2Y₁₁ cells, NF 340 inhibited the calcium response to BzATP, thus confirming that it is an antagonist of P2Y₁₁. Data published by King and Townsend-Nicholson state that reactive Red is another competitive inhibitor of this receptor while MRS 2179 does not inhibit it (174). Table 4.3 displays the IC₅₀ and pIC₅₀ values for the three described antagonists in 1321N1-hP2Y₁ versus 1321N1-hP2Y₁₁ cells. The results presented in this chapter will be of assistance in analysing the biphasic response to ADP and 2meSATP in clone 13 described in chapter 3.

Antagonist	IC ₅₀ (μ M \pm s.e.m.)		pIC ₅₀	
	1321N1-P2Y ₁	1321N1-P2Y ₁₁	1321N1-P2Y ₁	1321N1-P2Y ₁₁
MRS 2179	17.4 \pm 3.6	ND	4.8	ND
Reactive Red	ND	ND	ND	ND
NF 340	ND	0.28 \pm 0.05	ND	6.62

Table 4.3 The activity of antagonists in 1321N1-hP2Y₁ versus 1321N1-hP2Y₁₁ cells

This table shows the IC₅₀ and pIC₅₀ values for three antagonists in hP2Y₁-only versus hP2Y₁₁-only cells. The P2Y₁ antagonist, MRS 2179, behaves as a competitive inhibitor of hP2Y₁ in 1321N1-hP2Y₁ cells but does not affect hP2Y₁₁ activity in 1321N1-hP2Y₁₁ cells. The P2Y₁₁ antagonist NF 340 is a competitive inhibitor of hP2Y₁₁ but does not alter hP2Y₁ signalling. The P2Y selective antagonist Reactive Red inhibits the calcium response at higher ligand concentrations only in 1321N1-hP2Y₁ cells but is a full inhibitor of hP2Y₁₁ (as described in the literature). The ND sign (not determined) refers to antagonists that failed to inhibit the calcium response and for which it was not possible to determine IC₅₀ and pIC₅₀ values.

Chapter 5

Antagonist Experiments in CHO-K1-hP2Y₁₁ Clone 13

5.1 Introduction

The combined findings from Chapters 3 and 4 illustrate how the calcium responses of hP2Y₁ and hP2Y₁₁ differ in a one receptor only system versus a co-expressing system. The detection of biphasic calcium responses in the P2Y₁+P2Y₁₁ system suggests that co-expression could reconfigure the individual binding affinities of these two purinoceptors, thus creating novel sites of agonist and antagonist sensitivity. To verify this hypothesis and determine whether the biphasic effect is due to agonist binding to two separate populations of receptors with different ADP properties as opposed to two separate sites of the same receptor, a series of antagonist studies were performed in clone 13.

5.2 MRS 2179 Schild experiments in CHO-K1-hP2Y₁₁ clone 13

“An alternative method of estimating antagonistic power is to determine the concentration of B, which alters by a selected proportion (e.g. tenfold) the concentration of A needed to produce a selected effect” (225). In an article entitled “Why the Schild method is better than Schild realised”, David Colquhoun explains that the ‘beauty’ of the Schild experiment is that “the agonist does not appear at all. The nature of the agonist, its concentration, affinity and efficacy are all irrelevant.” Thus, the rightward shift of the concentration-response curve caused by antagonist addition should be the same, independently of the nature of the agonist or amplitude of the response (206). In light of these theoretical predictions, the biphasic concentration-response curve for ADP in clone 13 was tested in the presence of MRS 2179, NF 340 and Reactive Red to determine whether any of these ligands would shift this response to the right. ADP signalling constituted the main focus of these Schild experiments because this P2Y₁ selective ligand induced a biphasic response in clone 13, indicating the possible existence a novel site of agonist activity in the high-expressing clone.

5.2.1 Schild analysis of MRS 2179 activity at the ADP response

Concentration-response curves for increasing concentrations of ADP were generated in the absence and presence of 1µM, 10µM, 100µM and 316µM (log value: -6, -5, -4 and -3.5) MRS 2179. The high and low affinity sites were divided into separate

curves with fixed upper and lower limits, analysed individually using global non-linear regression and summed together to generate the average Schild curves shown in Figure 5.1. The control ADP curve was biphasic and progressed from its minimum to its maximum over four log units of agonist concentration (10nM to 100µM; log value: -8 to -4). The high affinity site occurred between 10nM to 1µM ADP (log value: -8 to -6), while the low affinity site went from 1µM to 100µM (log value: -6 to -4). The maximum response to ADP was observed at 100µM and constituted $92 \pm 3\%$ of the UTP control. Similarly, the ADP response in the presence of 1µM MRS 2179 was biphasic. Its maximum occurred at 100µM agonist and constituted $90.8 \pm 5\%$ of the UTP control.

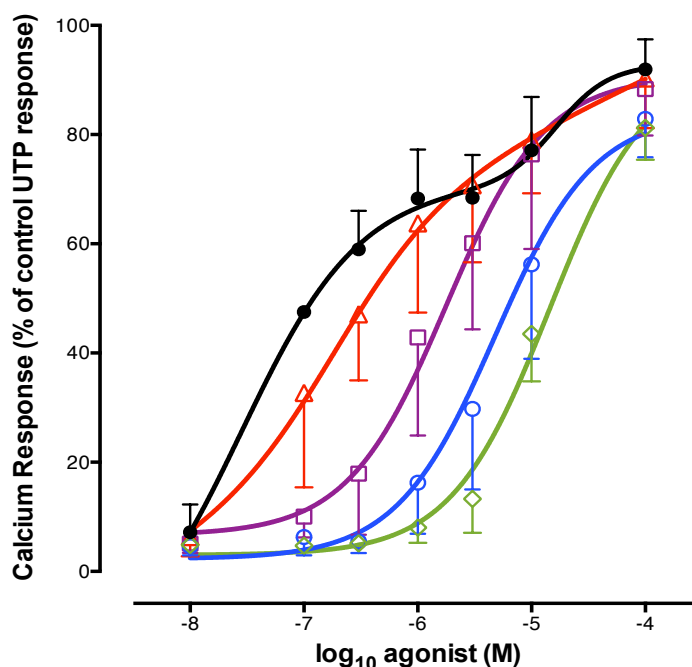


Figure 5.1 The effect of MRS 2179 on the calcium response to ADP in CHO-K1-hP2Y₁₁ clone 13

The response of CHO-K1-hP2Y₁₁ cells to increasing concentrations of ADP was tested in the absence (●) and presence of four different concentrations of the P2Y₁ antagonist MRS 2179: -3.5 (◇), -4 (○), -5 (□) and -6 (△). The results represent the average \pm s.e.m of four independent experiments each performed in triplicate and are expressed as a percentage of the response to 100µM UTP. Increasing concentrations of MRS 2179 caused a rightward shift of the ADP curves without affecting the maximum calcium response of the agonist, thus converting the biphasic response into a monophasic response in the presence of higher concentrations of MRS 2179.

The addition of 10µM MRS 2179 altered the biphasic response to ADP. In fact, it was not possible to fit a curve to the data corresponding to the high affinity site although

the calcium response at the low affinity site was retained. The resulting average curve was monophasic sigmoidal and progressed from its minimum to its maximum over three log units of agonist concentration, i.e. 100nM to 100 μ M (log value: -7 to -4). Its maximum response constituted $89 \pm 4\%$ of the UTP control at 100 μ M ADP. The addition of 100 μ M and 316 μ M MRS 2179 also suppressed agonist activity at the high affinity site and shifted the ADP response to the right of the previous curves. Both data sets generated a monophasic response that progressed from its minimum to its maximum over two log units of agonist concentration, i.e. 1 μ M to 100 μ M (log value: -6 to -4), corresponding to the high affinity site of the control biphasic curve. The average maximum response was $83 \pm 3.5\%$ and $81 \pm 3.4\%$ of the UTP control at 100 μ M ADP, respectively, and was not statistically significantly different from that of previous curves (p value = 0.2737).

The average EC₅₀ values of the ADP curves in the absence and presence of MRS 2179 are listed in Table 5.1. Agonist potencies at the high and low affinity sites of the control ADP curve were statistically significantly different (**; p value = 0.0069). ADP exhibited the same potency at the high affinity sites of the ADP and ADP + 1 μ M MRS 2179 curves (p value = 0.2993) and this site disappeared in the presence of 10, 100 and 316 μ M MRS 2179. Furthermore, the ADP response at the low affinity sites of the biphasic curves was similar to the monophasic ADP response in the presence of higher antagonist concentrations (p value = 0.0546), confirming that MRS 2179 does not inhibit the low affinity site of the response.

Antagonist Concentration	EC ₅₀₋₁ (μ M \pm S.E.M.)	EC ₅₀₋₂ (μ M \pm S.E.M.)	Fraction
ADP	0.028 \pm 0.01	16.7 \pm 3.3	0.55 \pm 0.20
ADP + 1 μ M MRS 2179	0.18 \pm 1.3	1.7 \pm 0.7	0.62 \pm 0.07
ADP + 10 μ M MRS 2179	ND	1.8 \pm 0.6	ND
ADP + 100 μ M MRS 2179	ND	4.8 \pm 1.6	ND

Table 5.1 The EC₅₀ shift of the calcium response to ADP in the presence of increasing concentrations of MRS 2179 in CHO-K1-hP2Y₁₁ clone 13

The EC₅₀ values for ADP concentration-response curves in the absence and presence of three different dilutions of MRS 2179 were calculated in CHO-K1-hP2Y₁₁ clone 13. The fractions of the biphasic curves, showing the contribution of the high affinity site to the response, are also shown. The results represent the average \pm s.e.m of four independent experiments, each performed in triplicate. ND (not determined) refers to replicates for which a value could not be determined.

To determine the nature of the antagonism exerted by MRS 2179 against ADP, the Schild curves were globally fit using the Gaddum/Schild EC₅₀ shift equation. Figure 5.2 shows the rightward shift of the ADP curves in the absence and presence of increasing concentrations of MRS 2179 in clone 13. The mean Schild slope of the curves, which measures how well the rightward shifts concord with the “prediction of competitive antagonism” (Prism Software Help), was 0.8 ± 0.08 . The mean K_B value for MRS 2179 was $0.5 \pm 0.2 \mu\text{M}$ and the mean pA₂ was 6.4 ± 0.2 . To further ascertain the extent of the shift produced by MRS 2179 against ADP, the dose ratios for antagonist concentrations 316 μM , 100 μM , 10 μM and 1 μM (log values: -3.5, -4, -5 and -6) were manually calculated and plotted using linear regression analysis. The data formed a straight line with a mean slope of 0.87 ± 0.13 , and the Schild plot is shown in figure 5.3. These results suggest that the antagonism exerted by MRS 2179 against ADP is competitive.

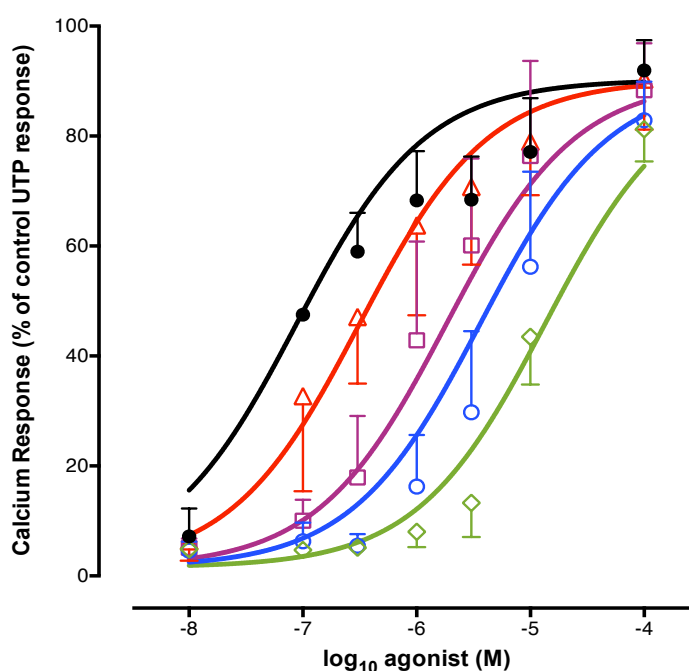


Figure 5.2 EC₅₀ Shift of the MRS 2179 and ADP Schild in CHO-K1-hP2Y₁₁ clone 13

The EC₅₀ shift of the calcium response to ADP in the presence of MRS 2179 was analyzed using the Gaddum equation in CHO-K1-hP2Y₁₁ clone 13. The log₁₀ concentrations of MRS 2179 used were: -3.5 (\diamond), -4 (\circ), -5 (\square) and -6 (\triangle). The results represent the average \pm s.e.m of four independent experiments each performed in triplicate and are expressed as a percentage of the response to 100 μM UTP.

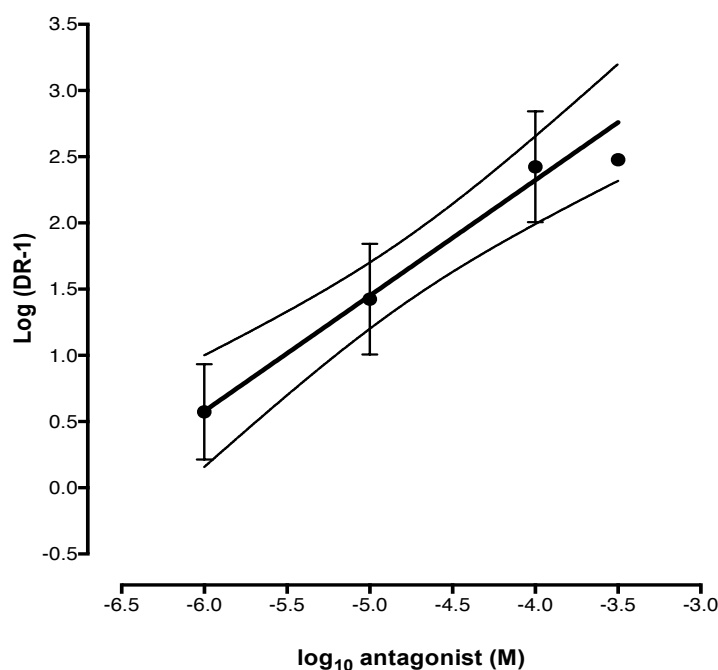


Figure 5.3 Schild plot for MRS 2179 against ADP in clone 13

The dose ratios for MRS 2179 concentrations 316 μ M, 100 μ M, 10 μ M and 1 μ M (log values: -3.5, -4, -5 and -6) tested against ADP were calculated manually and analysed using linear regression. The plotted values fell into a straight line with a slope of 0.87 ± 0.13 , indicating that MRS 2179 is a competitive antagonist of ADP. The results represent the average \pm s.e.m of four independent experiments, each performed in triplicate. The 95% confidence interval of the fit is represented by dotted lines.

5.2.2 Schild analysis of MRS 2179 activity at the 2meSATP response

To determine the effect of MRS 2179 on the biphasic response to 2meSATP, concentration-response curves were generated in the absence and presence of increasing antagonist concentrations, ranging from 1 μ M to 100 μ M (log value: -6 to -4). The data were analysed as per section 5.2.1. and the average Schild curves are shown in Figure 5.4. The control 2meSATP response was biphasic and progressed from its minimum to its maximum over four log units of agonist concentration, i.e. 10nM to 100 μ M (log value: -8 to -4), for all trials. The high affinity site ranged from 100nM to 1 μ M (log value: -8 to -6) while the low affinity response occurred from 1 μ M to 100 μ M (log value: -6 to -4) agonist. The maximum ADP response occurred at 100 μ M (log value: -4) and constituted $94 \pm 4\%$ of response to 100 μ M UTP control. The 2meSATP response in the presence of 1 μ M MRS 2179 (log value: -6) was also biphasic.

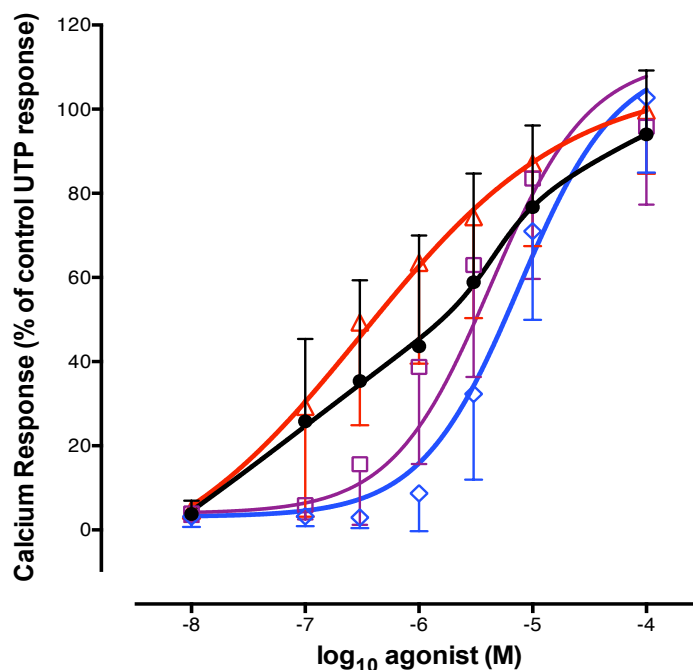


Figure 5.4 The effect of MRS 2179 on the calcium response to 2meSATP in CHO-K1-hP2Y₁₁ clone 13

The response of CHO-K1-hP2Y₁₁ cells to increasing concentrations of the P2Y₁ and P2Y₁₁ agonist 2meSATP was tested in the absence (●) and presence of three different concentrations of MRS 2179: -4 (◇), -5 (□) and -6 (▲). The results represent the average \pm s.e.m of six independent experiments each performed in triplicate and are expressed as a percentage of the response to 100 μ M UTP.

The addition of 10 μ M MRS 2179 altered the biphasic response to 2meSATP in clone 13. Non-linear regression failed to fit the data corresponding to the low affinity site. The resulting curve was monophasic sigmoidal with a maximum response of $95.8 \pm 4.8\%$ relative to the UTP control at 100 μ M 2meSATP. The highest concentration of antagonist tested, i.e. 100 μ M MRS 2179, also inhibited the low affinity site of the biphasic curve and resulted in a monophasic ADP response with a maximum of $102.7 \pm 5\%$ relative to the UTP control at 100 μ M 2meSATP.

The EC₅₀ values for 2meSATP in the presence and absence of MRS 2179 are shown in Table 5.2. The 2meSATP potencies were distinct at the high versus low affinity sites of the control 2meSATP (**; p value = 0.0014) and 2meSATP + 1 μ M MRS 2179 curves (*; p value = 0.0171). The agonist elicited the same response at the high affinity portions of both curves (p value = 0.21) and this site disappeared in the presence of higher antagonist concentrations. Furthermore, the 2meSATP potency at the low affinity site of the biphasic curves was the same as its potency in the presence of 10 and 100 μ M

MRS 2179 (p value = 0.0699), indicating that the antagonist did not inhibit the low affinity site.

Antagonist Concentration	EC ₅₀₋₁ ($\mu\text{M} \pm \text{S.E.M.}$)	EC ₅₀₋₂ ($\mu\text{M} \pm \text{S.E.M.}$)	Fraction
2meSATP	0.12 \pm 0.05	4.5 \pm 0.9	0.46 \pm 0.06
2meSATP + 1 μM MRS 2179	0.3 \pm 1.2	8.9 \pm 3.2	0.69 \pm 0.09
2meSATP + 10 μM MRS 2179	ND	2.4 \pm 0.7	ND
2meSATP + 100 μM MRS 2179	ND	4.2 \pm 0.8	ND

Table 5.2 The EC₅₀ shift of the calcium response to 2meSATP in the presence of increasing concentrations of MRS 2179 in CHO-K1-hP2Y₁₁ clone 13

The EC₅₀ values for 2meSATP concentration-response curves in the absence and presence of three different dilutions of MRS 2179 were calculated in CHO-K1-hP2Y₁₁ clone 13. The fractions of the biphasic curves, showing the contribution of the high affinity site to the response, are also shown. The results represent the average \pm s.e.m of four independent experiments, each performed in triplicate. ND (not determined) refers to replicates for which a value could not be determined.

The Schild data were analyzed using the Gaddum/Schild EC₅₀ shift equation to investigate the nature of the antagonism exerted by MRS 2179 against 2meSATP in clone 13 cells. As Figure 5.5 shows, the addition of increasing concentrations of antagonist provoked a rightward shift of the 2meSATP curves without affecting the maximum response. The mean Schild slope of the curves was 0.87 ± 0.07 . The mean K_B value for MRS 2179 against 2meSATP was $21.5 \pm 12.6 \mu\text{M}$ and the mean pA₂ value was 5.4 ± 0.5 . The dose ratios for antagonist concentrations 100 μM , 10 μM and 1 μM (log values: -3.5, -4, -5 and -6) were manually calculated and plotted using linear regression analysis. The data formed a straight line with a mean slope of 1 ± 0.3 , and the average Schild plot is shown in Figure 5.6 A. The large error bars (up to 39%) observed for all three points are due to the variability within the different experimental trials. To offer a more accurate depiction of the dose ratios, a representative Schild plot calculated from one individual repeat is displayed in Figure 5.6 B. As the graph shows, the points formed a straight line with a slope of 1. Gaddum and Schild plot analysis suggest that the antagonism exhibited by MRS 2179 against the 2meSATP response is competitive. Furthermore, MRS 2179 antagonised the high-affinity site of the curve only, indicating that the receptor acting at this site might correspond to P2Y₁.

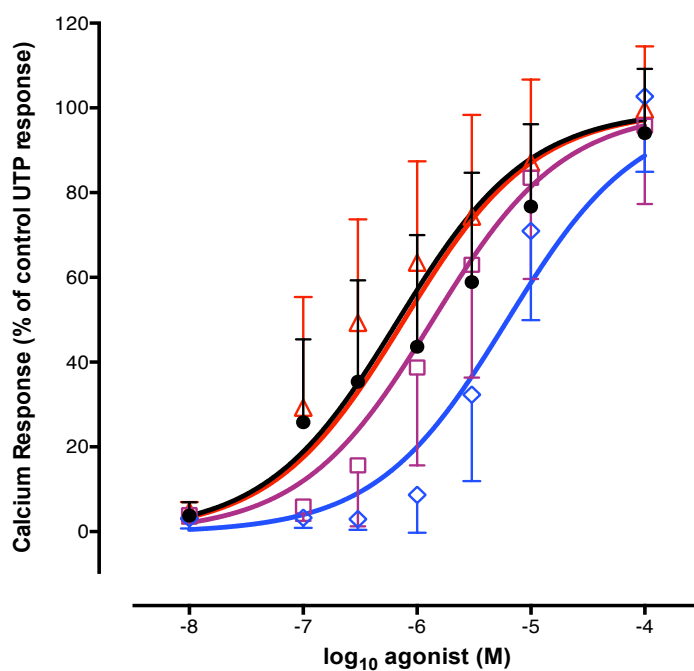


Figure 5.5 EC₅₀ Shift of the MRS 2179 and 2meSATP Schild in CHO-K1-hP2Y₁₁ clone 13

The EC₅₀ shift of the calcium response to 2meSATP as a function of increasing concentrations of MRS 2179 was analyzed using the Gaddum equation in CHO-K1-hP2Y₁₁ clone 13. The log₁₀ concentrations of MRS 2179 used were: -4 (◇), -5 (□) and -6 (△). The results represent the average ± s.e.m of six independent experiments each performed in triplicate and are expressed as a percentage of the response to 100µM UTP.

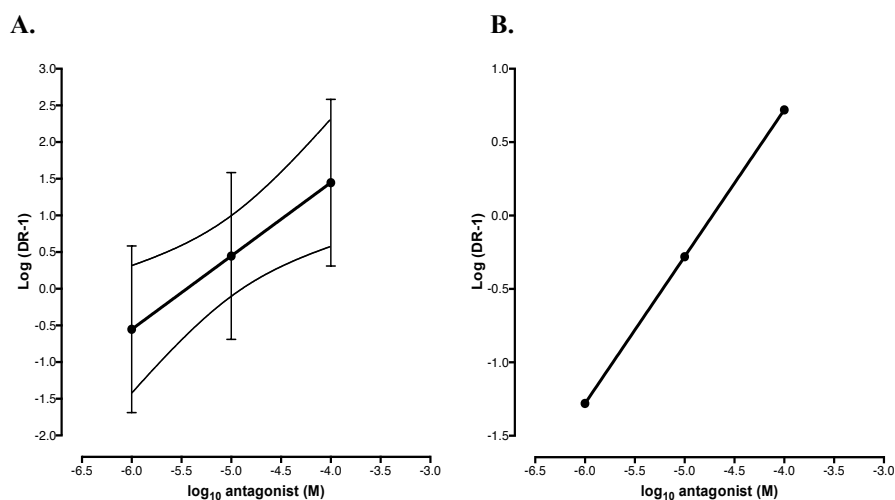


Figure 5.6 Schild plot for MRS 2179 against 2meSATP in clone 13

A. Average Schild plot for MRS 2179 against 2meSATP in clone 13. The concentration ratios for MRS 2179 concentrations 100 μ M, 10 μ M and 1 μ M (log values: -4, -5 and -6), were calculated manually and analysed using linear regression. The results represent the average \pm s.e.m of six individual experiments, each performed in triplicate. The 95% confidence interval of the fit is represented by dotted lines. The large error bars observed for the data points are due to variability within the experimental repeats. B. Representative Schild plot for MRS 2179 against 2meSATP in clone 13 obtained from one of the six individual experiments used to obtain the average plot shown in A. The dose ratios for MRS 2179 concentrations 100 μ M, 10 μ M and 1 μ M (log values: -4, -5 and -6), were calculated manually and analysed using linear regression. The results were calculated from one independent experiment performed in triplicate. The 95% confidence interval of the fit is represented by dotted lines.

5.3 NF 340 Schild analysis in CHO-K1-hP2Y₁₁ clone 13

To determine the effect of a P2Y₁₁ antagonist on the calcium response in clone 13, ADP concentration-response curves were generated in the presence and absence of different dilutions of NF 340. Data were analysed using global non-linear regression with a comparison of two equations (biphasic equation versus variable slope or four parameters equations) and the average concentration-response curves are shown in Figure 5.7. All the curves (control, ADP+1 μ M, ADP+10 μ M and ADP+100 μ M NF 340) progressed from their minimum to their maximum over four log units of agonist concentration, ranging from 100nM to 100 μ M (log value: -8 to -4) and were best fit using the biphasic model. Table 5.3 lists the EC₅₀ values of the Schild curves. Using one-way ANOVA analysis, there was a statistically significant difference between the EC₅₀₋₁ and EC₅₀₋₂ values of all the biphasic ADP curves (**, p value = 0.0075). The Gaddum/Schild EC₅₀ shift equation failed to fit the ADP+NF 340 data and yielded a

Schild slope of 0.0018, indicating that antagonist addition did not alter the potency of the ADP response in clone 13 cells. Global non-linear regression and Gaddum analysis of the ADP+NF 340 data thus reveal that the P2Y₁₁ antagonist NF 340 does not inhibit the biphasic response to ADP in clone 13.

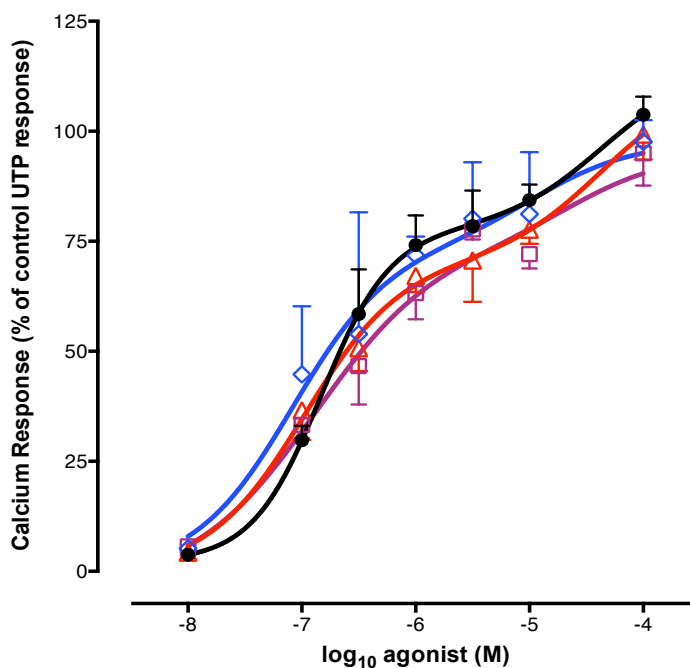


Figure 5.7 The effect of NF 340 on the calcium response to ADP in CHO-K1-hP2Y₁₁ clone 13

The response of CHO-K1-hP2Y₁₁ cells to increasing concentrations of the P2Y₁ agonist ADP was tested in the absence (●) and presence of three different concentrations of the P2Y₁₁ antagonist NF 340: -4 (◇), -5 (□) and -6 (△). The results represent the average ± s.e.m of one independent experiment performed in triplicate and are expressed as a percentage of the response to 100 μM UTP.

Antagonist Concentration	EC ₅₀₋₁ (μM)	EC ₅₀₋₂ (μM)
ADP	0.15	44
ADP + 1 μM NF 340	0.08	370
ADP + 10 μM NF 340	0.09	41
ADP + 100 μM NF 340	0.1	159

Table 5.3 The EC₅₀ shift of the calcium response to ADP in the presence of increasing concentrations of NF 340 in CHO-K1-hP2Y₁₁ clone 13

The EC₅₀ values for ADP concentration-response curves in the absence and presence of three different dilutions of NF 340 were calculated in CHO-K1-hP2Y₁₁ clone 13. Antagonist addition did not affect the potency of the high affinity and low affinity site of the ADP response. The shown EC₅₀ values were obtained from one experiment performed in triplicate.

5.4 Reactive Red Schild against ADP in CHO-K1-hP2Y₁₁ clone 13

Having studied the effect of a P2Y₁ and a P2Y₁₁ antagonist on agonist activity in clone 13, it was of interest to examine whether a P2Y-selective (P2Y₁ and P2Y₁₁) antagonist would affect the ADP response in this clone. Thus, concentration-response curves for ADP were generated in the absence and presence of 1 μ M, 10 μ M and 100 μ M Reactive Red (log value: -6 to -4). The data were analysed as per section 5.2.1. The fluorescence quenching caused by the encounter between the antagonist and the fluorophore dye was first addressed. This was achieved by calculating the baseline level of calcium fluorescence (F_0 ; average baseline fluorescence between $t = 0$ to 9.2 seconds) present in the cells prior to the addition of 100 μ M ADP at $t = 10$ seconds in the absence and presence of antagonist. The ADP + Reactive Red data sets were then normalized against the maximum ADP response of each individual curve to eliminate any possible interference with the results. Figure 5.8 shows the average ADP concentration response curves in the absence and presence of Reactive Red. Both the control ADP and ADP+1 μ M responses progressed from their minimum to their maximum over four log units of agonist concentration ranging from 10nM to 100 μ M (log value: -8 to -4) and were best fit using the biphasic equation. In contrast, the ADP+10 μ M Reactive Red curve spanned three log units of agonist concentration ranging from 100nM to 100 μ M (log value: -7 to -4) and was sigmoidal monophasic. Finally, it was not possible to fit the ADP+100 μ M Reactive Red data since this antagonist concentration completely inhibited the ADP response.

Table 5.4 displays the ADP potencies in the absence and presence of Reactive Red. The agonist displayed distinct potencies at the high versus low affinity sites of both the control ADP (**; p value = 0.0026) and ADP+1 μ M Reactive Red (*; p value = 0.0492) curves. There was no statistically significant difference between the ADP potency at the high affinity site of the biphasic curves (p value = 0.14) and this site vanished in the presence of higher antagonist concentrations. Further mathematical analysis revealed no statistically significant difference between the ADP potency at the low affinity site of the biphasic curves and its potency at the monophasic ADP + 10 μ M Reactive Red curve. Finally, the highest concentration of antagonist used, i.e. 100 μ M, completely inhibited the response to ADP, indicating that Reactive Red was able to antagonise both sites of the biphasic ADP response.

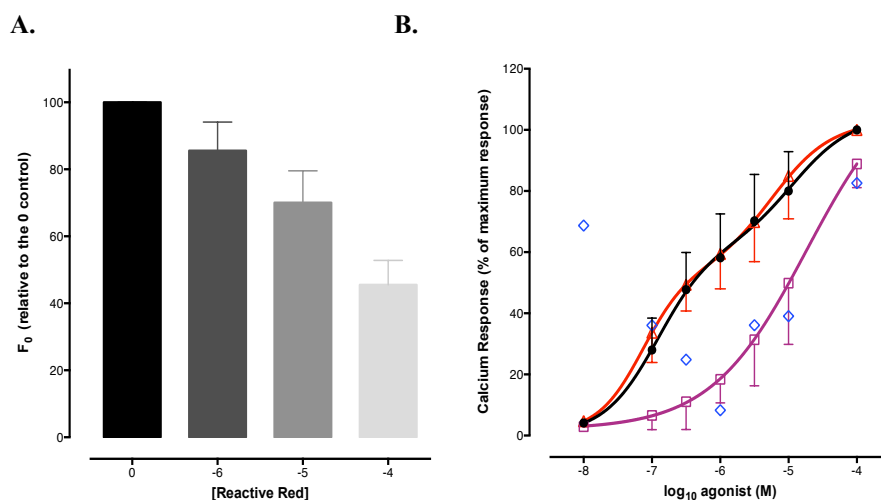


Figure 5.8 The effect of Reactive Red on the calcium response to ADP in CHO-K1-hP2Y₁₁ clone 13

The response of CHO-K1-hP2Y₁₁ cells to increasing concentrations of ADP was tested in the absence and presence of different concentrations of Reactive Red. *A.* Quenching of the baseline calcium fluorescence as a function of Reactive Red concentration in CHO-K1-hP2Y₁₁ clone 13. The level of basal calcium fluorescence (F_0) observed in CHO-K1-hP2Y₁₁ clone 13 cells prior to the addition of the maximum concentration of agonist tested, 100 μ M ADP (log value: -4), was calculated in the absence (0) and presence of increasing concentrations (1 μ M, 10 μ M and 100 μ M; log values: -6, -5 and -4) of Reactive Red. The results represent the average of 5 independent experiments each performed in triplicate and were normalized against the control F_0 . *B.* Reactive Red Schild against ADP in CHO-K1-hP2Y₁₁ clone 13. The log₁₀ concentrations of Reactive Red used against ADP were: (0) (●), -4 (◇), -5 (□) and -6 (△). The results represent the average \pm s.e.m of five representative experiments performed in triplicate and were normalized against the maximum ADP response of each individual curve to eliminate the quenching effect caused by the antagonist.

Antagonist Concentration	EC ₅₀₋₁ (μ M \pm S.E.M.)	EC ₅₀₋₂ (μ M \pm S.E.M.)
ADP	0.13 \pm 0.02	8.2 \pm 3.7
ADP + 1 μ M Reactive Red	0.1 \pm 0.02	7.1 \pm 3
ADP + 10 μ M Reactive Red	ND	5.81 \pm 0.7
ADP + 100 μ M Reactive Red	ND	ND

Table 5.4 The EC₅₀ shift of the calcium response to ADP in the presence of increasing concentrations of Reactive Red in CHO-K1-hP2Y₁₁ clone 13

The EC₅₀ values for ADP concentration-response curves in the absence and presence of three different dilutions of Reactive Red were calculated in CHO-K1-hP2Y₁₁ clone 13. The results represent the average \pm s.e.m of five independent experiments each performed in triplicate. The ND sign (not determined) refers to replicates for which no significant calcium response was detected.

To quantify the extent of the shift exerted by Reactive Red against the ADP curves in clone 13, the Schild data were analysed using the Gaddum/Schild EC₅₀ shift equation.

As Figure 5.9 shows, the addition of increasing dilutions of Reactive Red caused a rightward of the ADP sensitivity in clone 13 cells. The average Schild slope of the curves was 0.8 ± 0.18 . The mean K_B value was $1.1 \pm 0.2 \mu\text{M}$ and the mean pA_2 value was 6 ± 0.1 in clone 13 cells. The concentration ratios corresponding to the concentrations of antagonist used were calculated and they formed a line with a slope of 1, shown in Figure 5.10.

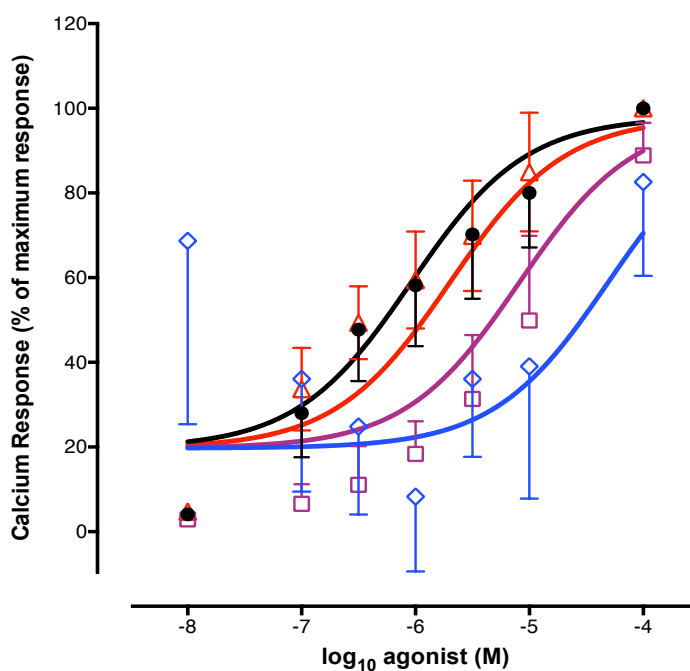


Figure 5.9 EC₅₀ Shift of the Reactive Red and ADP Schild in CHO-K1-hP2Y₁₁ clone 13

The EC₅₀ shift of the calcium response to ADP as a function of increasing concentrations of Reactive Red was analyzed using the Gaddum equation in CHO-K1-hP2Y₁₁ clone 13. The log₁₀ concentrations of Reactive Red used were: -4 (◇), -5 (◻) and -6 (▲). The analysis shows that increasing concentrations of antagonist caused a rightward shift of the response to ADP relative to the control response in the absence of antagonist (●). The results represent the average of five independent experiments each performed in triplicate and were normalized against the maximum ADP response to correct for the observed quenching effect.

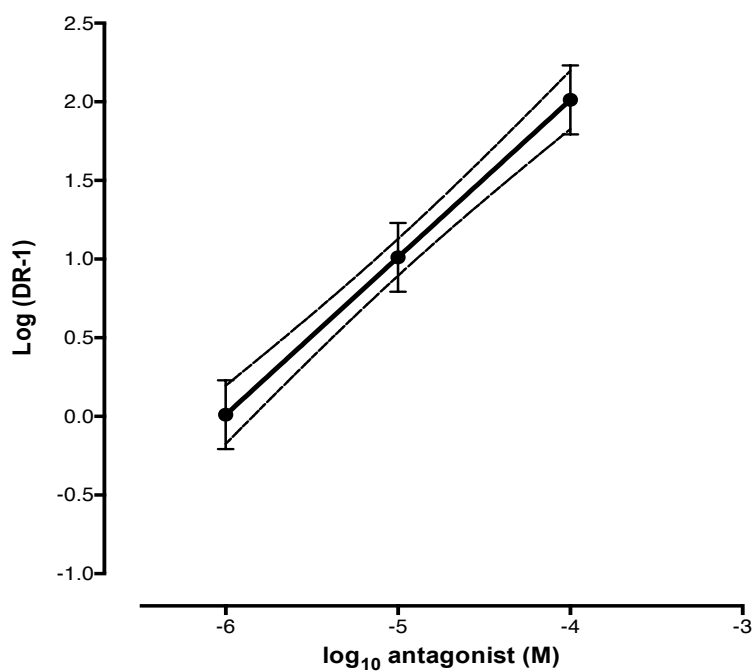


Figure 5.10 Schild plot for Reactive Red against ADP in clone 13

The dose ratios for Reactive Red concentrations tested against ADP, namely 100 μ M, 10 μ M and 1 μ M (log values: -4, -5 and -6), were calculated manually and analysed using linear regression. The plotted values formed a straight line with a slope of 1. The results represent the average \pm s.e.m of five independent experiments, each performed in triplicate. The 95% confidence interval of the fit is represented by dotted lines.

5.5 MRS 2179 inhibition curves in CHO-K1-hP2Y₁₁ clone 13

For an in-depth understanding of antagonist activity at the high versus low affinity sites of the curve, the biphasic responses to ADP and 2meSATP were divided into their constituent components. Two distinct agonist concentrations, one of which activates the high affinity site of the curve while the other stimulates the low affinity site, were used. The response to these ADP and 2meSATP concentrations was tested in the presence of increasing concentrations of MRS 2179, NF 340 and Reactive Red to examine antagonist action against each site individually. Inhibition experiments were also performed for BzATP in clone 13 to determine which antagonists would inhibit hP2Y₁₁ activity in the co-expressing system.

5.5.1 The calcium response to 100nM ADP in the presence of increasing concentrations of MRS 2179

The calcium response to 100nM (log value: -7) ADP was tested in the absence and presence of increasing concentrations of MRS 2179 ranging from 10nM to 100 μ M (log

value: -8 to -4) in clone 13 cells. Non linear regression analysis using a comparison of two equations (log(inhibitor) vs. response (three parameters) versus log(inhibitor) vs. response -- variable slope (four parameters)) was then performed and the average inhibition curves are shown in Figure 5.11. The data were best fit using the simple model or three parameters equation and produced a monophasic sigmoidal curve with a Hill slope of -1, indicating that the agonist and inhibitor competed for a single population of binding sites. The antagonist exerted its inhibitory effect in a concentration-dependent fashion over three log units of concentration, ranging from 316nM to 100 μ M (log value: -6.5 to -4). The response to 100nM ADP control constituted $49.8 \pm 2.7\%$ of the response to 100 μ M UTP control. The highest concentration of antagonist tested or 100 μ M MRS 2179 reduced the calcium response to $5 \pm 2.4\%$ of the UTP control and this value was statistically significant different from the ADP control (p value < 0.0001). The agonist response returned to control level at 316nM MRS 2179 as confirmed by statistical tests. The maximum response to 100nM ADP occurred in the presence of 10nM MRS 2179 (log value: -8) and was higher than the control ADP response (*; p value = 0.0235). The mean IC₅₀ value for MRS 2179 in clone 13 was $1.8 \pm 0.5\mu$ M and the mean pIC₅₀ value was 5.7.

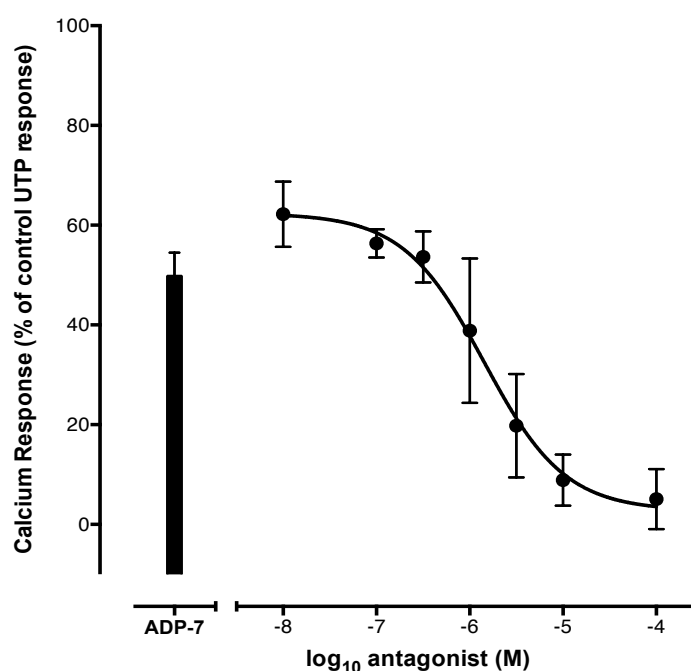


Figure 5.11 MRS 2179 inhibits the response to 100nM ADP in CHO-K1-hP2Y₁₁ clone 13

The effect of increasing concentrations of the P2Y₁ antagonist MRS 2179 on the calcium response to 100nM ADP was tested at 37°C in CHO-K1-hP2Y₁₁ clone 13. The results represent the average \pm s.e.m of six independent experiments each performed in quadruplicate and are expressed as a percentage of the response to 100 μ M UTP.

5.5.2 The calcium response to 100 μ M ADP in the presence of increasing concentrations of MRS 2179

The response to 100 μ M ADP (log value: -4) was tested in the presence of increasing concentrations of MRS 2179, ranging from 10nM to 100 μ M (log value: -8 to -4). As Figure 5.12 shows, the calcium fluorescence evoked by agonist addition was high and did not return to baseline for any antagonist concentration used, indicating that MRS 2179 does not inhibit the response to 100 μ M ADP in clone 13.

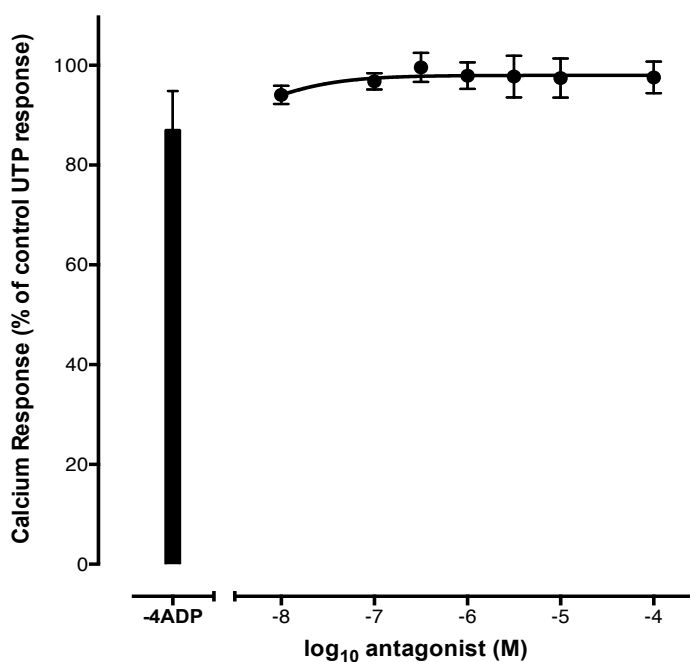


Figure 5.12 MRS 2179 does not affect the response to 100 μ M ADP in CHO-K1-hP2Y₁₁ clone 13

The effect of increasing concentrations of MRS 2179 on the calcium response to 100 μ M ADP (log value: -4) was tested at 37°C in CHO-K1-hP2Y₁₁ clone 13. The results represent the average \pm s.e.m of three independent experiments each performed in quadruplicate and are expressed as a percentage of the response to 100 μ M UTP.

5.5.3 The calcium response to 100nM 2meSATP in the presence of increasing concentrations of MRS 2179

The previous experiments examined the effect of MRS 2179 on the the biphasic ADP response in clone 13. The high affinity site of the biphasic 2meSATP curve, corresponding to 100nM 2meSATP (log value: -7), was also challenged using the same dilutions of MRS 2179. Non-linear regression analysis using a comparison of two

equations (log(inhibitor) vs. response (three parameters) versus log(inhibitor) vs. response -- variable slope (four parameters)) was then performed and the average inhibition curve is shown in Figure 5.13. The data were best fit using the three parameters model which produced a monophasic sigmoidal curve with a Hill slope of -1. The antagonist exerted its inhibitory action over three log units of concentration, ranging from 316nM to 100µM (log value: -6.5 to -4). The control response to 100nM 2meSATP was $56 \pm 2\%$ of the control UTP response. The highest concentration of antagonist tested, 100µM 2meSATP (log value: -4), reduced the calcium response to 100nM 2meSATP to $9.6 \pm 1.8\%$ of the UTP control. Low concentrations of antagonist, i.e. 316nM, 100nM and 10nM (log value: -6.5, -7 and -8), had no detectable effect on the response to 100nM 2meSATP, as confirmed by statistical analysis (p value = 0.9183). The average IC₅₀ value for MRS 2179 against 100nM 2meSATP was $2.3 \pm 0.5\mu\text{M}$ and the mean pIC₅₀ value was 5.6.

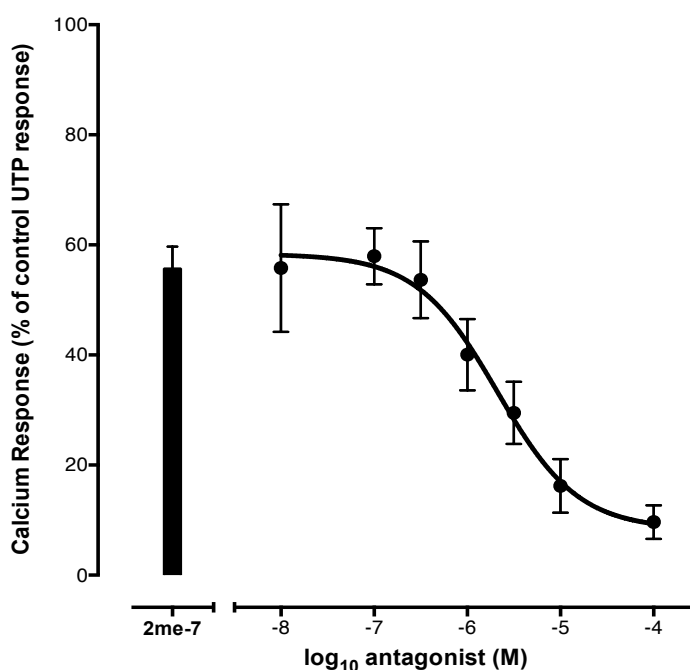


Figure 5.13 MRS 2179 inhibits the response to 100nM 2meSATP in CHO-K1-hP2Y₁₁ clone 13

The effect of increasing concentrations of MRS 2179 on the calcium response to 100nM 2meSATP was tested at 37°C in CHO-K1-hP2Y₁₁ clone 13. The results represent the average \pm s.e.m of three independent experiments each performed in quadruplicate and are expressed as a percentage of the response to 100µM UTP.

5.5.4 The calcium response to 100 μ M 2meSATP in the presence of increasing concentrations of MRS 2179

The response of clone 13 cells to 100 μ M 2meSATP was investigated in the presence of increasing dilutions of MRS 2179 and the resulting inhibition curve is shown in Figure 5.14. According to non-linear regression analysis using a comparison of two equations (log(inhibitor) vs. response (three parameters) versus log(inhibitor) vs. response -- variable slope (four parameters)), the MRS 2179 versus 100 μ M 2meSATP curve preferred the simple model. However, one-way ANOVA analysis showed no statistically significant difference between the calcium responses to 100 μ M 2meSATP in the presence of all concentrations of antagonist used (p value = 0.076). This indicates that MRS 2179 does not inhibit the response to 100 μ M 2meSATP in clone 13 cells.

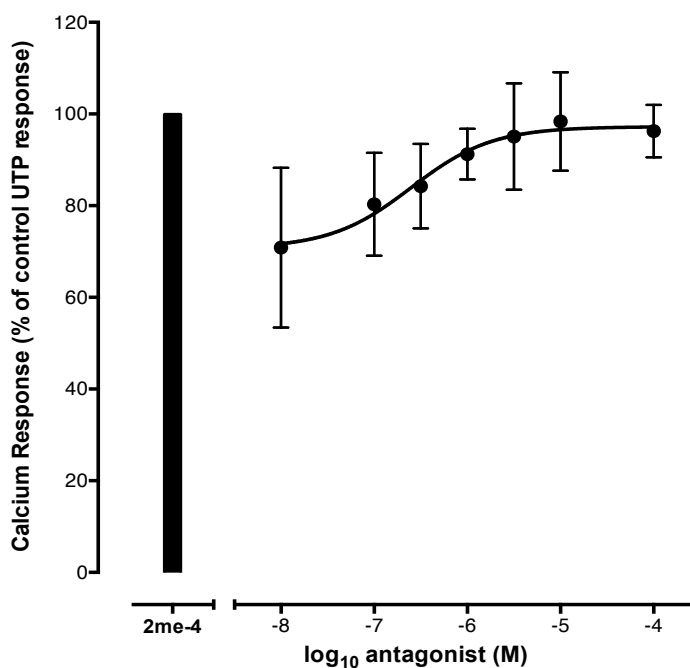


Figure 5.14 MRS 2179 does not affect the response to 100 μ M 2meSATP in CHO-K1-hP2Y₁₁ clone 13

The effect of increasing concentrations of MRS 2179 on the calcium response to 100 μ M 2meSATP (log value: -4) was tested at 37°C in CHO-K1-hP2Y₁₁ clone 13. The results represent the average \pm s.e.m of three independent experiments each performed in quadruplicate and are expressed as a percentage of the response to 100 μ M UTP.

5.5.5 The calcium response to 10 μ M BzATP in the presence of increasing concentrations of MRS 2179

To determine whether MRS 2179 would alter the calcium response to BzATP in clone 13, the cells were pre-incubated with increasing antagonist dilutions, ranging from 10nM to 100 μ M MRS 2179 (log value: -8 to -4). The mean inhibition curve for MRS 2179 against 10 μ M BzATP is shown in Figure 5.15. As the graph reveals, the Prism software was unable to fit a curve to the analysed data and it was represented with a line for visualization purposes. Using one-way ANOVA analysis, there was no statistically significant difference between the response to 10 μ M BzATP in the absence and presence of increasing concentrations of MRS 2179 (p value = 0.225). These results demonstrate that MRS 2179 is not an antagonist of BzATP in clone 13 cells.

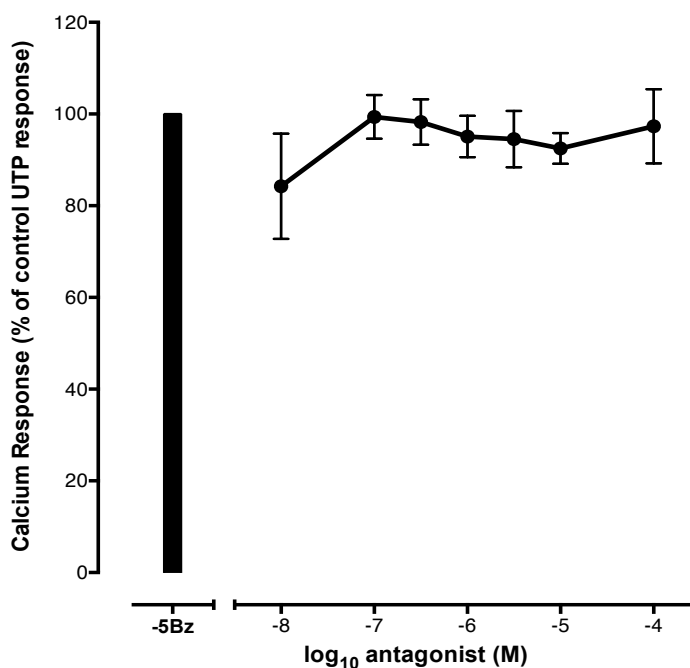


Figure 5.15 MRS 2179 does not affect the response to 10 μ M BzATP in CHO-K1-hP2Y₁₁ clone 13

The effect of increasing concentrations of MRS 2179 on the calcium response to 10 μ M BzATP (log value: -5) was tested at 37°C in CHO-K1-hP2Y₁₁ clone 13. The results represent the average \pm s.e.m of three independent experiments each performed in quadruplicate and are expressed as a percentage of the response to the 10 μ M BzATP control.

5.6 NF 340 Inhibition Curves in CHO-K1-hP2Y₁₁ Clone 13

To determine whether NF 340 would affect the ADP, 2meSATP and BzATP responses, inhibition experiments using increasing concentrations of antagonist versus a fixed concentration of agonist were carried out in CHO-K1-hP2Y₁₁ clone 13.

5.6.1 The calcium response to 100nM ADP in the presence of increasing concentrations of NF 340

The response of clone 13 cells to 100nM ADP (log value: -7) was assayed in the presence of serial concentrations of NF 340, ranging from 100nM to 100 μ M (log value: -8 to -4). Figure 5.16 shows the average inhibition curve for NF 340 versus 100nM ADP in clone 13. Using Prism analysis, the inhibition data were best fit using the simple model or three parameters equation. However, mathematical analysis showed no statistically significant difference between the control 100nM ADP response (which amounted to $31 \pm 7.3\%$ of the response to 100 μ M UTP control) and the agonist response measured in the presence of different antagonist concentrations (p value = 0.5745). In summary, NF 340 did not antagonize the response to 100nM ADP in clone 13 cells.

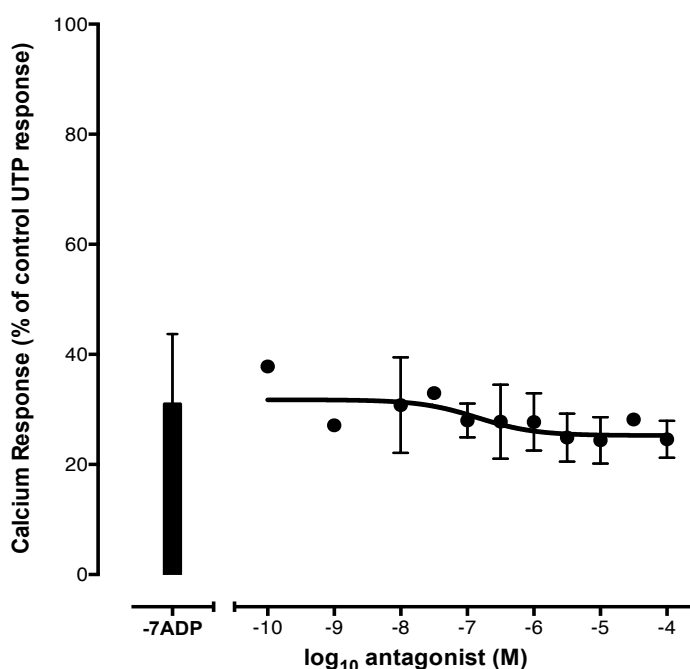


Figure 5.16 NF 340 does not affect the response to 100nM ADP in CHO-K1-hP2Y₁₁ clone 13

The effect of increasing concentrations of NF 340 on the calcium response to 100nM ADP (log value: -7) was tested at 37°C in CHO-K1-hP2Y₁₁ clone 13. The results represent the average \pm s.e.m of three independent experiments each performed in quadruplicate and are expressed as a percentage of the response to 100 μ M UTP.

5.6.2 The calcium response to 100µM ADP in the presence of increasing concentrations of NF 340

The low affinity site of the biphasic ADP response was then investigated using the same concentrations of NF 340. Prism software failed to fit a curve to the inhibition data shown in Figure 5.17. One-way ANOVA analysis revealed no statistically significant difference between the control 100µM ADP response and the response to 100µM ADP in the presence of antagonist (p value = 0.2568), indicating that NF 340 did not modify the calcium response to 100µM ADP. For visualisation purposes, the data were joined using a connecting line. The large error bars (up to 24%) observed for some data points resulted from the variability in the measured calcium response across the experimental repeats.

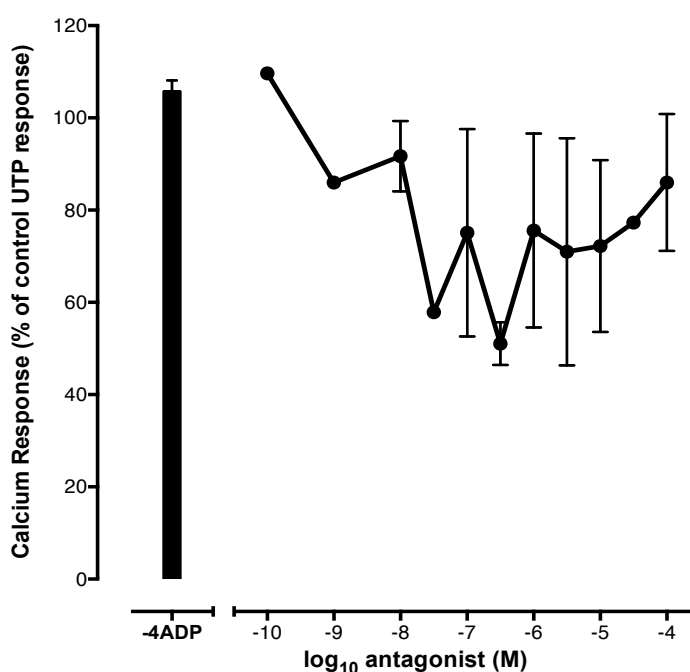


Figure 5.17 NF 340 does not affect the response to 100µM ADP in CHO-K1-hP2Y₁₁ clone 13

The effect of increasing concentrations of NF 340 on the calcium response to 100µM ADP (log value: -4) was tested at 37°C in CHO-K1-hP2Y₁₁ clone 13. The addition of NF 340 did not alter the calcium response to ADP. The results represent the average \pm s.e.m of three independent experiments each performed in quadruplicate and are expressed as a percentage of the response to 100µM UTP.

5.6.3 The calcium response to 100nM 2meSATP in the presence of increasing concentrations of NF 340

To investigate the antagonist profile of the bottom portion of the 2meSATP curve, 100nM 2meSATP (log value: -6) was added to clone 13 cells pre-incubated with inhibitor concentrations ranging from 10nM to 100 μ M NF 340. As Figure 5.18 shows, there was no statistically significant difference between the control 100nM 2meSATP response and the agonist response in the presence of increasing concentrations of antagonist (p value = 0.8358). The large error bars (up to 16%) detected for some data points arose from the variability in the measured calcium response to 100nM 2meSATP across the experimental trials.

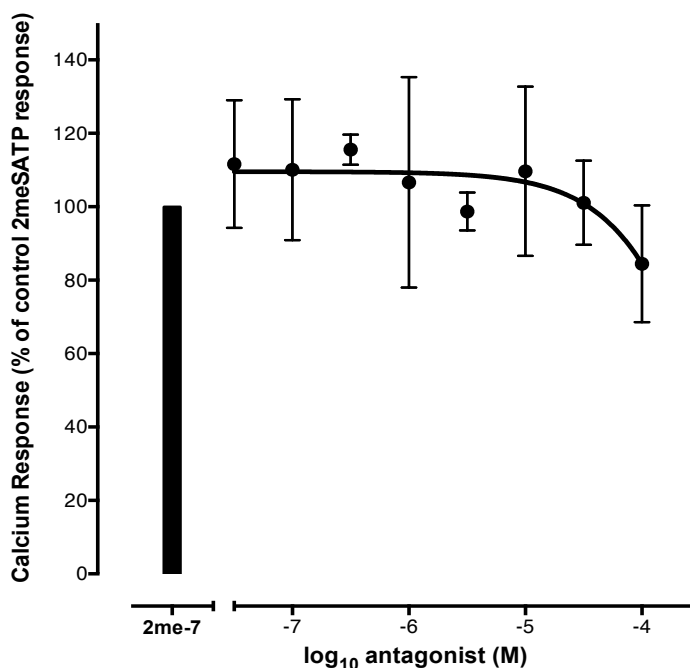


Figure 5.18 NF 340 does not affect the response to 100nM 2meSATP in CHO-K1-hP2Y₁₁ clone 13

The effect of increasing concentrations of NF 340 on the calcium response to 100nM 2meSATP (log value: -7) was tested at 37°C in CHO-K1-hP2Y₁₁ clone 13. The results represent the average \pm s.e.m of one independent experiment performed in triplicate and are expressed as a percentage of the response to the 100nM 2meSATP control.

5.6.4 The calcium response to 100 μ M 2meSATP in the presence of increasing concentrations of NF 340

To investigate the antagonist profile of the high affinity site of the 2meSATP response, 100 μ M (log value: -4) 2meSATP was added to clone 13 cells pre-incubated

with increasing dilutions of NF 340, ranging from 100nM to 100 μ M (log value: -8 to -4). Using one-way ANOVA analysis, there was no statistically significant difference between the control 100 μ M 2meSATP response and the agonist response in the presence of antagonist (p value = 0.0824), confirming that NF 340 does not antagonize the response to 100 μ M 2meSATP in clone 13 cells. The results are shown in Figure 5.19. For visualization purposes, the 100 μ M 2meSATP and NF 340 inhibition data points were joined using a connecting line.

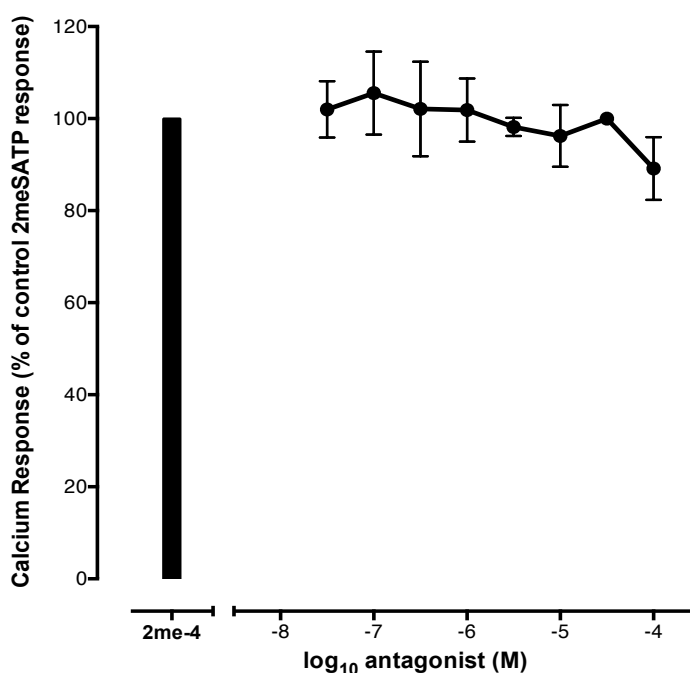


Figure 5.19 NF 340 does not affect the response to 100 μ M 2meSATP in CHO-K1-hP2Y₁₁ clone 13

The effect of increasing concentrations of NF 340 on the calcium response to 100 μ M 2meSATP (log value: -4) was tested at 37°C in CHO-K1-hP2Y₁₁ clone 13. The results represent the average \pm s.e.m of four independent experiments each performed in triplicate and are expressed as a percentage of the response to the 100 μ M 2meSATP control.

5.6.5 The calcium response to 10 μ M BzATP in the presence of increasing concentrations of NF 340

To determine whether NF 340 would affect the BzATP response in clone 13 cells, a fixed concentration of BzATP, namely 10 μ M (log value: -5), was added to increasing concentrations of NF 340, ranging from 100nM to 100 μ M (log value: -8 to -4). As Figure 5.20 reveals, NF 340 did not affect the calcium response to BzATP in clone 13. One-way

ANOVA analysis confirmed the absence of a statistically significant difference between the control BzATP and the BzATP response in the presence of antagonist (p value = 0.6905), indicating that NF 340 is not a competitive inhibitor of the BzATP response in clone 13 cells.

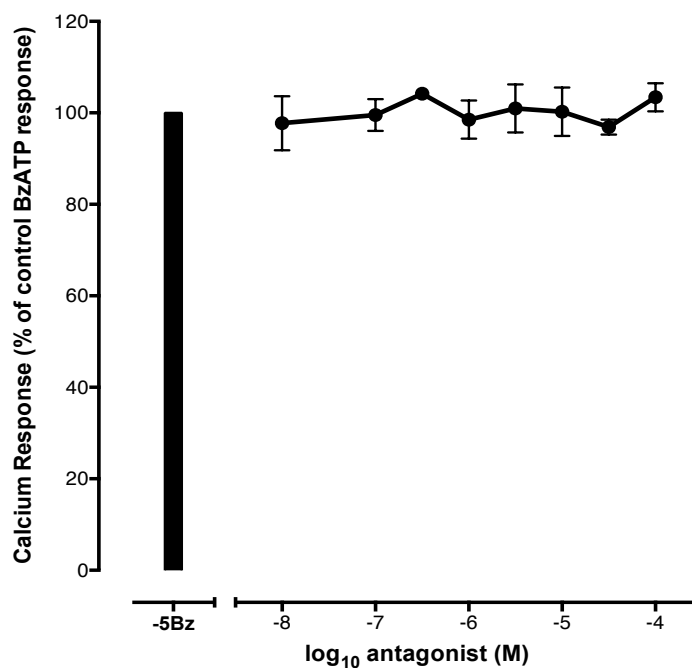


Figure 5.20 NF 340 does not affect the response to 10 μ M BzATP in CHO-K1-hP2Y₁₁ clone 13

The effect of increasing concentrations of NF 340 on the calcium response to 10 μ M BzATP (log value: -5) was tested at 37°C in CHO-K1-hP2Y₁₁ clone 13. The results represent the average \pm s.e.m of three independent experiments each performed in quadruplicate and are expressed as a percentage of the response to the 10 μ M BzATP control.

5.7 Reactive Red Inhibition Curves in CHO-K1-hP2Y₁₁ Clone 13

The last set of inhibition experiments explored the effect of Reactive Red, reported to antagonize both hP2Y₁ and hP2Y₁₁, on the response to these agonists in clone 13.

5.7.1 The calcium response to 100nM ADP in the presence of increasing concentrations of Reactive Red

The response to 100nM ADP (log value: -7) was tested in the presence of increasing concentrations of Reactive Red, ranging from 10nM to 100 μ M (log value: -8

to -4). Fluorescence quenching due to Reactive Red was first analysed. For this purpose, the baseline level of calcium fluorescence (F_0 ; average fluorescence for $t = 0$ to 9.2 seconds) present in the cells prior to agonist addition at $t = 10$ seconds in the absence and presence of antagonist was calculated and is shown in Figure 5.21A. Using one-way ANOVA analysis there was no statistically significant difference between the control F_0 values and the F_0 values of the cells pre-incubated with antagonist concentrations 100nM to 1 μ M (p value = 0.3059). However, there was a statistically significant difference in baseline fluorescence (F_0) between the control and the cells treated with 3.16 μ M Reactive Red (log value: -5.5) (*; p value = 0.0208), 10 μ M Reactive Red (log value: -5) (*; p value = 0.01), and 100 μ M Reactive (log value: -4) (****; p value < 0.0001). These results indicate that while antagonist concentrations 10nM to 1 μ M (log value: -8 to -6) did not interfere with the dye, antagonist concentrations 3.16 μ M to 100 μ M gradually provoked the quenching of the calcium fluorescence (log value: -5.5 to -4).

Having analysed the fluorescence quenching caused by Reactive Red, the calcium response to 100nM ADP over time was analysed in the absence and presence of antagonist. Graph 5.21 B. shows a representative time course of the 100nM ADP versus Reactive Red inhibition curve in clone 13 cells. As the traces show, Reactive Red concentrations ranging from 100 μ M to 3.16 μ M caused a progressive decrease of the calcium response to 100nM ADP leading to a complete suppression of the response at 10 μ M (-5) and 100 μ M (-4) antagonist. The calcium response was fully restored to control level starting from 1 μ M Reactive Red and concentrations ranging from 316nM to 100nM (log value: -6.5 to -8) had no effect on the ADP sensitivity.

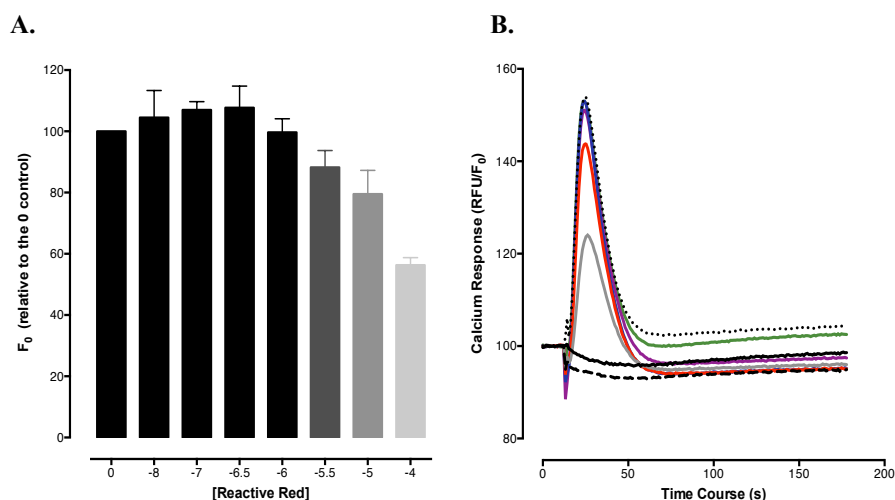


Figure 5.21 Time dependence of the response to 100nM ADP in the presence of increasing concentrations of Reactive Red in CHO-K1-hP2Y₁₁ clone 13

The calcium response to 100nM (log value: -7) ADP was measured over time in the presence of increasing concentrations of Reactive Red in CHO-K1-hP2Y₁₁ clone 13 cells. *A.* Quenching of the baseline calcium fluorescence as a function of Reactive Red concentration in CHO-K1-hP2Y₁₁ clone 13. The level of basal calcium fluorescence (F_0) observed in clone 13 cells prior to the addition of 100nM ADP (log value: -7) was analyzed in the absence (0) and presence of the increasing dilutions of Reactive Red. The results represent the average of three independent experiments each performed in quadruplicate and were normalized against the (0) control F_0 value. *B.* Time course of the Reactive Red and 100nM ADP inhibition curve. The log₁₀ concentrations of Reactive Red used were: -4 (—), -5 (—), -5.5 (—), -6 (—), -6.5 (—), -7 (—) and -8 (—). The calcium fluorescence elicited by the 100nM ADP control is also shown (···). The traces represent the mean calcium response obtained from one independent experiment performed in quadruplicate, divided by the baseline fluorescence measured prior to the introduction of ligand at $t=10$ seconds. The results are expressed as RFU/F_0 . Error bars have been omitted to ensure a better visualization of the curves.

To correct for the fluorescence quenching caused by Reactive Red, the F/F_0 values of each dataset were transformed against their own maximum response to 100nM ADP. Non-linear regression analysis using a comparison of two equations (log(inhibitor) vs. response (three parameters) versus log(inhibitor) vs. response -- variable slope (four parameters)) was performed and the average inhibition curve for Reactive Red versus 100nM ADP is shown in Figure 5.22. The antagonist exerted its inhibitory effect over two log units of concentration, ranging from 1 μ M to 100 μ M (log value: -6 to -4). The data were best fit using the three parameters equation and produced a monophasic sigmoidal curve with a Hill slope of -1. The mean IC_{50} value for Reactive Red against 100nM ADP was $2.9 \pm 0.8\mu$ M and the mean pIC_{50} value was 5.5.

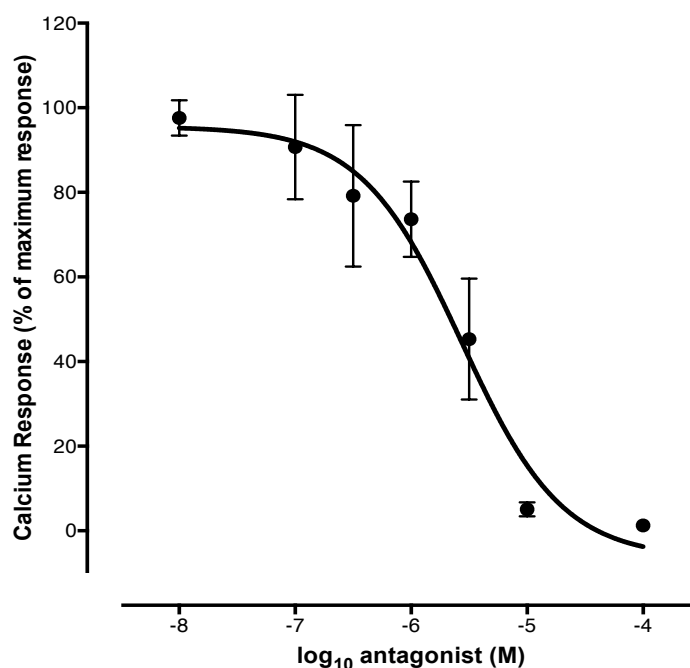


Figure 5.22 Reactive Red inhibits the response to 100nM ADP in CHO-K1-hP2Y₁₁ clone 13

The effect of increasing concentrations of Reactive Red on the calcium response to 100nM ADP (log value: -7) was tested at 37°C in CHO-K1-hP2Y₁₁ clone 13. The results represent the average \pm s.e.m of three independent experiments each performed in quadruplicate and are expressed as a percentage of the maximum response of each individual inhibition curve to correct for fluorescence quenching.

5.7.2 The calcium response to 100 μ M ADP in the presence of increasing concentrations of Reactive Red

Reactive Red was tested against 100 μ M ADP (log value: -4) to determine whether it would affect the low affinity site of the biphasic ADP curve. The fluorescence quenching provoked by Reactive Red was evaluated as described in section 5.7.1 and the calculated F_0 values are shown in Figure 5.23. Mathematical analysis revealed a statistically significant difference between the baseline fluorescence of cells treated with 1 μ M to 100 μ M (log value: -6 to -4) Reactive Red versus the control F_0 (****; p value < 0.0001), indicating that these antagonist concentrations caused fluorescence quenching. Figure 5.23 shows a representative time course of the inhibition curve of Reactive Red against 100 μ M ADP. As the traces indicate, antagonist concentrations ranging from 10nM to 3.16 μ M (log value: -8 to -5.5) did not alter the calcium response of clone 13 cells to 100 μ M ADP. In contrast, 10 μ M Reactive Red reduced the response of the cells to 100 μ M ADP while the highest concentrations of antagonist tested, i.e. 100 μ M Reactive Red, completely suppressed it.

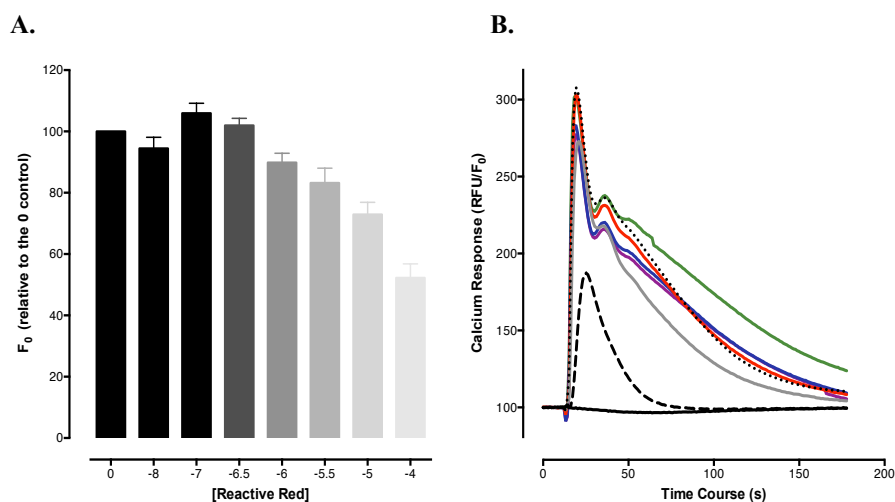


Figure 5.23 Time dependence of the response to 100µM ADP in the presence of increasing concentrations of Reactive Red in CHO-K1-hP2Y₁₁ clone 13

The calcium response to 100µM (log value: -4) ADP was measured over time in the presence of increasing concentrations of Reactive Red in CHO-K1-hP2Y₁₁ clone 13 cells. *A.* Quenching of the baseline calcium fluorescence as a function of Reactive Red concentration in CHO-K1-hP2Y₁₁ clone 13. The level of basal calcium fluorescence (F_0) observed in CHO-K1-hP2Y₁₁ clone 13 cells prior to the addition of 100µM ADP (log value: -4) was analysed in the absence (0) and presence of increasing concentrations of Reactive Red. The results represent the average of three independent experiments each performed in quadruplicate and were normalized against the (0) control F_0 value. *B.* Time course of the Reactive Red and 100µM ADP inhibition curve. The log₁₀ concentrations of Reactive Red used were: -4 (—), -5 (---), -5.5 (— · —), -6 (— · — · —), -6.5 (— · — · — · —), -7 (— · — · — · — · —) and -8 (— · — · — · — · — · —). The calcium fluorescence elicited by the 100µM ADP control is also shown (···). The traces represent the mean calcium response obtained from one independent experiment performed in quadruplicate, divided by the baseline fluorescence measured prior to the introduction of ligand at $t=10$ seconds. The results are expressed as RFU/F_0 . Error bars have been omitted to ensure a better visualization of the curves.

The F/F_0 values of the inhibition curves were transformed against their respective maximum responses to 100µM ADP to correct for fluorescence quenching. Figure 5.24 shows the average inhibition curve for Reactive Red against 100µM ADP. The preferred fit for the analysed data was the simple model or three parameters equations, which yielded a sigmoidal curve with a Hill slope of -1. The average IC_{50} value for Reactive Red versus 100µM ADP was $32 \pm 18\mu\text{M}$ while the average pIC_{50} value was 4.55 ± 0.25 . This experiment shows that Reactive Red inhibited the agonist response at maximum concentrations (10µM to 100µM) only.

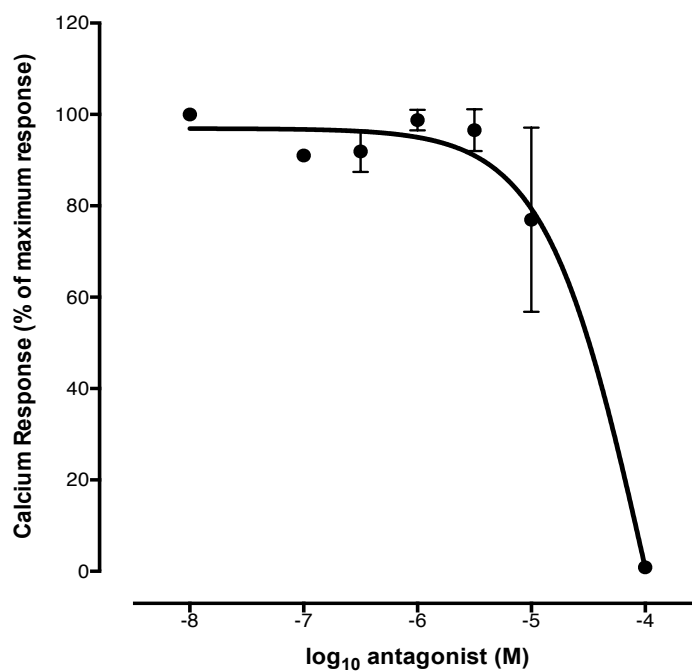


Figure 5.24 Reactive Red inhibits the response to 100µM ADP in CHO-K1-hP2Y₁₁ clone 13

The effect of increasing concentrations of Reactive Red on the calcium response to 100µM ADP (log value: -4) was tested at 37°C in CHO-K1-hP2Y₁₁ clone 13. These results represent the average \pm s.e.m of three independent experiments each performed in quadruplicate and are expressed as a percentage of the maximum response of each individual inhibition curve to correct for fluorescence quenching.

5.7.3 The calcium response to 100nM 2meSATP in the presence of increasing concentrations of Reactive Red

The biphasic calcium response to 2meSATP was studied using the same concentrations of Reactive Red to investigate whether the antagonist would affect the high and low affinity sites of the curve. Increasing antagonist concentrations, ranging from 10nM to 100µM (log value: -8 to -4), were first applied to 100nM 2meSATP (log value: -7) in clone 13 cells. The fluorescence quenching provoked by antagonist addition was analysed as per section 5.7.1 and the baseline fluorescence of control cells versus cells containing 10nM to 100µM Reactive Red is shown in Figure 5.25A. One-way ANOVA analysis revealed a statistically significant difference between the control basal fluorescence and the baseline fluorescence of cells pre-incubated with 100µM antagonist (log value: -4) only, indicating that the maximum concentration of Reactive Red resulted in fluorescence quenching. Figure 5.25 B. displays a representative time course of the Reactive Red versus 100nM 2meSATP inhibition curve in clone 13. As the traces indicate, antagonist concentrations ranging from 1µM to 100µM (log value: -6 to -4)

resulted in a concentration dependent decrease in the calcium response to 100nM 2meSATP in clone 13 cells while the maximum concentration of Reactive Red, i.e. 100 μ M, completely blocked this response. Lower antagonist concentrations, namely 10nM to 316nM, did not alter the response to 100nM 2meSATP as compared to the control.

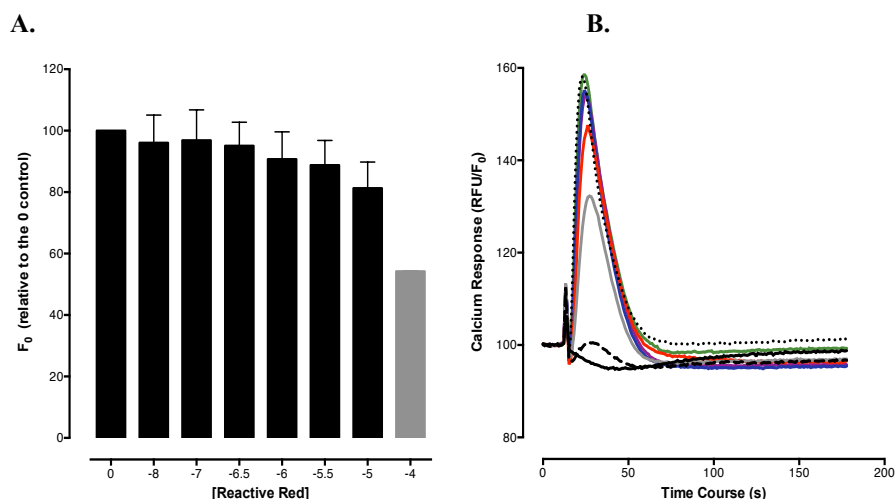


Figure 5.25 Time dependence of the response to 100nM 2meSATP in the presence of increasing concentrations of Reactive Red in CHO-K1-hP2Y₁₁ clone 13

The calcium response to 100nM (log value: -7) 2meSATP was measured over time in the presence of increasing concentrations of Reactive Red in CHO-K1-hP2Y₁₁ clone 13 cells. *A.* Quenching of the basal level of calcium fluorescence as a function of Reactive Red concentration in CHO-K1-hP2Y₁₁ clone 13. The level of basal calcium fluorescence (F_0) observed in CHO-K1-hP2Y₁₁ clone 13 cells prior to the addition of 100nM 2meSATP (log value: -7) was analyzed in the absence (0) and presence of increasing concentrations of Reactive Red. The results represent the average of three independent experiments each performed in quadruplicate and were normalized against the (0) control F_0 value. *B.* Reactive Red against 100nM 2meSATP inhibition curves in CHO-K1-hP2Y₁₁ clone 13. The calcium response to 100nM (log value: -7) 2meSATP was measured over time in the presence of increasing concentrations of the P2Y-selective antagonist Reactive Red in CHO-K1-hP2Y₁₁ clone 13 cells. The log₁₀ concentrations of Reactive Red used were: -4 (—), -5 (---), -5.5 (—), -6 (—), -6.5 (—), -7 (—) and -8 (—). The calcium fluorescence elicited by the 100nM 2meSATP control is also shown (··). The traces represent the mean calcium response obtained from one independent experiment performed in quadruplicate, divided by the baseline fluorescence measured prior to the introduction of ligand at $t=10$ seconds. The results are expressed as RFU/ F_0 . Error bars have been omitted to ensure a better visualization of the curves.

To eliminate the quenching effect of Reactive Red, the inhibition data were transformed against the maximum response to 100nM 2meSATP then analysed using non-linear regression as per section 5.7.1. Figure 5.26 shows the average inhibition curve for Reactive Red versus 100nM 2meSATP in clone 13. Two out of the three trials were best fit using the four parameters equation, while one trial was fit using the simple model

or three parameters equation. The average Hill slope for Reactive Red versus 100nM 2meSATP was -1.7 ± 0.3 , indicating that Reactive Red and 2meSATP might have been competing for a heterogeneous population of receptors. The mean IC₅₀ value for Reactive Red against 100nM 2meSATP was $22 \pm 17\mu\text{M}$ and the mean pIC₅₀ value was 4.97.

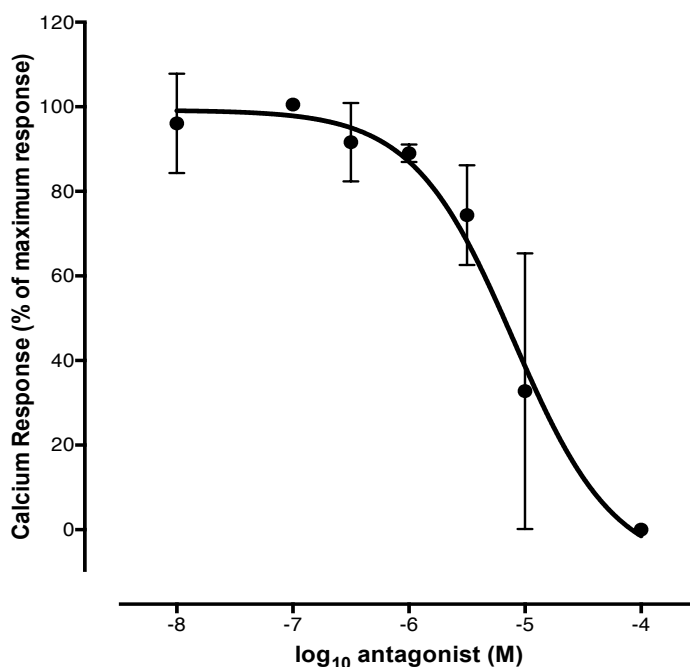


Figure 5.26 Reactive Red inhibits the response to 100nM 2meSATP in CHO-K1-hP2Y₁₁ clone 13

The calcium response of clone 13 cells to 100nM 2meSATP (log value: -7) was studied in the absence and presence of Reactive Red at physiological temperature. The results represent the average \pm s.e.m of three independent experiments each performed in triplicate or quadruplicate and are expressed as a percentage of the maximum response to 100nM 2meSATP to eliminate fluorescence quenching.

The large error bars detected for some concentrations (up to 58%) were caused by the variability of the responses obtained in the independent experimental trials. A representative inhibition curve from one independent trial is shown in Figure 5.27 for clarity purposes. The corresponding data were best fit using the four parameters equation, which produced a sigmoidal monophasic curve with a Hill slope of -1.88. In summary, this experiment shows that Reactive Red inhibits the response to 100nM 2meSATP in clone 13 and might be acting at a heterogeneous population of receptors.

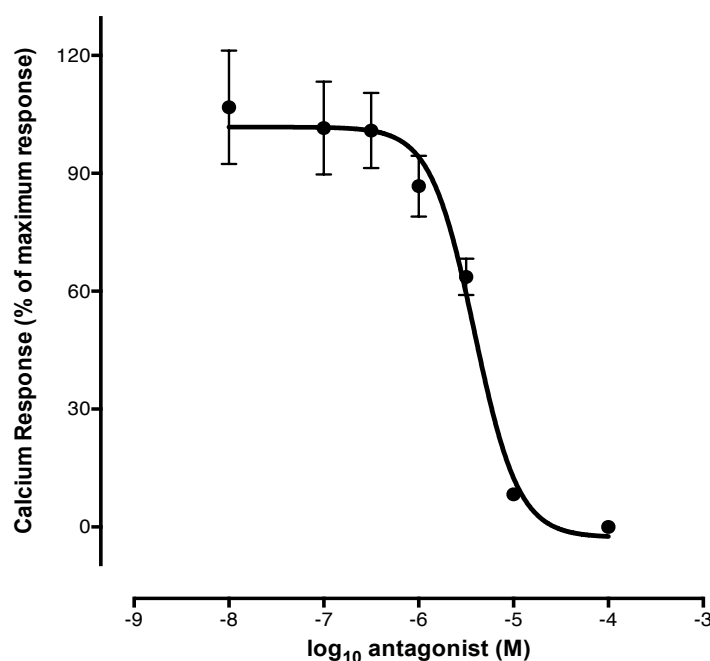


Figure 5.27 Representative inhibition curve for Reactive Red versus 100nM 2meSATP in CHO-K1-hP2Y₁₁ clone 13

The response to 100nM 2meSATP (log value: -4) was tested in the presence of increasing concentrations of Reactive Red, ranging from 10nM to 100 μ M (log value: -8 to -4), at 37°C in clone 13 cells. The results represent the average \pm s.e.m of one independent experiment performed in triplicate, and are expressed as a percentage of the maximum response to 100nM 2meSATP to correct for fluorescence quenching.

5.7.4 The calcium response to 100 μ M 2meSATP in the presence of increasing concentrations of Reactive Red

The response to 100 μ M 2meSATP (log value: -4) was tested in the presence of increasing concentrations of Reactive Red, ranging from 10nM to 100 μ M (log value: -8 to -4), in clone 13. To assess fluorescence quenching due to Reactive Red, the baseline fluorescence (F_0) of the control wells and the cells pre-incubated with different antagonist dilutions was calculated and is shown in figure 5.28A. One-way ANOVA analysis revealed a statistically significant difference between the control F_0 and the baseline fluorescence detected in the presence of the maximum concentration of antagonist tested, 100 μ M Reactive Red (****; p value < 0.0001), indicating that this concentration exerted a quenching effect. Figure 5.28 B. displays a representative time course of the Reactive Red and 100 μ M 2meSATP inhibition curve in clone 13 cells. Reactive Red concentrations 10nM to 10 μ M (log value: -8 to -5) did not alter the agonist response. In contrast, the maximum concentration of antagonist tested, namely 100 μ M 2meSATP, completely suppressed the response to the agonist.

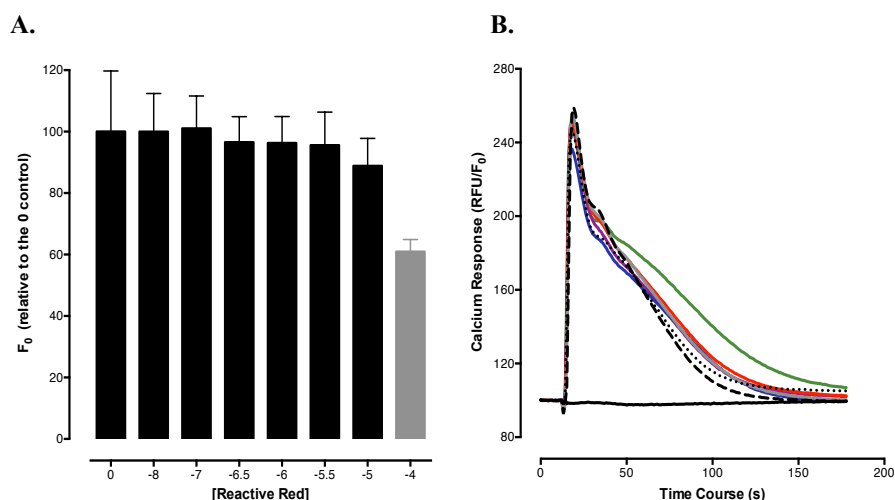


Figure 5.28 Time dependence of the response to 100µM 2meSATP in the presence of increasing concentrations of Reactive Red in CHO-K1-hP2Y₁₁ clone 13

The effect of increasing concentrations of Reactive Red on the calcium response to 100µM 2meSATP (log value: -4) was tested at 37°C in CHO-K1-hP2Y₁₁ clone 13. *A.* Quenching of the baseline calcium fluorescence as a function of Reactive Red concentration in CHO-K1-hP2Y₁₁ clone 13. The level of basal calcium fluorescence (F_0) observed in CHO-K1-hP2Y₁₁ clone 13 cells prior to the addition of 100µM 2meSATP (log value: -4) was analyzed in the absence (0) and presence of increasing concentrations of Reactive Red. The results represent the average of three independent experiments each performed in quadruplicate and were normalized against the (0) control F_0 value. *B.* Reactive Red against 100µM 2meSATP inhibition curves in CHO-K1-hP2Y₁₁ clone 13. The calcium response to 100µM (log value: -4) 2meSATP was measured over time in the presence of increasing concentrations of the P2Y-selective antagonist Reactive Red in CHO-K1-hP2Y₁₁ clone 13 cells. The log₁₀ concentrations of Reactive Red used were: -4 (—), -5 (---), -5.5 (—), -6 (—), -6.5 (—), -7 (—) and -8 (—). The calcium fluorescence elicited by the 100µM 2meSATP control is also shown (···). The traces represent the mean calcium response obtained from one independent experiment performed in quadruplicate.

The quenching effect of the antagonist was corrected by transforming the inhibition datasets against the maximum response to 100µM 2meSATP. Non-linear regression was performed as per section 5.7.1 and the average inhibition curve for Reactive Red against 100µM 2meSATP is shown in Figure 5.29. The Prism software was unable to fit a curve to the inhibition data, for which it was not possible to calculate an IC₅₀ value, and the points were represented with a connecting line.

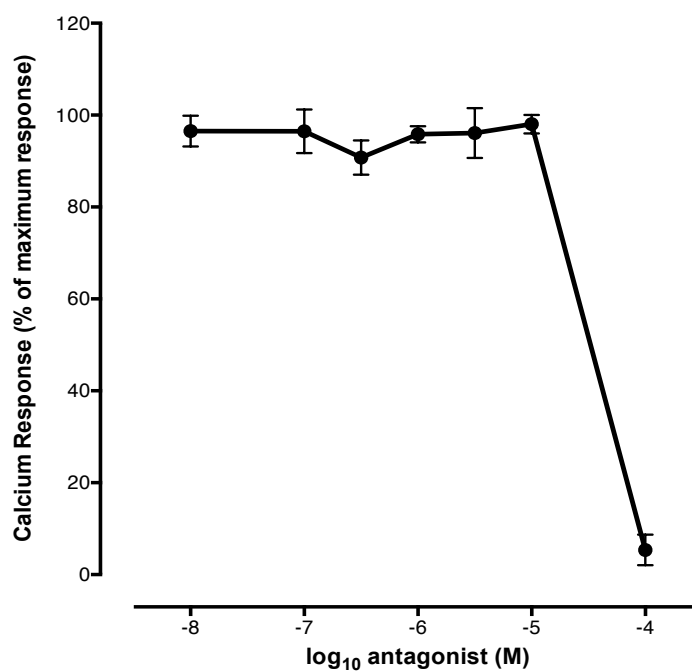


Figure 5.29 Reactive Red inhibits the response to 100 μ M 2meSATP in CHO-K1-hP2Y₁₁ clone 13

The response of clone 13 cells to 100 μ M 2meSATP (log value: -4) in the presence of increasing concentrations of Reactive Red was measured at 37°C. These results represent the average \pm s.e.m of three independent experiments each performed in quadruplicate and are expressed as a percentage of the maximum response to 100 μ M 2meSATP to correct for fluorescence quenching.

5.8 Conclusion

This chapter focused on antagonist action against ADP, 2meSATP and BzATP responses in the high-expressing CHO-K1-hP2Y₁₁ clone 13. The used antagonists were 1) MRS 2179, 2) NF 340 and 3) Reactive Red. The antagonist experiments were divided into two distinct experimental setups. The inhibitors were first tested using Schild experiments following which inhibition experiments were conducted. The objective behind this design was to investigate the components of the biphasic ADP and 2meSATP curves in clone 13 to determine whether tested antagonists would affect the high versus low affinity sites of the curves differently. This could help identify the population(s) of receptors involved in these sites.

Four Schild experiments were performed in clone 13: 1) ADP and MRS 2179, 2) 2meSATP and MRS 2179, 3) ADP and NF 340 and 4) ADP and Reactive Red. MRS 2179 resulted in a rightward shift of the ADP and 2meSATP responses and appeared to affect the high affinity site of the curve only. NF 340 did not alter the response of clone 13 to ADP. Reactive Red completely suppressed the biphasic ADP response, thus

inhibiting both sites of this response. The K_B and pA_2 values of MRS 2179, NF 340 and Reactive Red obtained from the Schild experiments are displayed in Table 5.5.

Schild	K_B ($\mu\text{M} \pm \text{s.e.m}$)	pA_2
ADP + MRS 2179	0.5 ± 0.2	6.4 ± 0.2
2meS _{ATP} + MRS 2179	22 ± 13	5.4 ± 0.5
ADP + NF 340	ND	ND
ADP + Reactive Red	1.1 ± 0.2	6 ± 0.1

Table 5.5 The K_B and IC_{50} values measured from Schild experiments in CHO-K1-hP2Y₁₁ clone 13

The K_B and IC_{50} values obtained from five Schild experiments conducted in clone 13 are displayed in this table. MRS 2179 was found to be a competitive inhibitor of the biphasic ADP and 2meS_{ATP} responses in clone 13. Reactive Red competitively inhibited the biphasic ADP response. NF 340, on the other hand, did not alter the sensitivity of clone 13 cells to ADP. The ND sign (not determined) refers to antagonists that failed to inhibit the calcium response and for which it was not possible to determine K_B and pA_2 values.

Inhibition experiments were then performed to examine antagonist action against the high versus low affinity sites of the biphasic ADP and 2meS_{ATP} curves individually as well as against the monophasic BzATP response. Eleven inhibition experiments were conducted and are shown in Table 5.6, which displays the IC_{50} values measured for each experiment. MRS 2179 competitively inhibited the response to 100nM ADP, which corresponds to the high affinity site of the ADP curve, but did not affect the response to 100 μ M ADP, which corresponds to agonist activity at the low affinity site of the curve. Similarly, MRS 2179 antagonized the high affinity site of the 2meS_{ATP} curve but did not affect the low affinity site of the curve. NF 340, which is reported to antagonize hP2Y₁₁ activity, did not affect the biphasic response to ADP and 2meS_{ATP} in clone 13. Surprisingly, NF 340 did not alter the response of clone 13 to BzATP either. Reactive Red antagonized the response to 100nM ADP but only reduced the response to 100 μ M ADP at maximum concentrations of antagonist. Moreover, it inhibited the response to 100nM 2meS_{ATP} but only suppressed the agonist response of the low affinity site at maximum antagonist concentrations.

These experiments reveal that MRS 2179, NF 340 and Reactive Red exhibited different effects at the high affinity versus low affinity sites of the biphasic ADP and 2meS_{ATP} curves in clone 13. This difference might be due to the presence of two distinct receptor populations with differing agonist affinities at each site, as opposed to a single

receptor population with two separate binding sites. In summary, the Schild and inhibition experiments performed in this chapter demonstrate that:

Inhibition Curve	IC ₅₀ ($\mu\text{M} \pm \text{s.e.m}$)
100nM ADP + MRS 2179	1.8 \pm 0.5
100μM ADP + MRS 2179	None
100nM 2meSATP + MRS 2179	2.3 \pm 0.5
100μM 2meSATP + MRS 2179	None
10μM BzATP + MRS 2179	None
100nM ADP + NF 340	None
100μM ADP + NF 340	None
100nM 2meSATP + NF 340	None
100μM 2meSATP + NF 340	None
10μM BzATP + NF 340	None
100nM ADP + Reactive Red	2.9 \pm 0.8
100μM ADP + Reactive Red	32 \pm 18
100nM 2meSATP + Reactive Red	22 \pm 17
100μM 2meSATP + Reactive Red	None

Table 5.6 The IC₅₀ values of MRS 2179, NF 340 and Reactive Red in CHO-K1-hP2Y₁₁ clone 13

The IC₅₀ values of the inhibition curves for MRS 2179, NF 340 and Reactive Red in clone 13 are shown in this table. MRS 2179 inhibited the calcium response to 100nM ADP and 100nM 2meSATP in clone 13 cells. NF 340 had no effect on the calcium response to ADP, 2meSATP and BzATP in clone 13 while Reactive Red altered the calcium response to 100nM ADP, 100 μM ADP and 100nM 2meSATP.

Chapter 6

Discussion

6.1 Introduction

The P2Y₁ and P2Y₁₁ receptors are closely related purinergic receptors that have been found to regulate the relaxation of smooth muscle cells (SMCs) in the taenia coli (174). Co-immunoprecipitation experiments have demonstrated that these receptors form a heteromer in HEK-293T cells and that dimerization induces the co-internalization of hP2Y₁₁, which does not internalize on its own following receptor activation (55). This discovery is exciting as it suggests that P2Y₁ and P2Y₁₁ oligomers might exist in the plasma membrane of SMCs and partake in their relaxation, implying that the P2Y₁:P2Y₁₁ dimer could be a potential target for anti-obesity drugs. To better understand the interaction between these receptors, recombinant models co-expressing P2Y₁ and hP2Y₁₁ were established in CHO-K1 cells and comprised endogenous P2Y₁ and transfected hP2Y₁₁. Two different CHO-K1-hP2Y₁₁ clones: 1) a clone expressing a low density of hP2Y₁₁ and 2) a clone expressing a high density of hP2Y₁₁, were subsequently selected and investigated. The rationale behind this endeavour was to generate two distinct receptor landscapes to mimic possible purinoceptor microenvironments in the SMCs of taenia coli cells, where the relative expression levels of P2Y₁ and P2Y₁₁ remain unknown. Pharmacological characterization of the two cell lines might reveal whether a change in the density of one receptor could affect the signalling of its partner receptor. Additionally, two control cell lines expressing one receptor each, namely 1321N1-hP2Y₁ and 1321N1-hP2Y₁₁, were created and characterized for comparison with the co-expressing P2Y₁ and hP2Y₁₁ systems.

6.2 The effect of co-expression on the BzATP response in CHO-K1-hP2Y₁₁ clones 6 and 13

6.2.1 The density of hP2Y₁₁ receptors affects the magnitude of the response to BzATP in clones 6 and 13

To determine whether the density of transfected hP2Y₁₁ affects the calcium response of the clones to BzATP, a potent hP2Y₁₁ agonist, the time course of the response to 100µM BzATP was analysed in the high-expressing clone 13 versus the low-expressing clone 6. As Figure 3.11 shows, the increase in calcium fluorescence was three

times higher in clone 13 than clone 6, as reflected by the large difference in the area under the curves (226,872). These results imply that as the levels of hP2Y₁₁ expression are increased, the exposure to a fixed concentration of BzATP increases as seen in clone 13. This could be due to the presence of a bigger population of hP2Y₁₁ receptors at the plasma membrane of this clone, resulting in more agonist binding and the activation of a larger reserve of G_{q/11} proteins. This, in turn, could cause more calcium release from intracellular stores, inducing a higher peak of calcium fluorescence in clone 13 versus 6.

6.2.2 BzATP is more potent in CHO-K1-hP2Y₁₁ clones 6 and 13 as compared to 1321N1-hP2Y₁₁

Despite the difference in the magnitude of the response in clones 13 and 6, BzATP displayed a similar potency at hP2Y₁₁ in the two clones, as demonstrated by the absence of a statistically significant difference between BzATP potency in clones 13 ($1.27 \pm 0.15 \mu\text{M}$) and 6 ($0.98 \pm 0.12 \mu\text{M}$) (ratio: 1.28; p value = 0.19). This indicates that an increase in P2Y₁₁ concentration does not necessarily correlate with an increase in monomeric P2Y₁₁, therefore the EC₅₀ remains unchanged.

Comparison with assays conducted in the control 1321N1-hP2Y₁ and 1321N-hP2Y₁₁ cells shows that BzATP does not stimulate the hP2Y₁ receptor. However, it activates the hP2Y₁₁ receptor expressed in 1321N1-hP2Y₁₁ cells with a potency of $3.1 \pm 0.26 \mu\text{M}$, which is statistically significantly different from this agonist's potency in clones 13 and 6 (**; p value = 0.0028; **, p value = 0.0012, respectively). The BzATP potency calculated in the studied 1321N1-hP2Y₁₁ cells agrees with a previously published EC₅₀ value for BzATP, namely $4.37 \pm 1.65 \mu\text{M}$, obtained from calcium experiments in 1321N1-hP2Y₁₁ cells (174) (p value = 0.2939). This published value is also statistically significantly different from the BzATP potency in clones 13 and 6 (**, p value = 0.0094). In 1321N1-hP2Y₁₁, the BzATP curve had a Hill slope of 1, indicating that agonist binding occurred at a single binding site. In clones 13 and 6 however, the Hill slopes were 1.59 ± 0.23 and 1.28 ± 0.07 . These values are greater than 1, which suggests possible positive cooperativity in agonist binding to the receptor or the presence of multiple binding sites.

These results show that, while BzATP is more potent in the clones as compared to the control 1321N1-hP2Y₁₁ cells, different levels of hP2Y₁₁ expression in CHO-K1-hP2Y₁₁ clones 13 versus 6 do not affect BzATP potency, indicating that potency is

independent of receptor density in the co-expressing cell lines. The different potency in clones 13 and 6 versus the control could result from distinct active receptor states of hP2Y₁₁ in the clones versus 1321N1-hP2Y₁₁ cells (226). These states could arise from conformational changes of hP2Y₁₁ due to physical interaction or functional crosstalk with P2Y₁ in the clones, leading to positive cooperativity and increased affinity of hP2Y₁₁ for BzATP. In conclusion, crosstalk could stabilize hP2Y₁₁ in a conformation with increased affinity for BzATP in the clones as compared to the control cells (227).

6.3 The effect of co-expression on the calcium response to ATP, ATP γ S and UTP in clones 13 and 6

6.3.1 Co-expression does not alter the potency of ATP at hP2Y₁₁ in clones 6 and 13

ATP has been reported to activate P2Y₁, P2Y₂ and P2Y₁₁ (210) receptors, all of which are expressed in CHO-K1-hP2Y₁₁ clones 13 and 6 (178, 208). The response to ATP was tested in the clones and was monophasic sigmoidal in both cases. There was no statistically significant difference in ATP potency in clones 13 versus 6 (47 ± 20 nM and 33 ± 6 nM, respectively; p value = 0.54). The Hill slope of the ATP curve was 0.75 ± 0.13 in clone 6, suggesting the existence of multiple binding sites (210, 228), and 1.1 ± 0.3 in clone 13. Closer inspection of the individual Hill slopes in clone 13 (0.61, 0.95 and 1.7) shows that two out of three trials point to positive cooperativity in agonist binding. This suggests the presence of multiple receptor sites for ATP in clones 13 and 6, consistent with the expression of P2Y₁, P2Y₂ and hP2Y₁₁ in these clones.

The ATP response in 1321N1-hP2Y₁₁ and 1321N1-hP2Y₁ was sigmoidal monophasic with a Hill slope of 1 in both cell lines. This response was more potent in 1321N1-hP2Y₁ versus 1321N1-hP2Y₁₁ cells (151 ± 40 nM and 9 ± 1.4 μ M, respectively; **, p value = 0.0028), suggesting that hP2Y₁ has greater affinity for ATP than hP2Y₁₁. ATP was more potent in clones 13 and 6 as compared to 1321N1-hP2Y₁₁ (**; p value = 0.0027 for both clones) and 1321N1-hP2Y₁ (*; p value = 0.0356).

The obtained values were compared with ATP potencies published in the literature. One of the first studies to describe an ATP response in CHO-K1 cells ($EC_{50} = 2.3 \pm 0.5$ μ M) associated this response with the activation of an endogenous P2Y₂ receptor (208). Another published value detected from calcium measurements in 1321N1-hP2Y₂

cells (176nM) (229) agreed with the ATP potency in clones 13 and 6, further highlighting the contribution of P2Y₂ to the ATP response. ATP potencies calculated from recent experiments in CHO-K1 cells using first and second generation calcium assay kits, i.e. 62.6nM and 72.6nM, (230) also matched the values measured in the clones, indicating that ATP potency in CHO-K1 cells is not affected by hP2Y₁₁ expression and density. Studies conducted by Communi et al. and Qi et al. in 1321N1-hP2Y₁₁ and CHO-K1-hP2Y₁₁ cells revealed that ATP promotes IP₃ but also cAMP generation in both cell lines (176-178, 211), which confirms the activation of hP2Y₁₁ by ATP. Interestingly, these studies also found that ATP was more potent in CHO-K1-hP2Y₁₁ versus 1321N1-hP2Y₁₁ cells (178), in agreement with the results observed in this project. In summary, analysis of the results and comparison with the literature show that the ATP response in clones 13 and 6 is most likely mediated by three receptors, namely endogenous haP2Y₁ and haP2Y₂ receptors and transfected hP2Y₁₁ receptors. This response is monophasic sigmoidal with a single EC₅₀ value, implying that the potencies of ATP at all three receptors overlap.

6.3.2 Co-expression does not alter the potency of ATP_γS at hP2Y₁₁ in clones 6 and 13

ATP_γS, like ATP, has been reported to activate P2Y₁, P2Y₂ and P2Y₁₁ receptors (210). The ATP_γS response in clones 13 and 6 was monophasic sigmoidal with a single EC₅₀ value. There was no statistically significant difference in ATP_γS potency in clones 13 versus 6 (274 ± 48nM and 260 ± 39nM, respectively; p value = 0.54), indicating that the density of transfected hP2Y₁₁ does not alter the calcium response to ATP_γS in the clones. The Hill slopes of the ATP curves were 1.16 ± 0.13 in clone 6 and 1.3 ± 0.1 in clone 13, suggesting the existence of multiple binding sites or positive cooperativity of the response. The ATP_γS potency in 1321N1-hP2Y₁₁ and 1321N1-hP2Y₁ cells (3.2 ± 0.26μM and 15.6 ± 3.6nM, respectively) was statistically significantly different from its potency in the clones. In fact, ATP_γS was more potent in clones 13 and 6 versus 1321N1-hP2Y₁₁ cells (***, p value = 0.0004 and ***, p value = 0.0003, respectively) and less potent in clones 13 and 6 versus 1321N1-hP2Y₁ cells (**, p value = 0.0058 and **, p value = 0.0033, respectively).

These results indicate that clones 13 and 6 display an ATP_γS profile specific to them and distinct from that of individual hP2Y₁ and hP2Y₁₁ receptors. The ATP_γS response in the clones is probably mediated by three different receptors (haP2Y₁, haP2Y₂

and hP2Y₁₁) and possesses a single EC₅₀ value, indicating that the agonist's potencies at the multiple binding sites overlap. The marked discrepancy in ATP γ S potency between 1321N1-hP2Y₁₁ and 1321N1-hP2Y₁ cells versus clones 13 and 6 could arise from differences in receptor subtypes among distinct species (human versus hamster), varying expression levels of receptors in the studied cells or the co-expression of hP2Y₁ and hP2Y₁₁, leading to enhanced P2Y₁₁ affinity and reduced P2Y₁ affinity of for ATP γ S.

6.3.3 The UTP response assumes a hP2Y₂-like character in clones 6 and 13

UTP is a potent agonist of the P2Y₂ receptor (210) but has also been reported to activate hP2Y₁₁ (153). The UTP response was tested in CHO-K1-hP2Y₁₁ clones 13 and 6, resulting in monophasic sigmoidal curves with a single EC₅₀ value each (89 ± 22 nM and 67 ± 22 nM, respectively). These values were not statistically significantly different (p value = 0.5221), signifying that the levels of hP2Y₁₁ expression do not alter the calcium response to UTP in the clones. The Hill slope of the UTP curve was 1.98 ± 0.6 in clone 6 and 1.2 ± 0.2 in clone 13, implying the presence of multiple binding sites to UTP or positive cooperativity. The UTP response was also investigated in the 1321N1-hP2Y₁₁ and 1321N1-hP2Y₁ controls. UTP failed to induce a calcium response in 1321N1-hP2Y₁₁ cells, which contradicts previous findings published in the literature (153). However, UTP produced a sigmoidal monophasic response in 1321N1-hP2Y₁ cells (EC₅₀ value= 382nM), indicating that this agonist activates hP2Y₁ receptors.

The UTP response observed in the various cell lines was compared with potencies reported in the literature. One of the first descriptions of UTP activity at P2Y₂ in CHO-K1 cells found a potency (2.8 ± 0.6 μ M) (208) that is different from the UTP potency detected in clones 13 and 6. A recent study in 1321N1-hP2Y₂ cells described a UTP potency of 73nM, in agreement with the values measured in the clones, thus highlighting the P2Y₂ component of the UTP response. The literature was ambivalent regarding UTP action at hP2Y₁₁ receptors. For instance, White et al., as well as previous assays performed in this laboratory, detected a UTP response in 1321N1-hP2Y₁₁ cells (153). In contrast, Morrow et al. failed to reproduce a UTP response in 1321N1-hP2Y₁₁ cells although the two laboratories (White and Morrow) utilized the same cell line handed from one laboratory to the other (229). This finding agrees with the lack of UTP action in 1321N1-hP2Y₁₁ cells observed in the present study. According to Morrow et al., a possible explanation for the UTP response detected by White et al. is contamination of the UTP solution with a

non-nucleotide agent acting at a non-purinergic receptor, thus triggering the observed calcium response (229).

In summary, the UTP response in CHO-K1-hP2Y₁₁ clones 13 and 6 was monophasic, hP2Y₂-like and independent of the levels of expression of hP2Y₁₁ receptors. Hill slope analysis suggested the presence of multiple binding sites or positive cooperativity. In fact, UTP not only activated P2Y₂, but also acted at P2Y₁, as confirmed by the UTP response observed in 1321N1-hP2Y₁ cells.

6.4 Co-expression reduces the affinity of hP2Y₁₁ for $\alpha\beta$ meATP and $\beta\gamma$ meATP in clones 6 and 13

The ATP derivatives $\alpha\beta$ meATP and $\beta\gamma$ meATP failed to produce a calcium response with a clear maximum in clones 13 and 6, and it was not possible to fit a curve to the data generated by these agonists. Control 1321N1-hP2Y₁ cells did not respond to $\alpha\beta$ meATP and $\beta\gamma$ meATP, indicating that these derivatives do not activate the hP2Y₁ receptor. In contrast, both agonists elicited a full monophasic calcium response in the control 1321N1-hP2Y₁₁ cells, in agreement with previous experiments performed in the laboratory using 1321N1-hP2Y₁₁ cells. The discrepancy in the behaviour of $\alpha\beta$ meATP and $\beta\gamma$ meATP in clones 13 and 6 versus 1321N1-hP2Y₁₁ cells suggests that co-expression could modify the binding properties of hP2Y₁₁ through possible interactions with P2Y₁ and/or P2Y₂, thus producing hP2Y₁₁ active states with a lower affinity for these methylene phosphate ligands.

6.5 Co-expression modifies the rank order of agonist potency in clones 6 and 13

The order of agonist potency in the studied cell lines (clone 6, clone 13, 1321N1-hP2Y₁₁ and 1321N1-hP2Y₁) were compared to determine whether co-expression and different levels of hP2Y₁₁ receptor expression affected agonist responses in clones 6 and 13. In the control 1321N1-hP2Y₁₁ cells, the order of agonist potency using 2meSATP as a reference was:

BzATP (0.3) \approx ATP γ S (0.3) > ATP (0.86) > 2meSATP (1) > $\beta\gamma$ meATP (6.1) > $\alpha\beta$ meATP (6.74).

It is consistent with the order of agonist potency previously reported for the hP2Y₁₁ receptor by Communi et al. (177). In the control hP2Y₁ cells, the order of agonist potency using 2meSATP as a reference was:

2meSATP (1) > ADP (1.23) > ATP γ S (3.32) > ATP (32) > UTP (81)

It matches the order of agonist potency reported by Schachter et al. and Filtz et al. (2meSATP > ADP > ATP γ S > ATP) for the hP2Y₁ receptor (231, 232). However, it disagrees with the order identified by Palmer et al. (ADP > 2meSATP > ATP) in which ADP had a higher potency in 1321N1-hP2Y₁ cells relative to 2meSATP (157). In the CHO-K1-hP2Y₁₁ clones, the rank order of potency of the tested agonists relative to 2meSATP was:

Clone 6: **2meSATP (1) > ATP (1.57) > ADP (1.67) > UTP (3.2) > ATP γ S (12) > BzATP (47)**

Clone 13: **2meSATP₁ (1) > ATP (2.2) > UTP (4.2) > ADP₁ (5.2) > ATP γ S (13) > BzATP (60) > ADP₂ (604) \approx 2meSATP₂ (639)**

Comparison of these results shows that co-expression does not modify the rank order of potency of 2meSATP in the co-expressing CHO-K1-hP2Y₁₁ clones 13 and 6 versus 1321N1-hP2Y₁ cells. However, higher levels of hP2Y₁₁ expression introduce a novel site of 2meSATP responsiveness in clone 13 that is 639 times less potent than the original site. In contrast, co-expression reduces the potency of hP2Y₁ for ADP, decreasing it from second most potent agonist in 1321N1-hP2Y₁ cells to third and fifth in clones 6 and 13. The increased levels of hP2Y₁₁ expression in clone 13 also introduce a second site of ADP responsiveness with lower agonist affinity. Furthermore, ATP is more potent in clones 13 and 6 as opposed to the 1321N1-hP2Y₁ and 1321N1-hP2Y₁₁ cells, indicating that the P2Y₁-P2Y₂-P2Y₁₁ co-expressing system has a higher affinity for ATP as compared to P2Y₁- or P2Y₁₁-only cells. This agrees with previously published findings by Qi et al. who detected an enhanced ATP response in CHO-K1-hP2Y₁₁ versus 1321N1-hP2Y₁₁ cells, explained by the presence of a larger hP2Y₁₁ receptor reserve or increased coupling of the receptor with the G_{q/11} pathway in CHO-K1-hP2Y₁₁ (178).

Comparison of the order of agonist potencies in CHO-K1-hP2Y₁₁ clones 13 and 6, 1321N1-hP2Y₁ and 1321N1-hP2Y₁₁ reveals that the agonist profile of clones 13 and 6 is a hybrid of P2Y₁ and hP2Y₁₁ signalling. In fact, co-expression seems to:

- 1- Increase the affinity of hP2Y₁₁ for BzATP, ATP, ATP γ S and reduce its affinity of for $\alpha\beta$ meATP and β meATP
- 2- Decrease the affinity of P2Y₁ for ATP γ S and ADP and enhance its affinity for ATP
- 3- Create novel sites of ADP and 2meSATP affinity with lower agonist potencies

Co-expression thus produces active P2Y₁ and hP2Y₁₁ receptor states with altered agonist affinities, leading to a unique pharmacological profile distinct from that of the individual receptors.

6.6 Co-expression alters the affinity of NF 340 to hP2Y₁₁ in clones 6 and 13

To determine the effect of co-expression on the antagonist profile of hP2Y₁₁, the response of clones 13 and 6 to 10 μ M BzATP was tested in the presence of increasing concentrations of NF 340, which inhibits hP2Y₁₁ activity with 520-fold selectivity over other purinoceptors (221). NF 340 failed to inhibit the calcium response to BzATP in both clones 13 (Figure 5.20) and 6 (data not shown). In contrast, NF 340 antagonised the response to 10 μ M BzATP in the control 1321N1-hP2Y₁₁ cells, showing that this compound was active. The average pIC₅₀ value for this antagonist in 1321N1-hP2Y₁₁ cells (6.62 \pm 0.09) agreed with the previously published pIC₅₀ value for this antagonist, i.e. 6.43 (221). NF 340 did not affect the response of 1321N1-hP2Y₁ cells to ADP, revealing that it is not an inhibitor of the P2Y₁ receptor. Furthermore, NF 340 did not inhibit the biphasic response to ADP and 2meSATP in clone 13. As the inhibition and Schild experiments were conducted in all cell lines using the same vial of NF 340 within the same period of time, it can be concluded that NF 340 is unable to inhibit the hP2Y₁₁ receptor when this receptor is co-expressed in the recombinant CHO-K1-hP2Y₁₁ clones. Thus, co-expression modifies the antagonist profile of hP2Y₁₁ regardless of its level of expression in the clones. Loss of NF 340 antagonism could result from a modification of the binding pocket of the receptor that alters its affinity for antagonist binding.

6.7 The high-affinity site of the response to ADP in CHO-K1-hP2Y₁₁ clone 13 is endogenous P2Y₁ receptor-mediated

6.7.1 The high-affinity site of the biphasic response in clone 13 has reduced affinity for ADP

In-depth analysis of the calcium response to BzATP, ATP and ATP γ S in CHO-K1-hP2Y₁₁ clones 13 and 6 shows that different levels of hP2Y₁₁ expression do not alter the calcium response of the clones to these agonists. However, co-expression seems to enhance the affinity of hP2Y₁₁ for these ligands in the clones as compared to 1321N1-hP2Y₁₁ cells. In contrast, ADP and 2meSATP triggered an additional layer of complexity in clone 13. ADP, a potent P2Y₁ agonist (158, 231, 233, 234), engendered a biphasic response with two distinct potencies in this clone, as compared to a monophasic response in clone 6. Mathematical analysis revealed a statistically significant difference between the ADP potency at the high-affinity site ($110 \pm 6\text{nM}$) versus the low-affinity site ($12.7 \pm 1.8\mu\text{M}$) of the curve in clone 13 (**; p value = 0.002), signifying that two distinct binding sites are involved in the biphasic ADP response.

The ADP potencies at the high and low affinity sites of the biphasic ADP response in clone 13 were statistically significantly different from the ADP potency in clone 6 (*; p value = 0.0246 and**; p value = 0.002, respectively). In the control 1321N1-hP2Y₁₁ cells, the ADP response attained 40% of the control carbachol response only and did not produce a measurable EC₅₀ value, indicating that hP2Y₁₁ does not fully respond to ADP. In contrast, ADP evoked a marked response in 1321N1-hP2Y₁ cells, the potency of which ($5.6 \pm 1\text{nM}$) matched the ADP potency in clone 6 (p value = 0.1989), indicating that human and hamster P2Y₁ have a similar affinity for ADP at low levels of hP2Y₁₁ expression. The ADP potency in 1321N1-hP2Y₁ cells was statistically significantly different from the ADP potency at the high and low affinity sites of the biphasic ADP response in clone 13 (****; p value < 0.0001 and **; p value = 0.002, respectively). These comparison indicate that higher levels of hP2Y₁₁ expression influence the sensitivity of CHO-K1-hP2Y₁₁ cells to ADP, reducing the affinity of endogenous P2Y₁ for ADP and producing a novel site of ADP responsiveness as seen in clone 13.

Comparison with the literature shows that the ADP response in untransfected CHO-K1 cells based on intracellular calcium measurements is monophasic (EC₅₀ value= $69 \pm 14\mu\text{M}$) (208). In CHO-K1-hP2Y₁₁ cells, Communi et al. found that ADP increased IP₃

content only without activating the cAMP pathway. Similarly, Qi et al. found that ADP increased calcium fluorescence in CHO-hP2Y₁₁ cells but failed to elicit a cAMP response with a clear maximum (178, 211). Since the transfected receptor did not fully respond to the agonist, it was not possible to calculate an EC₅₀ value for ADP in this cell line (178, 211). In contrast, the ADP potencies in different 1321N1-hP2Y₁ cell lines, i.e. 10nM (157) and 18.3nM (235), agreed with those observed in clone 6 and 1321N1-hP2Y₁ cells (p value = 0.3788). The ADP potency in these cell lines is thus consistent with published values and the ADP response in clone 6 can be attributed to the P2Y₁ receptor. On the other hand, the ADP potency at the low and high affinity sites of the biphasic ADP response in clone 13 differs from the ADP potency in clone 6, 1321N1-hP2Y₁ cells and published values.

A plausible explanation for the observed results is that high levels of hP2Y₁₁ expression in CHO-K1-hP2Y₁₁ cells provoke a conformational change in P2Y₁ that reduces its affinity for ADP and they generate a novel site of ADP affinity distinct from P2Y₁ and hP2Y₁₁. This low affinity site is a function of hP2Y₁₁ but assumes a P2Y₁-like character given its responsiveness to the P2Y₁ agonist ADP. Since hP2Y₁₁ 'density' is the only known variable in clones 6 and 13, it can be hypothesized that the increased levels of hP2Y₁₁ expression in clone 13 might trigger a physical interaction between the P2Y₁ and hP2Y₁₁ receptors, responsible for the formation of this novel site with altered binding and agonist properties.

6.7.2 The high-affinity site of the ADP response is inhibited by MRS 2179

To confirm that the high affinity site of the biphasic ADP curve in clone 13 is endogenous P2Y₁, the response to increasing concentrations of ADP was tested in the presence of four different concentrations of MRS 2179, a well-described P2Y₁ antagonist (170, 236-238). Increasing antagonist concentrations shifted the ADP response to the right and gradually abolished the biphasic response. The ADP potencies at the high affinity site of the control ADP and ADP+1μM MRS 2179 curves were similar but differed from the ADP potency at the low-affinity site of the curves. The higher concentrations of MRS 2179, i.e. 10 and 100μM, shifted the ADP sensitivity of the high-affinity site to the right, resulting in a monophasic response with the same ADP sensitivity as the low-affinity site of the response. The order of ADP potency at the various curves is:

$$\text{ADP (EC}_{50-1}) \approx \text{ADP (EC}_{50-1}) + 1\mu\text{M MRS 2179} > \text{ADP (EC}_{50-2}) \approx \text{ADP (EC}_{50-2}) + 1\mu\text{M MRS 2179} \approx \text{ADP} + 10\mu\text{M MRS 2179} \approx \text{ADP} + 100\mu\text{M MRS 2179}$$

These results show that MRS 2179 inhibits the high affinity site of the biphasic ADP response without affecting its low-affinity site. This suggests that the orthosteric binding sites at the high versus low affinity sites of the biphasic curve are distinct. The mean K_B ($500 \pm 200\text{nM}$) and pA_2 (6.4 ± 0.2) values for MRS 2179 in clone 13 agreed with previously published K_B , i.e. 102nM (238, 239) and 177nM (151, 210), and pA_2 values, i.e. 6.55 ± 0.05 (170), for this antagonist at $hP2Y_1$. Furthermore, increasing concentrations of MRS 2179 competitively antagonized the response to 100nM ADP in clone 13, in agreement with its inhibitory action against ADP in $1321N1-hP2Y_1$ cells and published data (236).

The biphasic ADP response in clone 13 was also tested in the presence of Reactive Red, previously reported to antagonize $P2Y$ receptors (174, 224, 240). The addition of $10\mu\text{M}$ Reactive Red shifted the biphasic ADP response to the right, converting it to a monophasic one, while the maximum antagonist concentration completely abolished it (Figure 5.8). This suggests that Reactive Red blocked the ADP response at both sites of the curve in a non-competitive fashion, in agreement with the mode of action previously reported for this antagonist (224). Furthermore, increasing concentrations of Reactive Red inhibited the response to 100nM ADP in a concentration-dependent fashion. This concurs with previously published data showing that Reactive Red inhibited the relaxations mediated by a $P2Y_1$ -like receptor in the guinea pig taenia coli (224). In contrast, the $hP2Y_{11}$ antagonist NF 340 did not affect the ADP sensitivity of the high affinity site of the ADP curve in clone 13. In summary, these antagonist experiments show that the high-affinity site of the biphasic ADP curve in clone 13 is inhibited by MRS 2179 and Reactive Red, both previously reported to antagonize $P2Y_1$ -mediated calcium responses, but is unaffected by NF 340, a $hP2Y_{11}$ inhibitor. Consequently, it can be hypothesized that the high-affinity site of the ADP response in clone 13 exhibits marked $P2Y_1$ -like properties and most probably consists of $P2Y_1$ receptors.

6.8 The high affinity site of the response to 2meSATP in CHO-K1-hP2Y₁₁ clone 13 is endogenous P2Y₁

6.8.1 The high-affinity site of biphasic 2meSATP curve in clone 13 has P2Y₁-like character

Similarly to ADP, the ATP derivative 2meSATP also evoked a complex biphasic response in clone 13 as opposed to a monophasic response in clone 6. The 2meSATP potencies at the high versus low affinity sites of the biphasic curve in clone 13 were statistically significantly different (****; p value < 0.0001). Unlike the ADP sensitivity of endogenous P2Y₁ in clone 13, which was altered by higher levels of hP2Y₁₁ expression in this clone compared to clone 6, the 2meSATP potency at the high-affinity site of the biphasic response in clone 13 was the same as its potency in clone 6 (p value = 0.9482). In contrast, the agonist potency of the low affinity site was statistically significantly different from that of clone 6 (****; p value < 0.0001). These results suggest that the same population of receptors is active at the high-affinity site of clone 13 and in clone 6 while a distinct population of receptors is acting at the low-affinity site of clone 13.

Comparison with the 2meSATP response in control 1321N1-hP2Y₁₁ and 1321N1-hP2Y₁ cells shows that the 2meSATP potency of the high-affinity site of the response in clone 13 was similar to its potency in 1321N1-hP2Y₁ cells (p value = 0.1654), suggesting that P2Y₁ could be responsible for the calcium response of this site. On the other hand, the agonist potency of the low affinity site of the biphasic 2meSATP curve in clone 13 was similar to its potency in 1321N1-hP2Y₁₁ cells (p value = 0.319), implying that hP2Y₁₁ or an hP2Y₁₁-like binding site might be operating at this site. Various mentions of 2meSATP action at purinoceptors were found in the literature. A pharmacological study in CHO-K1 cells described a partial 2meSATP response at a P2U receptor (now known as P2Y₂) (208) while the detailed analysis of adenosine triphosphate action in 1321N1-hP2Y₁ cells found a 2meSATP potency of 116nM (157). A third paper reported a mean 2mesATP potency of 1.36nM in hP2Y₁-expressing cells (235), in agreement with the potency found in 1321N1-hP2Y₁ cells in the present study. 2meSATP assays in CHO-K1-hP2Y₁₁ cells detected an increase in both IP₃ and cAMP content following agonist addition, although the concentration-response curve was monophasic (177, 178). This finding reveals that 2meSATP stimulates hP2Y₁₁ in recombinant cell lines expressing this receptor. It also shows that only high levels of hP2Y₁₁ expression can produce a biphasic

curve and that the appearance of a second site of 2meSATP affinity is a function of hP2Y₁₁ density. Taken together, these results indicate that the high affinity component of the 2meSATP response in clone 13 most likely corresponds to P2Y₁ while its low affinity component corresponds to P2Y₁₁. The two distinct populations of receptors mediating the biphasic response to 2meSATP in this clone thus correlate to two known and characterized receptors (P2Y₁ and hP2Y₁₁), unlike the low affinity site of the ADP response, which harbours an unknown component with novel properties and might be a P2Y₁+P2Y₁₁ hybrid.

6.8.2 The high affinity site of the biphasic 2meSATP curve is inhibited by MRS 2179

The biphasic response to 2meSATP was tested in the presence of the same antagonists used for ADP. The P2Y₁ antagonist MRS 2179 provoked a parallel rightward shift of the biphasic 2meSATP response, converting the biphasic curve into a monophasic one. The antagonist inhibited the high-affinity site of the curve only without affecting the low-affinity site, thus indicating that the high and low affinity sites possess different sensitivities for MRS 2179. Increasing concentrations of MRS 2179 and Reactive Red inhibited the calcium response to 100nM 2meSATP in a concentration-dependent fashion, further confirming that these antagonists inhibit the receptors active at the high affinity site of the 2meSATP response. In contrast, NF 340 failed to alter the calcium response to 100nM 2meSATP in this clone, implying that this antagonist has no effect on the high affinity site of the curve. In summary, the receptors present at the high affinity site of the biphasic 2meSATP curve in clone 13 are inhibited by MRS 2179 and Reactive Red but not by NF 340. Moreover, the 2meSATP potency at these receptors is similar to the 2meSATP potency at hP2Y₁. Thus, these receptors assume P2Y₁-like affinities, indicating that the high affinity site of the biphasic 2meSATP in clone 13 most likely consists of endogenous P2Y₁.

6.9 Pharmacological evidence for P2Y₁ and hP2Y₁₁ interactions

6.9.1 The low-affinity site of the response to ADP and 2meSATP in clone 13 has P2Y₁ and hP2Y₁₁-like characteristics

Agonist experiments in clones 13 versus 6 revealed that the low affinity site of the biphasic ADP and 2meSATP curves is a function of hP2Y₁₁ levels of expression. The

potency of ADP at this site is unique and does not match its potency at the P2Y₁ receptor and other purinoceptors expressed in the recombinant CHO-K1 cells. The 2meSATP potency at this site, however, matches its potency at the human P2Y₁₁ receptor. Schild plots and inhibition experiments in clone 13 showed that the P2Y₁ antagonist MRS 2179 does not antagonise the low affinity site of the biphasic curves, as opposed to its inhibitory action against the P2Y₁-like high-affinity site. The hP2Y₁₁ antagonist NF 340 also failed to alter the calcium response of these low-affinity sites. Hence, the low affinity site of the biphasic curves exhibits P2Y₁-like agonist affinity characterized by ADP responsiveness but a distinct antagonist profile from both P2Y₁ and hP2Y₁₁. In contrast to MRS 2179 and NF 340, 10µM to 100µM Reactive Red abolished the calcium response of the low-affinity site of the biphasic ADP and 2meSATP, in agreement with previous reports of Reactive Red antagonism at P2Y₁ (224) and P2Y₁₁ (174, 224) receptors. In fact, antagonist experiments in the guinea pig taenia coli revealed that Reactive Red depressed αβmeATP relaxations mediated by a P2Y₁₁-like receptor in a non-competitive fashion and with less potency than against the P2Y₁-like receptor (224). This effect is comparable to its action at the low-affinity site of the biphasic ADP and 2meSATP curves where it suppressed agonist response non-competitively and exhibited less potency than at the high-affinity site (19, 224).

In summary, higher levels of hP2Y₁₁ expression provoke the formation of a novel orthosteric site with a distinct pharmacology in clone 13. This low affinity site responds to ADP similarly to P2Y₁, possesses the same 2meSATP potency as hP2Y₁₁, lacks affinity for both the P2Y₁ antagonist MRS 2179 and the P2Y₁₁ inhibitor NF 340 and is inhibited by Reactive Red in an antagonistic fashion similar to its action against P2Y₁₁ in the guinea pig. In the case of the biphasic ADP response, the low-affinity site appears to be a hybrid of endogenous P2Y₁ and transfected hP2Y₁₁ with unique agonist/antagonist affinities (P2Y₁+P2Y₁₁). The low-affinity site of the biphasic 2meSATP curve showcases pharmacological properties similar to those of hP2Y₁₁ in clones 6 and 13 and most likely corresponds to hP2Y₁₁.

6.9.2 The low-affinity site of the response to ADP and 2meSATP results from the interaction between P2Y₁ and hP2Y₁₁ in clone 13

Agonist and antagonist experiments in clones 6 and 13 show that co-expression of P2Y₁ and hP2Y₁₁ affects the pharmacological profile of endogenous P2Y₁ and transfected hP2Y₁₁. Thus, both low and high levels of hP2Y₁₁ expression, represented by clone 6 and

13, increased the affinity of hP2Y₁₁ for BzATP, ATP, ATP γ S and decreased its affinity for $\alpha\beta$ meATP and $\beta\gamma$ meATP. Moreover, they decreased the affinity of P2Y₁ for ATP γ S and caused the loss of NF 340 antagonism at the human P2Y₁₁ receptor. Higher levels of hP2Y₁₁ expression introduced an additional layer of complexity to the co-expressing P2Y₁-hP2Y₁₁ system, resulting in novel sites of ADP and 2meSATP potency and decreased affinity of P2Y₁ for ADP. The low affinity sites of the biphasic curves displayed a lower potency for ADP and 2meSATP than their high-affinity sites and were blocked by Reactive Red only. These findings indicate that P2Y₁ and hP2Y₁₁ might interact when co-expressed in CHO-K1-hP2Y₁₁ clones 6 and 13. This crosstalk could provoke conformational changes in the ligand binding pockets of the receptors leading to altered active receptor states with novel agonist and antagonist affinities. It could also explain the positive cooperativity for ATP, ATP γ S and UTP binding observed in the CHO-K1-hP2Y₁₁ clones whereby P2Y₁ activation would enhance the binding of these agonists to hP2Y₁₁ in the clones as compared to 1321N1-hP2Y₁₁ cells. Co-expression of the two receptors and subsequent communication also abolishes the affinity of NF 340 for hP2Y₁₁ thus modifying the pattern of allosteric modulation of this receptor. Receptor co-expression could also alter the coupling of P2Y₁ and hP2Y₁₁ to cognate G_{q/11} proteins, resulting in further changes in the calcium response.

A plausible explanation for the altered properties of clone 13 may be that high hP2Y₁₁ reserves at the cellular membrane of clone 13 force increased oligomerisation with P2Y₁, leading to the formation of a second site of agonist sensitivity with novel pharmacological properties. An emergent feature of this site is its responsiveness to ADP, which normally exhibits no activity at individual hP2Y₁₁ receptors while a second characteristic is the absence of MRS 2179 and NF 340 antagonism at this site. Studies performed by Ecke et al. have previously reported the existence of a P2Y₁:hP2Y₁₁ oligomer resulting from direct physical interaction between P2Y₁ and P2Y₁₁ in HEK-293 cells (55). This oligomer was characterized using BzATP, MRS 2179 and the P2Y₁₁ antagonist NF 157, revealing that NF 157 was not able to inhibit the BzATP response in co-expressing cells, which concurs with the loss of NF 340 antagonism in clone 13. The researchers concluded that the P2Y₁:hP2Y₁₁ oligomer possesses a distinct pharmacological profile from its constitutive receptors, a notion increasingly supported by recent evidence (55). These discoveries support the conclusion that endogenous P2Y₁ and transfected hP2Y₁₁ form a hetero-oligomer at high levels of hP2Y₁₁ expression in CHO-K1-hP2Y₁₁ clone 13 cells. Furthermore, the current findings suggest that ADP,

2meSATP and Reactive Red bind to this P2Y₁:P2Y₁₁ oligomer active at the low affinity site of the biphasic responses, while MRS 2179 and NF 340 do not bind to it.

Two scenarios can be envisaged. According to the first, the biphasic response to ADP and 2meSATP is mediated by two distinct populations of binding sites: 1) P2Y₁ at the high-potency site of the curves and 2) P2Y₁:hP2Y₁₁ at the low-potency site. According to the second, the entire biphasic ADP response of clone 13 could be mediated by the P2Y₁:hP2Y₁₁ heteromer. In this scenario, the P2Y₁ component of the heteromer would account for the high affinity site of the curve while hP2Y₁₁ would mediate the low affinity response to ADP. This mechanism fits into the two state dimer receptor model described by Casadó et al. (241), according to which conformational modifications in one protomer of the dimer are transmitted to the partner protomer, indicating that the two subunits of the receptor dimer can interact, leading to negative or positive cooperativity (241).

6.10 Predictive analysis of the binding pocket and conformational rearrangements involved in P2Y₁ and hP2Y₁₁ interaction

The modified agonist and antagonist potencies observed in the co-expressing CHO-K1-hP2Y₁₁ clones signify that purinoceptor “cross-talk” provoked conformational reorganizations of the P2Y₁ and hP2Y₁₁ receptor structures. This raises questions as to what domains or amino acid residues of the receptors might have contributed to the altered affinities of the orthosteric sites for certain ligands. Modelling and mutagenesis studies of P2Y₁ and hP2Y₁₁ have uncovered the residues implicated in agonist and/or antagonist recognition and docking. For instance, studies of the human P2Y₁₁ receptor reveal that its binding pocket resides between TM2 and TM7 and is constrained by the residues Leu⁸² (TM2), Phe¹⁰⁹ (TM3), Leu¹¹³ (TM3), Pro³¹¹ (TM7) and Ala³¹³ (TM7) (242, 243). Amino acids involved in ligand binding in this receptor comprise Arg¹⁰⁶ (TM3), Phe¹⁰⁹ (TM3), Ser²⁰⁶ (TM5), Arg²⁶⁸ (TM6), Arg³⁰⁷ (TM6) and Met³¹⁰ (TM7) (242, 243). Residues necessary for ligand recognition include Arg¹⁰⁶ (TM3), Tyr²⁶¹ (TM6), Arg²⁶⁸ (TM6), Arg³⁰⁷ (TM6), Ala³¹³ (TM7) and Glu¹⁸⁶ (EL2) (242, 243). The positively charged arginine residues play a critical role in stabilizing bound ATP through electrostatic interactions with its triphosphate moiety while Ser²⁰⁶ engages in hydrogen bonding interaction with P_γ (242, 243). In light of these structural configurations, a plausible explanation for the increased affinity of hP2Y₁₁ for ATP and its derivatives BzATP and ATP_γS is that interaction with P2Y₁ could shift the residues of the binding cleft away

from TM7. This could in turn permit tighter binding and interaction of the arginine and serine residues of the ligand cavity with the triphosphate moiety of ATP, BzATP and ATP γ S, resulting in greater stability of ligand binding to hP2Y₁₁ and greater agonist potency. This modification of the binding pocket could also account for the lost affinity of NF 340 for hP2Y₁₁. Furthermore, a study by Qi et al. found that mutating Arg²⁶⁸ increases the potency of hP2Y₁₁ for ADP (211). This indicates that this basic residue plays an important role in distinguishing between nucleotide diphosphates and triphosphates and accounts for the preference of ATP over ADP in hP2Y₁₁ receptors (211, 242). Since the key feature of clone 13 is the appearance of a P2Y₁-hP2Y₁₁ heteromer with decreased potency for ADP, a potent agonist of P2Y₁ with no activity at monomeric hP2Y₁₁, the responsiveness of heteromeric hP2Y₁₁ to ADP could result from a conformational change that shields or displaces Arg²⁶⁸ away from the receptor's binding pocket, rendering hP2Y₁₁ more responsive to ADP.

The computational modelling and mutagenesis studies of the P2Y₁ receptor have shown that the amino acid residues involved in agonist binding also contribute to antagonist binding. Although the results originate from experiments at human P2Y₁, they were extrapolated to hamster P2Y₁ for the purpose of this discussion. According to the devised model, the “receptor architecture” conducive to ATP docking was also energetically favourable for MRS 2179 (242). The amino acid residues crucial for agonist stabilization include Arg¹²⁸ (TM3), Thr²²² (TM5), Lys²⁸⁰ (TM6) and Arg³¹⁰ (TM7) while residues involved in agonist recognition comprise Gln³⁰⁷ (TM7) and Ser³¹⁴ (TM7). Thr²²² and Lys²⁸⁰ are particularly important for binding of the adenosine moiety (151). Furthermore, a high degree of coordination of the β -phosphate is crucial for binding of adenosine phosphates to hP2Y₁, which explains the greater potency of ADP versus ATP at this receptor (151). Residues implicated in antagonist binding are: Arg¹²⁸ (TM3), Arg³¹⁰ (TM7) and Tyr¹³⁶ (TM3), while His¹³² (TM3), Tyr¹³⁶ (TM3) and Thr²²² (TM5) also fulfilled a modulatory function. P2Y₁-related changes observed in clone 13 included 1) reduced ADP potency at the high affinity site of the curve mediated by endogenous P2Y₁ and 2) loss of MRS 2179 activity at the P2Y₁:hP2Y₁₁ oligomer. Given that ADP and MRS 2179 binding requires Arg¹²⁸, Arg³¹⁰ and Thr²²², it can be hypothesized that interaction with hP2Y₁₁ caused the rearrangement of these residues into a conformation less energetically favourable for ADP and MRS 2179 by decreasing the coordination of the β -phosphate upon binding. These modifications could have also resulted in the impaired interaction of the 5' and 3'-monophosphate groups of MRS 2179 with the

positively charged residues of the binding pocket. Given the importance of this step for antagonist docking and stabilization, this alteration could explain the absence of MRS 2179 action at the heteromer.

Crystallization and modelling studies have identified a role for TM4, TM5 and the intracellular loop connecting TM3 and TM4 in dimeric interactions (28, 79) and suggested a number of dimerization interfaces with contacts between TM4-TM4, TM4-TM6 and TM5-TM6 (77). A closer inspection of the location of the residues involved in agonist and antagonist binding in P2Y₁ and hP2Y₁₁ reveals that many of the crucial amino acids are situated in TMs 3, 5 and 6 in both receptors. This implies that the transmembranes containing the residues important for ligand binding could also be involved in the interaction and dimerization between P2Y₁ and hP2Y₁₁. Conformational rearrangements due to cross-talk and oligomerisation could shift the location of these residues within the plane of the receptors, thus altering the docking and binding of agonists and antagonists.

6.11 Conclusions

The experiments conducted in this project have provided a detailed pharmacological profile of two recombinant cell lines: a low-expressing CHO-K1-hP2Y₁₁ clone 6 and a high-expressing CHO-K1-hP2Y₁₁ clone 13. Two distinct scenarios arise from the obtained results. At low levels of hP2Y₁₁ expression, co-expression was found to alter the affinity of BzATP, ATP γ S, ATP, UTP, α meATP, β meATP and NF 340 for hP2Y₁₁ in CHO-K1-hP2Y₁₁ clones as compared to 1321N1-hP2Y₁₁. High levels of hP2Y₁₁ expression produced biphasic responses to ADP and 2meSATP, characterized by the appearance of a low-affinity site with unique ligand potencies and selectivities. These results provide convincing proof of some form of interaction between P2Y₁ and hP2Y₁₁ in the co-expressing clones 6 and 13. They also suggest that the extent and dynamics of this interaction are different at low levels of hP2Y₁₁ expression as compared to higher levels, suggesting that different modes of interaction might be implicated in clone 6 versus 13. Hence, while evidence points to possible oligomerisation and physical communication between P2Y₁ and hP2Y₁₁ in clone 13, the nature of receptor cross-talk in clone 6 is more elusive. In fact, it seems that clone 6 constitutes an intermediary state between individual receptor pharmacology as detected in the control 1321N-hP2Y₁ and 1321N1-hP2Y₁₁ cell lines and oligomeric receptor interaction in clone 13.

The literature suggests that receptor interaction could be functional/indirect or physical/direct. Consequently, it can be argued that the crosstalk between endogenous P2Y₁ and hP2Y₁₁ is functional in clone 6 and might arise from signalling crosstalk as illustrated by the example of the mGlu_{1a} and GABA_B receptors (see Introduction). Increasing the density of the hP2Y₁₁ receptor reserve at the cellular membrane, as in the case of clone 13, seems to push this communication further, resulting in direct physical contact between the two receptors and the formation of a P2Y₁:hP2Y₁₁ complex with a unique signalling profile. According to Durroux (64), there are two distinct models of receptor dimerization. In the first model, receptors fluctuate between two dimeric states, the R~R state in which protomers are independent from one another and the R–R state in which protomers can interact. In the second model, receptors oscillate between a monomeric state and a dimeric state in which protomers are able to interact (241). The interaction between P2Y₁ and P2Y₁₁ as illustrated by the behaviours of clone 6 and 13 could fall into the second model of dimerization expounded by Durroux. Taken together, these observations lead to the following conclusion: **1) P2Y₁ and hP2Y₁₁ are proteins that display a propensity to interact when co-expressed. This interaction can be functional at lower receptor reserves or physical at higher receptor densities.**

For these interactions to occur, it is necessary that the communicating partners be recruited to common compartments permitting receptor organization and association. Cells have resolved this spatio-temporal dilemma by confining signalling proteins including GPCRs to membrane microdomains such as lipid rafts (244). The current GPCR literature argues that cells have accomplished an additional organisational feat by pooling GPCRs into receptor mosaics, defined as macromolecular assemblies of more than two receptors that interact directly to form various arrangements (87, 89, 94-96, 245). These topologies are regulated by conformational and allosteric interactions between members of these specialized signalling hubs (89, 245). Experimental evidence has suggested that P2Y receptors, including P2Y₁, localize to cholesterol-rich signalling microdomains or lipid rafts (55, 246, 247). This indicates that P2Y₁ and hP2Y₁₁ receptors (and possibly hP2Y₂) might localise to specific membrane microdomains in the recombinant CHO-K1-hP2Y₁₁ clones 6 and 13, thus enabling functional cross-talk, cooperativity, allosteric regulation, and oligomerisation between the two receptors, as detected in the clones. Interestingly, these recent findings suggest that while P2Y₁ and hP2Y₁₁ can form heteromers, they might even exist in macromolecular assemblies with other GPCRs such as P2Y₂. These assemblies or receptor mosaics may possess different

properties to receptor heteromers, thus explaining the absence of hP2Y₁₁ internalization in CHO-K1-hP2Y₁₁ clone 13, as opposed to the P2Y₁-induced internalization of hP2Y₁₁ observed by Ecke et al. in recombinant 1321N1 cells (55). The receptor mosaic might exert spatial and functional restraints on its receptor components, causing them to behave differently to monomers or heteromers.

Seeing as receptor dimerization confers novel signalling profiles to the heteromers, Franco et al. have advanced the notion of ‘dimer fingerprint’, defined as a specific pharmacological, biochemical or functional property exhibited by the receptor heteromer (248). This notion was applied to the distinct pharmacological entity observed at the low-affinity site of the biphasic ADP and 2meSATP responses in CHO-K1-hP2Y₁₁ clone 13, leading to the following conclusion: **2) The P2Y₁:hP2Y₁₁ heteromer occurring in CHO-K1-hP2Y₁₁ clone 13 possesses a unique dimer fingerprint. It responds to ADP, unlike individual hP2Y₁₁ receptors, but is not antagonized by MRS 2179 or NF 340, in contrast to individual P2Y₁ or hP2Y₁₁ receptors, respectively.**

Another interesting feature of calcium signaling in the high-expressing CHO-K1-hP2Y₁₁ clone 13 is that the biphasic 2meSATP and ADP curves integrate P2Y₁ and hP2Y₁₁ activity into a single signalling event. The significance of this observation lies in that P2Y₁ and P2Y₁₁ have been reported to mediate the rapid and slow relaxation of smooth muscle cells, respectively (174). Consequently, studies conducted in the guinea pig taenia coli have investigated these relaxations separately, activating and inhibiting each individually. The present study reveals that in certain instances, the components of the two phases of SMC relaxation can merge into a single continuous calcium occurrence with two distinct plateaus. Moreover, these two components can interact to form one signalling entity or P2Y₁:hP2Y₁₁ heteromer with a unique pharmacology. Two agonists, namely ADP and 2meSATP, were able to activate these two components simultaneously, while Reactive Red was able to block them simultaneously. It was also possible to inhibit the P2Y₁ component of the biphasic response separately from the heteromeric component using MRS 2179. However, it was not possible to target the oligomeric phase separately from the P2Y₁ phase using any of the antagonists tested in this study, as neither MRS 2179 nor NF 340 were active against the low-affinity site. Furthermore, it was not possible to inhibit the hP2Y₁₁ receptor as it displayed no affinity for NF 340 in the co-expressing clones 6 and 13. These observations of great pharmacological potential draw a bridge between the findings of this study and the inspiration behind it, namely the

investigation of P2Y₁ and P2Y₁₁ interactions to develop a drug that could target SMC relaxation in the stomach. This drug, if implemented, could function as a chemical gastric band in obese patients, thus replacing the invasive bariatric surgery or harmful anti-obesity drugs such as orlistat. They draw a roadmap for future pharmacological testing delineated by the following conclusion: **3) Co-expression often alters the agonist/antagonist profile of purinoceptors and produces oligomeric receptors with novel pharmacologic properties. This signalling diversification highlights the necessity to enlarge the current ligand repertoire by testing and developing novel drugs specific to monophasic and oligomeric populations of receptors that occur in the cellular membrane.**

This agrees with the conclusion drawn by Franco et al. in a review entitled “G-protein-coupled receptor heteromers: function and ligand pharmacology” (248). The researchers argue that the major shortcoming of the current drug industry lies in its failure to recognize the inherent complexity of receptor signalling in favour of the old-fashioned reductionist approach focusing on individual receptors characterized in single-transfected cells where oligomerisation does not occur. This simplification skews the real effect of drugs at receptors by ignoring the increasing evidence that receptors tend to interact or oligomerize in real organisms, thus altering or abolishing the affinities of ligands at targeted receptors. Franco et al. thus advise pharmaceutical companies to test potential drugs against therapeutically relevant heteromers, such as opioid or cannabinoid receptor heteromers for pain or dopamine/adenosine receptor heteromers for Parkinson’s disease (248). P2Y₁ and P2Y₁₁ can be added to this endeavour given their participation in a wide range of metabolic pathways and functions. In conclusion, the novel paradigm of receptor oligomerisation acknowledging the complexity of receptor behaviour at cellular membranes echoes the insight formulated by Martin Rodbell in his Nobel Prize lecture exactly twenty years ago, according to which “receptor-coupled signalling processes in general now seem more Bhudda-like in their structures, both in their stationary setting and the multi-component structures which appear to interact in a flickering fashion, more in keeping with the ephemeral relationship between action and inaction, between life and death”(249).

6.12 Future Work

The main objective behind this project was to study the interaction between P2Y₁ and P2Y₁₁, which mediate the fast and slow relaxation of smooth muscle cells in the

stomach, to develop an anti-obesity drug that could block this relaxation. Characterization of calcium responses in clones 6 and 13 suggests the existence of a P2Y₁:P2Y₁₁ heteromer with unique signalling properties. cAMP assays constitute a logical follow-up on these experiments and could discriminate between ligand activity at hP2Y₁₁ versus P2Y₁. Increased cAMP production would confirm the involvement of hP2Y₁₁ in the biphasic responses, although lack of cAMP increase would not disprove it. In fact, the coupling of dimers to G-proteins seems to be asymmetric with a 2:1 stoichiometry (250), implying that heteromerisation could decouple one protomer from its cognate G-protein. cAMP assays might thus offer insights into the G-protein stoichiometry of the P2Y₁:hP2Y₁₁ dimer.

Furthermore, radioligand binding assays could be performed to identify a “binding fingerprint” for this dimer using suitable radioligands. Possible candidates include radioactive ADP such as [2-³H] ADP (251) or [¹⁴C] ADP (252, 253), previously employed to study ADP binding to platelet membranes ($K_D = 0.35, 1$ and $0.5 \mu\text{M}$, respectively). In fact, deeming the current functional assays non-suitable for dimers, Casadó et al. have proposed a novel procedure for determining ligand affinities at the high- and low- affinity sites of biphasic responses using radioligand binding assays. This procedure reflects communication within the dimer with a “cooperativity index” and provides accurate K_D and B_{50} (concentration providing half saturation) values for agonists, useful for elucidating the rank order of potency of ligands at dimers (241). Most importantly, it can elucidate a specific property of the receptor or its dimer fingerprint (248). For instance, radioligand binding assays in cotransfected cells and rat striatum have revealed a main biochemical characteristic of the A₁R:A_{2A}R heteromer, i.e. the ability of A_{2A} activation to reduce the agonist affinity of A₁ receptors, thus providing a switch mechanism by which low and high concentrations of adenosine can respectively inhibit and stimulate glutamate release (254). Another example is the antagonistic A_{2A}:D₂ interaction whereby the stimulation of A_{2A} receptors reduces the affinity of dopamine D₂ agonist binding (46, 255).

As described in Chapter 3, unsuccessful attempts to quantify the level of hP2Y₁₁ expression in clone 13 versus 6 were made using reverse transcription of mRNA followed by PCR experiments. Since mRNA levels do not necessarily correlate with receptor density at the plasma membrane, more suitable techniques including ligand binding or fluorescence correlation spectroscopy could be applied. Confocal microscopy could be

used to study the colocalization of P2Y₁ and hP2Y₁₁ in clones 6 and 13. Additionally, lipid raft markers can be employed to determine if the two receptors are pooled to lipid rafts, which would facilitate receptor-receptor interaction. It might also be interesting to quantify hP2Y₁₁ densities in the intermediary clones between 6 and 13 to measure the lowest density of hP2Y₁₁ required to generate biphasic responses.

Together with functional assays, biochemical and biophysical methods are commonly employed tools for investigating GPCR oligomerisation. The existence of a P2Y₁:P2Y₁₁ oligomer has already been demonstrated (242). Since the nature of the low affinity site observed in the biphasic responses in clone 13 is unknown, molecular assays may allow clear identification of the P2Y₁:P2Y₁₁ entity as a functional heteromer in this clone. For instance, co-immunoprecipitation studies could be implemented using the constructs from Chapter 3 although caution should be warranted in interpreting these results due to artifactual aggregation of receptors. Biophysical techniques such as FRET and BiFC, which overcome this problem, offer a better platform for studying heteromerisation. BiFC has been previously used to identify GPCR oligomers such as A_{2A}:D₂ (93) and can be performed to monitor P2Y₁ and hP2Y₁₁ interactions in clone 13. It might also provide insight on the subcellular localisation of the oligomer, revealing whether it occurs in the plasma membrane or forms in the endoplasmic reticulum during receptor biogenesis. If P2Y₁ and hP2Y₁₁ are located in a receptor mosaic, they can homo- or hetero-oligomerize with other protomers such as endogenous P2Y₂. Previous research has shown that P2Y₂ forms constitutive homo-oligomer in non-hematopoietic and hematopoietic cells (256). It has also been reported to oligomerise with A₁ receptors both in cotransfected HEK293T cells (257) and in situ on the surface of neurons in various brain regions (258), generating a unique complex in which P2Y₂ activation inhibits agonist binding to the A₁ receptor (257). Seeing as P2Y₂ partakes in the calcium response to some of the agonists tested in this project (such as ATP and ATP γ S) and that Hill coefficients suggest positive cooperativity in these responses, it might be interesting to investigate whether P2Y₂ interacts or occurs in a receptor mosaic with any of the other purinoceptors in the clones. Possible interactions include: P2Y₁:P2Y₁, P2Y₁:hP2Y₁₁, hP2Y₁₁:hP2Y₁₁, P2Y₁:P2Y₂, P2Y₂:hP2Y₁₁, P2Y₂:P2Y₂, as previously identified (256), or even P2Y₁:P2Y₂:hP2Y₁₁. Multicolour BiFC, which allows the visualisation of two distinct GPCR-GPCR interactions simultaneously (259), can be employed to study these multiple associations using different pairs of tags, such as Cerulean C Terminal Fragment (-CC)/Cerulean N Terminal Fragment (-CN), Cerulean C Terminal Fragment (-

CC)/Venus N Terminal (-VN) Fragment or Venus C Terminal Fragment (-VC)/Venus N Terminal Fragment (-VN), to identify different dimers in parallel (93, 260). In conjunction with BiFC, which is irreversible nature, FRET or BRET assays can be used to study the formation and dissociation of the P2Y₁:hP2Y₁₁ oligomer (259), determine if agonist addition (for example, ADP or 2meSATP) increases or decreases oligomerisation, and assess the interaction affinities between purinoceptors in the receptor mosaic.

It does not suffice to demonstrate that P2Y₁ and hP2Y₁₁ oligomerise; it is also important to determine the sites at which this interaction occurs. The structural study of GPCRs has been traditionally hampered by the difficulty of crystallizing them. However, promising advances such as protein engineering, lipidic cubic phase-based crystallization and microfocus synchrotron beamlines are producing a ‘GPCR structural revolution’ (261). Consequently, the crystal structure of P2Y₁, P2Y₁₁ and P2Y₁:P2Y₁₁ might be resolved in the near future, permitting structural investigation of the conformational changes involved in oligomerisation using techniques such as NMR or Atomic Force Microscopy.

Alternatively, computational homology modelling, site-directed mutagenesis and BiFC can be combined to study this interaction. Computer simulations using methods such as coarse-grained modelling might shed light on the oligomer’s binding pocket and the transmembrane interfaces implicated in dimerization. Based on these predictions, hP2Y₁₁ residues that participate in heteromerisation or ligand binding can be modified using site-directed mutagenesis. New recombinant CHO-K1 cell lines expressing low and high levels of mutants can be developed and characterized to study the effect of mutations on the biphasic responses. Additional studies include development of BiFC-tagged hP2Y₁ and hP2Y₁₁ mutants transfected into null cells to test the interaction interfaces identified for both receptors using computational studies. The results from full-length sequence experiments can be verified in a sub-study where the individual domains/helices of interest in each receptor are mutated, tagged using complimentary fluorescent epitopes and tested to refine the map of residues involved in heteromerisation. Finally, the oligomer’s coupling to G-proteins can be studied with multicolour BiFC using different tags for G_{os}, G_{q/11}, hP2Y₁ and hP2Y₁₁ to prevent interference and ensure correct binding of the components.

An oligomer detected in a recombinant system is accepted if it exists in native tissue, implying that the P2Y₁:P2Y₁₁ heteromer is pharmacologically significant only if it occurs in tissue that endogenously expresses both receptors. It is thus important to study this oligomer in guinea pig taenia coli smooth muscle cells and eventually in human smooth muscle cells of the stomach. The relative densities of the two receptors in smooth muscle cells can be evaluated using ligand binding assays or fluorescence correlation spectroscopy to determine if receptor levels in native cells match those of clones 6, 13 or are specific to the tissue. Receptor densities can also be studied in different compartments of the plasma membrane to check if microenvironments of varying P2Y₁ and P2Y₁₁ densities containing different levels of oligomers versus monomers exist. Additionally, co-localisation studies can be performed to define the location of the receptors in the plasma membrane (lipid rafts, etc.) Furthermore, the oligomerisation and sub-localisation (endoplasmic reticulum, plasma membrane, etc.) of these two purinoceptors in native tissue can be tested using biochemical and biophysical studies such as coimmunoprecipitation and FRET or BRET. These experiments can be further extended to investigate the existence of a receptor mosaic mediating multiple interactions between purinoceptors in native tissue. Quantitative PCR (qPCR) and sequencing would first be performed to define the receptor subtypes present in the cells, followed by co-localisation studies to confirm that they are closely located. FRET or BRET can then be performed to test if the various receptors interact to form higher-order networks.

These biophysical studies investigating the presence of the signalling complex should be coupled to functional studies in native tissue to check if endogenous P2Y₁ and P2Y₁₁ exhibit the same ligand affinities as in clone 13. If biphasic responses to ADP and 2meSATP are detected in the native tissue, it might be worthwhile to perform specifically tailored functional and organ bath studies to elucidate the real effect of the low affinity site in a physiological context such as the relaxation of gut smooth muscle. These experiments would determine the relevance of the biphasic response to this phenomenon and consequently to a potential anti-obesity or 'thin' pill.

Additionally, it might be interesting to investigate whether P2Y₁ and P2Y₁₁ interact with M₃ receptors in smooth muscle cells. M₃ receptors cause contraction of these cells and counteract the fast and slow relaxations mediated by P2Y₁ and P2Y₁₁. The fine-tuning of stomach relaxation and contraction could involve cross-talk between the purinoceptors and M₃ receptors, a feature that might be relevant for anti-obesity studies.

Consequently, co-localisation, FRET, BRET and functional experiments could be applied to test this hypothesis and determine if M_3 receptors might affect $P2Y_1$ and $hP2Y_{11}$ interactions, as a feedback mechanism employed by the cells to control purinoceptor activity for instance.

If the $P2Y_1:P2Y_{11}$ heteromer proves relevant to gut smooth muscle relaxation in the native context, drug screening for agonists and antagonists should follow the pharmacological and biophysical studies. An initial selection of compounds can be achieved using supercomputer simulations of the oligomer, followed by functional assays to test the activity of the selected ligands in recombinant or native tissue. An interesting approach adopted recently is to design dual compounds that target the receptor partners in a heteromer (248). For instance, dual molecules composed of a xanthine and a dopamine analogue connected by a spacer of differing lengths are being developed against adenosine-dopamine heteromers in the context of Parkinson's disease (248, 262). These drug design endeavours might contribute to the discovery of a selective and potent $P2Y_1:P2Y_{11}$ antagonist, thus paving the way for the development of the anti-obesity drug. This compound could be delivered as a pill, an inhaler, transdermal adhesive patch or using advanced therapeutic systems such as inorganic or metal nanoparticles, micelles or carbon nanotubes (263). Alternatively, cutting-edge technologies, which offer new platforms for multi-dimensional tissue screening aimed at identifying drug targets and assessing their specificity and mode of action (264), could prove more useful than conventional cell-based assays in predicting targets (265). For instance, 3D tissue models of SMCs can be developed, using platforms such as OCELLO or organ-on-chip technologies, for pre-clinical phenotypic screening of huge libraries of compounds and the selection of targets depending on their affinity and selectivity.

Finally, to exploit the entire potential of this study, the functional and physical characterization of $P2Y_1:P2Y_{11}$ oligomers should be extended to other tissues of the body. Since these two receptors are ubiquitous and involved in many diseases, qPCR can be used to determine tissues in which they are co-expressed. This could uncover new roles for the oligomer, revealing its possible contribution to other disorder and its relevance as a drug target against these conditions.

In summary, the functional study of clones 6 and 13, which co-express P2Y₁ and hP2Y₁₁, indicates that they show characteristics distinct from those of the individual receptors, as proven by using different ligands. It was hypothesized that these properties result from the oligomerisation of P2Y₁ and transfected hP2Y₁₁. To further investigate this finding, several techniques can be employed to test oligomerisation in recombinant and native tissue, identify the interaction interfaces and screen for novel agonists and antagonists of this dimer. These endeavours could contribute to the development of an anti-obesity drug as a safer chemical alternative to gastric banding. It could also reveal alternative disorder conditions to which the oligomer contributes, thus offering additional ground for pharmaceutical research.

Chapter 7

References

1. Smith NJ & Milligan G (2010) Allostery at G protein-coupled receptor homo- and heteromers: uncharted pharmacological landscapes. *Pharmacological reviews* 62(4):701-725.
2. Foord SM, Jupe S, & Holbrook J (2002) Bioinformatics and type II G-protein-coupled receptors. *Biochemical Society transactions* 30(4):473-479.
3. Lefkowitz RJ (2007) Seven transmembrane receptors: a brief personal retrospective. *Biochimica et biophysica acta* 1768(4):748-755.
4. Lin HH (2013) G-protein-coupled receptors and their (Bio) chemical significance win 2012 Nobel Prize in Chemistry. *Biomedical journal* 36(3):118-124.
5. Latek D, Modzelewska A, Trzaskowski B, Palczewski K, & Filipek S (2012) G protein-coupled receptors--recent advances. *Acta biochimica Polonica* 59(4):515-529.
6. Wise A, Gearing K, & Rees S (2002) Target validation of G-protein coupled receptors. *Drug discovery today* 7(4):235-246.
7. Katritch V, Cherezov V, & Stevens RC (2012) Diversity and modularity of G protein-coupled receptor structures. *Trends in pharmacological sciences* 33(1):17-27.
8. Palczewski K, *et al.* (2000) Crystal structure of rhodopsin: A G protein-coupled receptor. *Science (New York, N.Y.)* 289(5480):739-745.
9. Cherezov V, *et al.* (2007) High-resolution crystal structure of an engineered human beta2-adrenergic G protein-coupled receptor. *Science (New York, N.Y.)* 318(5854):1258-1265.
10. Rasmussen SG, *et al.* (2007) Crystal structure of the human beta2 adrenergic G-protein-coupled receptor. *Nature* 450(7168):383-387.
11. Chien EY, *et al.* (2010) Structure of the human dopamine D3 receptor in complex with a D2/D3 selective antagonist. *Science (New York, N.Y.)* 330(6007):1091-1095.
12. Haga K, *et al.* (2012) Structure of the human M2 muscarinic acetylcholine receptor bound to an antagonist. *Nature* 482(7386):547-551.
13. Kruse AC, *et al.* (2012) Structure and dynamics of the M3 muscarinic acetylcholine receptor. *Nature* 482(7386):552-556.
14. Chun L, Zhang WH, & Liu JF (2012) Structure and ligand recognition of class C GPCRs. *Acta pharmacologica Sinica* 33(3):312-323.
15. Manglik A, *et al.* (2012) Crystal structure of the micro-opioid receptor bound to a morphinan antagonist. *Nature* 485(7398):321-326.
16. Granier S, *et al.* (2012) Structure of the delta-opioid receptor bound to naltrindole. *Nature* 485(7398):400-404.
17. Wu H, *et al.* (2012) Structure of the human kappa-opioid receptor in complex with JD1c. *Nature* 485(7398):327-332.
18. Thompson AA, *et al.* (2012) Structure of the nociceptin/orphanin FQ receptor in complex with a peptide mimetic. *Nature* 485(7398):395-399.
19. Jaakola VP, *et al.* (2008) The 2.6 angstrom crystal structure of a human A2A adenosine receptor bound to an antagonist. *Science (New York, N.Y.)* 322(5905):1211-1217.
20. Shimamura T, *et al.* (2011) Structure of the human histamine H1 receptor complex with doxepin. *Nature* 475(7354):65-70.

21. Rasmussen SG, *et al.* (2011) Structure of a nanobody-stabilized active state of the beta(2) adrenoceptor. *Nature* 469(7329):175-180.
22. Dupré DJHTE, Jockers R. (2012) GPCR signaling complexes- Synthesis, Assembly, Trafficking and Specificity. *Subcellular Biochemistry* 63.
23. Sciences TRSAo (Scientific Background on the Nobel Prize in Chemistry 2012. Studies of G-protein coupled receptors
24. Palczewski K (2010) Oligomeric forms of G protein-coupled receptors (GPCRs). *Trends Biochem Sci* 35(11):595-600.
25. Agnati LF, Fuxe K, Zini I, Lenzi P, & Hokfelt T (1980) Aspects on receptor regulation and isoreceptor identification. *Med Biol* 58(4):182-187.
26. Dupre DJ, Hammad MM, Holland P, & Wertman J (2012) Role of chaperones in G protein coupled receptor signaling complex assembly. *Sub-cellular biochemistry* 63:23-42.
27. Ciruela F, *et al.* (2011) Adenosine receptor containing oligomers: their role in the control of dopamine and glutamate neurotransmission in the brain. *Biochim Biophys Acta* 1808(5):1245-1255.
28. Fotiadis D, *et al.* (2003) Atomic-force microscopy: Rhodopsin dimers in native disc membranes. *Nature* 421(6919):127-128.
29. Margeta-Mitrovic M, Jan YN, & Jan LY (2000) A trafficking checkpoint controls GABA(B) receptor heterodimerization. *Neuron* 27(1):97-106.
30. Ng GY, *et al.* (1999) Identification of a GABAB receptor subunit, gb2, required for functional GABAB receptor activity. *The Journal of biological chemistry* 274(12):7607-7610.
31. Robbins MJ, *et al.* (2001) GABA(B2) is essential for g-protein coupling of the GABA(B) receptor heterodimer. *The Journal of neuroscience : the official journal of the Society for Neuroscience* 21(20):8043-8052.
32. Sullivan R, *et al.* (2000) Coexpression of full-length gamma-aminobutyric acid(B) (GABA(B)) receptors with truncated receptors and metabotropic glutamate receptor 4 supports the GABA(B) heterodimer as the functional receptor. *The Journal of pharmacology and experimental therapeutics* 293(2):460-467.
33. Pin JP, Galvez T, & Prezeau L (2003) Evolution, structure, and activation mechanism of family 3/C G-protein-coupled receptors. *Pharmacology & therapeutics* 98(3):325-354.
34. Prezeau L, *et al.* (2010) Functional crosstalk between GPCRs: with or without oligomerization. *Current opinion in pharmacology* 10(1):6-13.
35. Scarselli M, *et al.* (2001) D2/D3 dopamine receptor heterodimers exhibit unique functional properties. *The Journal of biological chemistry* 276(32):30308-30314.
36. Wang M, *et al.* (2010) Schizophrenia, amphetamine-induced sensitized state and acute amphetamine exposure all show a common alteration: increased dopamine D2 receptor dimerization. *Molecular brain* 3:25.
37. Strange PG (2005) Oligomers of D2 dopamine receptors: evidence from ligand binding. *Journal of molecular neuroscience : MN* 26(2-3):155-160.
38. Maggio R & Millan MJ (2010) Dopamine D2-D3 receptor heteromers: pharmacological properties and therapeutic significance. *Current opinion in pharmacology* 10(1):100-107.
39. Aizman O, *et al.* (2000) Anatomical and physiological evidence for D1 and D2 dopamine receptor colocalization in neostriatal neurons. *Nature neuroscience* 3(3):226-230.
40. George SR & O'Dowd BF (2007) A novel dopamine receptor signaling unit in brain: heterooligomers of D1 and D2 dopamine receptors. *TheScientificWorldJournal* 7:58-63.
41. Rashid AJ, *et al.* (2007) D1-D2 dopamine receptor heterooligomers with unique pharmacology are coupled to rapid activation of Gq/11 in the striatum.

- Proceedings of the National Academy of Sciences of the United States of America* 104(2):654-659.
42. So CH, *et al.* (2005) D1 and D2 dopamine receptors form heterooligomers and cointernalize after selective activation of either receptor. *Molecular pharmacology* 68(3):568-578.
 43. Marcellino D, *et al.* (2008) Identification of dopamine D1-D3 receptor heteromers. Indications for a role of synergistic D1-D3 receptor interactions in the striatum. *The Journal of biological chemistry* 283(38):26016-26025.
 44. Fiorentini C, *et al.* (2008) Reciprocal regulation of dopamine D1 and D3 receptor function and trafficking by heterodimerization. *Molecular pharmacology* 74(1):59-69.
 45. Hillion J, *et al.* (2002) Coaggregation, cointernalization, and codesensitization of adenosine A2A receptors and dopamine D2 receptors. *The Journal of biological chemistry* 277(20):18091-18097.
 46. Canals M, *et al.* (2003) Adenosine A2A-dopamine D2 receptor-receptor heteromerization: qualitative and quantitative assessment by fluorescence and bioluminescence energy transfer. *The Journal of biological chemistry* 278(47):46741-46749.
 47. Kearn CS, Blake-Palmer K, Daniel E, Mackie K, & Glass M (2005) Concurrent stimulation of cannabinoid CB1 and dopamine D2 receptors enhances heterodimer formation: a mechanism for receptor cross-talk? *Molecular pharmacology* 67(5):1697-1704.
 48. Marcellino D, *et al.* (2008) Antagonistic cannabinoid CB1/dopamine D2 receptor interactions in striatal CB1/D2 heteromers. A combined neurochemical and behavioral analysis. *Neuropharmacology* 54(5):815-823.
 49. Baragli A, Alturaihi H, Watt HL, Abdallah A, & Kumar U (2007) Heterooligomerization of human dopamine receptor 2 and somatostatin receptor 2 Co-immunoprecipitation and fluorescence resonance energy transfer analysis. *Cellular signalling* 19(11):2304-2316.
 50. Rocheville M, *et al.* (2000) Receptors for dopamine and somatostatin: formation of hetero-oligomers with enhanced functional activity. *Science (New York, N.Y.)* 288(5463):154-157.
 51. Yoshioka K, Saitoh O, & Nakata H (2001) Heteromeric association creates a P2Y-like adenosine receptor. *Proceedings of the National Academy of Sciences of the United States of America* 98(13):7617-7622.
 52. Yoshioka K, Hosoda R, Kuroda Y, & Nakata H (2002) Hetero-oligomerization of adenosine A1 receptors with P2Y1 receptors in rat brains. *FEBS letters* 531(2):299-303.
 53. Nakata H, Yoshioka K, Kamiya T, Tsuga H, & Oyanagi K (2005) Functions of heteromeric association between adenosine and P2Y receptors. *Journal of molecular neuroscience : MN* 26(2-3):233-238.
 54. Gines S, *et al.* (2000) Dopamine D1 and adenosine A1 receptors form functionally interacting heteromeric complexes. *Proc Natl Acad Sci U S A* 97(15):8606-8611.
 55. Ecke D, *et al.* (2008) Hetero-oligomerization of the P2Y11 receptor with the P2Y1 receptor controls the internalization and ligand selectivity of the P2Y11 receptor. *The Biochemical journal* 409(1):107-116.
 56. Wertman J & Dupre DJ (2013) G protein-coupled receptor dimers: look like their parents, but act like teenagers! *Journal of receptor and signal transduction research* 33(3):135-138.
 57. Salahpour A, *et al.* (2004) Homodimerization of the beta2-adrenergic receptor as a prerequisite for cell surface targeting. *The Journal of biological chemistry* 279(32):33390-33397.

58. Van Craenenbroeck K, *et al.* (2011) Dopamine D4 receptor oligomerization--contribution to receptor biogenesis. *The FEBS journal* 278(8):1333-1344.
59. Herrick-Davis K, Weaver BA, Grinde E, & Mazurkiewicz JE (2006) Serotonin 5-HT_{2C} receptor homodimer biogenesis in the endoplasmic reticulum: real-time visualization with confocal fluorescence resonance energy transfer. *The Journal of biological chemistry* 281(37):27109-27116.
60. Abd Alla J, Reeck K, Langer A, Streichert T, & Quitterer U (2009) Calreticulin enhances B2 bradykinin receptor maturation and heterodimerization. *Biochemical and biophysical research communications* 387(1):186-190.
61. Abd Alla J, Pohl A, Reeck K, Streichert T, & Quitterer U (2010) Establishment of an in vivo model facilitates B2 receptor protein maturation and heterodimerization. *Integrative biology : quantitative biosciences from nano to macro* 2(4):209-217.
62. Vilaradaga JP, Agnati LF, Fuxe K, & Ciruela F (2010) G-protein-coupled receptor heteromer dynamics. *Journal of cell science* 123(Pt 24):4215-4220.
63. Decailot FM, Rozenfeld R, Gupta A, & Devi LA (2008) Cell surface targeting of mu-delta opioid receptor heterodimers by RTP4. *Proceedings of the National Academy of Sciences of the United States of America* 105(41):16045-16050.
64. Maurel D, *et al.* (2008) Cell-surface protein-protein interaction analysis with time-resolved FRET and snap-tag technologies: application to GPCR oligomerization. *Nature methods* 5(6):561-567.
65. Carrillo JJ, Padiani J, & Milligan G (2003) Dimers of class A G protein-coupled receptors function via agonist-mediated trans-activation of associated G proteins. *The Journal of biological chemistry* 278(43):42578-42587.
66. Lee SP, *et al.* (2004) Dopamine D1 and D2 receptor Co-activation generates a novel phospholipase C-mediated calcium signal. *The Journal of biological chemistry* 279(34):35671-35678.
67. Pei L, *et al.* (2010) Uncoupling the dopamine D1-D2 receptor complex exerts antidepressant-like effects. *Nature medicine* 16(12):1393-1395.
68. O'Dowd BF, Ji X, Alijanian M, Nguyen T, & George SR (2011) Separation and reformation of cell surface dopamine receptor oligomers visualized in cells. *European journal of pharmacology* 658(2-3):74-83.
69. Diaz-Cabiale Z, *et al.* (2001) Adenosine A2A agonist CGS 21680 decreases the affinity of dopamine D2 receptors for dopamine in human striatum. *Neuroreport* 12(9):1831-1834.
70. Navarro G, *et al.* (2008) Detection of heteromers formed by cannabinoid CB1, dopamine D2, and adenosine A2A G-protein-coupled receptors by combining bimolecular fluorescence complementation and bioluminescence energy transfer. *TheScientificWorldJournal* 8:1088-1097.
71. Carriba P, *et al.* (2008) Detection of heteromerization of more than two proteins by sequential BRET-FRET. *Nature methods* 5(8):727-733.
72. Navarro G, *et al.* (2013) Detection of receptor heteromers involving dopamine receptors by the sequential BRET-FRET technology. *Methods in molecular biology (Clifton, N.J.)* 964:95-105.
73. Carriba P, *et al.* (2007) Striatal adenosine A2A and cannabinoid CB1 receptors form functional heteromeric complexes that mediate the motor effects of cannabinoids. *Neuropsychopharmacology : official publication of the American College of Neuropsychopharmacology* 32(11):2249-2259.
74. Cabello N, *et al.* (2009) Metabotropic glutamate type 5, dopamine D2 and adenosine A2a receptors form higher-order oligomers in living cells. *Journal of neurochemistry* 109(5):1497-1507.
75. Gonzalez-Maeso J, *et al.* (2008) Identification of a serotonin/glutamate receptor complex implicated in psychosis. *Nature* 452(7183):93-97.

76. Zoli M, *et al.* (1993) Receptor-receptor interactions as an integrative mechanism in nerve cells. *Molecular neurobiology* 7(3-4):293-334.
77. Simpson LM, Taddese B, Wall ID, & Reynolds CA (2010) Bioinformatics and molecular modelling approaches to GPCR oligomerization. *Current opinion in pharmacology* 10(1):30-37.
78. Niv MY & Filizola M (2008) Influence of oligomerization on the dynamics of G-protein coupled receptors as assessed by normal mode analysis. *Proteins* 71(2):575-586.
79. Liang Y, *et al.* (2003) Organization of the G protein-coupled receptors rhodopsin and opsin in native membranes. *The Journal of biological chemistry* 278(24):21655-21662.
80. Lee SP, O'Dowd BF, Rajaram RD, Nguyen T, & George SR (2003) D2 dopamine receptor homodimerization is mediated by multiple sites of interaction, including an intermolecular interaction involving transmembrane domain 4. *Biochemistry* 42(37):11023-11031.
81. Gouldson PR, *et al.* (2000) Dimerization and domain swapping in G-protein-coupled receptors: a computational study. *Neuropsychopharmacology : official publication of the American College of Neuropsychopharmacology* 23(4 Suppl):S60-77.
82. Bennett MJ, Schlunegger MP, & Eisenberg D (1995) 3D domain swapping: a mechanism for oligomer assembly. *Protein science : a publication of the Protein Society* 4(12):2455-2468.
83. Bennett MJ, Choe S, & Eisenberg D (1994) Domain swapping: entangling alliances between proteins. *Proceedings of the National Academy of Sciences of the United States of America* 91(8):3127-3131.
84. Gouldson PR, Snell CR, Bywater RP, Higgs C, & Reynolds CA (1998) Domain swapping in G-protein coupled receptor dimers. *Protein engineering* 11(12):1181-1193.
85. Gouldson PR, Snell CR, & Reynolds CA (1997) A new approach to docking in the beta 2-adrenergic receptor that exploits the domain structure of G-protein-coupled receptors. *Journal of medicinal chemistry* 40(24):3871-3886.
86. Gouldson PR & Reynolds CA (1997) Simulations on dimeric peptides: evidence for domain swapping in G-protein-coupled receptors? *Biochemical Society transactions* 25(3):1066-1071.
87. Agnati LF, Guidolin D, Villardaga JP, Ciruela F, & Fuxe K (2010) On the expanding terminology in the GPCR field: the meaning of receptor mosaics and receptor heteromers. *Journal of receptor and signal transduction research* 30(5):287-303.
88. Fuxe K, *et al.* (2010) The changing world of G protein-coupled receptors: from monomers to dimers and receptor mosaics with allosteric receptor-receptor interactions. *Journal of receptor and signal transduction research* 30(5):272-283.
89. Agnati LF, Fuxe K, & Ferre S (2005) How receptor mosaics decode transmitter signals. Possible relevance of cooperativity. *Trends in biochemical sciences* 30(4):188-193.
90. Costanzi S, Mamedova L, Gao ZG, & Jacobson KA (2004) Architecture of P2Y nucleotide receptors: structural comparison based on sequence analysis, mutagenesis, and homology modeling. *Journal of medicinal chemistry* 47(22):5393-5404.
91. Gandia J, *et al.* (2008) Detection of higher-order G protein-coupled receptor oligomers by a combined BRET-BiFC technique. *FEBS letters* 582(20):2979-2984.
92. Park PS & Wells JW (2004) Oligomeric potential of the M2 muscarinic cholinergic receptor. *Journal of neurochemistry* 90(3):537-548.

93. Vidi PA, Chemel BR, Hu CD, & Watts VJ (2008) Ligand-dependent oligomerization of dopamine D(2) and adenosine A(2A) receptors in living neuronal cells. *Molecular pharmacology* 74(3):544-551.
94. Agnati LF, Fuxe K, Zoli M, Rondanini C, & Ogren SO (1982) New vistas on synaptic plasticity: the receptor mosaic hypothesis of the engram. *Medical biology* 60(4):183-190.
95. Agnati LF, *et al.* (2004) On the molecular basis of the receptor mosaic hypothesis of the engram. *Cellular and molecular neurobiology* 24(4):501-516.
96. Agnati LF, *et al.* (2003) Possible role of intramembrane receptor-receptor interactions in memory and learning via formation of long-lived heteromeric complexes: focus on motor learning in the basal ganglia. *Journal of neural transmission. Supplementum* (65):1-28.
97. Agnati LF, Tarakanov AO, Ferre S, Fuxe K, & Guidolin D (2005) Receptor-receptor interactions, receptor mosaics, and basic principles of molecular network organization: possible implications for drug development. *Journal of molecular neuroscience : MN* 26(2-3):193-208.
98. Fuxe K, Marcellino D, Guidolin D, Woods AS, & Agnati LF (2008) Heterodimers and receptor mosaics of different types of G-protein-coupled receptors. *Physiology (Bethesda, Md.)* 23:322-332.
99. Tsai CJ, del Sol A, & Nussinov R (2008) Allosterity: absence of a change in shape does not imply that allosterity is not at play. *Journal of molecular biology* 378(1):1-11.
100. Gunasekaran K, Ma B, & Nussinov R (2004) Is allosterity an intrinsic property of all dynamic proteins? *Proteins* 57(3):433-443.
101. Del Sol A, Arauzo-Bravo MJ, Amoros D, & Nussinov R (2007) Modular architecture of protein structures and allosteric communications: potential implications for signaling proteins and regulatory linkages. *Genome biology* 8(5):R92.
102. Agnati LF, *et al.* (2010) Receptor-receptor interactions: A novel concept in brain integration. *Progress in neurobiology* 90(2):157-175.
103. Barki-Harrington L, Luttrell LM, & Rockman HA (2003) Dual inhibition of beta-adrenergic and angiotensin II receptors by a single antagonist: a functional role for receptor-receptor interaction in vivo. *Circulation* 108(13):1611-1618.
104. Szidonya L, Cserzo M, & Hunyady L (2008) Dimerization and oligomerization of G-protein-coupled receptors: debated structures with established and emerging functions. *The Journal of endocrinology* 196(3):435-453.
105. Gonzalez-Maeso J, *et al.* (2007) Hallucinogens recruit specific cortical 5-HT(2A) receptor-mediated signaling pathways to affect behavior. *Neuron* 53(3):439-452.
106. Stanasila L, Perez JB, Vogel H, & Cotecchia S (2003) Oligomerization of the alpha 1a- and alpha 1b-adrenergic receptor subtypes. Potential implications in receptor internalization. *The Journal of biological chemistry* 278(41):40239-40251.
107. Hirono M, Yoshioka T, & Konishi S (2001) GABA(B) receptor activation enhances mGluR-mediated responses at cerebellar excitatory synapses. *Nature neuroscience* 4(12):1207-1216.
108. Kamikubo Y, *et al.* (2007) Postsynaptic GABAB receptor signalling enhances LTD in mouse cerebellar Purkinje cells. *The Journal of physiology* 585(Pt 2):549-563.
109. Rives ML, *et al.* (2009) Crosstalk between GABAB and mGlu1a receptors reveals new insight into GPCR signal integration. *The EMBO journal* 28(15):2195-2208.
110. Drury AN & Szent-Gyorgyi A (1929) The physiological activity of adenine compounds with especial reference to their action upon the mammalian heart. *J Physiol* 68(3):213-237.

111. Holton P & Perry WL (1951) On the transmitter responsible for antidromic vasodilatation in the rabbit's ear. *J Physiol* 114(1-2):240-251.
112. Holton FA & Holton P (1952) The vasodilator activity of spinal roots. *J Physiol* 118(3):310-327.
113. Holton P (1959) The liberation of adenosine triphosphate on antidromic stimulation of sensory nerves. *J Physiol* 145(3):494-504.
114. Burnstock G, Campbell G, Satchell D, & Smythe A (1997) Evidence that adenosine triphosphate or a related nucleotide is the transmitter substance released by non-adrenergic inhibitory nerves in the gut. 1970. *Br J Pharmacol* 120(4 Suppl):337-357; discussion 334-336.
115. Burnstock G, Cocks T, Kasakov L, & Wong HK (1978) Direct evidence for ATP release from non-adrenergic, non-cholinergic ("purinergic") nerves in the guinea-pig taenia coli and bladder. *European journal of pharmacology* 49(2):145-149.
116. Burnstock G (1977) The purinergic nerve hypothesis. *Ciba Foundation symposium* (48):295-314.
117. Burnstock G (1976) Purinergic receptors. *J Theor Biol* 62(2):491-503.
118. Burnstock G & Kennedy C (1985) Is there a basis for distinguishing two types of P2-purinoceptor? *General pharmacology* 16(5):433-440.
119. Seifert R & Schultz G (1989) Involvement of pyrimidinoceptors in the regulation of cell functions by uridine and by uracil nucleotides. *Trends in pharmacological sciences* 10(9):365-369.
120. Abbracchio MP & Burnstock G (1994) Purinoceptors: are there families of P2X and P2Y purinoceptors? *Pharmacol Ther* 64(3):445-475.
121. Ralevic V & Burnstock G (1998) Receptors for purines and pyrimidines. *Pharmacological reviews* 50(3):413-492.
122. Burnstock G (2004) Introduction: P2 receptors. *Current topics in medicinal chemistry* 4(8):793-803.
123. Abbracchio MP, *et al.* (2006) International Union of Pharmacology LVIII: update on the P2Y G protein-coupled nucleotide receptors: from molecular mechanisms and pathophysiology to therapy. *Pharmacological reviews* 58(3):281-341.
124. Salati LM, Gross CJ, Henderson LM, & Savaiano DA (1984) Absorption and metabolism of adenine, adenosine-5'-monophosphate, adenosine and hypoxanthine by the isolated vascularly perfused rat small intestine. *The Journal of nutrition* 114(4):753-760.
125. Schuster S & Kenanov D (2005) Adenine and adenosine salvage pathways in erythrocytes and the role of S-adenosylhomocysteine hydrolase. A theoretical study using elementary flux modes. *The FEBS journal* 272(20):5278-5290.
126. Bodin P & Burnstock G (2001) Purinergic signalling: ATP release. *Neurochem Res* 26(8-9):959-969.
127. Burnstock G (2006) Historical review: ATP as a neurotransmitter. *Trends Pharmacol Sci* 27(3):166-176.
128. Silinsky EM, Gerzanich V, & Vanner SM (1992) ATP mediates excitatory synaptic transmission in mammalian neurones. *British journal of pharmacology* 106(4):762-763.
129. Burnstock G (2009) Purinergic cotransmission. *F1000 Biol Rep* 1:46.
130. Westfall DP, Stitzel RE, & Rowe JN (1978) The postjunctional effects and neural release of purine compounds in the guinea-pig vas deferens. *European journal of pharmacology* 50(1):27-38.
131. Fedan JS, Hogaboom GK, O'Donnell JP, Colby J, & Westfall DP (1981) Contribution by purines to the neurogenic response of the vas deferens of the guinea pig. *European journal of pharmacology* 69(1):41-53.
132. Burnstock G (1990) Noradrenaline and ATP as cotransmitters in sympathetic nerves. *Neurochemistry international* 17(2):357-368.

133. Ventura S, Dewalagama RK, & Lau LC (2003) Adenosine 5'-triphosphate (ATP) is an excitatory cotransmitter with noradrenaline to the smooth muscle of the rat prostate gland. *Br J Pharmacol* 138(7):1277-1284.
134. Charles H.V H (1996) Purinergic cotransmission: parasympathetic and enteric nerves. *Seminars in Neuroscience* 8(4):207-215.
135. Cotrina ML, *et al.* (1998) Connexins regulate calcium signaling by controlling ATP release. *Proceedings of the National Academy of Sciences of the United States of America* 95(26):15735-15740.
136. Queiroz G, Meyer DK, Meyer A, Starke K, & von Kugelgen I (1999) A study of the mechanism of the release of ATP from rat cortical astroglial cells evoked by activation of glutamate receptors. *Neuroscience* 91(3):1171-1181.
137. Hazama A, Hayashi S, & Okada Y (1998) Cell surface measurements of ATP release from single pancreatic beta cells using a novel biosensor technique. *Pflugers Archiv : European journal of physiology* 437(1):31-35.
138. Fields RD & Stevens B (2000) ATP: an extracellular signaling molecule between neurons and glia. *Trends in neurosciences* 23(12):625-633.
139. Fields RD & Burnstock G (2006) Purinergic signalling in neuron-glia interactions. *Nature reviews. Neuroscience* 7(6):423-436.
140. Kenakin TP, Bond RA, & Bonner TI (1992) Definition of pharmacological receptors. *Pharmacol Rev* 44(3):351-362.
141. Bruns RF & Fergus JH (1989) Solubilities of adenosine antagonists determined by radioreceptor assay. *The Journal of pharmacy and pharmacology* 41(9):590-594.
142. Abbracchio MP, F. C, Fredholm BB, & Williams M (1993) Purinoceptor Nomenclature: A Status Report. *Drug Development Research* (28):207-213.
143. Sattin A & Rall TW (1970) The effect of adenosine and adenine nucleotides on the cyclic adenosine 3', 5'-phosphate content of guinea pig cerebral cortex slices. *Molecular pharmacology* 6(1):13-23.
144. van Calker D, Muller M, & Hamprecht B (1979) Adenosine regulates via two different types of receptors, the accumulation of cyclic AMP in cultured brain cells. *Journal of neurochemistry* 33(5):999-1005.
145. Abbracchio MP, *et al.* (2003) Characterization of the UDP-glucose receptor (re-named here the P2Y14 receptor) adds diversity to the P2Y receptor family. *Trends Pharmacol Sci* 24(2):52-55.
146. Jacobson KA, Jarvis MF, & Williams M (2002) Purine and pyrimidine (P2) receptors as drug targets. *J Med Chem* 45(19):4057-4093.
147. Erb L, *et al.* (1995) Site-directed mutagenesis of P2U purinoceptors. Positively charged amino acids in transmembrane helices 6 and 7 affect agonist potency and specificity. *J Biol Chem* 270(9):4185-4188.
148. Jiang Q, *et al.* (1997) A mutational analysis of residues essential for ligand recognition at the human P2Y1 receptor. *Mol Pharmacol* 52(3):499-507.
149. Conigrave AD, *et al.* (1998) Pharmacological profile of a novel cyclic AMP-linked P2 receptor on undifferentiated HL-60 leukemia cells. *Br J Pharmacol* 124(7):1580-1585.
150. King BF & Townsend-Nicholson A (2003) Nucleotide and Nucleoside Receptors. *Tocris Reviews* 23:1-12.
151. Moro S, *et al.* (1998) Human P2Y1 receptor: molecular modeling and site-directed mutagenesis as tools to identify agonist and antagonist recognition sites. *Journal of medicinal chemistry* 41(9):1456-1466.
152. Moro S, Hoffmann C, & Jacobson KA (1999) Role of the extracellular loops of G protein-coupled receptors in ligand recognition: a molecular modeling study of the human P2Y1 receptor. *Biochemistry* 38(12):3498-3507.

153. White PJ, Webb TE, & Boarder MR (2003) Characterization of a Ca²⁺ response to both UTP and ATP at human P2Y₁₁ receptors: evidence for agonist-specific signaling. *Molecular pharmacology* 63(6):1356-1363.
154. Communi D, et al. (2001) Identification of a novel human ADP receptor coupled to G(i). *J Biol Chem* 276(44):41479-41485.
155. King BF (2002) 2-Chloro-N⁶-methyl-(N)-methanocarba-2'-deoxyadenosine-3',5'-bisphosphate is a selective high affinity P2Y₁ receptor antagonist: commentary on Boyer et al. *Br J Pharmacol* 135(8):1839-1840.
156. Webb TE, et al. (1993) Cloning and functional expression of a brain G-protein-coupled ATP receptor. *FEBS Lett* 324(2):219-225.
157. Palmer RK, Boyer JL, Schachter JB, Nicholas RA, & Harden TK (1998) Agonist action of adenosine triphosphates at the human P2Y₁ receptor. *Molecular pharmacology* 54(6):1118-1123.
158. Boyer JL, Romero-Avila T, Schachter JB, & Harden TK (1996) Identification of competitive antagonists of the P2Y₁ receptor. *Molecular pharmacology* 50(5):1323-1329.
159. Boyer JL, Adams M, Ravi RG, Jacobson KA, & Harden TK (2002) 2-Chloro N⁶-methyl-(N)-methanocarba-2'-deoxyadenosine-3',5'-bisphosphate is a selective high affinity P2Y₁ receptor antagonist. *Br J Pharmacol* 135(8):2004-2010.
160. Boyer JL, Mohanram A, Camaioni E, Jacobson KA, & Harden TK (1998) Competitive and selective antagonism of P2Y₁ receptors by N⁶-methyl 2'-deoxyadenosine 3',5'-bisphosphate. *British journal of pharmacology* 124(1):1-3.
161. Mathieu R, Baurand A, Schmitt M, Gachet C, & Bourguignon JJ (2004) Synthesis and biological activity of 2-alkylated deoxyadenosine bisphosphate derivatives as P2Y₁ receptor antagonists. *Bioorg Med Chem* 12(7):1769-1779.
162. Kim HS, et al. (2003) 2-Substitution of adenine nucleotide analogues containing a bicyclo[3.1.0]hexane ring system locked in a northern conformation: enhanced potency as P2Y₁ receptor antagonists. *J Med Chem* 46(23):4974-4987.
163. Fam SR, et al. (2005) P2Y₁ receptor signaling is controlled by interaction with the PDZ scaffold NHERF-2. *Proceedings of the National Academy of Sciences of the United States of America* 102(22):8042-8047.
164. Lee SY, Wolff SC, Nicholas RA, & O'Grady SM (2003) P2Y receptors modulate ion channel function through interactions involving the C-terminal domain. *Molecular pharmacology* 63(4):878-885.
165. Ayyanathan K, et al. (1996) Cloning and chromosomal localization of the human P2Y₁ purinoceptor. *Biochem Biophys Res Commun* 218(3):783-788.
166. Moore DJ, et al. (2001) Expression pattern of human P2Y receptor subtypes: a quantitative reverse transcription-polymerase chain reaction study. *Biochim Biophys Acta* 1521(1-3):107-119.
167. Haseruck N, et al. (2004) The plaque lipid lysophosphatidic acid stimulates platelet activation and platelet-monocyte aggregate formation in whole blood: involvement of P2Y₁ and P2Y₁₂ receptors. *Blood* 103(7):2585-2592.
168. Leon C, et al. (1999) Defective platelet aggregation and increased resistance to thrombosis in purinergic P2Y₁ receptor-null mice. *J Clin Invest* 104(12):1731-1737.
169. Fabre JE, et al. (1999) Decreased platelet aggregation, increased bleeding time and resistance to thromboembolism in P2Y₁-deficient mice. *Nat Med* 5(10):1199-1202.
170. Leon C, et al. (2001) Key role of the P2Y₁ receptor in tissue factor-induced thrombin-dependent acute thromboembolism: studies in P2Y₁-knockout mice and mice treated with a P2Y₁ antagonist. *Circulation* 103(5):718-723.

171. Tsim KW & Barnard EA (2002) The signaling pathways mediated by P2Y nucleotide receptors in the formation and maintenance of the skeletal neuromuscular junction. *Neurosignals* 11(1):58-64.
172. Buvinic S, *et al.* (2006) P2Y1 and P2Y2 receptor distribution varies along the human placental vascular tree: role of nucleotides in vascular tone regulation. *J Physiol* 573(Pt 2):427-443.
173. Gallagher JA (2004) ATP P2 receptors and regulation of bone effector cells. *J Musculoskelet Neuronal Interact* 4(2):125-127.
174. King BF & Townsend-Nicholson A (2008) Involvement of P2Y1 and P2Y11 purinoceptors in parasympathetic inhibition of colonic smooth muscle. *J Pharmacol Exp Ther* 324(3):1055-1063.
175. Guzman SJ, *et al.* (2010) P2Y1 receptors inhibit long-term depression in the prefrontal cortex. *Neuropharmacology* 59(6):406-415.
176. Communi D, Govaerts C, Parmentier M, & Boeynaems JM (1997) Cloning of a human purinergic P2Y receptor coupled to phospholipase C and adenylyl cyclase. *The Journal of biological chemistry* 272(51):31969-31973.
177. Communi D, Robaye B, & Boeynaems JM (1999) Pharmacological characterization of the human P2Y11 receptor. *British journal of pharmacology* 128(6):1199-1206.
178. Qi AD, Kennedy C, Harden TK, & Nicholas RA (2001) Differential coupling of the human P2Y(11) receptor to phospholipase C and adenylyl cyclase. *British journal of pharmacology* 132(1):318-326.
179. Boeynaems JM, Communi D, Savi P, & Herbert JM (2000) P2Y receptors: in the middle of the road. *Trends Pharmacol Sci* 21(1):1-3.
180. Conigrave AD, *et al.* (2001) P2Y(11) receptor expression by human lymphocytes: evidence for two cAMP-linked purinoceptors. *Eur J Pharmacol* 426(3):157-163.
181. Suh BC, Kim TD, Lee IS, & Kim KT (2000) Differential regulation of P2Y(11) receptor-mediated signalling to phospholipase C and adenylyl cyclase by protein kinase C in HL-60 promyelocytes. *Br J Pharmacol* 131(3):489-497.
182. von Kügelgen I & Wetter A (2000) Molecular pharmacology of P2Y-receptors. *Naunyn-Schmiedeberg's Archives of Pharmacology* 362(4):310-323.
183. Communi D, Suarez-Huerta N, Dussossoy D, Savi P, & Boeynaems JM (2001) Cotranscription and intergenic splicing of human P2Y11 and SSF1 genes. *J Biol Chem* 276(19):16561-16566.
184. Wilkin F, *et al.* (2001) The P2Y11 receptor mediates the ATP-induced maturation of human monocyte-derived dendritic cells. *J Immunol* 166(12):7172-7177.
185. la Sala A, *et al.* (2002) Dendritic cells exposed to extracellular adenosine triphosphate acquire the migratory properties of mature cells and show a reduced capacity to attract type 1 T lymphocytes. *Blood* 99(5):1715-1722.
186. Schnurr M, *et al.* (2003) ATP gradients inhibit the migratory capacity of specific human dendritic cell types: implications for P2Y11 receptor signaling. *Blood* 102(2):613-620.
187. Jiang L, *et al.* (1997) Extracellular ATP triggers cyclic AMP-dependent differentiation of HL-60 cells. *Biochem Biophys Res Commun* 232(3):626-630.
188. Conigrave AD, *et al.* (2000) Extracellular ATP-dependent suppression of proliferation and induction of differentiation of human HL-60 leukemia cells by distinct mechanisms. *Biochem Pharmacol* 60(11):1585-1591.
189. van der Weyden L, Rakyian V, Luttrell BM, Morris MB, & Conigrave AD (2000) Extracellular ATP couples to cAMP generation and granulocytic differentiation in human NB4 promyelocytic leukaemia cells. *Immunol Cell Biol* 78(5):467-473.
190. Nguyen TD, Meichle S, Kim US, Wong T, & Moody MW (2001) P2Y11, a purinergic receptor acting via cAMP, mediates secretion by pancreatic duct epithelial cells. *Am J Physiol Gastrointest Liver Physiol* 280(5):G795-804.

191. Feng C, Mery AG, Beller EM, Favot C, & Boyce JA (2004) Adenine nucleotides inhibit cytokine generation by human mast cells through a Gs-coupled receptor. *J Immunol* 173(12):7539-7547.
192. Amisten S, Melander O, Wihlborg AK, Berglund G, & Erlinge D (2007) Increased risk of acute myocardial infarction and elevated levels of C-reactive protein in carriers of the Thr-87 variant of the ATP receptor P2Y11. *Eur Heart J* 28(1):13-18.
193. Xiao Z, *et al.* (2011) P2Y11 impairs cell proliferation by induction of cell cycle arrest and sensitizes endothelial cells to cisplatin-induced cell death. *J Cell Biochem* 112(9):2257-2265.
194. Vaughan KR, *et al.* (2007) Inhibition of neutrophil apoptosis by ATP is mediated by the P2Y11 receptor. *J Immunol* 179(12):8544-8553.
195. Sanders KM (2000) Postjunctional electrical mechanisms of enteric neurotransmission. *Gut* 47 Suppl 4:iv23-25; discussion iv26.
196. Zhou XB, *et al.* (2001) A molecular switch for specific stimulation of the BKCa channel by cGMP and cAMP kinase. *J Biol Chem* 276(46):43239-43245.
197. Burnstock G (2006) Pathophysiology and therapeutic potential of purinergic signaling. *Pharmacological reviews* 58(1):58-86.
198. Filippov IB, Vladimirova IA, Ganitkevich VY, & Shuba MF (2004) Adenylate cyclase-mediated modulation of interaction between excitatory and inhibitory synaptic influences on smooth muscles. *Neurophysiology* 36(5):391-397.
199. Sojo V (2012) Conformation-Activity Relationship of G-Protein-Coupled Receptors: Computational Modelling of the human P2Y1 receptor.
200. Chen C & Okayama H (1987) High-efficiency transformation of mammalian cells by plasmid DNA. *Molecular and cellular biology* 7(8):2745-2752.
201. Barcroft J & Hill AV (1910) The nature of oxyhaemoglobin, with a note on its molecular weight. *The Journal of physiology* 39(6):411-428.
202. Hill AV (1910.) The possible effects of the aggregation of the molecules of hemoglobin on its dissociation curves. *Proceedings of the Physiological Society* 40:4-6.
203. Walker JS, Li X, & Buttrick PM (2010) Analysing force-pCa curves. *Journal of muscle research and cell motility* 31(1):59-69.
204. Colquhoun D (2006) The quantitative analysis of drug-receptor interactions: a short history. *Trends in pharmacological sciences* 27(3):149-157.
205. Goutelle S, *et al.* (2008) The Hill equation: a review of its capabilities in pharmacological modelling. *Fundamental & clinical pharmacology* 22(6):633-648.
206. Colquhoun D (2007) Why the Schild method is better than Schild realised. *Trends in pharmacological sciences* 28(12):608-614.
207. Marcet B, Chappe V, Delmas P, & Verrier B (2004) Pharmacological and signaling properties of endogenous P2Y1 receptors in cystic fibrosis transmembrane conductance regulator-expressing Chinese hamster ovary cells. *The Journal of pharmacology and experimental therapeutics* 309(2):533-539.
208. Iredale PA & Hill SJ (1993) Increases in intracellular calcium via activation of an endogenous P2-purinoceptor in cultured CHO-K1 cells. *British journal of pharmacology* 110(4):1305-1310.
209. Michel AD, Chessell IP, Hibell AD, Simon J, & Humphrey PP (1998) Identification and characterization of an endogenous P2X7 (P2Z) receptor in CHO-K1 cells. *British journal of pharmacology* 125(6):1194-1201.
210. King BF & Townsend-Nicholson A (2003) Nucleotide and Nucleoside Receptors *Tocris* 23.
211. Qi AD, Zambon AC, Insel PA, & Nicholas RA (2001) An arginine/glutamine difference at the juxtaposition of transmembrane domain 6 and the third

- extracellular loop contributes to the markedly different nucleotide selectivities of human and canine P2Y₁₁ receptors. *Molecular pharmacology* 60(6):1375-1382.
212. Bradley KK & Bradley ME (2001) Purine nucleoside-dependent inhibition of cellular proliferation in 1321N1 human astrocytoma cells. *The Journal of pharmacology and experimental therapeutics* 299(2):748-752.
 213. Brown JH, *et al.* (1997) Pathways and roadblocks in muscarinic receptor-mediated growth regulation. *Life sciences* 60(13-14):1077-1084.
 214. Yagle K, Lu H, Guizzetti M, Moller T, & Costa LG (2001) Activation of mitogen-activated protein kinase by muscarinic receptors in astroglial cells: role in DNA synthesis and effect of ethanol. *Glia* 35(2):111-120.
 215. Guizzetti M & Costa LG (2001) Activation of phosphatidylinositol 3 kinase by muscarinic receptors in astrocytoma cells. *Neuroreport* 12(8):1639-1642.
 216. Guizzetti M & Costa LG (2000) Muscarinic receptors, protein kinase C isozymes and proliferation of astroglial cells: effects of ethanol. *Neurotoxicology* 21(6):1117-1121.
 217. Guizzetti M, Thompson BD, Kim Y, VanDeMark K, & Costa LG (2004) Role of phospholipase D signaling in ethanol-induced inhibition of carbachol-stimulated DNA synthesis of 1321N1 astrocytoma cells. *Journal of neurochemistry* 90(3):646-653.
 218. Nieto M, Kennedy E, Goldstein D, & Brown JH (1994) Rapid heterologous desensitization of muscarinic and thrombin receptor-mediated phospholipase D activation. *Molecular pharmacology* 46(3):406-413.
 219. Tang X, Wang L, Proud CG, & Downes CP (2003) Muscarinic receptor-mediated activation of p70 S6 kinase 1 (S6K1) in 1321N1 astrocytoma cells: permissive role of phosphoinositide 3-kinase. *The Biochemical journal* 374(Pt 1):137-143.
 220. Tang X, Batty IH, & Downes CP (2002) Muscarinic receptors mediate phospholipase C-dependent activation of protein kinase B via Ca²⁺, ErbB3, and phosphoinositide 3-kinase in 1321N1 astrocytoma cells. *The Journal of biological chemistry* 277(1):338-344.
 221. Meis S, *et al.* (2010) NF546 [4,4'-(carbonylbis(imino-3,1-phenylene-carbonylimino-3,1-(4-methyl-phenylene)-carbonylimino))-bis(1,3-xylene-alpha,alpha'-diphosphonic acid) tetrasodium salt] is a non-nucleotide P2Y₁₁ agonist and stimulates release of interleukin-8 from human monocyte-derived dendritic cells. *The Journal of pharmacology and experimental therapeutics* 332(1):238-247.
 222. Lazareno S & Birdsall NJ (1993) Estimation of antagonist K_b from inhibition curves in functional experiments: alternatives to the Cheng-Prusoff equation. *Trends in pharmacological sciences* 14(6):237-239.
 223. Leff P & Dougall IG (1993) Further concerns over Cheng-Prusoff analysis. *Trends in pharmacological sciences* 14(4):110-112.
 224. Bultmann R & Starke K (1995) Reactive red 2: a P2y-selective purinoceptor antagonist and an inhibitor of ecto-nucleotidase. *Naunyn-Schmiedeberg's archives of pharmacology* 352(5):477-482.
 225. Clark AJ & Raventos J (1937) The Antagonism of Acetylcholine and of Quaternary Ammonium Salts.
 226. Watson C, *et al.* (2000) The use of stimulus-biased assay systems to detect agonist-specific receptor active states: implications for the trafficking of receptor stimulus by agonists. *Molecular pharmacology* 58(6):1230-1238.
 227. Hall DA (2000) Modeling the functional effects of allosteric modulators at pharmacological receptors: an extension of the two-state model of receptor activation. *Molecular pharmacology* 58(6):1412-1423.
 228. Prinz H (2010) Hill coefficients, dose-response curves and allosteric mechanisms. *Journal of chemical biology* 3(1):37-44.

229. Morrow GB, Nicholas RA, & Kennedy C (2014) UTP is not a biased agonist at human P2Y₁₁ receptors. *Purinergic signalling* 10(4):581-585.
230. Li X, Llorente I, & Brasch M (2008) Improvements in live cell analysis of G protein coupled receptors using second generation BD calcium assay kits. *Current chemical genomics* 2:10-15.
231. Schachter JB, Li Q, Boyer JL, Nicholas RA, & Harden TK (1996) Second messenger cascade specificity and pharmacological selectivity of the human P2Y₁-purinoceptor. *British journal of pharmacology* 118(1):167-173.
232. Filtz TM, Li Q, Boyer JL, Nicholas RA, & Harden TK (1994) Expression of a cloned P2Y purinergic receptor that couples to phospholipase C. *Molecular pharmacology* 46(1):8-14.
233. Boyer JL, Lazarowski ER, Chen XH, & Harden TK (1993) Identification of a P2Y-purinergic receptor that inhibits adenylyl cyclase. *The Journal of pharmacology and experimental therapeutics* 267(3):1140-1146.
234. Vigne P, Feolde E, Breittmayer JP, & Frelin C (1994) Characterization of the effects of 2-methylthio-ATP and 2-chloro-ATP on brain capillary endothelial cells: similarities to ADP and differences from ATP. *British journal of pharmacology* 112(3):775-780.
235. Takasaki J, *et al.* (2001) Molecular cloning of the platelet P2T(AC) ADP receptor: pharmacological comparison with another ADP receptor, the P2Y(1) receptor. *Molecular pharmacology* 60(3):432-439.
236. Kaiser RA & Buxton IL (2002) Nucleotide-mediated relaxation in guinea-pig aorta: selective inhibition by MRS2179. *British journal of pharmacology* 135(2):537-545.
237. Baurand A, *et al.* (2001) Inhibition of platelet function by administration of MRS2179, a P2Y₁ receptor antagonist. *European journal of pharmacology* 412(3):213-221.
238. Baurand A & Gachet C (2003) The P2Y(1) receptor as a target for new antithrombotic drugs: a review of the P2Y(1) antagonist MRS-2179. *Cardiovascular drug reviews* 21(1):67-76.
239. Camaioni E, Boyer JL, Mohanram A, Harden TK, & Jacobson KA (1998) Deoxyadenosine bisphosphate derivatives as potent antagonists at P2Y₁ receptors. *Journal of medicinal chemistry* 41(2):183-190.
240. Hansmann G, Bultmann R, Tuluc F, & Starke K (1997) Characterization by antagonists of P2-receptors mediating endothelium-dependent relaxation in the rat aorta. *Naunyn-Schmiedeberg's archives of pharmacology* 356(5):641-652.
241. Casado V, *et al.* (2007) Old and new ways to calculate the affinity of agonists and antagonists interacting with G-protein-coupled monomeric and dimeric receptors: the receptor-dimer cooperativity index. *Pharmacology & therapeutics* 116(3):343-354.
242. Ecke D, Fischer B, & Reiser G (2008) Diastereoselectivity of the P2Y₁₁ nucleotide receptor: mutational analysis. *British journal of pharmacology* 155(8):1250-1255.
243. Zylberg J, Ecke D, Fischer B, & Reiser G (2007) Structure and ligand-binding site characteristics of the human P2Y₁₁ nucleotide receptor deduced from computational modelling and mutational analysis. *The Biochemical journal* 405(2):277-286.
244. Ostrom RS & Insel PA (2004) The evolving role of lipid rafts and caveolae in G protein-coupled receptor signaling: implications for molecular pharmacology. *British journal of pharmacology* 143(2):235-245.
245. Agnati LF, *et al.* (2005) How proteins come together in the plasma membrane and function in macromolecular assemblies: focus on receptor mosaics. *Journal of molecular neuroscience : MN* 26(2-3):133-154.

246. Kaiser RA, Oxhorn BC, Andrews G, & Buxton IL (2002) Functional compartmentation of endothelial P2Y receptor signaling. *Circulation research* 91(4):292-299.
247. Amadio S, Vacca F, Martorana A, Sancesario G, & Volonte C (2007) P2Y1 receptor switches to neurons from glia in juvenile versus neonatal rat cerebellar cortex. *BMC developmental biology* 7:77.
248. Franco R, *et al.* (2008) G-protein-coupled receptor heteromers: function and ligand pharmacology. *British journal of pharmacology* 153 Suppl 1:S90-98.
249. Rodbell M (1995) Signal transduction: evolution of an idea. *Environmental health perspectives* 103(4):338-345.
250. Kamal M, Maurice P, & Jockers R (2011) Expanding the Concept of G Protein-Coupled Receptor (GPCR) Dimer Asymmetry towards GPCR-Interacting Proteins. *Pharmaceuticals* 4(12):273-284.
251. Jefferson JR, Harmon JT, & Jamieson GA (1988) Identification of high-affinity (Kd 0.35 μ mol/L) and low-affinity (Kd 7.9 μ mol/L) platelet binding sites for ADP and competition by ADP analogues. *Blood* 71(1):110-116.
252. Lips JP, Sixma JJ, & Schiphorst ME (1980) Binding of adenosine diphosphate to human blood platelets and to isolated blood platelet membranes. *Biochimica et biophysica acta* 628(4):451-467.
253. Bauvois B, Legrand C, & Caen JP (1980) Interaction of adenosine and adenylnucleotides with the human platelet membrane. Further characterization of the ADP binding sites. *Haemostasis* 9(2):92-104.
254. Ciruela F, *et al.* (2006) Presynaptic control of striatal glutamatergic neurotransmission by adenosine A1-A2A receptor heteromers. *The Journal of neuroscience : the official journal of the Society for Neuroscience* 26(7):2080-2087.
255. Ferre S, von Euler G, Johansson B, Fredholm BB, & Fuxe K (1991) Stimulation of high-affinity adenosine A2 receptors decreases the affinity of dopamine D2 receptors in rat striatal membranes. *Proceedings of the National Academy of Sciences of the United States of America* 88(16):7238-7241.
256. Kotevic I, Kirschner KM, Porzig H, & Baltensperger K (2005) Constitutive interaction of the P2Y2 receptor with the hematopoietic cell-specific G protein G(α 16) and evidence for receptor oligomers. *Cellular signalling* 17(7):869-880.
257. Suzuki T, Namba K, Tsuga H, & Nakata H (2006) Regulation of pharmacology by hetero-oligomerization between A1 adenosine receptor and P2Y2 receptor. *Biochemical and biophysical research communications* 351(2):559-565.
258. Namba K, Suzuki T, & Nakata H (2010) Immunogold electron microscopic evidence of in situ formation of homo- and heteromeric purinergic adenosine A1 and P2Y2 receptors in rat brain. *BMC research notes* 3:323.
259. Vidi PA, Przybyla JA, Hu CD, & Watts VJ (2010) Visualization of G protein-coupled receptor (GPCR) interactions in living cells using bimolecular fluorescence complementation (BiFC). *Current protocols in neuroscience / editorial board, Jacqueline N. Crawley ... [et al.]* Chapter 5:Unit 5.29.
260. Vidi PA & Watts VJ (2009) Fluorescent and bioluminescent protein-fragment complementation assays in the study of G protein-coupled receptor oligomerization and signaling. *Molecular pharmacology* 75(4):733-739.
261. Ghosh E, Kumari P, Jaiman D, & Shukla AK (2015) Methodological advances: the unsung heroes of the GPCR structural revolution. *Nature reviews. Molecular cell biology* 16(2):69-81.
262. Vendrell M, *et al.* (2007) Novel ergopeptides as dual ligands for adenosine and dopamine receptors. *Journal of medicinal chemistry* 50(13):3062-3069.

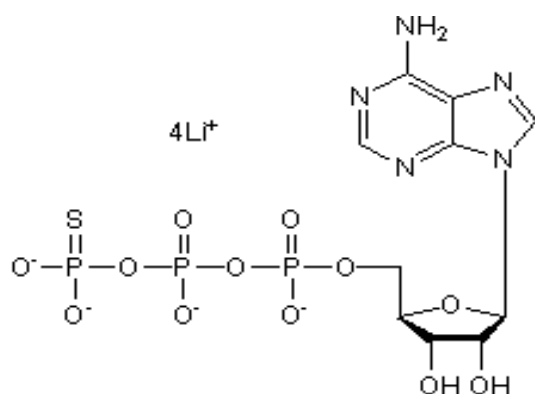
263. Safari J & Zarnegar Z (2014) Advanced drug delivery systems: Nanotechnology of health design A review. *Journal of Saudi Chemical Society* 18(2):85-99.
264. Nam KH, Smith AS, Lone S, Kwon S, & Kim DH (2014) Biomimetic 3D Tissue Models for Advanced High-Throughput Drug Screening. *Journal of laboratory automation*.
265. Imamura Y, *et al.* (2015) Comparison of 2D- and 3D-culture models as drug-testing platforms in breast cancer. *Oncology reports*.

Appendix 1

List of Ligands

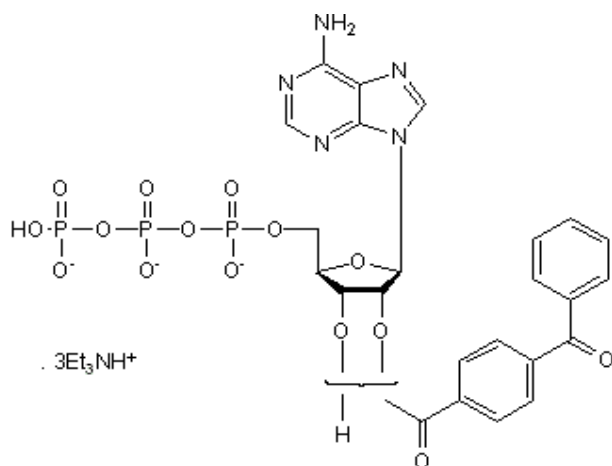
1- ATP γ S

Chemical Name: Adenosine-5'-(γ -thio)-triphosphate tetralithium salt



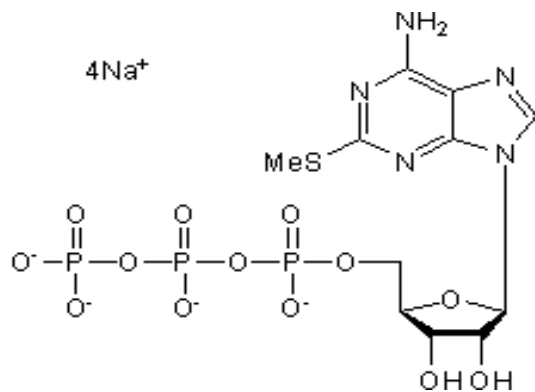
2- BzATP

Chemical Name: 2'(3')-O-(4-Benzoylbenzoyl)adenosine-5'-triphosphate tri(triethylammonium) salt



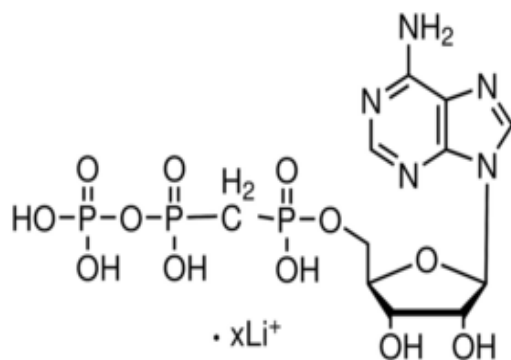
3- 2meSATP

Chemical Name: 2-Methylthioadenosine-5'-triphosphate tetrasodium salt



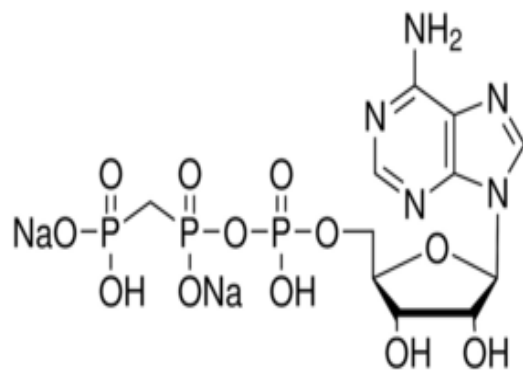
4- $\alpha\beta$ meATP

Chemical name: α,β -Methyleneadenosine 5'-triphosphate lithium salt



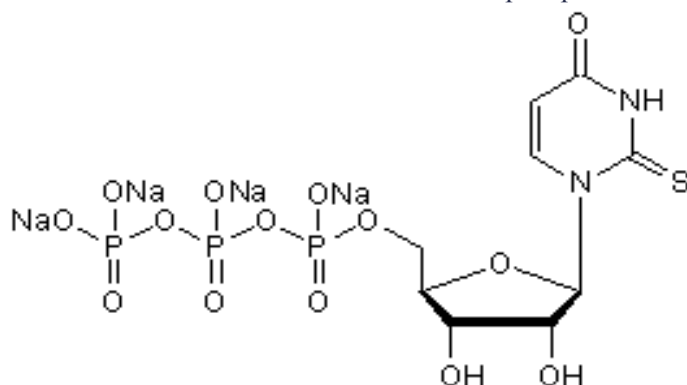
5- $\beta\gamma$ meATP:

Chemical name: β,γ -Methyleneadenosine 5'-triphosphate disodium salt



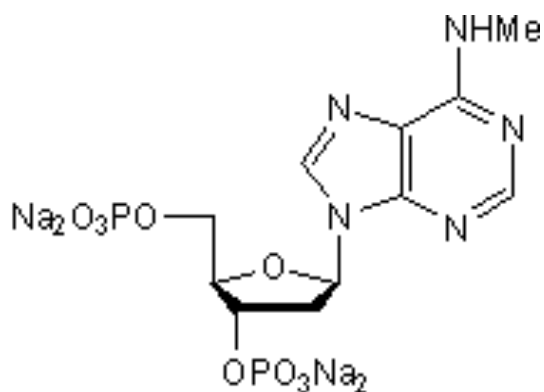
6-UTP:

Chemical name: 2-Thiouridine 5'-triphosphate tetrasodium salt



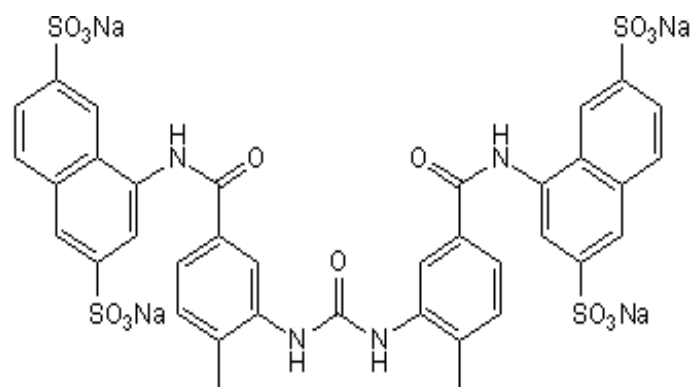
7- MRS 2179 :

Chemical Name: 2'-Deoxy-N6-methyladenosine 3',5'-bisphosphate tetrasodium salt



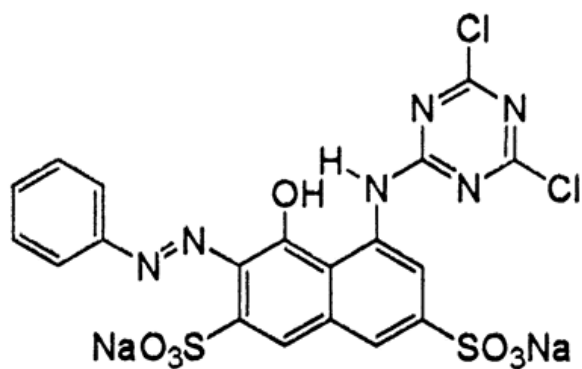
8- NF 340:

Chemical Name: 4,4'-(Carbonylbis(imino-3,1-(4-methyl-phenylene)carbonylimino))bis(naphthalene-2,6-disulfonic acid) tetrasodium salt



9- Reactive Red :

Molecular Formula: C₁₉H₁₀Cl₂N₆Na₂O₇S₂



The structures of ADP and ATP are shown in Figure 1- in the Chapter I (introduction).